Journal of Industrial Technology Vol. 19(1), 2010 - ICONT 2009, 1-16

PRELIMINARY ULCEROGENIC EVALUATION OF PIROXICAM – LOADED LIPOSOMES

Y. Azhar[1,2], H.S. Chiong[1,*], S. Malarvili[1], M.N. Somchit[1,2] and K.H. Yuen[3]

[1]Faculty of Medicine and Health Sciences, Universiti Putra Malaysia,
[2]Sports Academy, Universiti Putra Malaysia, 43400 UPM Serdang, Selangor, Malaysia;
[3]School of Pharmaceutical Sciences, Universiti Sains Malaysia, 11800 Minden, Penang, Malaysia.

***(chionghs@yahoo.com)**

ABSTRACT : Liposomal drug delivery system, a promising lipid-based nanoparticle technology, was used in the present work to encapsulate lipophilic non-steroidal anti-inflammatory drug, piroxicam. A 14 days sub-acute study was conducted to gather the preliminary toxicological information. All treated samples were freshly prepared prior to experiments. Rats (male Sprague Dawley; body weight 180-220 g; n=6/group) were intragastically fed with samples once a day in the morning. All rats were sacrificed by overdose of diethyl ether and median laparotomy was performed to isolate the stomach, liver and kidney. Stomach was opened along the greater curvature, rinsed carefully with saline and blotted dry before subjected to macroscopic evaluation. Stomach lesions were characterized into 6-score value. Stomach was cut and fixed in 10% formalin before subjected to routine histopathology processing. Tissues were observed under light microscope and lesion was characterized based on cellular morphological changes. Rats dosed with piroxicam (12, 18 and 24 mg/kg) exhibit significant ulcer scoring when compared to negative control group. Although the ulcer score for other treatment groups (blank liposomes and piroxicam-loaded liposomes) were found to be elevated, no statistically significant difference was obtained. Histologically, encasulation reduced the gastric inflammation. In conclusion, findings showed that the encapsulation of piroxicam into liposomes had the potential to reduce gastric ulceration problem in animal model.

KEYWORDS : Piroxicam, liposomes, nanoparticles, drug delivery

INTRODUCTION

Piroxicam (4-hydroxy-2-methyl-N-(pyridine-2-yl)-2H-1,2-benzothiazine-3-carboxamide-1,2-dioxide), an oxicam derivative, is a well-known non-steroidal anti-inflammatory compound with analgesic, anti-inflammatory and anti-pyretic effects (Canto *et al.*, 1999; Starek & Krzek, 2009). It has been prescribed for acute or long-term treatment of a wide variety of human diseases including rheumatoid arthritis, osteoarthritis, ankylosing spondylitis, acute gout, acute muscular and skeletal disorders as well as various pain states (Baudrimonta *et al.*, 1995 and Martin, 2003).

Despite its potent efficacy effects, piroxicam has also been associated with various side effects such as dizziness, skin rash, gastrointestinal, hepatic and renal symptoms (Canto *et al.,* 1999; Dalmora *et al.*, 2001; Sweetman, 2007). The most prominent side effects are gastrointestinal such as ulceration and hemorrhage, occurring in about 20 % of treated patients (Smith & Reynard, 1995). Its long plasma half-life may be associated with a particularly high incidence of gastrointestinal bleeding in the elderly (Neal, 2003). Thus, it is important to develop therapeutic and drug delivery systems that will minimize these adverse effects.

As one of the most promising nanoparticle technologies, liposomal delivery system is particularly attractive to achieve this objective. Liposomes are microscopic spherical vesicles composed of lipid bilayers which are formed by phospholipids dispersed in water (Gulati *et al.,* 1998). Drugs loaded in liposomes have been shown in various studies to exhibit improved therapeutic indices and pharmacological properties, mainly through the alteration of its biodistribution (Schilling & Metra, 1990 and Story, 1991).

MATERIALS AND METHODS

Materials

Two types of commercially available proliposomes, namely Pro-lipo™ Duo and Pro-lipo™ C which contained 50% and 40% unsaturated soybean phosphatidylcholine respectively and suspended in hydrophilic medium consisted of glycerol and ethanol, were obtained from Lucas Meyer, France. Piroxicam and dimethylsulfoxide were purchased from Sigma, USA.

Preparation of piroxicam-loaded and blank liposomes

Stock piroxicam solution (60 mg/ml) was prepared by dissolving piroxicam in dimethylsulfoide. Stock solution was then added into proliposomes (Pro-lipo™ Duo or Pro-lipo™ C) in a beaker with moderate stirring (125 ± 25 rpm) for 1 hour at room temperature. Next, this proliposomes mixture was converted to concentrated piroxicam-loaded liposomal suspension by drop-wise addition of distilled water. This liposomal suspension was stirred (hydrated) for 1 hour at room temperature before further diluted with distilled water to achieve final concentration of 1.2 mg/ml piroxicam. The ratio consists of; stock piroxicam solution: Pro-lipo™: distilled water (hydration): distilled water (dilution) was 1:5:9:35 w/w/w/w. Blank liposomes were prepared according to the same procedure except that dimethylsulfoxide was used instead of stock piroxicam solution.

Animals

40 *Sprague Dawley* rats (180-220 g) were used. Rats were checked for any signs of abnormalities before they were randomly assigned to different treatment groups (n=6). All rats were kept in standard cages at 23 ± 2 °C with 12 hours light/dark cycle in the animal house of FMHS, UPM and fed with commercial pellets once a day in the morning. The pellets fed was at 10 % of body weight. Tap water was provided *ad libitum* and bedding was changed twice a week to maintain hygiene and provide a clean environment to rats. All rats were first acclimatised to the laboratory environment for at least 1 week before subjected to experiments.

Repeated dosing

A 14 days sub-acute toxicity study was conducted to gather the preliminary toxicological information. All treated samples were prepared fresh prior to experiments. Rats in each group were intragastically fed (20 ml/kg) with samples once a day in the morning. The study was approved by the Animal Care and Use Committee (ACUC) FMHS, UPM.

Body weight and behavioural changes

The body weight and behavioural changes of each rat were recorded daily throughout the treatment period.

Collection of blood for bioassay

Blood samples (about 4 ml) were collected on the 15th day by cardiac puncture under diethyl ether anesthesia. Serum AST and ALT level were studied to assess liver function. Blood urea nitrogen and creatinine concentrations were studied to assess renal function.

Organs sampling and weight

All rats were sacrificed by overdose of diethyl ether anesthization after blood samples were collected. Median laparotomy was performed to isolate the stomach, liver and kidneys. All freshly isolated organs were cleaned and weighed.

Gastric ulcers evaluation

Stomach was opened along the greater curvature, rinsed carefully with saline and blotted dry before subjected to macroscopic evaluation. Stomach lesions were characterized into 6-score value according to Minano *et al.,* (1987). Photograph was taken using digital camera.

Histopathology study

Stomach was cut and fixed in 10 % formalin for at least 2 days. Fixed stomach were put into separated cassettes before subjected to routine histopathology processing (tissue processing, embedding, trimming 20 μm, sectioning 4 μm, Hematoxylin and Eosin staining and mounting). Tissues were observed under light microscope and lesion was scored and characterized based on cellular morphological changes.

Statistical analysis

Data was expressed as mean ± S.D. from four different animal and analyzed using 1-way ANOVA and Dunnet post-hoc test. Values of $P<0.05$ were considered significant.

RESULTS

Body weight changes

After 14 days of treatment administration, there were no significant body weight changes in comparison to Control (2 % DMSO) except for the group which received Prolipo C + 24 mg/kg Piroxicam (Table 1). Body weight of the rat in this treatment group decreased gradually but significantly from day 4 until day 15.



Figure 1. *Stomach of C1 (2 % DMSO)*

Table 1. Body weight

Treatment	Day														
	1	2	3	4	5	6	7	8	9	10	11	12	13	14	15
Control (2% DMSO)	195.55 ± 6.81	196.46 ± 11.92	191.56 ± 11.89	203.34 ± 15.18	201.35 ± 15.50	212.52 ± 16.79	202.83 ± 14.54	198.14 ± 11.79	208.26 ± 14.43	209.14 ± 16.34	215.02 ± 15.44	206.80 ± 14.52	214.63 ± 15.73	212.24 ± 13.82	202.06 ± 13.25
12mg/kg Piroxicam	190.64 ± 5.59	197.21 ± 4.72	191.65 ± 6.94	202.32 ± 6.18	195.85 ± 8.90	188.36 ± 9.35 °	199.36 ± 9.40	198.88 ± 10.32	204.72 ± 9.04	195.21 ± 13.79	211.98± 13.35	196.91 ± 12.25	191.44 ± 14.45	200.25 ± 14.99	199.84 ± 13.37
18mg/kg Piroxicam	195.67 ± 7.77	185.38 ± 5.38	193.76 ± 10.09	189.53 ± 11.86	189.33 ± 15.13	184.30 ± 17.27 °	190.41 ± 9.64	200.61 ± 12.36	202.71 ± 16.9	202.06 ± 15.55	192.66 ± 17.07	201.49 ± 17.48	198.42 ± 16.91	187.83 ± 16.08	193.97 ± 18.25
24mg/kg Piroxicam	196.02 ± 6.49	189.01 ± 6.70	193.07 ± 9.43	195.05 ± 6.90	192.39 ± 7.90	194.39 ± 10.90	188.84 ± 12.21	186.19 ± 15.00	187.73 ± 19.96	197.55 ± 11.60	196.35 ± 12.43	196.96 ± 10.37	192.85 ± 16.32	189.75 ± 20.25	179.04 ± 22.77
Prolipo C	192.39 ± 9.54	185.46 ± 2.93	189.48 ± 5.05	192.53 ± 5.64	192.29 ± 3.25	191.97 ± 2.53	198.53 ± 3.72	201.44 ± 4.22	201.925 ± 7.18	201.20 ± 4.09	208.59 ± 5.18	106.9 ± 7.03	204.07 ± 5.25	205.32 ± 10.90	198.96 ± 7.66
Prolipo Duo	192.77 ± 18.38	192.69 ± 23.15	196.81 ± 27.53	202.80 ± 27.36	200.06 ± 27.03	207.91 ± 25.76	210.97 ± 26.96	213.26 ± 27.62	208.65 ± 24.99	217.11 ± 28.47	215.39 ± 28.41	209.68 ± 28.35	215.38 ± 31.18	219.12 ± 30.51	211.57 ± 28.8
Prolipo C + 24mg/kg Piroxicam	189.39 ± 4.85	186.01 ± 3.79	178.57 ± 3.85	175.21 ± 5.98 °	174.47 ± 5.09 °	177.24 ± 3.44 °	176.6 ± 2.28 °	174.16 ± 1.18	173.59 ± 3.11 °	173.59 ± 8.12 °	172.14 ± 10.73 °	169.61 ± 16.29 °	167.54 ± 19.62 °	156.82 ±18.045 °	160.71 ±21.84 °
Prolipo Duo + 24mg/kg Piroxicam	180.00 ± 4.19 °	184.58 ± 8.24	185.73 ± 8.51	186.38 ± 7.90	190.23 ± 8.58	192.28 ± 8.02	193.21 ± 7.54	189.67 ± 4.90	193.95 ± 6.64	196.72 ± 7.41	184.25 ± 5.56 °	194.61 ± 4.57	194.73 ± 0.48	195.25 ± 5.78	180.32 ± 0.57

Values were Mean ± Standard deviation
° $P < 0.05$, significantly different from control group

Organ weight to body weight ratio

Stomach weight to body weight ratio showed that three groups were significantly higher than Control group (Table 2). The groups were Prolipo Duo + 24 mg/kg Piroxicam Prolipo C + 24 mg/kg Piroxicam and 12 mg/kg Piroxicam. For liver weight, the highest value came from Prolipo Duo + 24 mg/kg Piroxicam. Other groups that displayed significant increment in liver weight when compared to the control group were Prolipo C + 24 mg/kg Piroxicam, 24 mg/kg Piroxicam, 18 mg/kg Piroxicam and 12 mg/kg Piroxicam. Four groups gave significantly higher kidney weight when compared to the control group. However, the most significant highest value came from Prolipo Duo + 24 mg/kg Piroxicam.

Table 2 . Organ weight to body weight ratio

Treatment	Stomach	Liver	Kidney
Control (2% DMSO)	0.670832 ± 0.048594	3.237619 ± 0.193143	0.716495 ± 0.05678
12mg/kg Piroxicam	0.872077 ± 0.053801 °	4.288409 ± 0.179706 °	0.929997 ± 0.066729 °
18mg/kg Piroxicam	0.72605 ± 0.046346	4.081415 ± 0.696476 °	0.786586 ± 0.047875
24mg/kg Piroxicam	0.674098 ± 0.099035	4.47709 ± 0.634317 °	0.872431 ± 0.157971 °
Prolipo C	0.668991 ± 0.034931	3.672334 ± 0.359752	0.82347 ± 0.093624
Prolipo Duo	0.687751 ± 0.086311	4.025596 ± 0.75869	0.796354 ± 0.068134
Prolipo C + 24mg/kg Piroxicam	0.805654 ± 0.176519 °	4.882853 ± 0.711552 °	0.920644 ± 0.084558 °
Prolipo Duo + 24mg/kg Piroxicam	0.901748 ± 0.03512 °	5.38697 ± 0.87699 °	1.109934 ± 0.099593 °

Values were Mean ± Standard deviation

° $P < 0.05$, significantly different from control group



Figure 2. *Stomach of T1 (24 mg/kg Piroxicam)*

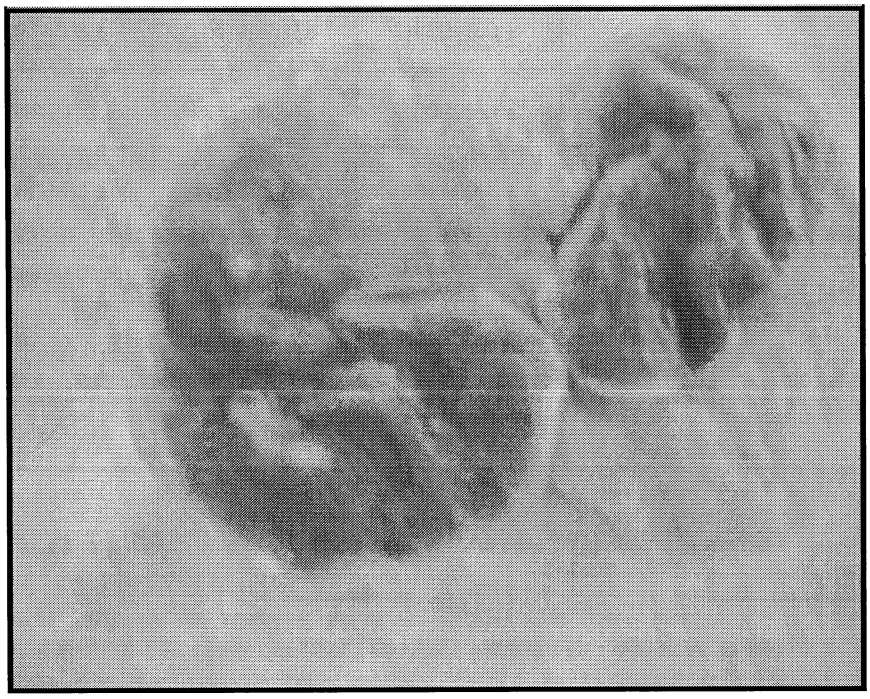

Figure 3. *Stomach of T2 (18 mg/kg Piroxicam)*

Gastric ulcer evaluation

Results for gastric ulcer scoring are shown in Table 3. The lowest ulcer scoring was from group Prolipo Duo + 24 mg/kg Piroxicam (0.50) and the highest was from the group that received 12 mg/kg Piroxicam (2.17). Mean score for all groups was 1.30 and only 3 groups' score was below this mean. The groups were Prolipo Duo + 24 mg/kg Piroxicam (0.50), Control (2 % DMSO) (0.67) and Prolipo Duo (1.25). Histologically, gastric inflammation was reduced in its severity due to encapsulation with liposome.

Table 3. Gastric ulcer evaluation

Treatment	Scoring
Control (2 % DMSO)	0.67 ± 0.52
12 mg/kg Piroxicam	2.17 ± 0.75 °
18 mg/kg Piroxicam	2.00 ± 0.71 °
24 mg/kg Piroxicam	1.50 ± 1.05
Prolipo C	2.00 ± 1.83
Prolipo Duo	1.25 ± 0.50
Prolipo C + 24 mg/kg Piroxicam	1.33 ± 1.15
Prolipo Duo + 24 mg/kg Piroxicam	0.50 ± 0.58

Values were Mean ± Standard deviation

° $P < 0.05$, significantly different from control group

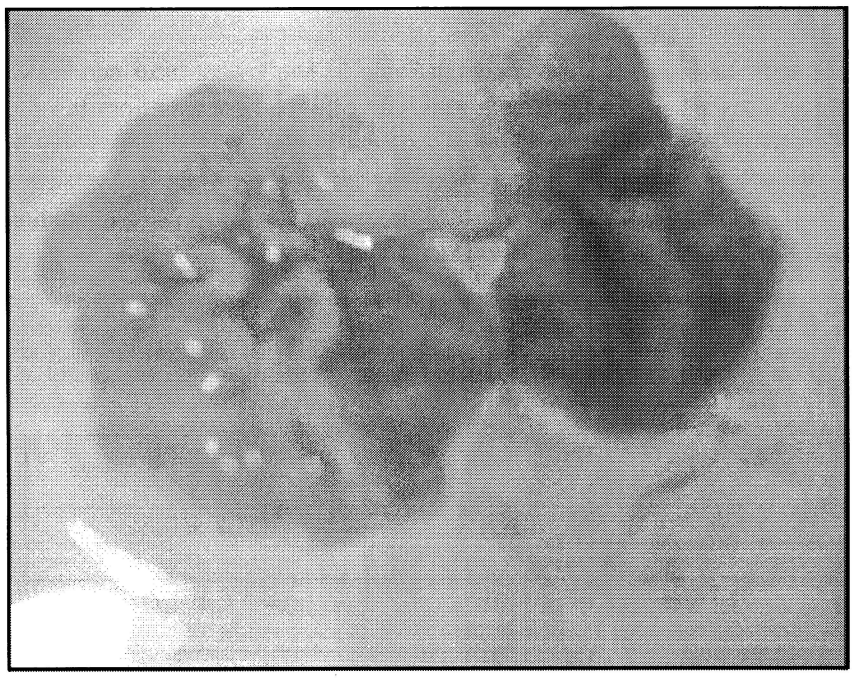

Figure 4. *Stomach of T3 (12 mg/kg Piroxicam)*

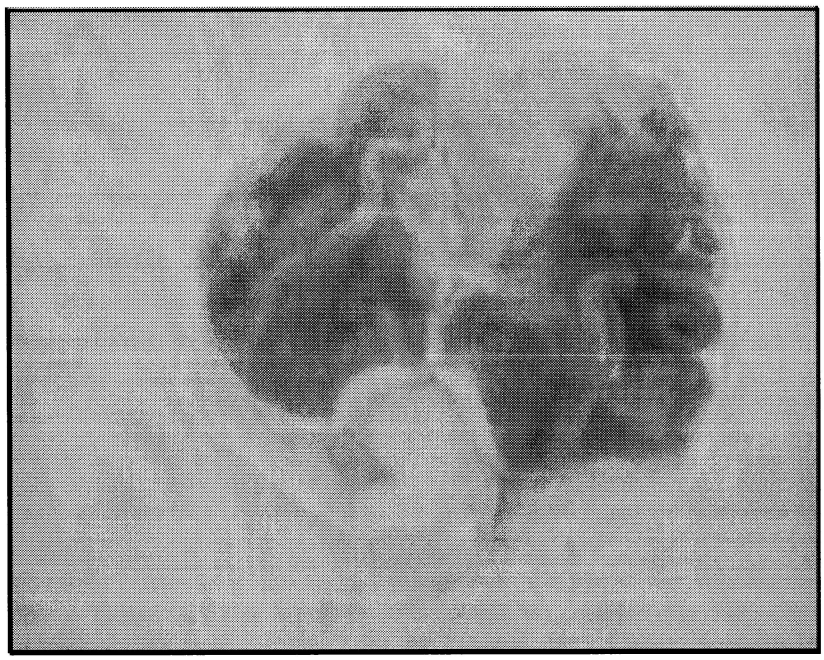

Figure 5. *Stomach of C2 (Prolipo C)*

Liver and kidney function test

AST (Aspartate aminotransferase)

The value of AST for Control (2 % DMSO) was 2.18 u/L (Table 4). The lowest value of AST was from group Prolipo Duo + 24 mg/kg Piroxicam (1.50 u/L). Prolipo C + 24 mg/kg Piroxicam also demonstrated a low value of AST (1.70 u/L). Among the treatment groups where only piroxicam without encapsulation was tested, the dose of 18 mg/kg Piroxicam gave the highest value of AST (2.06 u/L)

Table 4 . Liver and kidney function test

Treatment	Parameters			
	AST	ALT	Creatinine	Urea
Control (2 % DMSO)	2.18 ± 0.12	1.00 ± 0.14	0.26 ± 0.04	4.97 ± 0.35
12 mg/kg Piroxicam	1.78 ± 0.22	1.02 ± 0.10	0.23 ± 0.02	4.87 ± 0.6
18 mg/kg Piroxicam	2.06 ± 0.21	1.12 ± 0.22	0.21 ± 0.05	6.17 ± 0.52
24 mg/kg Piroxicam	1.55 ± 0.42 °	0.95 ± 0.44	0.21 ± 0.08	5.8 ± 3.1
Prolipo C	2.05 ± 0.24	1.28 ± 0.13	0.29 ± 0.03	5.79 ± 0.11
Prolipo Duo	1.95 ± 0.24	0.98 ± 0.21	0.26 ± 0.03	5.41 ± 0.76
Prolipo C + 24 mg/kg Piroxicam	1.70 ± 0.57	0.75 ± 0.07	0.16 ± 0.12	7.91 ± 1.51 °
Prolipo Duo + 24 mg/kg Piroxicam	1.50 ± 0.66 °	0.77 ± 0.15	0.32 ± 0.06	8.32 ± 0.75 °

Values were Mean ± Standard deviation
° $P < 0.05$, significantly different from control group

ALT (Alanine Transaminase)

ALT value for both Prolipo Duo + 24 mg/kg Piroxicam and Prolipo C + 24 mg/kg Piroxicam were 0.77 u/L and 0.75 u/L. It was lower when compared to either Control group (1.00 u/L) or 24 mg/kg Piroxicam without encapsulation (0.95 u/L). The highest value of AST was obtained from 18 mg/kg Piroxicam.

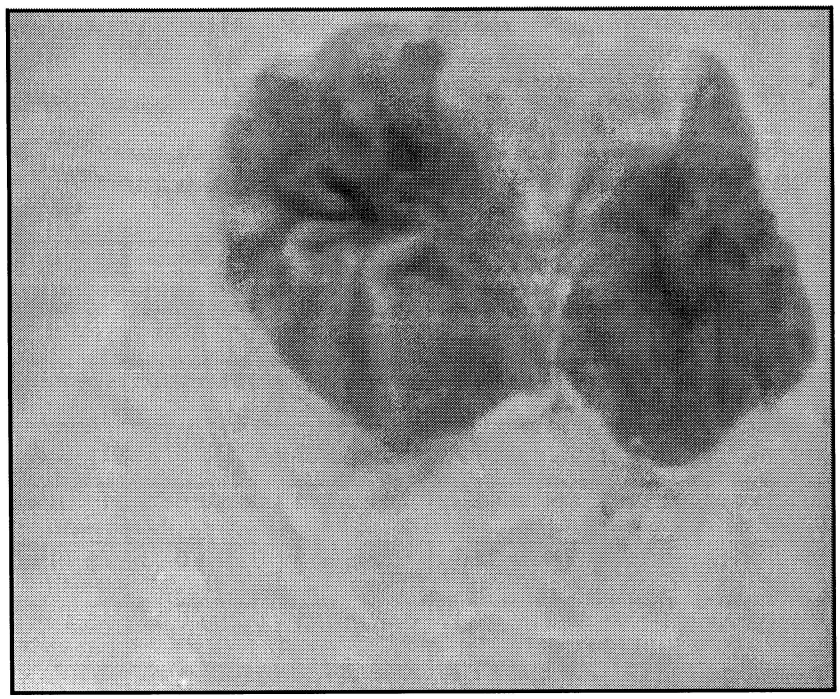

Figure 6. *Stomach of C3 (Prolipo Duo)*

Creatinine

There was no statistical significance in creatinine values for all groups. However, the highest value of creatinine was showed by Prolipo Duo + 24 mg/kg Piroxicam (0.32 mg/dL)

Blood Urea

Both Prolipo Duo + 24 mg/kg Piroxicam and Prolipo C + 24 mg/kg Piroxicam caused significant increment in blood urea when compared to Control group. The highest value of blood urea was shown by Prolipo Duo + 24 mg/kg Piroxicam (8.32 mmol/L) followed by Prolipo C + 24 mg/kg Piroxicam (7.91 mmol/L).

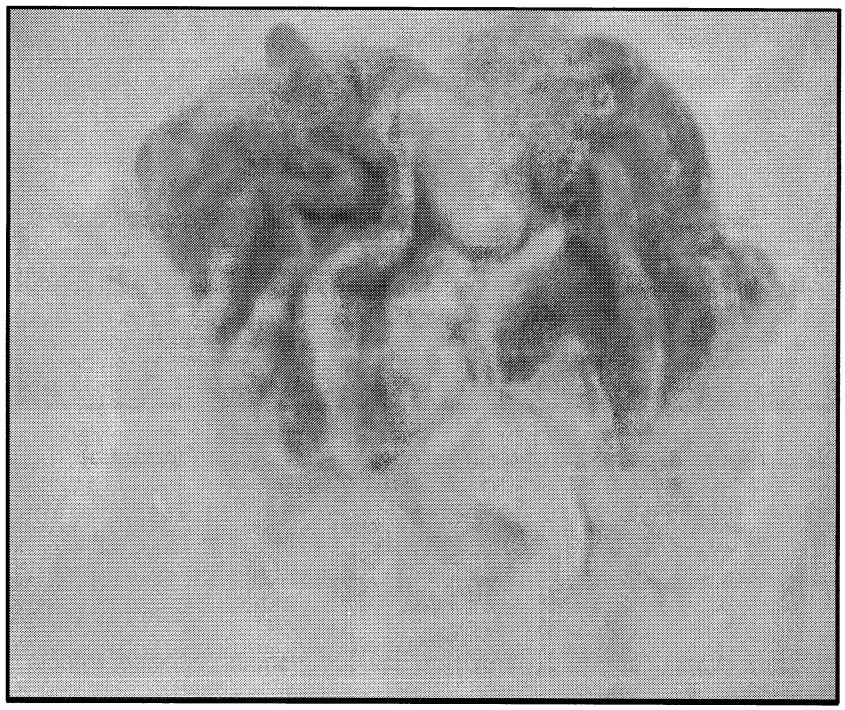

Figure 7. *Stomach of C1 (Prolipo C + 24 mg/kg Piroxicam)*



Figure 8. *Stomach of C1 (Prolipo Duo + 24 mg/kg Piroxicam)*

DISCUSSION

As a commonly prescribed drug, piroxicam caused various adverse effects including dizziness, skin rash, liver problems, kidney problems and stomach problems in the elderly (Martin, 2003; Dalmora *et al.*, 2001; Neal, 2003). In the current work, a preliminary study was conducted in our effort to evaluate and compare the degree of toxic effects caused by piroxicam alone and piroxicam-loaded in liposomes.

Over the years, the clinical usage of NSAIDs had been known to cause an upset stomach and gastrointestinal ulcers (Stone *et al.*, 2004). It was originally postulated that both the therapeutic activity and adverse effects of NSAIDs were the result of the inhibition in prostaglandin biosynthesis via COX enzyme, and were thereby inseparable (Trummlitz & Ryn, 2001). Thus, the decrement in production of protective prostaglandins within the gastrointestinal tract could easily lead to direct irritation of mucosal lining by the orally administrated NSAIDs. In the current study, decrease in gastric ulcer formation was a good indicator for the use of liposome vesicles to deliver piroxicam in the future.

Phospholids from liposomes could have contributed to surface hydrophobicity of gastroduodenal mucosa. This could act as a natural barrier to topical irritant action of piroxicam on the stomach's wall, which eventually caused ulcer formation to be reduced.

On the other hand, several other parameters obtained in this study reflected that kidney from the tested animal showed a pattern of kidney problem. Blood urea value and kidney to body weight ratio was higher in piroxicam-loaded liposomal samples. Renal effects usually appeared as a result of decreased production of prostaglandins that cause vasodilation of the renal vessels (Stone *et al.*, 2004). Even though kidney problem had been reported in non-encapsulated NSAIDs (Perneger *et al.*, 1994), the effect was just slightly high. This may be due to elimination of 65 % piroxicam was through renal as glucuronide conjugates of the free acid and hydroxylated metabolites (Smith & Reynard, 1995; Neal, 2003). Findings in current work suggested that encapsulation of piroxicam in liposomes could not effectively solve the kidney problem.

CONCLUSION

In conclusion, the encapsulation of piroxicam in liposomes had the potential to solve part of the adverse effects such as gastric ulcer which was caused by oral administration of piroxicam. However, certain problems still exist, especially to the kidney. Current work could not conclude whether these problems were caused by the piroxicam itself or liposomes. Further study need to be done to answer this question.

ACKNOWLEDGEMENT

This work was supported by Fundamental Research Grant Scheme from the Ministry of Higher Education, Malaysia (04-10-07-277FR).

REFERENCES

Baudrimonta, I., Murnb, M., Betheder, A.M., Guilcher, J. & Creppy E.E. (1995). Effect of piroxicam on the nephrotoxicity induced by ochratoxin a in rats. *Toxicology.* **147**: pp 1-4.

Canto, G. S., Dalmora, S. L. & Oliveira, A. G. (1999). Piroxicam encapsulated in liposomes: Characterization and in vivo evaluation of topical anti-inflammatory effect. *Drug Dev. Ind. Pharm.* **25(12)**: pp 1235-1239.

Dalmora M. E., Dalmora S. L. & Oliveira A. G. (2001). Inclusion complex of piroxicam with [beta]-cyclodextrin and incorporation in cationic microemulsion. In vitro drug release and in vivo topical anti-inflammatory effect. *Int. J. Pharm.* **222**: pp 45-55.

Gulati, M., Grover, M., Singh, S. & Singh, M. (1998). Lipophilic drug derivatives in liposomes. *Int. J. Pharm.* **165**: pp 129–168.

Martin, E.A. (2003). Piroxicam. In: *Oxford concise medical dictionary,* 6th ed., Market House Book Ltd., Oxford, pp 537.

Neal, M.J. (2003). Non-steroidal anti-inflammatory drugs. In: *Medical pharmacology at a glance,* 4th edition. Blackwell Science Ltd., Oxford, pp 70-71.

Perneger, T. V., Whelton, P.K. & Klag, M. J. (1994). Risk of kidney failure associated with the use of acetaminophen, aspirin, and nonsteroidal antiinflammatory drugs. *N. Engl. J. Med.* **331**: pp 1675-1679.

Schilling, R. J. & Mitra, A. K. (1990). Intestinal mucosal transport of insulin. *Int. J. Pharm.* **62(1)**: pp 53-64.

Smith, C.M. & Reynard, A.M. (1995). Inflammation and nonsteroidal antiinflammatory drugs: Prostaglandin and non-prostaglandin synthesis inhibitors. In: *Essentials of pharmacology.* W.B. Sauders Company, Pennsylvania, pp 147-163.

Starek, M. & Krzek, J. (2009). A review of analytical techniques for determination of oxicams, nimesulide and nabumetone. *Talanta.* **77**: pp 925–942.

Stone, M. B., Palmieri, R. M. and Ingersoll, C.D. (2004). The role of non-steroidal anti-inflammatory drugs for the treatment of delayed onset muscle soreness in sport. *International Sport Med. J.* **5(2)**: 147- 154.

Story, M. J. (1991). Oral delivery of peptides has become a reality. In: *Peptides: theoretical and practical approaches to their delivery,* Capsugel Library, New Brunswick, pp 53-67.

Sweetman, S.C. (2007). Piroxicam. In: *Martindale: The complete drug references,* 35th ed., Pharmaceutical Press, London, pp 101-102.

Trummlitz, G. and Ryn, J.V. (2001). The pharmacology of new-generation nonsteroidal anti-inflammatory agents: Selective COX-2 inhibitors. *Int. Sport Med. J.* **2(6)**: pp 1-8.

Journal of Industrial Technology Vol. 19(1), 2010 - ICONT 2009, 17 - 30

PREPARATION AND IN-VITRO EVALUATION OF BLANK AND PIROXICAM-LOADED LIPOSOMES

H.S. Chiong[1], M.N. Somchit[1,2,*], Y. Azhar[1,2], S.G.M. Ong[3] and K.H. Yuen[3]

[1] Faculty of Medicine and Health Sciences, Universiti Putra Malaysia
43400 UPM Serdang, Selangor, Malaysia.

[2] Sports Academy, Universiti Putra Malaysia
43400 UPM Serdang, Selangor, Malaysia.

[3] School of Pharmaceutical Sciences, Universiti Sains Malaysia
11800 Minden, Penang, Malaysia.

***(nazrul.hakim@gmail.com)**

ABSTRACT : Liposomal drug delivery system, a promising lipid-based nanoparticle technology, was used in the present work to encapsulate a lipophilic non-steroidal anti-inflammatory drug, piroxicam. A simple proliposomes method was optimised for rapid production of blank and drug-loaded liposomes. Various *in-vitro* techniques were selected, modified and validated for the evaluation of drug entrapment and size profiles of prepared liposomal samples. In the present study, a rapid and specific isocratic High Performance Liquid Chromatography (HPLC) method was successfully developed and employed for quantification of piroxicam in prepared liposomal samples. Dimethylsulfoxide was tested to be the most appropriate solvent system for liposomal samples preparation. Results showed that Pro-lipo™ Duo allowed higher amount of piroxicam to be entrapped into liposomes and gave a higher percentage of entrapment efficiency when compared to Pro-lipo™ C. However, Pro-lipo™ C produced smaller and more homogenous liposomes samples compared to those using Pro-lipo™ Duo. In conclusion, current work successfully demonstrated optimised procedures in preparation and evaluation of liposome-based drug delivery system for piroxicam.

KEY WORDS : Liposomes, proliposomes, piroxicam, HPLC, encapsulation, particle size

INTRODUCTION

Piroxicam (trade name: Feldene) is a potent non-steroidal anti-inflammatory drug with long plasma elimination half-life (Canto *et al.*, 1999; Rasetti-Escargueil & Grange, 2005). Piroxicam has been prescribed for the treatment of a wide variety of human diseases including rheumatoid arthritis, osteoarthritis and ankylosing spondylitis (Dalmora *et al.*, 2001; Martin, 2003). Despite its prominent analgesic, anti-inflammatory and anti-pyretic properties, piroxicam has been associated with various adverse reactions including gastrointestinal, hepatic and renal symptoms (Canto *et al.*, 1999; Sweetman, 2007). Piroxicam has also been reported for its slow absorption and low bioavailability when administered orally (Tagliati *et al.*, 1999). Due to these clinical drawbacks, a strategy to reduce toxicity and increase pharmacological effect of piroxicam is deemed highly relevant.

Liposomal drug delivery system appears to be an ideal strategy to provide better therapeutic efficacy and patient safety over existing drug formulations, mainly through alteration in biodistribution of the entrapped therapeutic agent (Schilling & Metra, 1990; Story, 1991; Hens & Romero, 2006). Liposomes are actually spherical nanoparticles comprising one or more concentric lipid bilayers that fully enclose an aqueous interior (Xiang & Anderson, 2006; Elsayed *et al.*, 2007). These microscopic vesicles are formed spontaneously when phospholipids are dispersed in aqueous medium due to the hydrophilic interaction of the lipid head groups with water (Vemuri & Rhodes, 1995).

For the past thirty years, a variety of procedures to load drug molecules into liposome vesicles have been developed and summarized in several reviews (Vemuri & Rhodes, 1995; Sharma & Sharma, 1997). Most of the preparation techniques such as reverse-phase evaporation, ether injection and freeze-thaw method are tedious in nature and required long preparation time (Vemuri & Rhodes, 1995). In current work, an attempt has been made to develop a new liposome-based drug delivery system for piroxicam using a simple technique known as proliposomes method. The proliposomes method, which is based on conversion of initial concentrated ethanolic phospholipids mixture into liposomal suspensions by addition of excess aqueous phase, has been characterised by an extremely high entrapment efficacy when compared to other methods based on passive entrapment (Perret *et al.*, 1991; Turanek *et al.*, 1997).

MATERIALS AND METHODS

Materials

Pro-lipo™ Duo and Pro-lipo™ C, which contained 50 % and 40 % unsaturated soybean phosphatidylcholine respectively and suspended in hydrophilic medium consisting of glycerol and ethanol, were obtained from Lucas Meyer (France). Piroxicam,

dimethylsulfoxide, glycerol and Triton X-100 were purchased from Sigma (USA). Dichloromethane, chloroform, acetonitrile and sodium dihydrogen phosphate 1-hydrate were from Merck (Germany). Methanol and ethanol are originated from Mallinckrodt Chemicals (USA). Hydrochloric acid was purchased from J.T. Baker (Thailand). All solvents and chemicals used were of analytical or HPLC grade.

HPLC method validation

HPLC method was validated by establishing basic analytical requirements of the system performance to be appropriate for quantitative determination of piroxicam. Acceptance criterions were set according to the current US FDA ORA laboratory procedure (2009).

Instrumentation and chromatographic condition

The HPLC system consisted of a Jasco (Japan) PU-980 Intelligent HPLC pump, Rheodyne 7125 (Cotati, USA) sample injector fitted with 50 μl sample loop, Jasco (Japan) UV-975 Intelligent UV/VI Detector and Hitachi (Japan) D-2500 Chromato-Integrator. A Jones Chromatography Genesis C18 column (4 μm, 150 x 4.6 mm I.D.) (UK), fitted with a refillable guard column (Upchurch Scientific, USA) and packed with Perisorb® RP-18 (30-40 μm, pellicular) powder (Upchurch Scientific, USA), was used for the chromatographic separation. The mobile phase consisted of 0.02 M sodium dihydrogen orthophosphate 1-hydrate and acetonitrile (53:47, v:v) was adjusted to pH 3.2 using 5 M hydrochloric acid, and was delivered at a flow rate of 1 ml/minute. The detection wavelength was set at 360 nm with a sensitivity range of 0.005 a.u.f.s. and the amount of piroxicam was quantified using peak area.

Stock solution and standard preparation

A stock solution of piroxicam at 1 mg/ml was prepared by dissolving accurate amount of drug in mobile phase and stored in airtight glass tubes protected against light. From stock solution, the working piroxicam standard solutions at concentrations of 8, 4, 2, 1, 0.5, 0.25, 0.125, 0.0625 and 0.03125 μg/ml were prepared by serial dilutions with mobile phase. Freshly prepared standard solutions were used to construct the standard curve daily.

System suitability

System suitability was assessed by six replicate analyses of the drug at a concentration of 0.5 μg/ml. The acceptance criterion was ± 2.0% for the percent coefficient of variation (% CV) for both peak areas and retention times.

Detection and quantitation limits

Limits of detection (LOD) and quantitation (LOQ) were estimated from the signal-to-noise ratio. The detection limit was defined as the lowest concentration level resulting in a peak area of three times the baseline noise. The quantitation limit was defined as the lowest concentration level that provided a peak area with a signal-to-noise ratio higher than 10, with precision (% CV) and accuracy (% error) within ± 2.0 %.

Linearity

Calibration curves (n = 6) were constructed by plotting the peak areas versus the concentration of standard solutions. Linearity of method was assayed by analysing the calculation of a nine-point linear plot in the range of 0.03125 – 8 μg/ml with six replicates, based on linear regression analysis. The acceptable criteria set for linear regression coefficient was ≥ 0.995.

Precision and accuracy

Both intra-day and inter-day validation were carried out. For intra-day precision and accuracy, six replicates of each of the five selected concentrations (8, 2, 0.5, 0.125 and 0.03125 μg/ml) were determined in a single day. For inter-day evaluation, analysis was carried out over six sets of each of the selected concentrations (8, 2, 0.5, 0.125 and 0.03125 μg/ml), with a calibration curve was constructed for each set of analyses. The acceptance criterion was set at ± 2.0 % for precision (% CV) and ± 3.0 % for accuracy (% error).

Preparation and in-vitro evaluation of liposomes

Choice of solvent system

Dissolution of piroxicam in various types of organic solvents, namely dimethylsulfoxide, glycerol, dichloromethane, chloroform, acetonitrile, methanol and ethanol, was evaluated to select the most suitable solvent system for liposomal samples preparation. Briefly, accurate amount of piroxicam was initially weighed into test tubes before different types of solvent were added respectively to form 60 mg/ml drug solution. All duplicate drug solution samples were mixed well at room temperature (25°C ± 2°C) before centrifugation at 12800 G for 15 minutes (MiniSpin® plus, Eppendorf, Germany) in order to sediment any of the undissolved drug particle in solution samples (Mugabea *et al.*, 2006).

Liposomal samples preparation

Two types of commercially available proliposomes, namely Pro-lipo™ Duo and Pro-lipo™ C, were used respectively to prepare the liposomal samples. These proliposomes mixture were used as received and the method of preparation was in accordance to the manufacturer's recommendation with some modifications. Firstly, a stock piroxicam solution (60 mg/ml) was freshly prepared by dissolving piroxicam in dimethylsulfoxide. The stock piroxicam solution was then added into selected proliposomes in a beaker with moderate stirring (125 ± 25 rpm) for 60 minutes. This proliposomes mixture was then converted to concentrated piroxicam-loaded liposomal suspension by drop-wise addition of distilled water. This liposomal suspension was stirred (hydrated) continuously for 60 minutes at room temperature before further dilution with distilled water. The proportion by weight of Pro-lipo™: piroxicam solution: distilled water (hydration): distilled water (dilution) was 5: 1: 9: 25. The blank liposomes were prepared according to the same procedure except that dimethylsulfoxide was used instead of stock piroxicam solution. All formulations were produced in three batches respectively to ensure their reproducibility.

Drug entrapment analysis

Drug entrapment profile (entrapment capacity and efficiency) of liposomal samples was evaluated using the following *in-vitro* techniques. Duplicate samples for analysis were prepared from each of the three individual batches of liposomal samples (n = 6).

Total piroxicam determination

To determine the concentration of the total piroxicam in prepared liposomal samples, Triton X-100 (0.2 % in final concentration) was added into the liposome suspensions in order to lyse the liposome structure and release all entrapped drug (Mugabea *et al.*, 2006). The mixture was vortexed for 30 seconds (Barnstead/Thermolyne, USA) and diluted with mobile phase before quantification using the HPLC method described in previous section.

Free undissolved piroxicam determination

Liposomal samples were first centrifuged at 12800 G for 15 minutes (MiniSpin® plus, Eppendorf, Germany) to precipitate all undissolved and unentrapped hydrophobic drug. In a separate pre-experiment study, longer duration of centrifugation (up to 60 minutes) at 12800 G did not cause significant increment of total drug in sediment. This finding suggested that current centrifugation condition was sufficient to precipitate all undissolved drug particle, while retaining blank liposomes, drug-loaded liposomes and dissolved drug in the supernatant. The supernatant was then discarded and the remaining sediment was reconstituted with mobile phase before subjected to HPLC analysis.

Free dissolved piroxicam determination

Complete precipitation of liposomes and free drug particles (undissolved form) could be achieved by ultracentrifugation method (Song *et al.*, 2005). Liposomal samples were ultracentrifugated at 300,000 G and 20 °C for 90 minutes using a TLA-110 rotor in Optima™ MAX-XP ultracentrifuge (Beckman Coulter, USA). The supernatant, which contained only the dissolved drug (confirmed by the absence of appreciable liposomal particles using particle size analyser), was then collected. These supernatant samples were diluted with mobile phase before subjected to quantification using similar HPLC method.

Calculation

The drug-loading capacity in liposomal samples and the entrapment efficiency of piroxicam were calculated using the following formulas.

$$\text{Entrapment capacity } (\mu g \text{ piroxicam / g Pro-lipo}^{TM}) = \frac{\text{Total drug} - \text{Free undissolved drug} - \text{Free dissolved drug}}{\text{Total Pro-lipo}^{TM}}$$

$$\text{Entrapment efficiency } (\%) = \frac{\text{Total drug} - \text{Free undissolved drug} - \text{Free dissolved drug}}{\text{Total drug}} \times 100$$

Particle size analysis

Size profile (particle size and size distribution) of prepared liposomal samples were determined by photon correlation spectroscopy technique using Zetasizer Nano S (Malvern Instrument, UK). The procedure for particle size analysis entailed dispersing 10 μl of liposomal samples with 500 μl distilled water in a low volume disposable sizing cuvette. The particle size and size distribution were measured by the instrument as ZAve and polydispersity index respectively. For each formulation, two measurements were taken on two separate samples from three individual bathes of liposomal samples.

Statistical analysis

Descriptive statistics and standard regression curve analysis (without forcing through zero) were performed by use of Microsoft® Office Excel 2007 software (Microsoft, USA). Independent samples *t*-test for comparison between two groups; and one-way analysis of variance (ANOVA) followed by Tukey's multiple comparison test among groups were carried out using SPSS 16.0 (SPSS Inc., Chicago). *P* values less than 0.05 ($P<0.05$) were taken as the limit of significance.

RESULTS AND DISCUSSION

HPLC method validation

Validation was a basic requirement to ensure the quality and reliability of results obtained from a particular HPLC method used in quantitative measurement of analyte (Ermer, 2005). In this study, a newly developed isocratic HPLC-UV method was successfully validated for the determination of piroxicam in prepared samples. This rapid and specific HPLC method used a simple mobile phase composition that was easy to prepare with little or no variation. On top of that, this method had a rapid run time ($\leq$ 7.5 minutes) and relatively low flow rate (1 ml/min) which allowed the analysis of large number of samples with less mobile phase that prove to be cost-effective.

Chromatogram (Figure 1) showed that the piroxicam peak, with a retention time of 5.2 minutes, was well resolved and free of interference. The % CV of peak area and retention time was 1.9 % and 0.1 % respectively, indicating the suitability of the system for good and reproducible determination of piroxicam. The LOD was found to be 0.007813 μg/ml, whereas the LOQ, being lowest concentration used in the construction of calibration curves with % CV and % error less than 20 %, was determined as 0.03125 μg/ml. Standard calibration curves (n = 6) showed good linearity over the range of concentration used (Table 1). In both intra-day and

inter-day analysis, all validation data obtained, satisfy the requirement of within 2.0 % for % CV and % error (Table 2), hence ensuring an accurate and precise quantification of piroxicam in tested solution samples.

Table 1. Results of regression analysis of the linearity data for piroxicam

Analysis	Mean (n = 6)	S.D.	% CV
Correlation coefficient	0.9999	0.0001	0.0108
Intercept	0.0012	0.0077	654.0128
Slope	6.5384E-06	2.78187E-07	4.2546

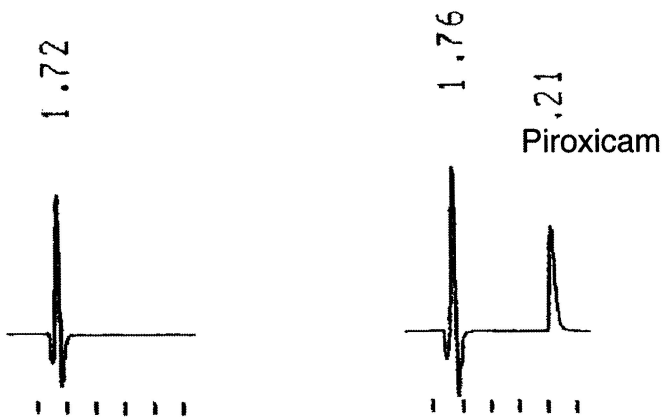

Figure 1. *HPLC chromatograms of (A) mobile phase and (B) piroxicam. Retention times in minutes were shown*

Table 2. Intra-day and inter-day reproducibility data for piroxicam solution

Analysis	Nominal Concentration (μg/ml)	Measured Concentration (μg/ml)		Precision (% CV)	Accuracy (% error)
		Mean (n = 6)	S.D.		
Intra-day	0.03125	0.03072	0.00056	1.83156	-1.69050
	0.125	0.12670	0.00230	1.81744	1.36125
	0.5	0.50976	0.00920	1.80518	1.95209
	2	2.02719	0.03876	1.91200	1.35948
	8	7.89640	0.03389	0.42921	-1.29503
Inter-day	0.03125	0.03166	0.00051	1.60536	1.30257
	0.125	0.12559	0.00240	1.90833	0.47171
	0.5	0.49571	0.004234	0.85419	-0.85817
	2	2.00490	0.010627	0.53005	0.24505
	8	8.03809	0.039162	0.48720	0.47612

Choice of solvent system

The use of a solvent system was of crucial importance for preparing liposome encapsulated lipophilic drugs such as piroxicam (Lucchetti *et al.*, 1996). Organic solvents had been reported for their capability to facilitate uniform and molecular dispersion of lipids and lipophilic compounds among themselves. Hence, the encapsulation of drugs in liposomes could be facilitated (Vemuri & Rhodes, 1995; Sharma & Sharma, 1997). However, when selecting a solvent system for a given process, it was important to keep in mind the purity, solubility and safety limits of the solvent (Vemuri & Rhodes, 1995).

In this part of study, dimethylsulfoxide, dichloromethane and chloroform were short-listed based on their effectiveness in dissolving piroxicam. No sediment was observed in the centrifuged clear yellowish piroxicam solution samples, indicating that drug was completely dissolved in these organic solvents (confirmed by the absence of sediment even when duration of centrifugation was prolonged up to 60 minutes). Based on our literature review,

dimethylsulfoxide was deemed as the most suitable solvent for preparing piroxicam-loaded liposomes in the current project. Being one of the strongest aprotic organic solvent, dimethylsulfoxide was miscible in water and relatively less hazardous when compared to the halogenated hydrocarbon solvents: dichloromethane and chloroform (Mallinckrodt, 1997, 1998a,b). Literature had also reported that dimethylsulfoxide was particularly useful in preparation of liposomal sample for compounds which were poorly-soluble in aqueous solution (Szoka, 1991).

Drug entrapment profile (entrapment capacity and efficiency)

Piroxicam was incorporated within the lipid bilayers of liposomes due to its lipophilic nature (Lucchetti *et al.*, 1996). Nevertheless, the effectiveness of drug-loading into the compartmentalized system of liposomes was largely dependent on the type and compositions of lipid, buffer contents and preparation procedures used (Vemuri & Rhodes, 1995; Basu & Basu, 2002). Data obtained in current study showed that both entrapment capacity (actual amount of piroxicam which was able to be loaded into liposomes) and entrapment efficiency (percent fraction of total input piroxicam which successfully been entrapped in liposomes) for Pro-lipo™ Duo were significantly higher than Pro-lipo™ C (Table 3).

Table 3. Drug entrapment profiles for Pro-lipo™ Duo and Pro-lipo™ C (n=6 ± S.E.M.)

Type of Pro-lipo™	Entrapment capacity (μg piroxicam /g Pro-lipo™)	Entrapment efficiency (%)
Duo	728.7 ± 41.9 [a]	14.1 ± 0.9 [a]
C	490.0 ± 85.1 [b]	8.7 ± 1.4 [b]

Values with different alphabetical superscripts differ significantly at $p<0.05$ between each other for the same entrapment profile (Independent samples *t*-test)

These findings indicated that Pro-lipo™ Duo was relatively more effective in preparing piroxicam-loaded liposomes. Better entrapment profiles of Pro-lipo™ Duo could be attributed by its relatively higher unsaturated soybean phosphatidylcholine content, as suggested by Turanek *et al.*, (1997). This higher amount of phosphatidylcholine in the proliposomes mixture resulted in a larger surface area for drug interaction during the stirring and hydration process. In addition, the presence of a larger drug-loading volume in lamellar

phase of liposomes prepared using Pro-lipoTM Duo would in turn lead to a proportionally higher amount of piroxicam to be successfully entrapped.

Liposome size profile (particle size and size distribution)

Another critical parameter in preparation of liposomes for drug delivery was the particle size profile. The vesicles size would influence the extent of drug encapsulation in liposomes (Sharma & Sharma, 1997). It had also been reported that the size of liposomes would affect the effectiveness of entrapped drug interaction with cells, as well as its circulation half life and bioavailability (Elorza *et al.*, 1993; Chen & Langer, 1998). Results for particle size analysis were presented in Table 4.

Table 4. Particle size profiles for Pro-lipo™ Duo and Pro-lipo™ C (n = 12 ± S.E.M.)

Type of Pro-lipo™	Piroxicam (mg/ml)	ZAve (nm)	Polydispersity index
Duo	0	389.6 ± 3.6 [a]	0.483 ± 0.008 [a]
	1.5	355.9 ± 8.0 [b]	0.454 ± 0.012 [ab]
C	0	303.0 ± 5.2 [c]	0.429 ± 0.007 [b]
	1.5	291.9 ± 11.4 [c]	0.417 ± 0.024 [b]

Values with different alphabetical superscripts differ significantly at $p<0.05$ between each other for the same particle profile (ANOVA followed by Tukey's test)

In general, all samples (blank and drug-loaded liposomes) prepared in the current work using both types of Pro-lipo™ posed sufficiently small particle size in the nanometer range and relatively narrow size distribution. However, data showed that liposomes formed using Pro-lipo™ Duo was significantly bigger in particle size and size distribution compared to those prepared using Pro-lipo™ C. This discrepancy could be attributed to the differences of phosphatidylcholine and hydrophilic medium content in these two proliposome mixtures. Higher concentration of phosphatidylcholine in Pro-lipo™ Duo allowed an increased number of lipid bilayers formed during preparation of these multilamellar vesicles. On top of that, liposomes prepared using Pro-lipo™ Duo could be subjected to relatively less vigorous shear force during stirring and hydration period due to its more viscous drug-proliposomes mixture. As a result,the final liposomal samples prepared using Pro-lipo™ Duo had bigger particle size and were less homogenous.

This study also revealed that the encapsulation of piroxicam in liposomes caused decrement in particle size and polydispersity index. As drug particles were incorporated within lipid bilayers of liposomes, the bonds that held successive bilayers decreased. In turn, the vesicle which had a looser packing would caused the liposomes to have a smaller particle size and a relatively more homogenous sample (Fa *et al.*, 2007).

CONCLUSION

Current work successfully demonstrated optimised procedures which were simple and practical for the preparation and *in-vitro* evaluation of piroxicam-loaded liposomes. In summary, preparation of liposomes using Pro-lipo™ Duo was able to yield liposomal samples with better drug entrapment profile. On the other hand, Pro-lipo™ C yielded smaller and more homogenous blank and piroxicam-loaded liposomes.

ACKNOWLEDGEMENT

This work was supported by Fundamental Research Grant Scheme from the Ministry of Higher Education, Malaysia (04-10-07-277FR). We acknowledge the use of instrument and technical assistance by Hovid Sdn. Bhd. and Renogenic Sdn. Bhd.

REFERENCES

Basu, S.C. and Basu, M. (2002). Preparation, isolation and characterisation of liposomes containing natural and synthetic lipids. In: *Liposome methods and protocols*, Humana Press, New Jersey, pp 3-16.

Canto, G.S., Dalmora, S.L. and Oliveira, A.G. (1999). Piroxicam encapsulated in liposomes: Characterisation and *in vivo* evaluation of topical anti-inflammatory effect. *Drug Dev. Ind. Pharm.* **25(12)**: pp 1235-1239.

Chen, H.M., Langer, R. (1998). Oral particle delivery: Status and future trends. *Adv. Drug Del. Rev.* **34(2-3)**: pp 339-350.

Dalmora, M.E., Dalmora, S.L. and Oliveira A.G. (2001). Inclusion complex of piroxicam with β-cyclodextrin and incorporation in cationic microemulsion. *In vitro drug* release and i*n vivo* topical anti-inflammatory effect. *Int. J. Pharm.* **222**: pp 45–55.

Elorza, B., Elorza, M.A., Sainz, M.C., Chantres, J.R. (1993). Análysis of the particle size distribution and the internal volume of liposomal preparations. *J. Pharm.* Sci., **82(11)**: pp 1160-1163.

Elsayed, M.M.A., Abdallah, O.Y., Naggar, V.F. and Khalafallah, N.M. (2007). Lipid vesicles for skin delivery of drugs: Reviewing three decades of research. I*nt. J. Pharm.* **332**: pp 1–16.

Ermer, J. (2005). Analytical validation within the pharmaceutical environment. In: *Method Validation in Pharmaceutical Analysis: A Guide to Best Practice,* WILEY-VCH Verlag GmbH & Co. KGaA, Weinheim, pp 3-19.

Fa, N., Lins, L., Courtoy, P.J., Dufrêne, Y., Van Der Smissen, P., Brasseur, R., Tyteca, D., Mingeot-Leclercq, M.-P. (2007). Decrease of elastic moduli of DOPC bilayers induced by a macrolide antibiotic, azithromycin. *Biochim. Biophys. Acta.* **1768**: pp 1830–1838.

Food and Drug Administration (2009). Appendix 1- ORA validation and verification guidance for human drug analytical methods. ORA laboratory procedure, document ORA-LAB.5.4.5., Feb., Food and Drug Administration, USA.

Hens, A.G., Romero, J.M.F. (2006). Analytical methods for the control of liposomal delivery systems. *Trend Anal. Chem.* **25(2)**: pp 167-178.

Lucchetti, G., Assogna, G., Bagnato, P. (1996). Liposomal piroxicam formulations. United States Patent number: 5505960, Apr., United States Patent, USA.

Mallinckrodt, B.I. (2007). Chloroform, MSDS number: C2915. Material Safety Data Sheet, May, Mallinckrodt Baker Inc., New Jersey.

Mallinckrodt, B.I. (2008a). Dimethyl Sulfoxide, MSDS number: D7120. Material Safety Data Sheet, Feb., Mallinckrodt Baker Inc., New Jersey.

Mallinckrodt, B.I. (2008b). Methylene Chloride, MSDS number: M4420. Material Safety Data Sheet, Aug., Mallinckrodt Baker Inc., New Jersey.

Martin, E.A. (2003). Piroxicam. In: Oxford Concise Medical Dictionary, 6th edition, Market House Book Ltd., Oxford, pp 537.

Mugabea, C., Azghani, A. and Omria, A. (2006). Preparation and characterisation of dehydration–rehydration vesicles loaded with aminoglycoside and macrolide antibiotics. *Int. J. Pharm.* **307**: pp 244–250.

Perrett, S., Golding, M. and Williams, W.P. (1991). A simple method for the preparation of liposomes for pharmaceutical applications: Characterization of the liposomes. *J. Pharm. Pharmacol.* **43**: pp 54–161.

Rasetti-Escargueil, C. and Grange V. (2005). Pharmacokinetic profiles of two tablet formulations of piroxicam. *Int. J. Pharm.* **295**: pp 129–134.

Schilling, R.J. and Mitra, A.K. (1990). Intestinal mucosal transport of insulin. *Int. J. Pharm.* **62(1)**: pp 53-64.

Sharma, A., Sharma, U.S. (1997). Liposomes in drug delivery: progress and limitations. I*nt. J. Pharm.* **154**: pp 123-140.

Song, K.H., Chung, S.J. and Shim, C.K. (2005). Enhanced intestinal absorption of salmon calcitonin (sCT) from proliposomes containing bile salts. *J. Control. Rel.* **106**: pp 298– 308.

Story, M.J. (1991). Oral delivery of peptides has become a reality. In: *Peptides: theoretical and practical approaches to their delivery*, Capsugel Library, New Brunswick, pp 53-67.

Sweetman, S.C. (2007). Piroxicam. In: *Martindale: The complete drug references,* 35th edition, Pharmaceutical Press, London, pp 101-102.

Szoka, F. C.Jr. (1991). Preparation of liposome and lipid complex compositions. United States Patent number: 5077057, Dec., United States Patent, USA.

Tagliati, C.A., Kimura, E., Nothenberg, M.S., Santos, S., Oga, S. (1999). Pharmacokinetic profile and gastric effect of zinc-piroxicam in rats. *Gen. Pharmacol.* **33**: pp 67–71.

Turanek, J., Zaluska, D., Neca, J. (1997). Linkup of a fast protein liquid chromatography system with a stirred thermostated cell for sterile preparation of liposomes by the proliposome–liposome method: Application to encapsulation of antibiotics, synthetic peptide immunomodulators and a photosensitiser. *Anal. Biochem.* **249**: pp 131–139.

Vemuri, S., Rhodes, C.T. (1995). Preparation and characterization of liposomes as therapetic delivery systems: A review. *Pharm. Acta Helv.* **70**: pp 95-111.

Xiang, T.X. and Anderson, B.D. (2006). Liposomal drug transport: A molecular perspective from molecular dynamics simulations in lipid bilayers. *Adv. Drug Del.* Rev. **58**: pp1357–1378.

Journal of Industrial Technology Vol. 19(1), 2010 - ICONT 2009, 31 - 40

MEASUREMENT OF DYNAMIC MECHANICAL PROPERTIES OF NANOSILICA/ POLYPROPYLENE COMPOSITES USING SPLIT HOPKINSON PRESSURE BAR APPARATUS (SHPBA)

Hazizan Md Akil, *Mohd Firdaus Omar, Zainal Arifin Ahmad

[1]School of Material and Mineral Resource Engineering
Universiti Sains Malaysia
11300 Seberang Perai Selatan
Pulau Pinang, Malaysia

***(hazizan@eng.usm.my)**

ABSTRACT : The paper presents the results on dynamic mechanical properties of Nanosilica/Polypropylene (PP-SiO_2) composite at various strain rates using compression Split Hopkinson Pressure Bar (SHPB) technique. The stress-strain response for Nanosilica /Polypropylene composites at strain rates of nearly 1400 s^{-1} are demonstrated and then compared with those exposed at static and quasi-static of strain. In addition, the effect of filler contents (SiO_2) towards dynamic mechanical properties of the composite was successfully investigated. From the SHPB test, it was found that the dynamic mechanical properties of Nanosilica/Polypropylene composites are significantly affected by the levels of strain rate. Higher dynamic mechanical properties in terms of flow stress and compression modulus were recorded for higher strain as compared to lower strain rate over the span of strain rate investigated. Ultimately, an almost linear improvement in the dynamic compression modulus was observed as a function of filler content where it constantly increases with the increase of silica loading at each of strain rate investigated (up to 1350 s^{-1})

KEYWORDS : Nanosilica/Polypropylene (PP-SiO_2), Split Hopkinson Pressure Bar, mechanical properties

INTRODUCTION

In the past few years, Polymer Matrix Composites (PMCs) have been widely used in engineering applications due to their low production cost and light weight. Filling the polymer matrix with particle will remarkably improve the mechanical properties of the material due to the fantastic characterization of the particles itself, such as size, surface and quantum effects (Yaping, *et al.*, 2003; Victor *et al.*, 2003; and Huang *et al.*, 2005). Polymeric materials are subjected to dynamic loading and high-strain-rate deformation in a variety of important applications such as aircraft and automotive components, as well as during high-speed processes such as extrusion and blow molding (Chen *et al.*, 2002).

Generally, it is believed that all materials behave differently under static and dynamic conditions. However, the dynamic mechanical properties of PMCs at high strain rate are rarely reported and documented. Base on this concern, in order to ensure the safety use of PMCs at high strain rate loading condition, it is necessary to measure the dynamic mechanical properties of these materials under high strain rate which is not achievable using conventional Universal Testing Machine (UTM).

Generally, there are many available techniques in studying the dynamic mechanical properties of materials, which are reviewed by Hamouda *et al.*, in 1998. Among those techniques, the Split Hopkinson Pressure Bar technique is one of the most widely used for high strain rate testing (Lee & Kim, 2003; Zhao, 2003; and Woldesenbet & Peter, 2009). The important characterization of SHPB technique is highly depending on the capability of the technique to obtain stress-strain curve as output which holds useful information to characterize materials. The primary objective of the current study is to characterize the dynamic mechanical properties of PP-SiO_2 nanocomposites using the SHPBA. Besides that, the effect of filler loading towards dynamic behaviour of PP-SiO_2 was also investigated. In addition, the characteristic of the PP-SiO_2 nanocomposites at different level of strain rates was also successfully demonstrated. Ultimately, compressive stress-strain curves of PP-SiO_2 nanocomposites were presented and compared statiscally to determine the stress-strain curve.

MATERIALS AND METHODS

Polypropylene homopolymer (TITANPRO PM-255) used as matrix was supplied by Titan PP polymers (M) Sdn. Bhd. Fumed nanosilica (nano-SiO_2) used as filler was obtained from Sigma-Aldrich with average particle size of 7 nm. At the compounding stage, nanosilica filler and PP polymer matrix were mixed by using an internal mixer, Thermo Haake Polydrive R600 fitted with cam blades. The mixing was carried out at temperature of 180 °C with rotor

speed of 60 rpm for the period of 8 min. Following that, at compression moulding stage, the cylindrical specimens were compression molded in an electrically heated hydraulic press at 180 °C. The button mould with 28 mm thickness and 12 mm diameter was used for preparing the specimen under static and dynamic test, respectively. Finally, the molded specimens were cut into the required shape for the static and dynamic mechanical testing using a band saw. The geometrical sizes of static specimens were prepared in accordance to the ASTM Designation E9-89 (12 mm x 18 mm). For dynamic testing, the specimens were cut into specific size which is based on previous studies (12 mm x 6 mm) (Nakai & Yokoyama, 2008).

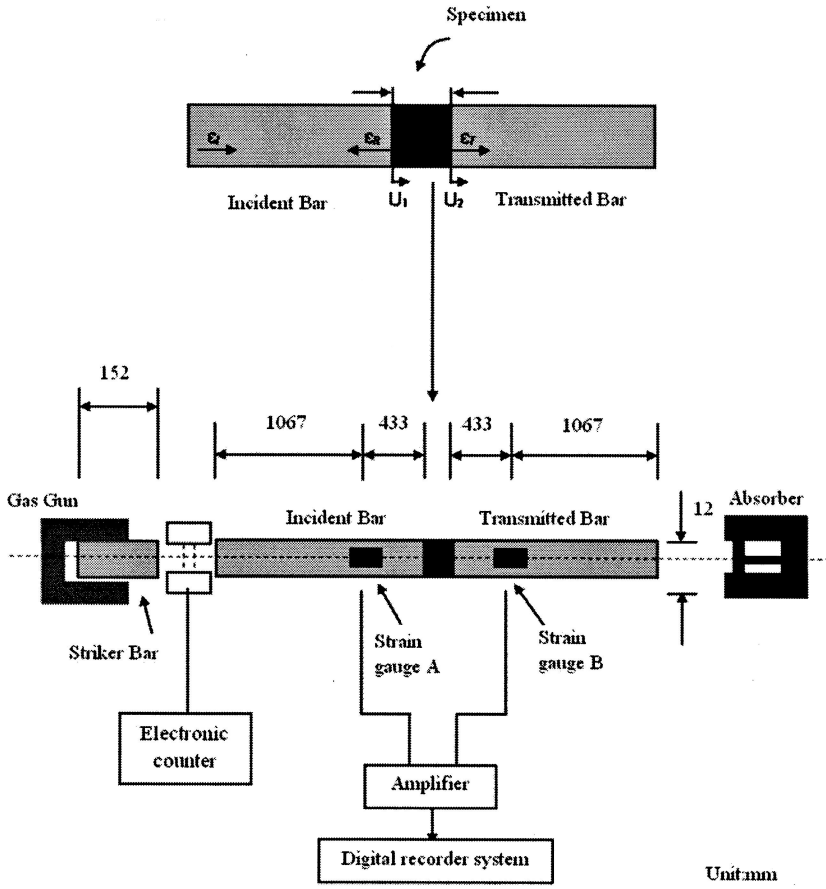

Figure 1. *The schematic diagram of SHPB apparatus*

TEST PROCEDURE

Static Compression Test

Static compression test were conducted on an Axial-Torsion Universal Testing Machine following ASTM Designation E9-89. A constant crosshead speed of 1 mm/min and 10 mm/min corresponding to the strain rate of 9.3×10^{-4} and 9.3×10^{-3} s^{-1} were applied to PP-SiO_2 nanocomposites specimens at room temperature. Both ends of the specimen were adequately lubricated with wax in order to reduce the frictional effect.

Dynamic Compression Test

A conventional Split Hopkinson Pressure Bar (SHPB) apparatus normally has the same general components which include a striker bar that was usually propelled by a gas chamber, incident bar, transmitter bar, absorber, strain gauges, strain transducer with signal conditioners and a mean of digital storage. In practice, a high strength material is needed in order to reduce the drastic impedance mismatch between the specimen and the bar which results in a transmitted strain signal with very low S/N ratio (Nakai *et al.*, 2008). Thus, in the current SHPB testing, a high strength silver steel bar is used to meet the requirement. A schematic diagram of compression SHPBA used in this study (KHT-52-CT) is shown in Figure 1. The diameter of the striker bar, incident bar and transmitter bar is 12 mm, and their length are 152, 1500 and 1500 mm, respectively. Three average high strain rates were applied to PP- SiO_2 nanocomposites specimens which are 1021 s^{-1}, 1150 s^{-1} and 1340 s^{-1}.

RESULTS AND DISCUSSION

Effect of strain rate

The effect of strain rate on the high strain rate behaviour of PP-SiO_2 nanocomposites (filler loading up to 5 %) is presented in Figure 2. The average strain rates applied during this high velocity impact test are 9.3×10^{-4} s^{-1}, 9.3×10^{-3} s^{-1}, 1021 s^{-1}, 1150 s^{-1} and 1340 s^{-1}.

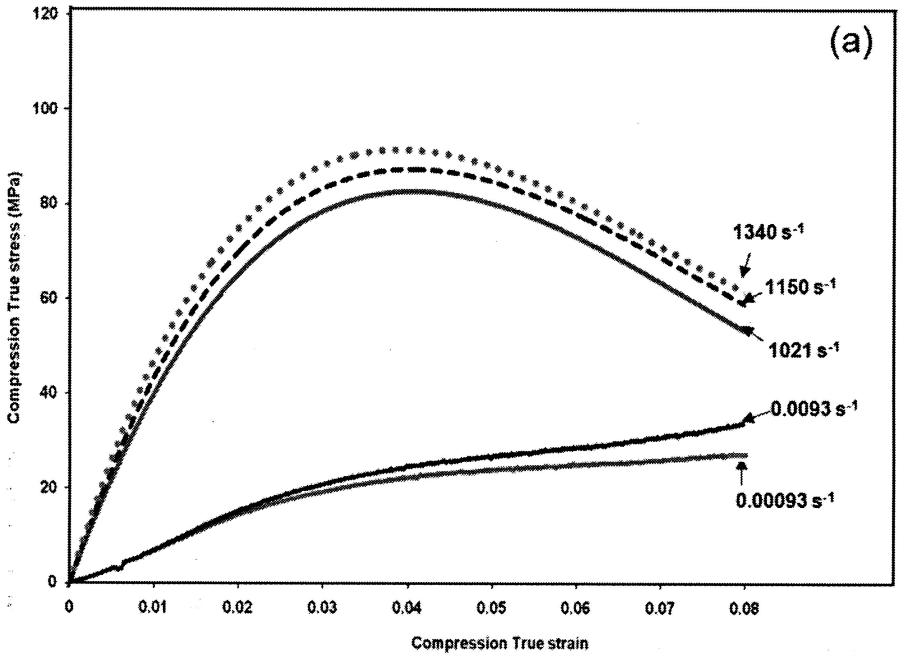
(a)
Compression True stress (MPa)
Compression True strain
1340 s-1
1150 s-1
1021 s-1
0.0093 s-1
0.00093 s-1
0
20
40
60
80
100
120
0
0.01
0.02
0.03
0.04
0.05
0.06
0.07
0.08

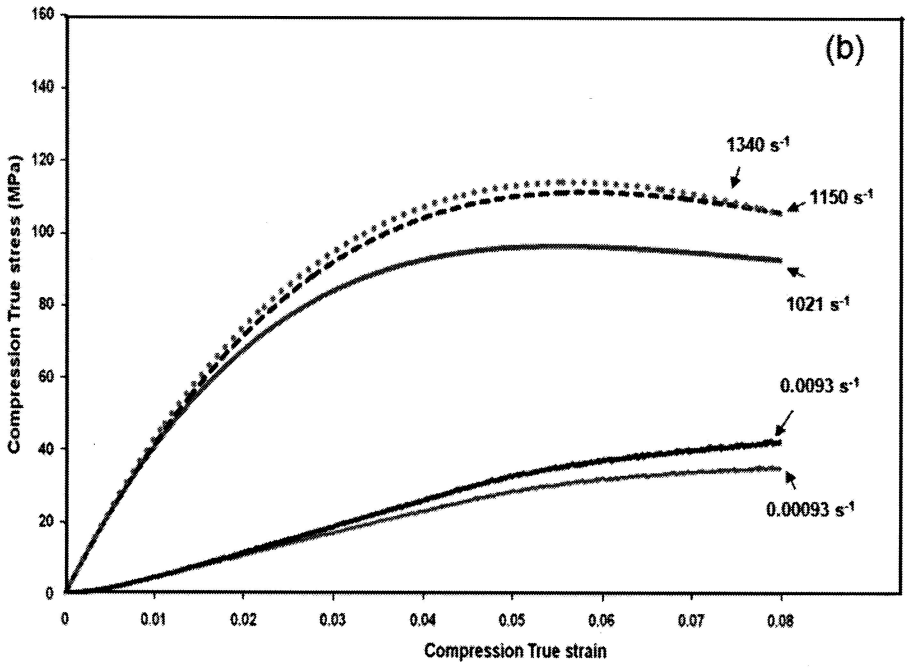
(b)
Compression True stress (MPa)
Compression True strain
1340 s-1
1150 s-1
1021 s-1
0.0093 s-1
0.00093 s-1
0
20
40
60
80
100
120
140
160
0
0.01
0.02
0.03
0.04
0.05
0.06
0.07
0.08

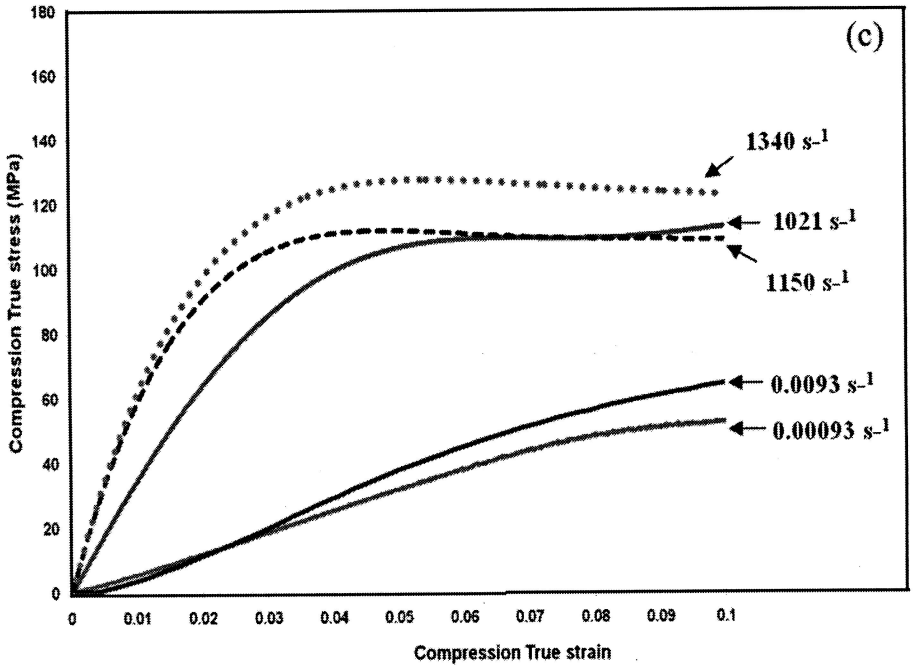

Figure 2. *Variation of stress/strain response of (a) PP-neat under, (b) PP-3 % SiO_2 and c) PP-5 % SiO_2 under various loading rates.*

As can be seen in Figure 2, all composites (PP-neat, PP-3 % SiO_2 and PP-5 % SiO_2) are strongly affected by the levels of strain rate. Obviously, the yield stress as well as the flow stress of the composites increase dramatically as the strain-rate increases. It has been reported that, the increase in stress has a close relationship to the secondary molecular processes (Yazhou & Yulong, 2007) where increasing strain-rate will decrease the molecular mobility of the polymer chains and thus make the material stiffens.

The 2.5 % flow stress of these composites exhibits a great rate dependent characteristic, as shown in Figure 3. However, both static and dynamic conditions show different rate dependent characteristic. At lower strain rate (static), the 2.5 % flow stress exhibits linear relation to the strain rate. Whereas, a dramatic increase in strain rate sensitivity is observed at high strain rate (Dynamic). The explanation of this phenomenon is still not clear but previous studies have interpreted this characteristic is due to the deformation mechanism from thermally activated flow mechanism (static) to a viscous drag dominating flow process (dynamic) (Yazhou & Yulong, 2007).

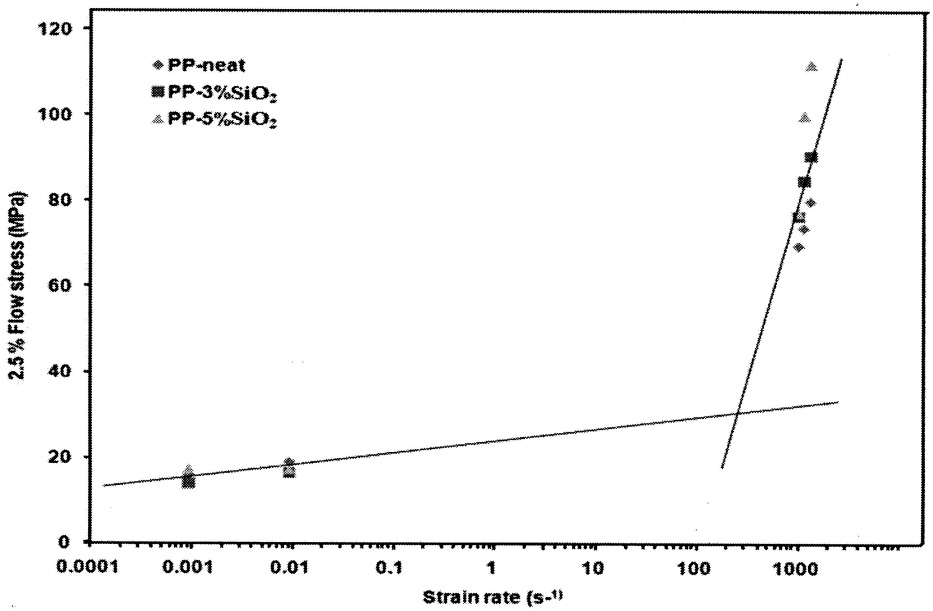

Figure 3. *Measured 2.5 % flow stress as a function of strain rate(s^{-1}) for PP-SiO_2 nanocomposites.*

Effect of filler loading

Effect of filler loading on static and dynamic compression modulus of PP-SiO_2 nanocomposites is depicted in Figure 4. Both conditions show a significant improvement in term of modulus elasticity over the range of strain rate investigated. Due to the fact that the modulus is measured before any significant plastic deformation takes place, it does not take into consideration the interaction between fillers and the polymer matrix. Thus, the increment was driven by the addition of rigid nanoparticles to PP matrix and also the presence of the mobility and deformability of the matrix by introducing a mechanical restraint (Leong, 2004).

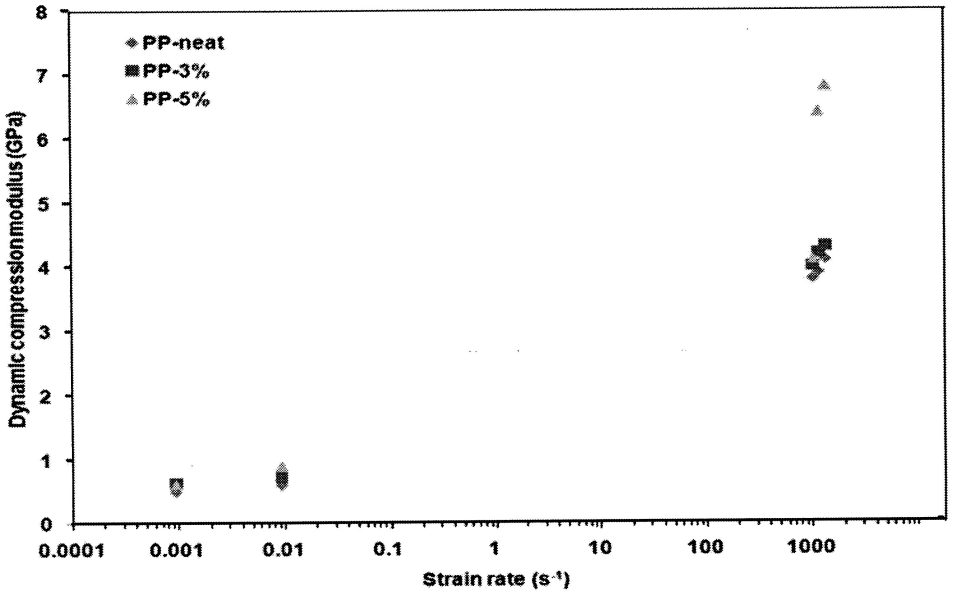

Figure 4. *Effect of filler loading on static and dynamic compression modulus of PP-SiO_2 nanocomposites.*

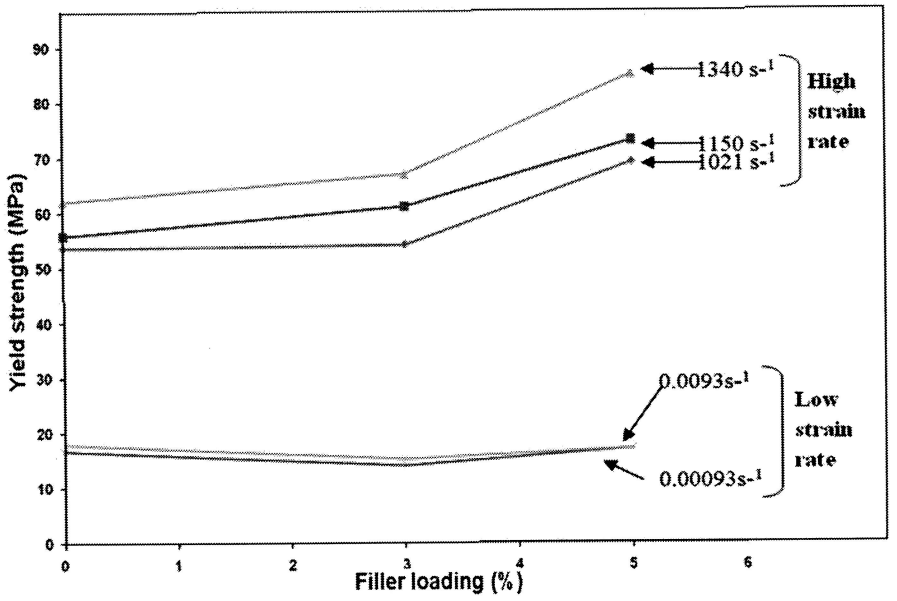

Figure 5. *Effect of filler loading on strength of PP-SiO_2 nanocomposites.*

Finally, the correlation between nanoparticles effect and loading rates is revealed in Figure 5. From the graph, it can be seen that at low strain rate, there is no significant effect between yield strength and the particle contents. However, at high strain rate, the strength of the composite is enhanced greatly with particle contents than that of the PP-neat. This characteristic enhancement was driven by the excellent dispersion of nanoparticle which reduces the stress concentration and thus make the material becomes stronger.

CONCLUSION

The static and dynamic characteristic of PP-SiO_2 nanocomposites at various loading rate (10^{-4} s^{-1} to 103 s^{-1}) with different nanoparticles contents (0-5 %) was successfully performed using compression Split Hopkinson Pressure Bar Apparatus (SHPBA). From the result, some important conclusions could be drawn:

- Compression modulus, yield strength and the 2.5 % flow stress of PP-SiO_2 nanocomposites increase greatly with increasing strain rate.
- Optimum filler loading added into these nanocomposite systems gives a significant improvement in terms of rigidity and strength properties where higher yield strength and compression modulus were recorded for higher filler loading over a span of strain rate investigated.

ACKNOWLEDGEMENT

The authors would like to acknowledge the Universiti Sains Malaysia (USM) (Grant no: 1001/ PBAHAN/ 8043057 & 811070) and the Universiti Malaysia Perlis (UNIMAP) for sponsoring and giving financial assistance during this research work. H.M. Akil wants to thank to Prof. Takashi Yokoyama from the Okayama University of Science, Department of Mechanical Engineering, for his valuable suggestions, during several discussions, regarding this research effort.

REFERENCES

Chen, W., Lu, F., and Cheng. M., (2002). Tension and compression tests of two polymers under quasi static and dynamic loading. *Polymer Testing.* **21**: pp. 113–121.

Hamouda, A. M. S. and Hashmi M. S. J., (1998). Testing of composite materials at high rates of strain: advances and challenges. *Materials Processing Technology.* **77**: pp.327–336.

Huang, C.J., Fu, S.Y., Zhang, Y.H., Lauke, B., Li, L.F., and Ye, L. (2005). Cryogenic properties of SiO_2/epoxy nanocomposites. *Cryogenics.* **45**: pp. 450–454.

Lee, O.S. and Kim, M.S., (2003). Dynamic material property characterization by using split Hopkinson pressure bar. *Nuclear Engineering and Design.* **226**: pp. 119-125.

Leong, Y. W., Abu Bakar, M. B. A, Ishak, Z. A. M., Ariffin, A. and Pukanszky, B. (2004). Comparison of the mechanical properties and interfacial interaction between talc, kaolin and calcium carbonate filled polypropylene composites. *J. Appl. Polym. Sci.*, **91**: pp. 3315-3326.

Nakai, K., and Yokoyama, T., (2008). Strain rate dependence of compressive stress-strain loops of several polymers. *Journal of Solid Mechanics and Materials Engineering.* **2**: pp 557-566.

Victor, M. F., Evora, and Arun, S., (2003). Fabrication, characterization, and dynamic behaviour of polyester/TiO_2 nanocomposites. *Materials Science and Engineering A.* **361**: pp. 358–366.

Woldesenbet, E. and Peter, S., (2009). Volume fraction effect on high strain rate properties of syntactic foam composites, *J. Mater. Sci.*, **44**: pp. 1528-1539.

Yaping, Z., Ying Z., and Rongchang N., (2003). Effects of nanoparticles SiO_2 on the performance of nanocomposites. *Materials Letters.* **57**: pp. 2940–2944.

Yazhou, G., and Yulong, (2007). L.Quasi-static/dynamic response of SiO_2–epoxy nanocomposites. *Materials Science and Engineering A.* **45**: pp. 330–335.

Zhao, H. (2003). Material behaviour characterization using SHPB techniques, tests and simulations. *Computers and Structures.* **81**: pp. 1301-1310.

Journal of Industrial Technology Vol. 19(1), 2010 - ICONT 2009, 41 - 60

THERMAL CONDUCTIVITY ESTIMATION OF OXIDE NANOFLUID IN WATER - INFLUENCE OF PARTICLE PROPERTIES

K.V.Sharma*, W.H.Azmi, Rizalman Mamat, S.M.Zuhairi, K.Kadirgama, R.A.Bakar

Faculty of Mechanical Engineering, Universiti Malaysia Pahang,
26600 Pekan, Pahang, Malaysia

***(kvsharmajntu@gmail.com)**

ABSTRACT : The theoretical and experimental analysis for the determination of heat transfer coefficient is mostly based on metallic oxide nanofluids by different investigators. Information regarding the properties at different volume concentration and temperature is required for the estimation of heat transfer coefficient. The two most important properties which are experimentally determined are viscosity and thermal conductivity. Investigators have been estimating the properties of metallic oxide nanoparticles at different ambient temperatures and with different base liquids. The present work is an attempt to analyse the available data and obtain a single linear regression equation for the estimation of thermal conductivity of water based nanofluids considering particle size, volume concentration and temperature useful for designer. It has been observed that the ratio of heat capacities of the nanoparticle to nanofluid has a profound influence on the values of thermal conductivity. The equation could predict the values of thermal conductivity ratio of ZnO nanofluid satisfactorily. The inclusion of heat capacity ratio term in the regression equation has vastly improved the predictability of thermal conductivity of water based nanofluids.

KEYWORDS : Nanofluid, thermal conductivity, regression equation, heat capacity ratio

INTRODUCTION

The estimation of experimental nanofluid thermal conductivity at different volume concentrations is done using the principle of heat conduction under steady or transient state. The determination of thermo-physical properties and especially thermal conductivity is important for evaluating heat transfer coefficients either for single or two phase flow. With limitations for the prediction of thermal conductivity from theory as of now, experimental data of various investigators for water based Al_2O_3 and CuO nanofluids is subjected to regression. Equations for the determination of thermal conductivity are developed as a function of percentage volume concentration, temperature and sometimes with the consideration of particle size valid in the experimental range. However, no single equation is available to predict the thermal conductivity of oxide nanofluids covering the entire range of experimental data considering all the variables involved.

The different models for the determination of effective thermal conductivity of two phase solid-liquid mixtures are based on the classical analysis of Maxwell (1881) and form the basis for the determination of nanofluid thermal conductivity. Various theoretical models are since being developed to predict the thermal conductivity of nanofluids. Even though nanoparticles are many orders smaller, suitable terms are included in the Maxwell's model by the investigators to take into consideration the dynamic factors associated with nanofluids. The contributions of different investigators for the determination of effective thermal conductivity of two phase metal and metallic oxide mixtures often repeated in literature are presented.

Maxwell (1881)

$$K_{eff} = K_{bf}\left[\frac{K_p + 2K_{bf} + 2\,\phi\left(K_p - K_{bf}\right)}{K_p + 2K_{bf} - \phi\left(K_p - K_{bf}\right)}\right] \tag{1}$$

The model predicts satisfactorily for spherical shaped particles at low volume concentration ϕ and at ambient conditions.

Bruggemen (1935)

The effective thermal conductivity of solid-liquid mixtures taking into account the interactions among the randomly distributed particles with no limitation on the particle volume concentration has been proposed by Bruggemen (1935) in implicit form given by equation (2):

$$\phi\left[\frac{K_p - K_{eff}}{K_p + 2K_{eff}}\right] + (1-\phi)\left[\frac{K_{bf} - K_{eff}}{K_{bf} + 2K_{neff}}\right] = 0 \quad (2)$$

where K_{eff} is estimated with Eq. (1) and K_{neff} is the net effective thermal conductivity of the two phase fluid which is to be determined.

Hamilton-Crosser (1962)

$$K_{nf} = K_{bf}\left[\frac{K_p + (n-1)K_{bf} - \phi(n-1)(K_{bf} - K_p)}{K_p + (n-1)K_{bf} + \phi(K_{bf} - K_p)}\right] \quad (3)$$

where the empirical shape factor 'n' defined by $n = 3/\psi$ and ψ is the sphericity defined as the ratio of the surface area of a sphere with the volume equal to that of the average particle. The Hamilton-Crosser model reduces to Maxwell model when $\psi = 1$ and is found to be in agreement with experimental data for $\phi < 30$ %. The model is valid as long as the conductivity of the particles is larger by a factor of 100 than the conductivity of the continuous phase. All these models are basically applicable for micro/millimetre sized particles suspended in base fluids. As the influence of particle size is not included in the analyses, the thermal conductivity of the nanofluid predicted by these models deviate from the experimental values.

Pak and Cho (1998)

The experiments by Pak and Cho (1998) may be considered as a pioneering work in estimating the properties of Al_2O_3 nanofluid for the determination of heat transfer coefficients in the turbulent range. A regression equation has been presented by them for the determination of thermal conductivity valid for volume concentration of $\phi < 3.0$ % given by equation (4)

$$k_{nf} = k_w(1 + 7.47\phi) \quad (4)$$

Yu and Choi (2003)

A modified model of Maxwell is proposed by Yu and Choi (2003) to predict the effective thermal conductivity of nanofluids. They assumed that the base fluid molecules are close to the surface of the nanoparticles to form a solid like layered structure having thermal conductivity higher than that of the base fluid. They combined the thermal conductivities of

the solid particles and the nanolayer to arrive at equivalent thermal conductivity of particle given by

$$K_{pe} = K_p \left[\frac{\gamma\{2(1-\gamma) + (1+\beta)^3(1+2\gamma)\}}{-(1-\gamma) + (1+\beta)^3(1+2\gamma)} \right] \quad (5)$$

where γ is the ratio of thermal conductivity of the layer to that of particle and β is the ratio of nanolayer thickness to the particle radius. The layer thermal conductivity varies in the range of 10 K_{bf} to 100 K_{bf} and thickness of 1 to 2 nm. The nanofluid thermal conductivity can be estimated from equation (6) with the aid of equation (5)

$$K_{nf} = K_w \left[\frac{K_{pe} + 2K_w + 2(K_{pe} - K_w)(1+\beta)^3\phi}{K_{pe} + 2K_w - (K_{pe} - K_w)(1+\beta)^3\phi} \right] \quad (6)$$

Das *et al.*, (2003)

Lee *et al.*, (1999) conducted experiments for the determination of thermal conductivity in water and ethylene glycol (EG) with Al_2O_3 and CuO nanoparticles of sizes 38 and 24 nm respectively. The experimental data with Al_2O_3/water and Al_2O_3/EG is observed to be in close agreement, whereas CuO/water and CuO/EG nanofluids showed higher values when compared with Hamilton-Crosser model. They reasoned for obtaining lower values of thermal conductivity with Al_2O_3/water due to larger particle size of 38 nm used when compared with the values of Masuda *et al.*, (1993) who used 13 nm size particles. However, the deviation of experimental values of CuO nanofluids when compared with Hamilton-Crosser could not be explained.

Das *et al.*, (2003) reasoned that the agreement between the data of Lee *et al.*, (1999) for Al_2O_3/water with Hamilton-Crosser model is purely accidental due to agglomeration of the nanoparticles. In order to explain the deviation of CuO nanofluids with Hamilton-Crosser model, they conducted experiments at different temperatures with 29 nm CuO nanoparticles in water. They observed the thermal conductivity of CuO/water nanofluid to increase from 2 to 10.8 % at 1 % volume concentration and 9.4 to 24.3 % at 4 % volume concentration measured at temperatures between 21 and 55 °C. They reasoned that Hamilton-Crosser model is insensitive to temperature and thus showed the dependence of nanofluid thermal conductivity on temperature and volume concentration.

Koo and Kleinstreuer (2004)

They proposed a model to determine the effective thermal conductivity of nanofluid as the sum of Maxwell's model and a term due to Brownian motion. It takes into account the effect of particle size, volume concentration, temperature and properties of base fluid as well as nanoparticles subjected to Brownian motion given by equation (7)

$$K_{nf} = K_{bf}\left[\frac{K_p + 2K_{bf} - 2(K_{bf} - K_p)\phi}{K_p + 2K_{bf} + (K_{bf} - K_p)\phi}\right] + 5 \times 10^4 \beta \phi \rho_{bf} C_{pbf} f(T,\phi)\sqrt{\frac{kT}{\rho_p d_p}} \quad (7)$$

where β represents the fraction of the liquid volume which travels with a particle and decreases with particle volumetric concentration because of the viscous effect of moving particles. They introduced an empirical equation for $f\ (T,\phi)$ using the experimental data of Das *et al.*, (2003) for CuO nanofluids given by equation (8)

$$f(T,\phi) = (-6.04\ \phi + 0.4705)T + (1722.3\phi - 134.63) \quad (8)$$

which is valid in the range of 1 % < ϕ < 4 % and 300 < T < 325 K. Regression equation for the estimation of β proposed by them is given in Table 1.

Table 1. Value of β to be used with Equation (7) of Koo and Kleinstreuer (2004)

Type of particles	β	Concentration in %
Au-citrate, Ag-citrate and CuO	$0.0137(100\ \phi)^{-0.8229}$	ø < 1 %
CuO	$0.0011(100\ \phi)^{-0.7272}$	ø > 1 %%
Al_2O_3	$0.0017(100\ \phi)^{-0.0841}$	ø > 1 %%

Chon *et al.*, (2005)

An empirical correlation for the determination of thermal conductivity of Al_2O_3 nanofluid with their experimental data has been proposed by Chon *et al.*, (2005) given by equation (9)

$$\frac{k_{nf}}{k_{bf}} = 1 + 64.7\phi^{0.7460}\left(\frac{d_{bf}}{d_p}\right)^{0.3690}\left(\frac{k_p}{k_{bf}}\right)^{0.7476} \mathrm{Pr}_{bf}^{0.9955}\,\mathrm{Re}^{1.2321} \tag{9}$$

where d_{bf} is the molecular diameter of the base fluid, $\mathrm{Re} = \dfrac{\rho_{bf} K_B T}{3\pi\mu_{bf}^2 \iota_{bf}}$, ι_{bf} is the mean free path for water and K_B is the Boltzmann constant used in their analysis.

Xue and Xu (2005)

Xue and Xu (2005) developed an implicit relation for the determination of copper oxide nanofluid in water and ethylene glycol, based on a model that nanoparticles have shells between the surface of the solid particle and the surrounding liquid given as in equation (10)

$$\left(1-\frac{\phi}{\omega}\right)\left[\frac{K_{nf}-K_{bf}}{2K_{nf}+K_{bf}} + \frac{\phi}{\omega}\frac{(K_{nf}-K_i)(2K_i+k_p)-\omega(K_p-K_i)(2K_i+k_{nf})}{\omega(2K_{nf}+k_i)(2K_i+k_p)+2\omega(K_p-K_i)(K_i-k_f)}\right]=0 \tag{10}$$

where $\omega = \left[r_p \Big/ (r_p + t)\right]^3$ is the thermal conductivity of the interfacial shell, r_p is the radius of nanoparticles and 't' represents the thickness of the shell which is different for different nanofluids.

Prasher *et al.*, (2006)

The combined Maxwell-Garnett conduction model and the convection caused by the Brownian motion of the suspended nanoparticles is said to be responsible for thermal conductivity enhancement of nanofluids by Prasher *et al.*, (2006). Based on the model, they proposed an equation for thermal conductivity ratio given by equation (11)

$$\frac{k_{nf}}{k_{bf}} = \left(1+4\times10^4\,\mathrm{Re}^m\,\mathrm{Pr}_{bf}^{0.33}\,\phi\right)\left[\frac{\{k_p(1+2\alpha)+2k_m\}+2\phi\{k_p(1-\alpha)-k_m\}}{\{k_p(1+2\alpha)+2k_m\}-\phi\{k_p(1-\alpha)-k_m\}}\right] \tag{11}$$

where

$m = 2.5 \pm (15\% \text{ of } 2.5)$ for water based nanofluids

$m = 1.6 \pm (15\% \text{ of } 1.6)$ for ethylene glycol based nanofluids

$m = 1.05 \pm (15\% \text{ of } 1.05)$ for oil based nanofluids

$k_m = k_{bf}\left(1 + 0.25\ \mathrm{Re}\,\mathrm{Pr}\right)$ is the matrix conductivity

$\mathrm{Re} = \frac{1}{\upsilon}\sqrt{\frac{18KT}{\pi\rho_p d_p}}$ is the Brownian-Reynolds number

$\alpha = 2R_b k_m / d_p$ nanoparticles Biot number

R_b - interfacial thermal resistance between nanoparticles and different fluids

Li and Peterson (2006)

The effects of variations in temperature and volume fraction on thermal conductivity of copper oxide and aluminum oxide nanofluids have been investigated experimentally by Li and Peterson (2006). The experiments were conducted with nanoparticles of average size of 29 and 36 nm respectively of CuO and Al_2O_3, temperatures ranging from 27.5 to 34.7 °C at 2 %, 4 %, 6 %, and 10 % volume fractions. They reported that the nanoparticle material, diameter, volume fraction, and bulk temperature to have a significant impact on the effective thermal conductivity of these suspensions. A two-factor linear regression analysis for the estimation of thermal conductivity ratio based on the temperature and volume fraction is presented for aluminum oxide and copper oxide nanofluids respectively as (equations 12a and 12b)

$$k_{r=}\frac{k_{nf}}{k_w} = 1.0 + 3.761088\ \phi + 0.017924\ T - 0.30734 \qquad (12a)$$

$$k_{r=}\frac{k_{nf}}{k_w} = 1.0 + 0.7644815\ \phi + 0.018689\ T - 0.46215 \qquad (12b)$$

Jang and Choi (2007)

The proposed theoretical model involves four modes, contributing to the energy transfer which is responsible for enhancement of thermal conductivity of nanofluids. The first mode is collision between the base fluid molecules, the second is the thermal diffusion in nanoparticles, the third is the collision of nanoparticles with each other due to Brownian motion and the fourth is collision between base fluid molecules and nanoparticles by thermally induced fluctuations. The equation for determining effective thermal conductivity of nanofluid is given by equation (13) as

$$k_{nf} = k_{bf}(1-\phi) + \beta_1 k_p \phi + C_1 \frac{d_{bf}}{d_p} k_{bf} \mathrm{Re}_{d_p}^2 \mathrm{Pr}_{bf} \phi \qquad (13)$$

where

$$C_1 = 18 \times 10^6; \qquad \mathrm{Re}_{d_p} = \frac{C_{RM} d_p}{\upsilon}; \qquad C_{RM} = \frac{kT}{3\pi \mu_{bf} d_p l_{bf}};$$

$\beta_1 = 0.01$ is a constant considering the Kapitza resistance per unit area. The equivalent diameter; $d_{bf} = 0.384$ and mean free path; $l_{bf} = 738$ nm at 300 K, for water based nanofluids.

Vajjha and Das (2009)

Vajjha and Das (2009) measured the thermal conductivities of aluminum oxide, copper oxide and zinc oxide nanofluid with nanoparticles dispersed in the ethylene glycol (EG) and water in the ratio of 60:40 by mass. They conducted experiments in the temperature range of 298 to 363 K and up to 10 % volume concentration and developed a relation for the estimation of nanofluid thermal conductivity as presented in equation (14)

$$K_{nf} = K_{bf}\left[\frac{K_p + 2K_{bf} - 2\left(K_{bf} - K_p\right)\phi}{K_p + 2K_{bf} + \left(K_{bf} - K_p\right)\phi}\right] + 5 \times 10^4 \beta_2 \phi \rho_{bf} C_{pbf} f(T, \phi)\sqrt{\frac{kT}{\rho_p d_p}} \qquad (14)$$

The values β_2 of can be obtained from Table 2. The experimental data is subjected to regression to include the dependence of temperature and concentration on thermal conductivity as in equation (15)

$$f(T,\phi) = (2.8217 \text{ x } 10^{-2}\ \phi + 3.917 \text{ x } 10^{-3}) \left(\frac{T}{T_0}\right)$$

$$+ (-3.0669 \text{ x } 10^{-2}\ \phi - 3.91123 \text{ x } 10^{-3}) \quad (15)$$

Table 2. Value of β_2 to be used with Equation (14) of Vajjha and Das (2009)

Type of particles	β_2	Concentration	Temperature
Al_2O_3	$8.4407(100\phi)^{-1.07304}$	$1\% \le \phi \le 10\%$	$298K \le T \le 363K$
ZnO	$8.4407(100\phi)^{-1.07304}$	$1\% \le \phi \le 7\%$	$298K \le T \le 363K$
CuO	$9.881(100\phi)^{-0.9446}$	$1\% \le \phi \le 6\%$	$298K \le T \le 363K$

Murshed *et al.* (2009)

Murshed *et al.*, (2008) solved the steady state heat conduction equation with appropriate boundary conditions in cylindrical and spherical coordinates and compared the results with their experimental data for TiO_2, Al in ethylene glycol, Al_2O_3 in water and CNT in engine oil and showed satisfactory agreement with their theory. Later they (2009) included the dynamic Brownian motion to the static conduction model for deriving the equation for effective thermal conductivity of nanofluid, which has the flexibility to be reduced to Maxwell equation in the absence of interaction between the particle and interfacial layer and to that of base liquid in the absence of nanoparticles.

Mintsa *et al.* (2009)

Experiments to estimate the thermal conductivity of nanofluids in the temperature range of 20-50 °C and up to 18 % volume concentration of alumina/water and copper oxide/water nanofluids has been undertaken by Mintsa *et al.*, (2009). They observed that particles with smaller size yielded higher thermal conductivities and the difference increased with increase in temperature. Linear regression equation as a function of volume concentration for alumina/ water developed by them is given by equation (16)

$$\frac{k_{nf}}{k_w} = 1.0 + 1.72\,[\phi] \quad (16)$$

They however did not include the effect of temperature and particle dimension to determine their influence on thermal conductivity.

DATA ANALYSIS

Efforts to estimate thermal conductivity of suspended solid particles in liquid has been a subject of interest Maxwell (1881), Bruggemen (1935), Hamilton-Crosser (1962), Pak and Cho (1998), Yu and Choi (2003), Das *et al.*, (2003), Koo and Kleinstreuer (2004), Chon *et al.*, (2005), Xue and Xu (2005), Prasher *et al.*, (2006), Li and Peterson (2006), Jang and Choi (2007), Vajjha and Das (2009), Murshed *et al.*, (2009), Mintsa *et al.*, (2009), Sharma *et al.*, (2009).

Pak and Cho (1998) have presented a regression equation for the determination of thermal conductivity as a function of volume concentration, while Koo and Kleinstreuer (2004) improved the Maxwell theoretical model and introduced functional dependence on volume concentration and temperature, based on Brownian motion. Chon *et al.*, (2005) included volume concentration and thermal conductivity ratio of the particle to the base fluid in their equation. The effect of temperature is indirectly included through the Prandtl number, however the value of its index obtained by them is close to unity. The dynamic motion of the nanoparticles is incorporated through the Reynolds number which includes the mean free path of water. Prasher *et al.*, (2006) has introduced various non-dimensional terms for the determination of thermal conductivity in his equation. Xue and Xu (2005) developed an implicit relation based on a model that nanoparticles have shells between the surface of the solid particle and the surrounding liquid. It can be observed that different models have been developed to determine the thermal conductivity of nanofluids with the consideration of Brownian motion or with the concept of an interface between the surface of the particle and the liquid. Certain models include parameter such as mean free path of water used in the process of obtaining dimensionless terms.

Experimental studies resulted in the development of regression equations which are specific to the nanofluid in the experimental range conducted. Also, the experimental data obtained could not be compared with that of others for the reason that the particle size or temperature range and or the base liquid could be different, making it difficult to understand the reasons for deviation in the values obtained. Most of investigators have developed different equations for Al_2O_3 and CuO nanofluids in water as a function of either volume concentration or temperature or both. It is fairly established that the thermal conductivity of nanofluids is dependent on volume concentration, temperature and the particle size. A regression equation has been developed based on the available experimental data on Al_2O_3

and CuO nanofluids with 191 experimental values, taking into consideration the particle size, temperature and concentration applicable for a wide range of operating parameters given by equation (17)

$$k_r = \frac{k_{nf}}{k_w} = 0.9808 + 0.0142\,[\phi] + 0.2718\left[\frac{T_{nf}}{70}\right] - 0.1020\left[\frac{d_{np}}{150}\right] \quad (17)$$

valid in the range of $13 < d < 150\ nm$, $0 < \phi < 20\ \%$, $20 < T_{nf} < 70$ and obtained with AD of 2.8 % and SD of 3.5 %. A plot between the thermal conductivity ratio and temperature for different particle diameters is shown in Figure 1. It is observed, that the experimental data could not be predicted with Eq. (17) closely. Hence the data is further investigated to determine the parameter influencing the thermal conductivity of nanofluid.

Normally, the density of a material decreases with the increase in size due to voids. However, Mintsa *et al.*, (2009) have stated that the density of Al_2O_3 nanoparticles of 36 nm size is 3600 and 3880 kg/m^3 for 47 nm size particle indicating that the density increases with particle size. The density of the particle at other sizes is not available, a non-linear regression equation for estimation of density at any particle size is developed assuming the particles will attain a value of 4100 kg/m^3 that of solid at 150 nm. The specific heat of bulk Al_2O_3 material is considered as the specific heat of the nanoparticles. The density of 29 nm CuO nanoparticles is taken from Mintsa *et al.*, (2009) as 6500 kg/m^3 and specific heat as 531 J/kg K for consideration in the analysis. The heat capacity of the nanofluid is estimated from the law of mixtures using the equations available in literature. Hence, considering the ratio of nanoparticles to nanofluid heat capacity, the experimental data is subjected to regression analysis. The equation obtained is:

$$k_r = \frac{k_{nf}}{k_w} = 0.786 + 0.019\,[\varphi] + 0.266\left[\frac{T_{nf}}{70}\right] - 0.106\left[\frac{d_{np}}{150}\right] + 0.249\left[\frac{(\rho C)_p}{(\rho C)_{nf}}\right] \quad (18)$$

with AD of 2.8 % and SD of 3.5 %. Sarma *et al.*, (2009) developed a single equation for the determination of Nusselt number for Al_2O_3 and CuO nanofluids making use of the published data earlier.

RESULTS AND DISCUSSION

The experimental values of thermal conductivity available in open literature for Al_2O_3/ water and CuO/water nanofluids is plotted in Figure 1 with temperature for different particle diameters. Figure 2 is drawn for the same parameters as shown in Figure 1 however with the consideration of heat capacity ratios. The inclusion of heat capacity term in the regression analysis has yielded the prediction of the experimental data well encompassing the entire range of particle diameters, temperature range of experimentation with more generality into

the gamut of experimental data. A comparison of Figures 3 and 4 brings out the influence of heat capacity ratio on thermal conductivity ratio shown along with the data of Mintsa *et al.*, (2009) for Al_2O_3/water nanofluid. The effect of particle diameter on thermal conductivity ratio is shown in Figures 5 and 6. It is evident from the experimental data that the particle diameter shows considerable influence on thermal conductivity and decreases with increase in diameter. However, it can be observed that the thermal conductivity ratio decreases to a value less than one with increasing values of particle size. This might be due to the use of the data given by Mintsa *et al.*, (2009) between particle size and density used in the regression analysis which is in contradiction to the values of the densities 3205, 3008 and 3076 kg/m^3 respectively for 38, 50 and 80 nm size of particles reported by Risha *et al.*, (2007). Further, at a particular particle diameter, the thermal conductivity increases with increase in temperature as shown in the Figures 5 and 6 for 20 and 40 °C. The thermal conductivity data in the widely used particle diameter is in the range of 29 - 47nm and for a wide range of nanofluid volume fraction is shown encompassing the entire experimental data in Figure 8 for heat capacity ratio term HR = 0.5 in comparison with Figure 7 where the heat capacity term in the thermal conductivity equation is ignored.

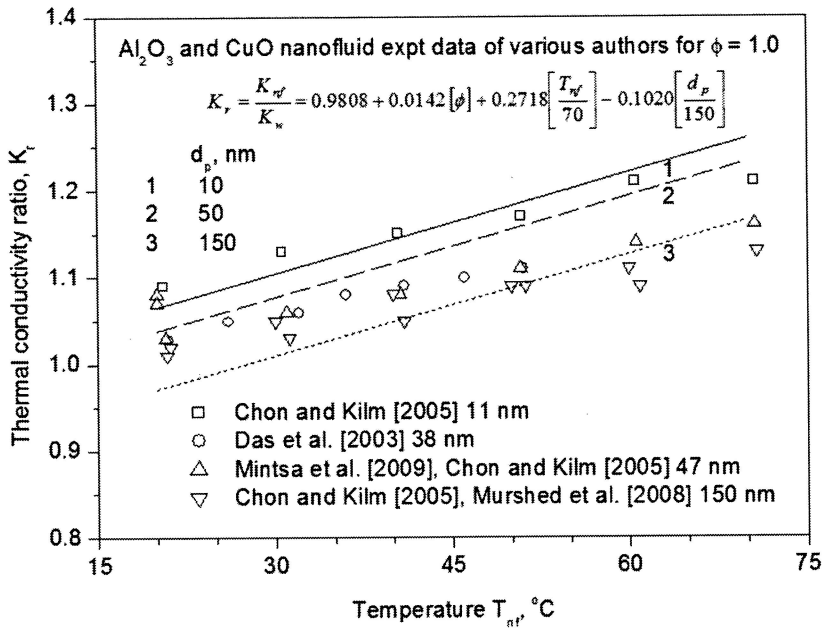

Figure 1. *Experimental data of thermal conductivity ratio of Al_2O_3 and CuO nanofluids with temperature*

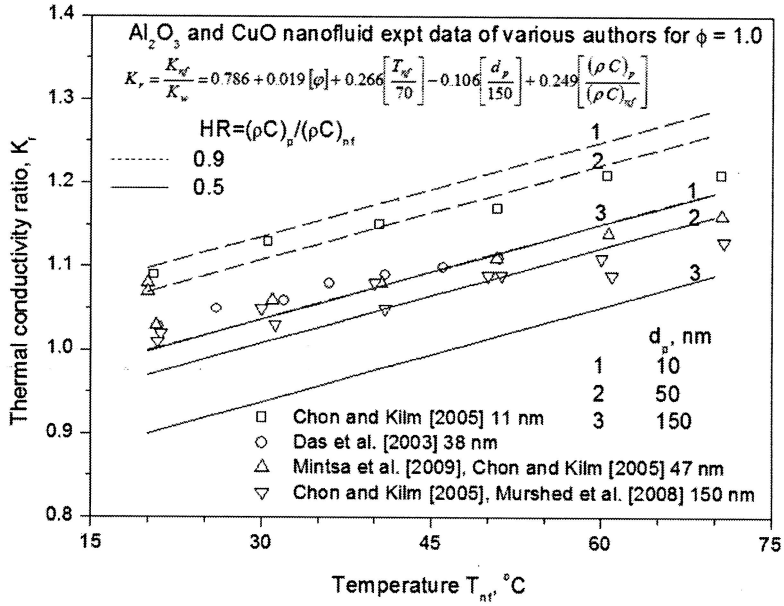

Figure 2. *Experimental data of thermal conductivity ratio of Al_2O_3 and CuO nanofluids with temperature for different values of HR*

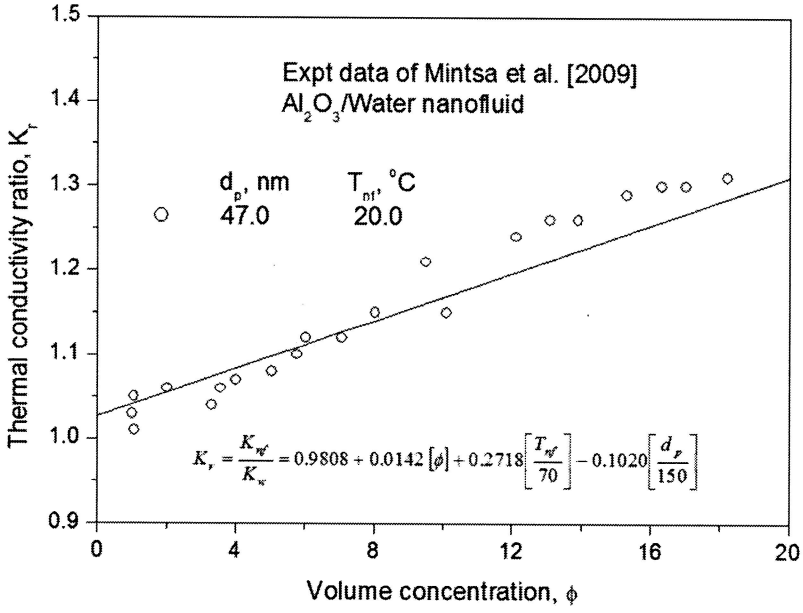

Figure 3. *Experimental data of thermal conductivity ratio Al_2O_3 nanofluid with ϕ*

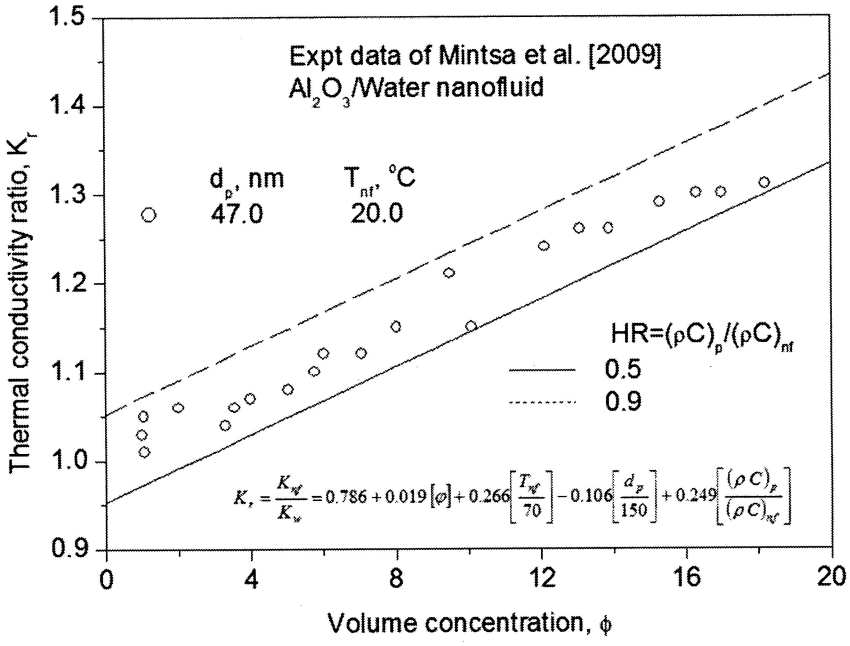

Figure 4. *Experimental data of thermal conductivity ratio of Al_2O_3 nanofluid with ϕ for different values of heat capacity ratio, HR*

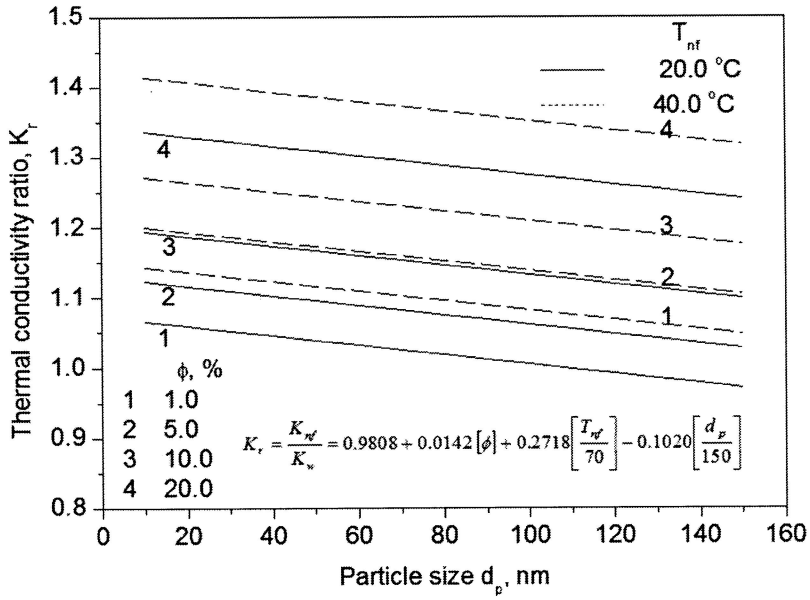

Figure 5. *Variation of thermal conductivity ratio with particle diameter – Effect of ϕ and temperature*

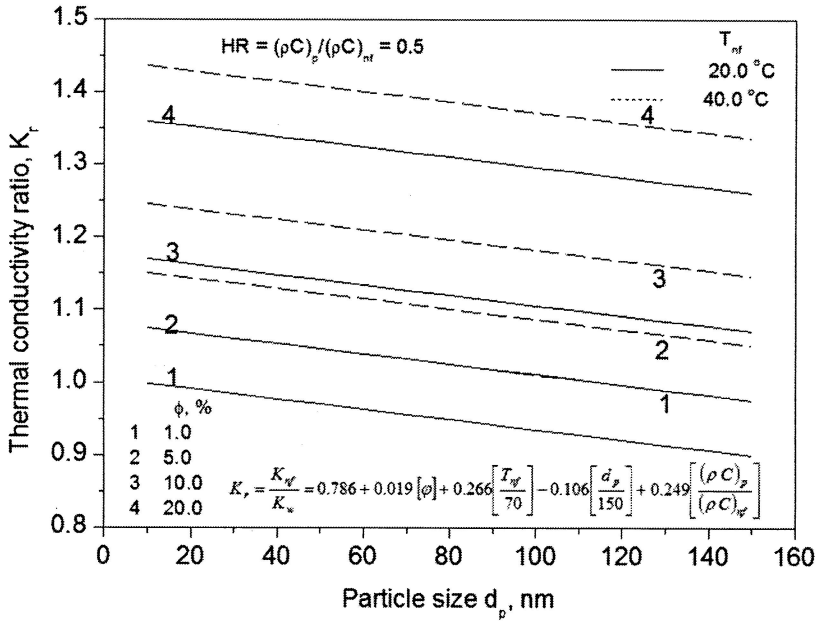

Figure 6. *Variation of thermal conductivity ratio with particle diameter – Effect of ϕ and temperature for HR = 0.5*

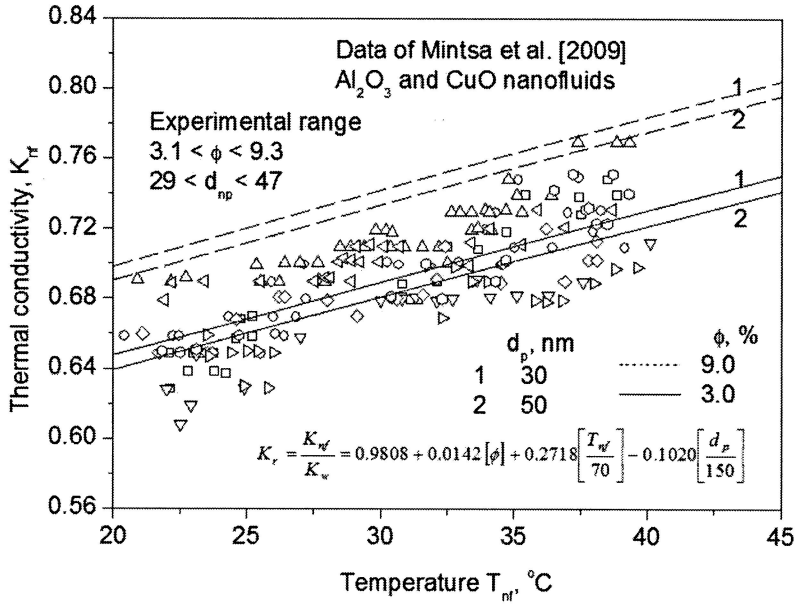

Figure 7. *Variation of thermal conductivity with temperature for different particle diameters and ϕ*

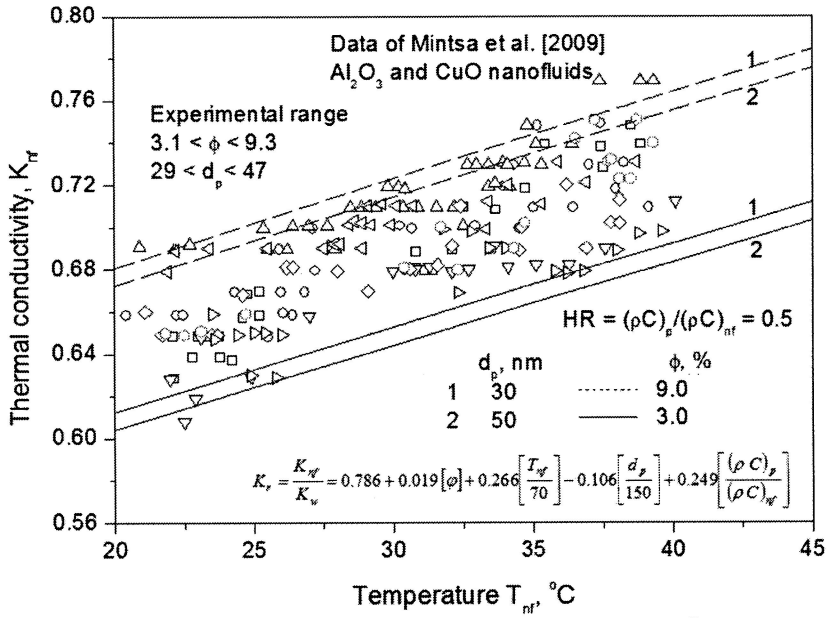

Figure 8. *Variation of thermal conductivity with temperature for different particle diameters and ϕ for heat capacity ratio HR = 0.5*

In order to show the significance of heat capacity ratio term HR and the applicability of the equation for water based nanofluid, the experimental data of Vajjha and Das (2009) for ZnO/ EG-water based nanofluid is shown in Figure 10 for different particle diameters, volume concentration of the nanofluid and temperature. The data is chosen as it is obtained for a wide range of temperatures, particle diameter and volume concentration, conducted with 60:40 EG/W base fluid. The trend exhibited by the experimental data is in satisfactory agreement with the values predicted by Eq. (18). There is a sharp contrast in Figure 9 drawn using Eq. (17) where the heat capacity term is not considered. The deviation of the experimental data can be attributed to the variation in particle density and the effect of specific heat with temperature. Thus, the objective of bringing out the significance of heat capacity ratio in the estimation of thermal conductivity ratio is achieved. Further investigation to substantiate the influence of these parameters on thermal conductivity is being carried out.

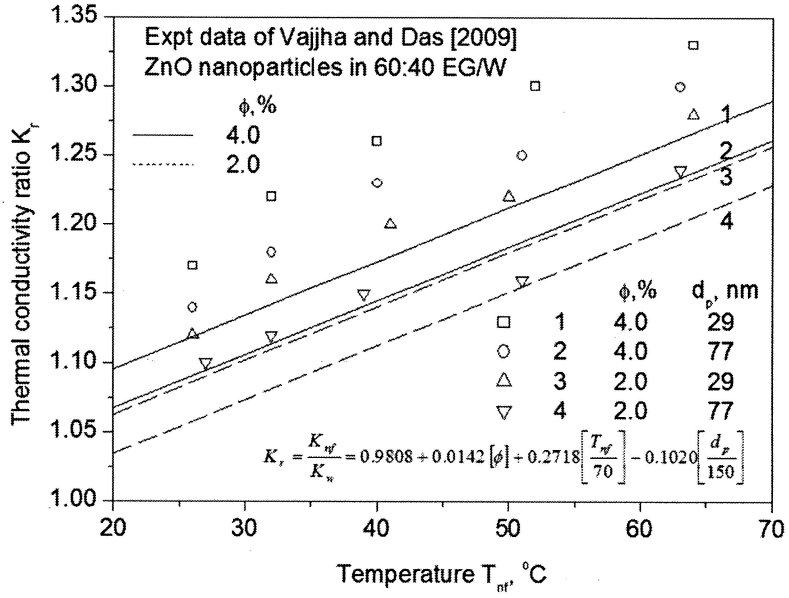

Figure 9. *Comparison of thermal conductivity ratio estimated with Eq. (17) with experimental values for ZnO nanofluid with 60:40 EG/W base fluid for different ϕ and particle diameters*

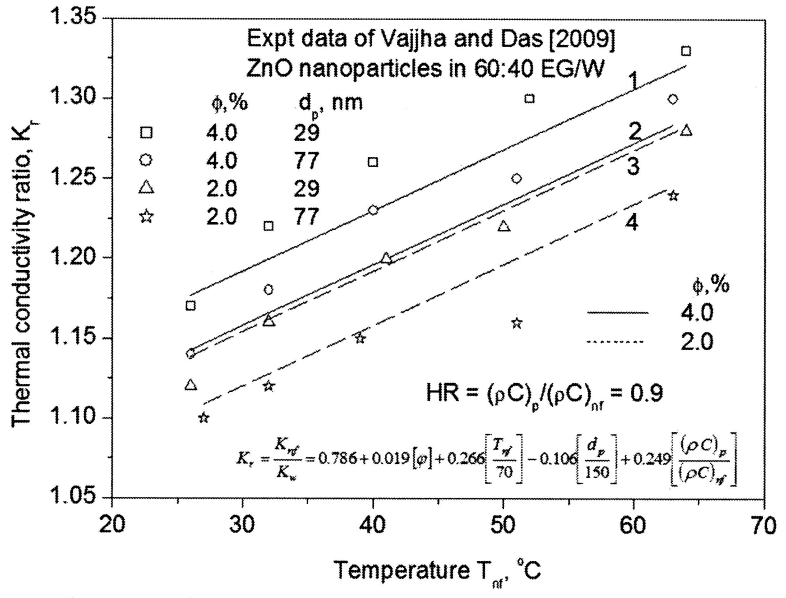

Figure 10. *Comparison of thermal conductivity ratio estimated with Eq. (18) with experimental values for ZnO nanofluid with 60:40 EG/W base fluid for different and particle diameters for HR = 0.9*

CONCLUSIONS

The following conclusions are drawn from the present study

(a) The thermal conductivity of nanofluid is dependent on volume fraction, diameter of the nanoparticles, temperature of the nanofluid and ratio of heat capacity of the particle to nanofluid.

(b) The heat capacity term included in the regression equation predicts thermal conductivity better based on the observations made with Al_2O_3 water and CuO/ water experimental data.

(c) The variation of particle density with size, specific heat of nanoparticles, size distribution has an influence on the thermal conductivity of nanofluid. This might be the reason for the deviation between the values obtained by different investigators.

ACKNOWLEDGEMENT

The financial support as short grant with RDU No.100349 by the Universiti Malaysia Pahang is gratefully acknowledged

REFERENCES

Bruggemen D.A.G. (1935). Berechnung verschiedener physikalischer Konstanten von heterogenen Substanzen. I. Dielektrizitatskonstanten und Leitfahigkeiten der Mischkorper aus isotropen Substanzen, *Ann Phys. Leipzig.,* **24**: pp 636-679.

Chon, C.H., Kihm, K.D., Lee S.P. and Choi, S.U.S. (2005). Empirical correlation finding the role of temperature and particle size for nanofluid (Al_2O_3) thermal conductivity enhancement, *Applied Physics Letters.* **85**: pp 1-3.

Chon, C.H., and Kihm, K.D. (2005). Thermal conductivity enhancement of nanofluids by Brownian motion, *J.Heat Transfer.* **127**: pp 810.

Das, S.K., Putra, N., Theisen, P. and Roetzel, W. (2003). Temperature dependence of thermal conductivity enhancement for nanofluid, *J. Heat Transfer.* **125**: pp 567–574.

Hamilton, R.L. and Crosser, O.K. (1962). Thermal conductivity of heterogeneous two component systems, *I&EC Fundamentals.* **1 (3)**: pp 187-191.

Jang S.P. and Choi, S.U.S. (2007). Effects of various parameters on nanofluid thermal conductivity, *J.Heat Transfer.* **129**: pp 617- 623.

Koo, J. and Kleinstreuer, C. (2004). A new thermal conductivity model for nanofluids. *J.Nanoparticle Res.* **6**: pp 577–588.

Lee, S., Choi, S. U. S., Li, S., and Eastman, J. A. (1999). Measuring thermal conductivity of fluids containing oxide nanoparticles. *J. Heat Transfer.* **121**: pp 280–289.

Li, C.H., and Peterson, G.P. (2006). Experimental investigation of temperature and volume fraction variations on the effective thermal conductivity of nanoparticles suspensions (nanofluids). *Journal of Applied Physics.* **99 (8)**: art. no. 084314.

Masuda, H., Ebata, A., Teramae, K., and Hishinuma, N. (1993). Alteration of thermal conductivity and viscosity of liquid by dispersing ultra fine particles. *Netsu Bussei.* **4(4)**: (1993) 227–233.

Maxwell, J.C. (1881). A treatise on electricity and magnetism, 2nd Edition, 1, Clarendon press, Oxford, U.K., pp 435.

Mintsa, H.A., Roy, G., Nguyen, C.T. and Doucet, D. (2009). New temperature dependent thermal conductivity data for water based nanofluids, *International Journal of Thermal Sciences.* **48**: pp 363-371.

Murshed, S.M.S., Leong, K.C., and Yang, C. (2009). A combined model for the effective thermal conductivity of nanofluids, *Applied Thermal Engineering.* **29**: pp 2477-2483.

Murshed, S.M.S., Leong, K.C. and Yang, C. (2008). Investigations of thermal conductivity and viscosity of nanofluids, *International Journal of Thermal Sciences.* **47**: pp 560-568.

Pak, B.C. and Cho Y.I., (1998). Hydrodynamic and heat transfer study of dispersed fluids with submicron metallic oxide particles, *Experimental Heat Transfer.* **11**: pp 151-170.

Ravi Prasher., Bhattacharya P., and Phelan. P.E. (2006). Brownian motion based convective conductive model for the effective thermal conductivity of nano fluids, *J. Heat Transfer, Trans. ASME.* **128**: pp 588-595.

Risha, G.A., Son, S.F., Yetter, R.A., Yang, V., and Tappan B.C. (2007). Combustion of nano-aluminum and liquid water, *Proceedings of the Combustion Institute.* **31**: pp 2029-2036.

Sarma, P.K., Kedarnath, C., Ramnarayanan, C.P., Kishore, P.S., Ramakrishna, K., Dharma Rao, V. and Srinivas, V. (2009). Some turbulent convective heat transfer characteristics in a tube with nano-particle inclusion in the base medium, 2nd issue, *Int. J. Heat and Technology,* Vol. 28, June 2010.

Sharma, K.V., Syam Sundar, L. and Sarma P.K.,(2009). Estimation of heat transfer coefficient and friction factor in the transition flow with low volume concentration of Al_2O_3 Nanofluid flowing in a circular tube and with twisted tape insert, *International Communications in Heat and Mass Transfer.* **36**: 503-507.

Vajjha, R.S. and Das, D.K. (2009). Experimental determination of thermal conductivity of three nanofluids and development of new correlations. *International Journal of Heat and Mass Transfer.* **52**: pp 4675-4682.

Xue, Q., and Xu W.M. (2005). A model of thermal conductivity of nanofluids with interfacial shells. *Material Chemistry and Physics.* **90 (2)**: pp 298-301.

Yu.W., and Choi, S.U.S. (2003). The role of interfacial layers in the enhanced thermal conductivity of nanofluids. A renovated Maxwell model? *Journal of Nanoparticle Research.* **5**: pp 167-171.

NOMENCLATURE

d	diameter
k	Boltzmann constant
K	thermal conductivity
k_m	mean thermal conductivity
γ	ratio of thermal conductivity of the layer to that of particle
ϕ	volume concentration in percentage

Subscripts

bf	base fluid
eff	effective
nf	nanofluid
p	particle

Journal of Industrial Technology Vol. 19(1), 2010 - ICONT 2009, 61 - 70

SURFACTANT ASSISTED SYNTHESIS OF COBALT NANOPARTICLES VIA POLYOL ROUTE

C.S. Khe, A. Azizan*, Z. Lockman

School of Materials and Mineral Resources Engineering
Universiti Sains Malaysia, Seberang Perai Selatan,
14300 Nibong Tebal, Pulau Pinang, Malaysia.

***(azizan@eng.usm.my)**

ABSTRACT : Cobalt nanoparticles were successfully prepared by polyol method with the assistant of a surfactant, i.e. sodium dodecyl sulfate (SDS). Transmission Electron Microscope (TEM) and Scanning Electron Microscope (SEM) were employed to calculate the particles size distribution and observation of the morphology of cobalt nanoparticles. X-Ray Diffraction (XRD) confirmed the co-existance of HCP- and FCC- cobalt in the same cobalt sample. Pure cobalt powder was obtained and confirmed by Energy Dispersive X-ray Analysis (EDX). Ultraviolet-visible spectrophotometer (UV-Vis) had been employed to investigate the evolution of cobalt nanoparticles in the synthesis. Effects of surfactants on the formation of cobalt nanoparticles were investigated and discussed.

KEYWORDS : Cobalt nanoparticles, polyol, sodium dodecyl sulphate (SDS)

INTRODUCTION

Nanoparticles constitute a major class of nanomaterials. The size dependent properties of nanoparticles include chemical and physical characteristics which make it the focus of numerous researchers. Cobalt is categorized under magnetic materials. Magnetic nanoparticles have their particular potential applications which include ferrofluids, magnetic data storage, environmental remediation, drug delivery, catalysis and variety of innovative applications (Chikazumi *et al.*, 1987, Chow *et al.*, 2002, Takafuji *et al.*, 2004., Partha *et al.*, 2008, Conroy *et al.*, 2008, and Park *et al.*, 2005). Without any incorporation of surfactant or protective agent, the magnetic nanoparticles will easily be agglomerated and grow in micron or submicron-meter in size. Since most of the properties of nanoparticles are greatly dependent on their size, therefore, to keep them physically isolated from one another is an important stage to achieve. Therefore, in this work we try to use SDS as a protective agent or surfactant in order to achieve the above mentioned purpose.

MATERIALS AND METHODS

In a typical experiment, $CoCl_2.6H_2O$ (1 mmol) was first dissolved in 25 ml ethylene glycol (EG). At the same time, SDS was dissolved in a beaker with 25 ml EG under constant stirring. Control sample is S1 without any surfactant added. For the samples of S2, S3 and S4, the SDS added was 0.5 g, 1.0 g and 1.5 g respectively. These two solutions were then mixed up and transferred to three necks flask. The mixture was then stirred for 20 minutes after 2 mmol of NaOH and 5 mmol of N_2H_4 were added. The mixture was refluxed for 1 hour at 180 °C, and the mixture was cooled to room temperature. The black precipitation was washed with ethanol for several times to remove impurities and finally kept in the sampling bottle.

X-ray Diffraction was performed using D5000 Siemens Diffractometer with a Cu-Kα (λ=0.154021 nm) radiation source. Micrographs were taken using Leo Supra 50 Variable Pressure Field Emission Scanning Electron Microscope (VPFESEM) and CM 12 Philips Transmission Electron Microscope (TEM). The elemental analysis was performed using EDX attached to SEM. UV visible measurement was conducted using the Perkin Elmer double beam spectrophotometer with a 10 mm optical path length quartz cuvette.

RESULTS AND DISCUSSION

Previous studies (Eastoe *et. al.,* 1996) reported that Ultraviolet Visible spectroscopy has been utilised as an effective tool to detect or monitor the evolution of metal species during the synthesis of colloidal metal cluster. The concentration of the metal species in the

solution can be analyzed quantitatively according to the absorption spectral obtained. Figure 1 presents the UV-vis spectral of control sample at different reaction times. Prior to the reaction, the absorption peak was located at 203.31 nm and had shifted to higher wavelength when the reaction started. After 60 minutes reflux, the absorption peak was located at 205.80 nm. This indicated that there is a formation of aggregation of small cobalt nanocrystallites with increased reaction time. As reported previously, larger nanoparticles show absorption peak at higher wavelength (Madler *et al.*, 2002; and Tani *et al.*, 2002). According to the Beer – Lambert's law, the absorbance is directly proportional to the concentration of the absorbing species (Dieter *et al.*, 2001). In this work, the concentration of cobalt nanoparticles is referred to the concentration of the absorbing species. The absorbance intensity increases as the reaction time increased as depicted in Figure 1. Therefore, the formation of the cobalt nanoparticles can be monitored in this work.

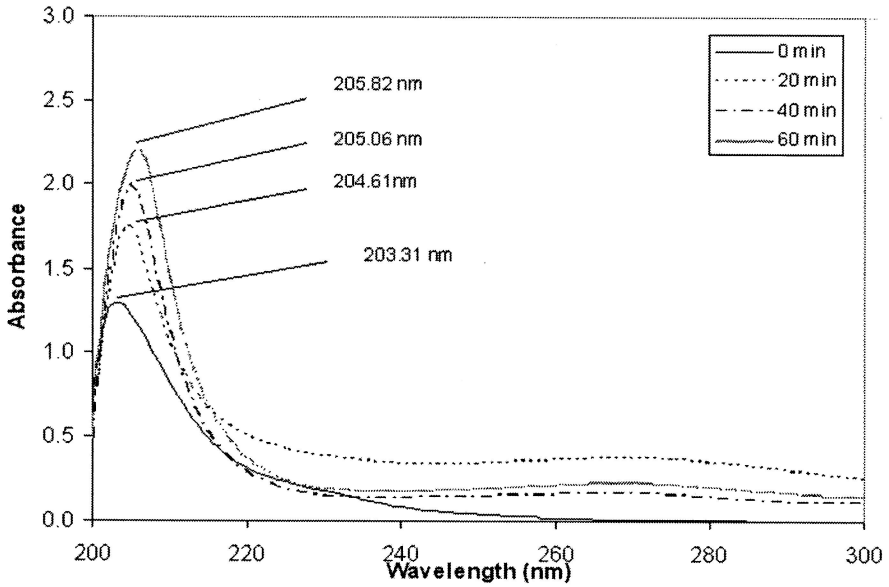

Figure 1. *UV-vis spectroscopy of control sample at different reaction times*

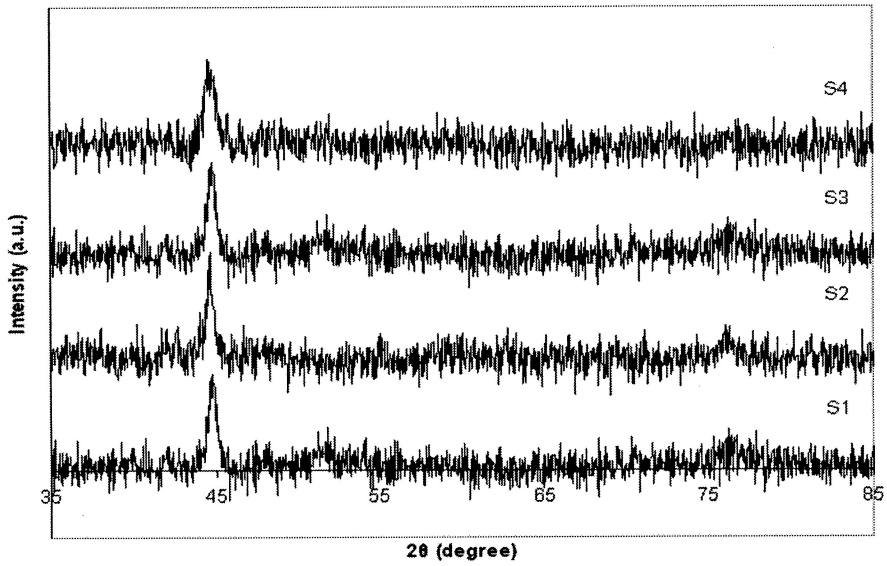

Figure 2. *XRD patterns of the as prepared cobalt particles*

Figure 2 shows the XRD diffraction of the cobalt particles produced by polyol method. Broadening peaks of the samples indicated the formation of the cobalt nanocrystallines especially in S4 sample with highest concentration of SDS. No oxide peaks were observed which indicates that the powder produced was purely cobalt powder. The JCPDS data, for these four samples showed the coexistence of both FCC and HCP structure, which is relatively a stable phase and this is normally due to the lower activation energy for the formation of stacking faults in the atomic planes (Sun & Murray, 1999).

Figure 3 presents the Transmission Electron Micrograph and Scanning Electron Micrograph as well as the histogram of particle size distribution of S1 without addition of any surfactant. The TEM micrograph shown in Figure 3 (a), demonstrates that the cobalt particles obtained are highly agglomerated. Most of the small particles are bound together which results in a black image of a big lump of nanoparticles. However, from the SEM micrograph shown in Figure 3 (b), it can be seen that the morphology of the control sample is made up of many spherical particles that are stacked on one another. The mean particle size was calculated from this micrograph and displayed in Figure 3 (c). The mean particle size obtained was 645 nm.

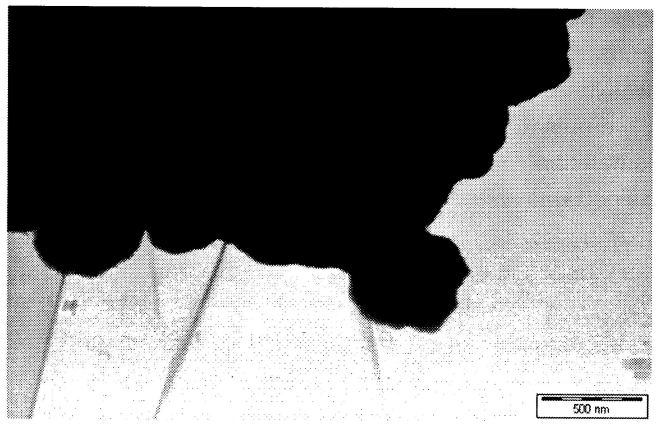

(a)

Figure 3. *(a) TEM image of S1, Control sample without SDS added*

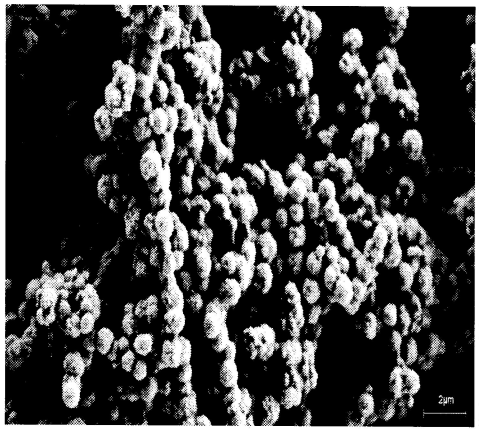

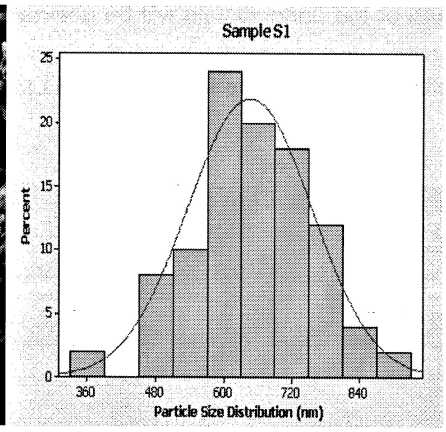

(b) (c)

Figure 3. *(b) SEM image of S1, (c) Mean particle size obtained was 645 nm*

Figures 4 - 6 show the TEM images and the particle size distribution histogram of samples with additional surfactant of sodium dodecyl sulphate (SDS). TEM image for S2 was shown in Figure 4 (a). It was found that quite a number of nanoparticles were isolated from each other, which is probably due to the absorption of the SDS molecules on the surfaces that prevents them from agglomeration. Figure 4 (b) presents the size histogram of S2, where the average particle size obtained was about 24.14 nm. As the SDS concentration increases to 1.0 g and 1.5 g for the following two samples, the cobalt nanoparticles obtained were getting smaller in size which can be seen in the TEM micrographs obtained that was displayed in Figure 5 (a) and Figure 6 (a) respectively. The size distribution histograms in Figures 5 (b) and 6 (b) demonstrate the average size for S3 and S4 which is 10.82 nm and 7.52 nm respectively.

It is believed that the tiny crystalline nuclei were formed in the supersaturated solution followed by the crystal growth. The added surfactant some how controls the size of the nanoparticles (Giselle *et al.*, 2007, Zhao *et al.*, 2006 and Sook *et al.*, 2009). In this case, SDS molecules served as absorbing molecules. The absorption of SDS molecules on the facets of the first formed cobalt nanocrystals is important for the growth of the nanoparticles. The growth of the cobalt nanocrystals will be slowed down as the SDS molecules are absorbed on the crystals faces. As the concentration of the SDS increased in the solution, the growth of the nanocrystals will be getting slower as all the facets of nanocrystals were experiencing passivation. As a result, cobalt nanoparticles that was obtained in this work were getting smaller in size from sample S1 to S4.

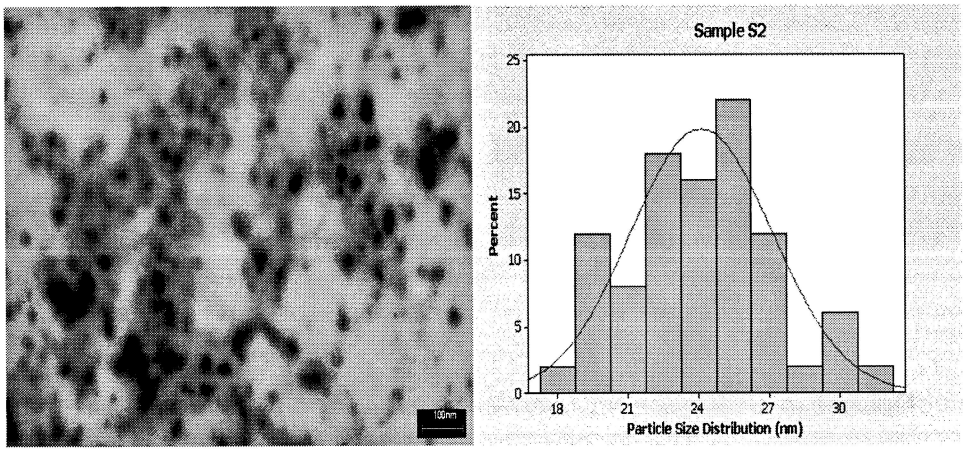

(a) (b)

Figure 4. *(a) Sample S2 with 0.5 g SDS. (b) Mean particle size obtained was 24.14 nm*

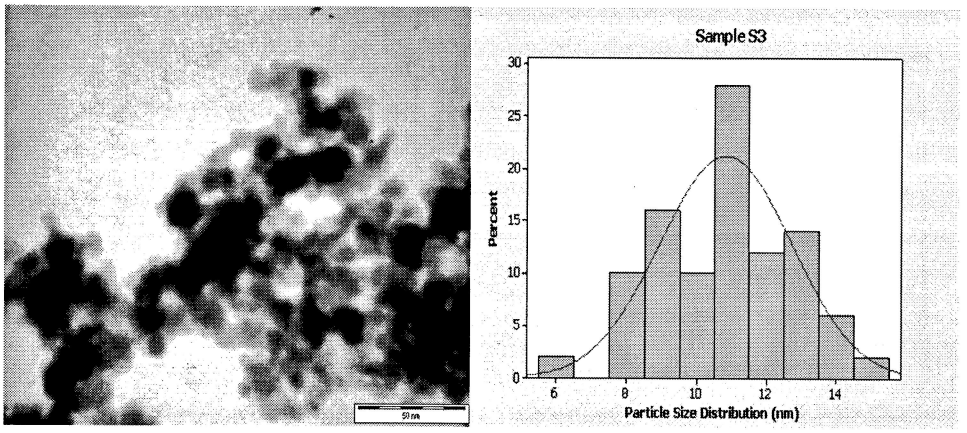

(a) (b)

Figure 5. *(a) Sample S3 with 1.0 g SDS. (b) Mean particle size obtained was 10.82 nm*

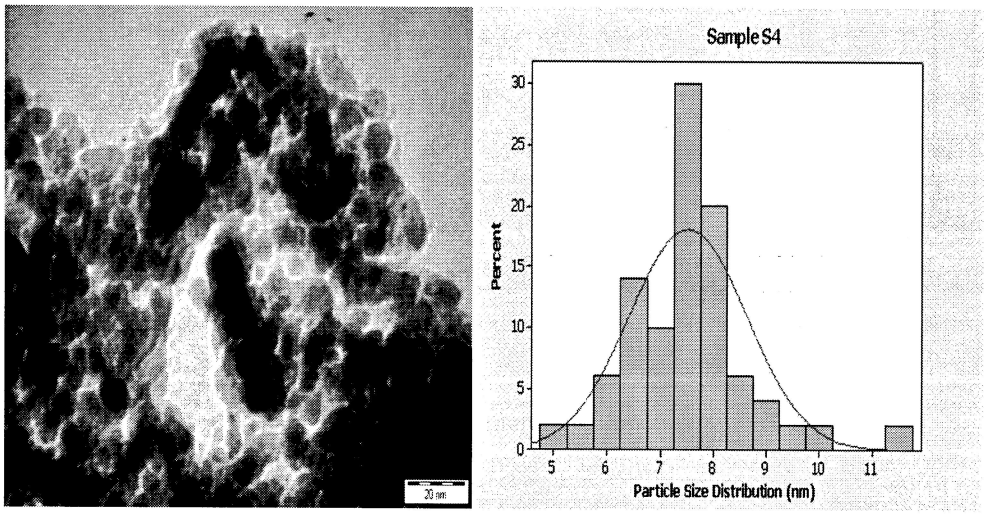

(a) (b)

Figure 6. *(a) Sample S4 with 1.5 g SDS. (b) Mean particle size obtained was 7.52 nm*

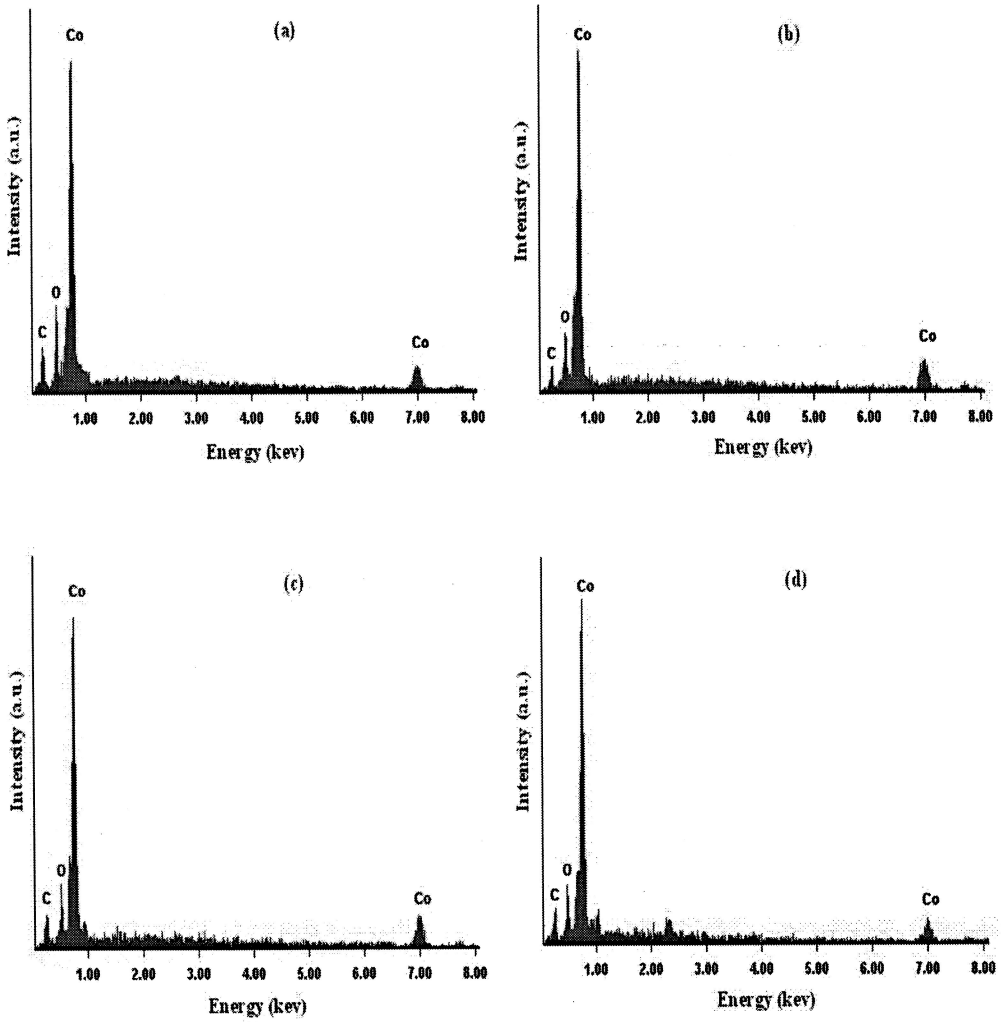

Figure 7. *EDX spectra for sample (a) S1 (b) S2 (c) S3 and (d) S4*

In order to know the purity of the cobalt powder that was obtained through the polyol method, Energy Dispersive X-ray analysis (EDX) was used as presented in Figure 7. All samples showed high percentage of cobalt which is more than 80 wt. %. Carbon and Oxygen elements emerged in these spectra and may be attributed to the absorbed surfactant on the surface of the particles that was not clearly washed out. The presence of oxygen and carbon could be attributed to both SDS and EG which possess both elements in their chemical structure (Chrystal *et al.*, 2002).

CONCLUSION

The results pointed to the fact that samples without sodium dodecyl sulfate, will produce nanoparticles that are highly agglomerated. Addition of sodium dodecyl sulfate in the samples reduced the agglomeration significantly and the cobalt nanoparticles of less than 30 nm were produced.

ACKNOWLEDGEMENT

The authors would like to thank USM, USM fellowship and the E-Science fund (305/PBAHAN/6013344) for the financial support.

REFERENCES

Chikazumi, S., Taketomi, S., Ukita, M., Mizukami, M., Miyajima, H., Setogawa, M., Kurihara, Y. (1987). Physics of Magnetic Fluids. *J. Magn. Magn. Mater.* **65**: pp 245-251.

Chow, G.M., Ding, J., Zhang, J. (2002). Enhanced magnetization of nanostructured granular Ni/[Cu(II)–C–O] films. *Appl. Phys. Lett.* **80**: pp 1028-1030.

Chrystal, D. B., Max L. B., Lalith, P., Malcolm, D. E. F. (2002). Molecular Dynamics Simulation of Sodium Dodecyl Sulfate Micelle in Water: Micellar Structural Characteristics and Counterion Distribution. *J. Phys. Chem.* **B 106**: pp 3788-3793.

Conroy, S., Lee, S.H., Zhang, M.Q. (2008). Magnetic nanoparticles in magnetic resonance imaging and drug delivery. *Advanced Drug Delivery Reviews.* **60**: pp 1252-1265.

Dieter, B. and Urs Peter F. (2001). Quantitative modulated excitation Fourier Transform Infrared Spectroscopy. *Rev. Sci. Instrum.* **72**: pp 3782-3785.

Eastoe, J., Stebbing, S., Dalton, J., Heenan, R.K. (1996). Preparation of colloidal cobalt using reversed micelles. *Colloid Surf. A Physicochem Eng. Asp.* **119**: pp 123-131.

Giselle G. C., Joao J. K., Wido H. S., Dante H. M., Adilson J.A. de O., Aldo J.G. Z. (2007). Nickel nanoparticles obtained by a modified polyol process: Synthesis, characterization and magnetic properties. *J. Colloid and Int. Sci.* **311**: pp 461-468.

Madler, L., Stark, W.J. and Pratsinis, S.E. (2002). Rapid synthesis of stable ZnO quantum dots. *J. Appl. Phys.* **92**: pp 6537-6540.

Park, J., Kang, E., Son, S.U., Park, H.M., Lee, M.K., Kim, J., Kim, J.W., Noh, H.J., Park, J.H., Bae, C.J., Park, J.G., Hyeon, T. (2005). Monodisperse Nanoparticles of Ni and NiO: Synthesis, Characterization, Self-Assembled Superlattices, and Catalytic Applications in the Suzuki Coupling Reaction. *Adv. Mater.* **17**: pp 429-434.

Partha, G., Gang, H., Mrinmoy, D., Chae, K. K., Vincent M. R. (2008). Gold nanoparticles in delivery applications. *Advanced Drug Delivery Reviews.* **60**: pp 1307-1315.

Sook, Y. M., Takafumi K., Tohru S. (2009). CTAB Assisted synthesis of Size and shape controlled gold nanoparticles in SDS aqueous solution. *Mater. Lett.* **63**: pp 2038-2040.

Sun, S. and Murray, C.B. (1999). Synthesis of monodisperse cobalt nanocrystals and their assembly into magnetic superlattices. *J. Appl. Phys.* **85**: pp 4325-4330.

Takafuji, M., Ide, S., Ihara, H., Xu, Z. (2004). Preparation of Poly(1-vinylimidazole)-Grafted Magnetic Nanoparticles and Their Application for Removal of Metal Ions. *Chem. Mater.* **16**: pp 1977-1983.

Tani, T., Madler, L. and Pratsinis, S.E. (2002). Synthesis of ZnO/SiO_2 Composite Nanoparticles by Flame Spray Pyrolysis. *J. Mater. Sci.* **37**: pp 4627-4632.

Zhao, J., Chen, W.X., Zheng, Y.F., Li, X., Xu, Z.D. (2006). Microwave polyol synthesis of Pt/C catalysts with size controlled Pt particles for methanol electrocatalytic oxidation *J. Mater. Sci.* **41**: pp 5514-5518.

Journal of Industrial Technology Vol. 19(1), 2010 - ICONT 2009, 71 - 79

FABRICATION AND CHARACTERIZATION OF ELECTRODEPOSITED ONE-DIMENSIONAL NANOSTRUCTURES

Kok Kuan Ying[1], Ng Inn Khuan[1], Nur Ubaidah Saidin[1]*, Nurazila Mat Zali[1], Siti Salwa Zainal Abidin[1] and Nosang V. Myung[2]

[1] Malaysian Nuclear Agency, Bangi, 43000 Kajang, Selangor D. E.
[2] Department of Chemical and Environmental Engineering, University of California-Riverside, Riverside, California 92521.

***(ubaidah@nuclearmalaysia.gov.my)**

ABSTRACT : Electrochemical synthesis including electrodeposition, electroless deposition, and galvanic displacement offers tremendous versatility as a cost-effective method for synthesizing one-dimensional nanostructures such as nanowires, nanotubes, as well as radial and axial heterostructures. In this study, high aspect ratios ferromagnetic nickel nanowires with well-controlled dimensions and structures were first synthesized via template-assisted electrochemical deposition using anodized alumina membranes as scaffolds. Co-axial heterostructures or nanotubes were subsequently synthesized by galvanically displacing the sacrificial Ni nanowires with Te, Pd and Ag. It was found that the orientations of the electrodeposited Ni nanowires were governed by the deposition current and electrolyte conditions, while the composition and microstructural transformation of the nanowires via galvanic displacement process were governed by the temperature, reaction time and concentration of the electrolytes. Structural evolution of the nanostructures obtained was investigated using various microscopy, diffraction and probe-based techniques and the growth mechanisms involved were discussed.

KEYWORDS : Template-assisted electrodeposition, galvanic displacement, nanowires

INTRODUCTION

One-dimensional nanostructures have found improved performance in devices such as photovoltaic, gas sensor and magnetic sensor due to its dimensionality and functionality (Searly, 2008; Yang & Poeppelmeier, 2006). The advancement of electrochemical synthesis techniques in creating various structures of one-dimensional materials has provided the opportunity to innovate new materials architectures for achieving new functionalities in a cost-effective way. Template-assisted electrodeposition, for example, allows the deposition of high aspect ratio nanostructures such as single elemental or heterostructure nanowires (Fert & Piraux 1999; Laocharoensuk *et al.*, 2007) while galvanic displacement of the materials allows the transformation of materials to nanostructures such as nanotubes or coaxial nanowires (Xiao *et al.*, 2007; Lv *et al.*, 2009) to achieve the desired chemistry, morphology and microstructures.

Galvanic displacement is an electroless deposition process that takes advantage of the difference in the standard electrode potentials of different elements, leading to localised cathodic and anodic reactions without the use of additive, applied current and complicated procedures. Various metallic nanotubes such as Au, Pd, Pt, Ag, Cu and binary intermetallic compounds like Bi-Te, Pd-Ag have been synthesized via this process (Li *et al.*, 2002; Xiao *et al.*, 2007; Sun, Mayer and Xia, 2003). In this study, nickel nanowires were synthesized by template-assisted electrodeposition. The electrolyte conditions and the deposition currents were varied systematically in order to examine this effect on the crystal structure, morphology and chemistry of the nanowires. By galvanically displacing Ni nanowires with Te, Pd and Ag, various structures were obtained, the microstructures of which were then examined using a range of microscopy, diffraction and probe-based techniques.

MATERIALS AND METHODS

Using commercially available anodized alumina (Whatman Anodisc 13) as templates, Ni nanowires with approximately 200 nm diameters were synthesized at fixed current densities of 10 mA cm^{-2} and 50 mA cm^{-2} respectively using a two-electrode system with platinum as the counter electrode and alumina template as the working electrode. Prior to electrodeposition, the back side of the templates were sputter-coated with a layer of Au through seven consecutive sputtering runs at 20 mA for 3 minutes.

Two types of Ni electrolyte baths with different cations were used: E1 consisting of 1 M $NiCl_2.6H_2O$ + 0.5 M H_3BO_3 while E2 consisting of 1 M $NiSO_4.6H_2O$ + 0.5 M H_3BO_3. After electrodeposition, the gold-sputtered layer were removed using gold etching solution constituting 2.5 g KI, 10 ml I_2 and 90 ml H_2O. The template was subsequently dissolved in

1 M NaOH solution. The nanowires were concentrated by centrifuging and rinsing in nanopure water and the process was repeated for three times to remove the NaOH solution and finally suspended in isopropyl alcohol.

2 μL of the nanowire suspension was then dispensed on a silicon wafer to allow the solvent to evaporate. A 2 μL electrolyte solution consisting of 10 mM X + 1 M HNO_3 was dispensed onto the nanowires, where X is TeO_2, $Pd(NO_3)_2$ and $AgNO_3$ to galvanically displace the nanowires with Te, Pd and Ag respectively. The reaction was conducted at room temperature for 20 min.

The microstructures and morphology of the nanowires were examined using a Scanning Electron Microscope (FEI QUANTA 400) equipped with an X-ray Energy Dispersive Spectrometer (EDS) and operating at an accelerating voltage of 30 kV. The crystallographic information on the nanowires was obtained using X-ray diffractions performed on an X-ray diffractometer (Panalytical X-Pert PRO MPD) operating at 40 kV and 20 mA using Cu Kα radiation.

RESULTS AND DISCUSSION

Figure 1 shows the Scanning Electron Microscopy (SEM) images of the Ni nanowire arrays and the free standing nanowires after being released from the templates. Nanowires with uniform lengths and diameters were obtained. The length of the nanowires was governed by the deposition time with the average diameter maintained at 200 nm.

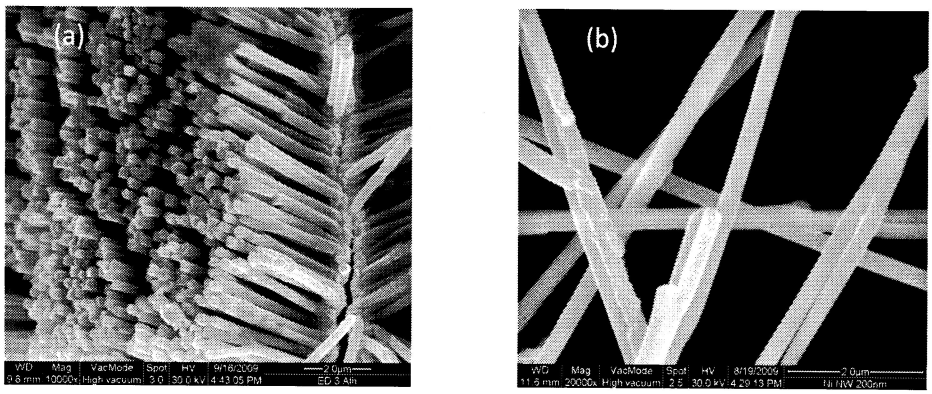

Figure 1. *SEM images of (a) nickel nanowire arrays. The nanowires exhibit regular cylindrical shape with uniform lengths and diameters. The template has been removed while the base of the nanowires is still attached to the gold layer. The nanowires are partially oriented to reveal their lengths. (b) free standing nickel nanowires after removal of gold layer and template*

The X-ray diffraction patterns in Figure 2 shows that the wires are polycrystalline with face-centred-cubic structure, as evident from the presence of three diffraction peaks close to 2θ angles of 44.5°, 51.8° and 76.4°, corresponding to Ni(111), Ni(002) and Ni(022) diffractions respectively. The preferred orientation of the nanowires depends on the types of electrolytes used as well as the current densities during deposition. The most intense peak switches from 022 to 111 for Ni deposited using electrolyte E1 when current density changes from 1 mA cm^{-2} to 50 mA cm^{-2}, while the reverse occurred for Ni deposition using electrolyte E2.

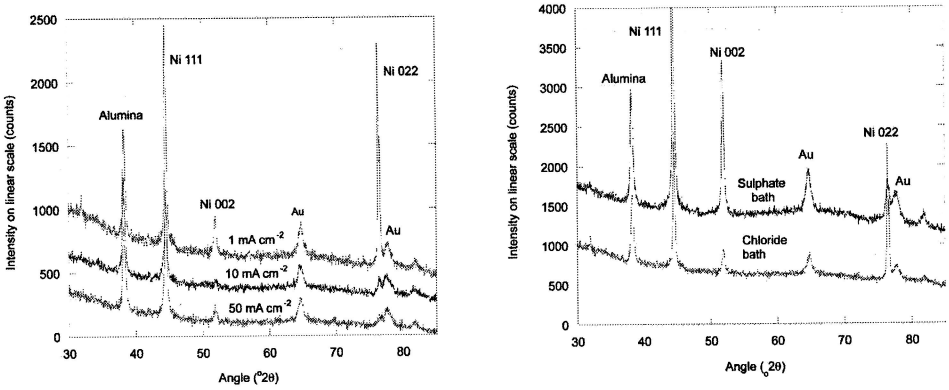

Figure 2. *X-ray diffractograms of nickel nanowires prepared using (a) electrolyte E1 with current density of 1 mA cm^{-2}, 10 mA cm^{-2} and 50 mA cm^{-2}, and (b) electrolytes E1 (chloride bath) and E2 (sulphate bath) with current density of 1 mA cm^{-2}. The preferred orientation of the nanowires is affected by the current density and the electrolyte used.*

Figure 3 shows the SEM images of the nanostructures obtained after galvanic displacement of Ni nanowires with Pd, Te and Ag respectively. The Energy Dispersive X-ray Spectroscopy (EDS) results recorded from the samples after displacement reaction reveal that the Ni nanowires were fully transformed to Pd, Te and Ag after 20 min immersion in respective electrolyte solutions at room temperature.

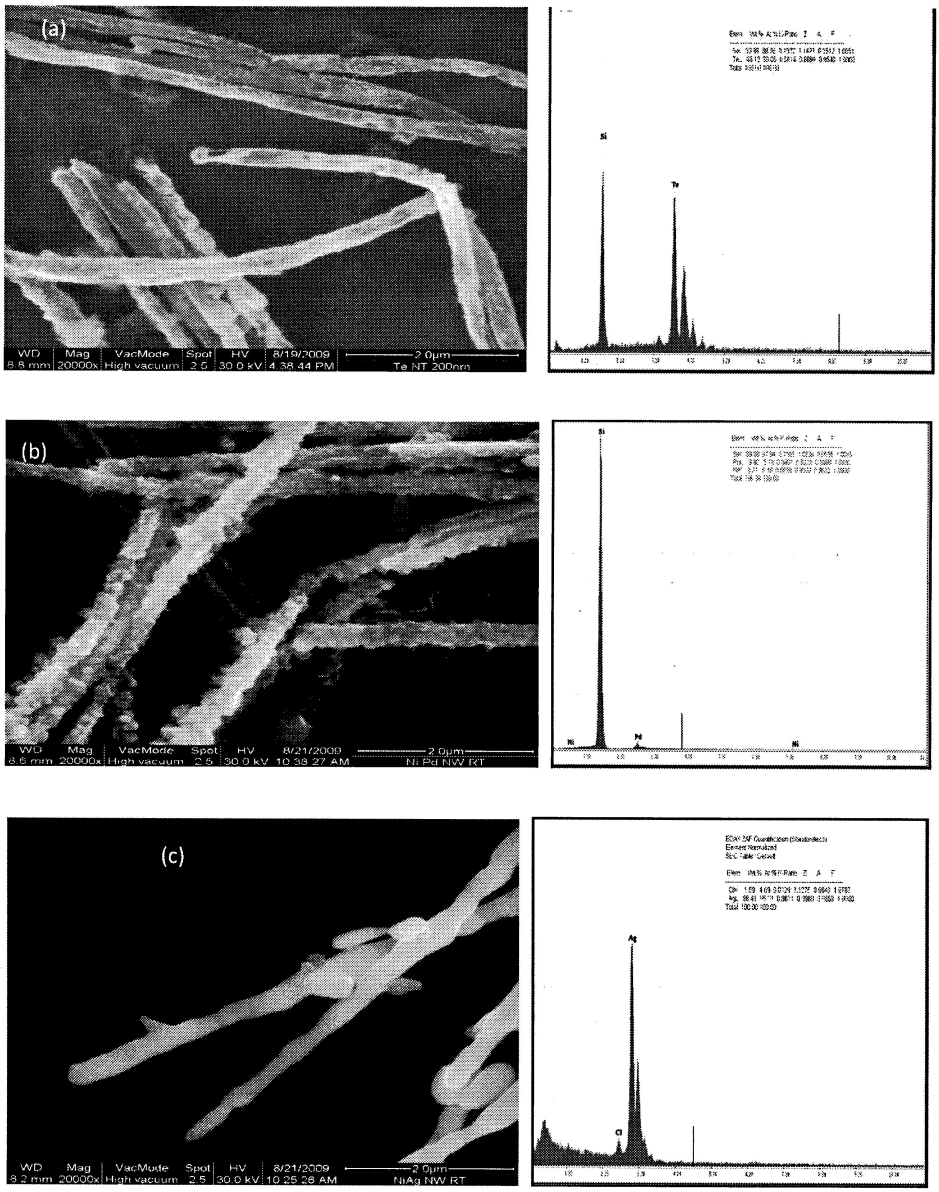

Figure 3. *SEM images and EDS spectrums of the nanostructures formed after galvanically displacing nickel nanowires with (a) Te (b) Pd and (c) Ag electrolytes at room temperature for 20 min. No Ni was present in the EDS spectrums indicating complete displacement of Ni. (a) and (b) shows Te and Pd nanotube structures with rough and grainy morphologies while (c) shows Ag nanowires of smooth morphology*

A more detailed study on the morphological and structural changes induced by the galvanic displacement process of nickel nanowires was carried out using $Pd(NO_3)_2$ solution of different concentrations, temperatures and reaction times and the results were shown in Figure 4. From the EDS results in Figure 5, Pd was found to fully displace nickel nanowires forming Pd nanotubes at 60 °C for a reaction time as low as 10 min while incomplete displacement of Ni (16 %) was observed for similar reaction time at room temperature. Increasing reaction time yields rougher and grainier morphologies due to aggregation of Pd particles along the surface of the nanowires. The optimum condition for full-displacement of Ni nanowires with Pd having uniform morphology was achieved using 1 mM Pd solution at 60 °C for 10 min.

The driving force of the galvanic displacement reaction comes from the difference in the reduction potential gaps between Ni^{2+}/Ni and Pd^{2+}/Pd according to the following reaction equation:

$$Ni^0\ (s) + 2\ Pd^+\ (aq) \rightarrow 2\ Pd^0\ (s) + Ni^{2+}\ (aq) \qquad (1)$$

The exchanged reaction is initiated from the external surfaces of the nickel nanowires with Pd ions accepting electrons from Ni to form Pd nucleus which chained up to form a coating. As the reaction proceeds, Pd evolves into a very thin shell at the edges of Ni nanowires while nickel nanowires dissolve to form a uniform channel along the nanowire axis. Longer reaction time tends to thicken the Pd surface with aggregation of Pd particles to form rough Pd nanotubes.

CONCLUSION

In this work, various one-dimensional nanostructures ranging from nanowires and nanotubes had been successfully synthesized using a combination of template-assisted electrodepositon and galvanic displacement techniques. Orientation of the nanowires produced was found to be governed by the current densities and the types of cations present in the electrolyte bath. We have also demonstrated that composition and microstructural transformations of the nanowires via galvanic displacement process were controlled by the temperature, reaction time and concentration of the electrolytes used. This technique can be applied to the synthesis of a wide range of nanomaterials and is potentially promising for commercial exploitation because it is simple, cheap and can be easily scaled up for industrial production.

Concentration of $Pd(NO_3)_2$ solution	Room temperature		60 °C	
	10 min	30 min	10 min	30 min
1 mM	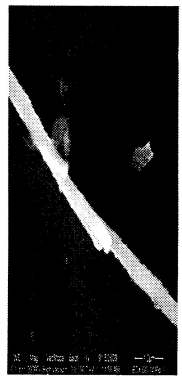 Partially displaced	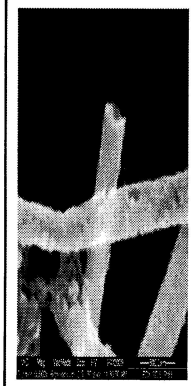 Fully displaced	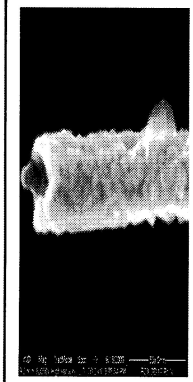 Fully displaced	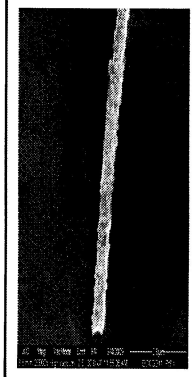 Fully displaced
10 mM	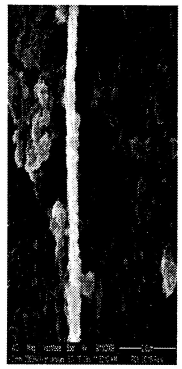 Partially displaced	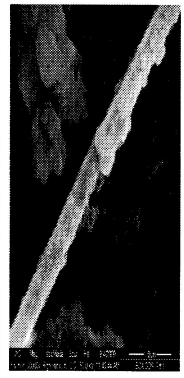 Fully displaced	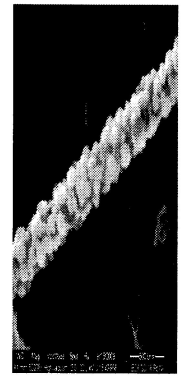 Fully displaced	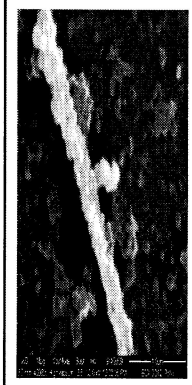 Fully displaced

Figure 4. *Microstructural evolution of the nickel nanowires displaced using different conditions of $Pd(NO_3)_2$ solution.*

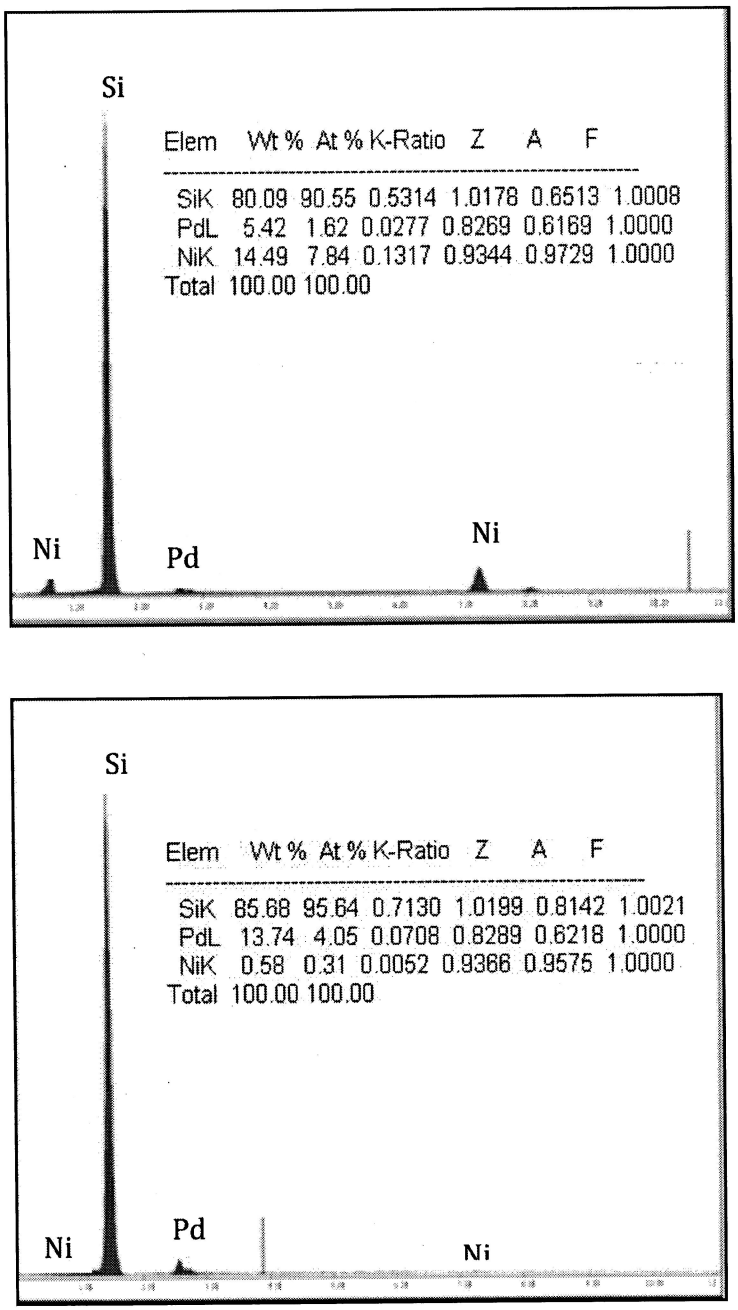

Figure 5. *EDS spectrums obtained for nickel nanowires that have been (a) displaced in 1 mM $Pd(NO_3)_2$ solution at room temperature for 10 min, and (b) fully displaced in 1 mM Pd(NO3)2 solution at 60°C for 10 min*

ACKNOWLEDGEMENT

The authors would like to acknowledge the Malaysian Government for funding this work (Science Fund Grant No: 03-03-01-SF0030).

REFERENCES

Fert, A. and Piraux, L. (1999). Magnetic Nanowires. *J. of Mag and Mag Mat.* **200**: pp 338 – 358.

Laocharoensuk R, Sattayasamitsathit S, Burdick J, Kanatharana P, Thavarungkul P and Wang J. (2007). Shape-Taoilored Porous Gold Nanowires: From Nano Barbells to Nano Step-Cones. *ACS Nano.***1 (5)**: pp 403 – 408.

Li, H., Liang, C., Liu, Zhong, K., Tong, Y., Liu, P. and Hope, G.A. (2009). Synthesis of Indium Nanowires by Galvanic Displacement and Their Optical Properties. *Nanoscale Res. Lett.* **4**: pp 47 – 53.

Lv, S., Suo, H., Zhoud, T., Wang, C, Jing, S., Fu, Q., Xu, Y. and Zhao C. (2009). Effect of Synthesis Route on the Morphologies of Silver Nanostructues by Galvanic Displacement Reaction. *Solid State Communications.* **149**: pp 227 – 230.

Searly, C. (2008). Winning the Memory Race, *Materials today.* **11 (6)**: pp 16 – 18.

Sun Y. G., Mayer, B. and Xia Y. N. (2002). Template-Engaged Replacement Reaction: A One-Step Approach to the Large-Scale Synthesis of Metal Nanostructures with Hollow Interiors. *Nano Letters.* **2 (5)**: pp 481 – 485.

Xiao, F., Yoo, B., Lee K. H. and Myung, N. V. (2007). Synthesis of Bi_2Te_3 Nanotubes by Galvanic displacement. *J. Am. Chem. Soc.* **129**: pp10068 – 10069.

Yang, P. and Poeppelmeier, K. (2006). Nanowires, *Inorganic Chemistry.* **45**: pp 7509 – 7510.

Journal of Industrial Technology Vol. 19(1), 2010 - ICONT 2009, 81 - 96

THE STRUCTURAL AND ELECTRICAL PROPERTIES OF AG/POLYANILINE (PANI) CORE-SHELL NANOCOMPOSITE

M. Alshaikh and *Roslan Md Nor

Department of Physics, Faculty of Science,
University of Malaya, 50603 Kuala Lumpur, Malaysia

***(rmdnor@um.edu.my)**

ABSTRACT : The formation of Ag nano particles using PVP (polyvinylpyrrolidone) as stabilizer to limit the growth of particles have been prepared by thermal process then coated by PANI (polyaniline) 'in situ' encapsulation chemical method, in which PANI was synthesized from its aniline monomer in the presence of sulfuric acid at 5°C. The objective of fabricating Ag/ PVP coated with PANI was to improve the solubility of PANI in organic solvents. The morphology of Ag/PANI nanocomposites was studied using TEM and SEM which showed that the particle size increased with increasing Ag concentration in the composite, owing to the aggregation effect. FT-IR spectroscopy and Energy Dispersion X-ray (EDX) have been used to characterize the resulting materials. The results showed that the presence of Ag nanoparticles in the composite has no effect on the formation of PANI (ES) form. The scope of our study was achieved by producing partially soluble and conductive PANI and Ag/PANI core-shell, 15 mg/ 10 ml, 20 mg/ 10 ml and 2.6×10^{-3} S/cm, 1.1×10^{-3} S/cm, respectively.

KEYWORDS : Core–shell nanocomposites, polyaniline, silver nanoparticles

INTRODUCTION

There is much interest in nanoparticle conducting polymers for various applications such as gas sensors, biosensors, electrode material and catalysts (Alok Srivastava *et al.*, 2006), (Aoife Morrin *et al.*, 2005), (Cui *et al.*, 1998). Polyaniline (PANI) is the most suitable polymer for development of new devices because of its reproducible synthesis, stability and its electrical properties which can be changed. By controlling the degree of doping (chemically), PANI can be converted from insulator to a semiconductor (Cho *et al.*, 2004; Morrin *et al.*, 2005; and Gangopadhyay *et al.*, 2000). Strong protonic acids, like DBSA (Xue *et al.*, 2006) or sulfuric acids function as proton dopants (Huang *et al.*, 1986). However, poor solubility and difficult processability make applications very limited. To overcome these problems, the properties of the conducting polymer could be modified by their interaction with other substances. (Moulton *et al.*, 2004).

The syntheses of metal–organic polymer and polymer–inorganic nanoparticles have potential use in technological applications and have attracted much attention recently due to their interesting properties (Xu, *et al.*, 2006; Malta *et al.*, 2003; Grubbs *et al.*, 2005; and Naderi, *et al.*, 2006). These particles not only combine the advantageous properties of metals and polymers but also exhibit many new characters that single-phase materials do not have. Early studies related to organic-inorganic junction generally involved polyaniline and Au (Xian *et al.*, 2006), polypyrrole–Fe nanocomposites (Chipara *et al.*, 2007) and polypyrrole/silver nanocomposites on gold substrate (Liu *et al.*, 2005). Ag/Polymer possessing unique properties has attracted intensive research for their potential applications in biological labeling and photoconducting sensors. Surface modification of Ag is necessary to make them useful in diverse applications. However, because of the hydrophobic surface property of some polymer, congregation and oxidation of Ag are common, (Pomogailo *et al.*, 2003; Yakuphanoglu *et al.*, 2006; Jing *et al.*, 2007; Kang *et al.*, 2006; and Feng *et al.*, 2006).

To prepare the nanoscale materials successfully, several approaches have been employed like physical mixing (Akelah *et al.*, 1995), sol–gel technique (Jang *et al.*, 2000), in-situ chemical polymerization in the aqueous solution with the presence of polymer monomer and inorganic particles, emulsion technology (He *et al.*, 2005) and sonochemical process (Kumar *et al.*, 2000). However, stabilizing Ag nanoparticles in bulk polymer remained a challenge. In this study, Ag/PVP nanoparticles were formed by thermal process. Core-shell silver (Ag)–polyaniline (PANI) nanocomposites have been synthesized by the in-situ chemical encapsulation polymerization method with different Ag concentrations. The morphological and electrical characterizations of the PANI/Ag nanocomposites were discussed. In addition, the improvement of its solubility was investigated.

MATERIALS AND METHODS

Chemicals

Silver nitrate was obtained from Bendosen, ascorbic acid from HmbG, polyvinylpyrrolidone (PVP) were purchased from Shanghai, sulfuric acid and aniline monomer were purchased from Merck, ammonium per sulfate (APS) was purchased from Aldrich and n-methyl-2-pyrrolidone (NMP) from Fluka.

Instrumentation

Morphological investigations were carried out using Scanning Electron Microscopy (SEM) [FEI Quanta 200 F (Philips)] and Transmission Electron Microscopy (TEM) (HITACHI, H-7650) at an acceleration voltage of 120 kV. The samples were diluted in ethanol then sonicated for 30 minutes prior to placing it by drops on the carbon coated copper grids. The elemental compositions of the pure PANI and PANI/Ag nanocomposites were estimated by Energy Dispersion X-ray (EDX) (Oxford Instruments, model 5431. X-ray diffraction pattern was taken with a Siemens D 500 model with CuKα source (λ=1.5418 °A). All scans were recorded in the 2θ region of 5 - 80°. FTIR spectra were recorded with a Thermo Scientific Nicolet iS10 FT-IR Spectrometer. The conductivity of the samples were measured by using Impedance analyzer - meter (Hioki 3531, Z Hi Tester). The samples were prepared as 0.66 mm diameter pellets by pressing the powder under hydraulic pressure of 3 tonnes.

Synthesis of Ag /PANI core-shell nanocomposite

Reduction of the silver salt (0.21 g) in aqueous solution of polyvinylpyrrolidone (0.7 g) as a stabilizer leads to the formation of silver nanoparticles in the presence of ascorbic acid as a reducing agent (0.45 g). The mixture was dissolved in 50 ml distilled water and stirred for 30 minutes at room temperature. The resulting homogenous solution was sealed and heated in a furnace at 110 °C for 24 hours. Finally, brown golden color of silver nanoparticles was obtained.

The PANI/Ag nanocomposite was prepared by in-situ chemical oxidation polymerization of aniline monomer in the presence of silver nanoparticles solution. In a typical synthesis process, aniline monomer (15.2 mmol) was added to 15.2 mmol of sulfuric acid in 80 ml distilled water under constant stirring in an ice bath for 1 hour which is followed by addition of the aqueous solution of ammonium per sulfate (15.3 mmol that was dissolved in 20 ml deionized (DI) water) for 10 minutes. Then the previously prepared Ag nanoparticles solution was added. The mixture was allowed to react for 2 hours under constant stirring at 5 °C. The green mixture was sealed and kept refrigerated for 24 hours. The resultant

product was centrifuged then dried in oven for overnight. The pure PANI was synthesized using similar chemical polymerization method as described above in the absence of silver solution.

RESULTS AND DISCUSSION

The morphology of polyaniline with an aggregated granular form of particles with particle size of 40-80 nm was shown in Figure 1. TEM and SEM images of PANI/Ag at different concentration of Ag/PVP solution in the composites reveal different particle size of nanosilver being formed. Both low and high concentration of Ag/PANI (L) and Ag/PANI (H) (50 ml) demonstrates the cubic shaped of Ag nanoparticles (black spots) which are uniformly dispersed in PANI. The size of the core increased with increasing Ag/PVP concentration in composite. The average diameters of the composite are ~5 nm and ~25 nm for APNI/Ag (L) and APNI/Ag (H), respectively (Figure 3). The EDX results show the presence of Ag, S, O and C in the prepared composites (Figure 4). The silver content (intensity) in the composite increased with increasing Ag/PVP concentration. Pure PANI exhibits zero intensity for Ag, whilst the intensity of both oxygen and carbon increased due to the presence of $AgNO_3$ and PVP in Ag/PANI respectively. In addition, the intensity of S in pure PANI is higher than that of Ag/PANI which indicates that the formation of PANI in Ag/PANI is less than that of pure PANI due to the incorporation of Ag nanoparticles.

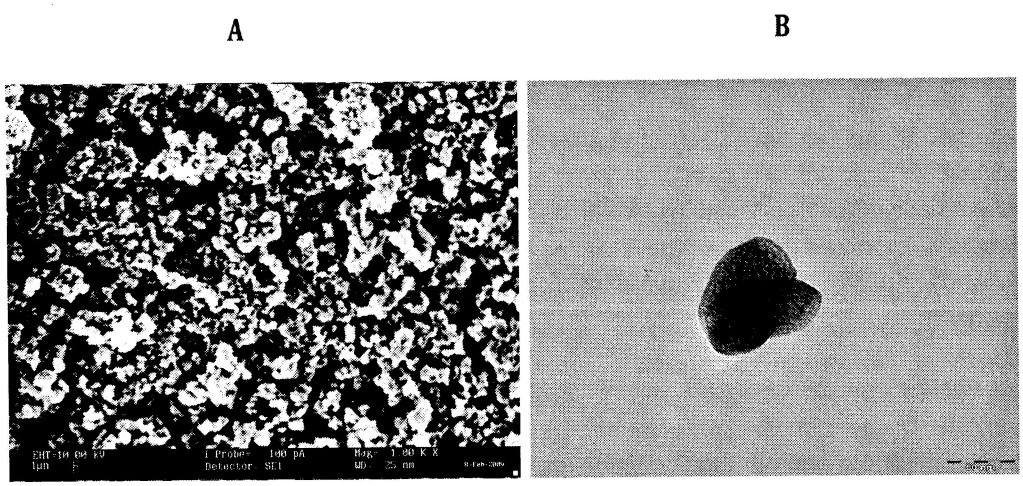

Figure 1. *A) SEM image of pure PANI; B.) TEM of Pure PANI*

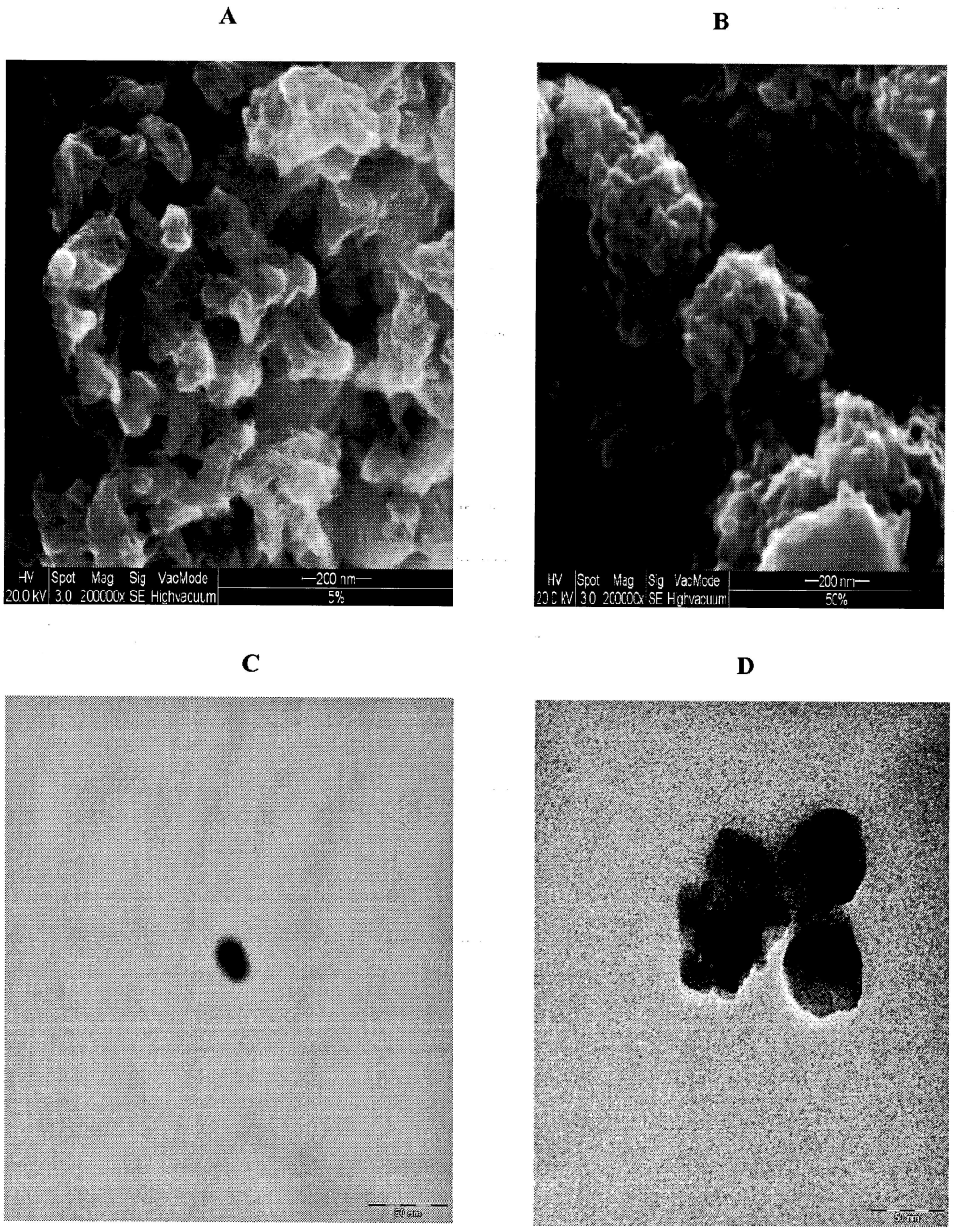

Figure 2. *SEM at 200000x (A. Ag/PANI (L), B. Ag/PANI (H)) and TEM at 50 nm (C. Ag/PANI (L), D. Ag/ PANI (H))*

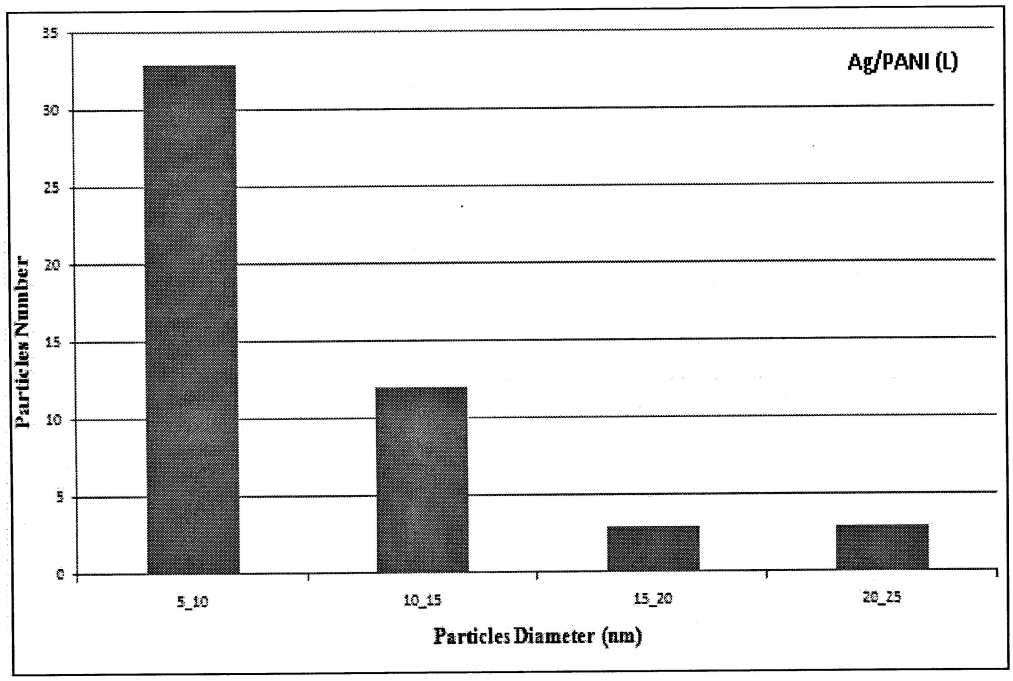

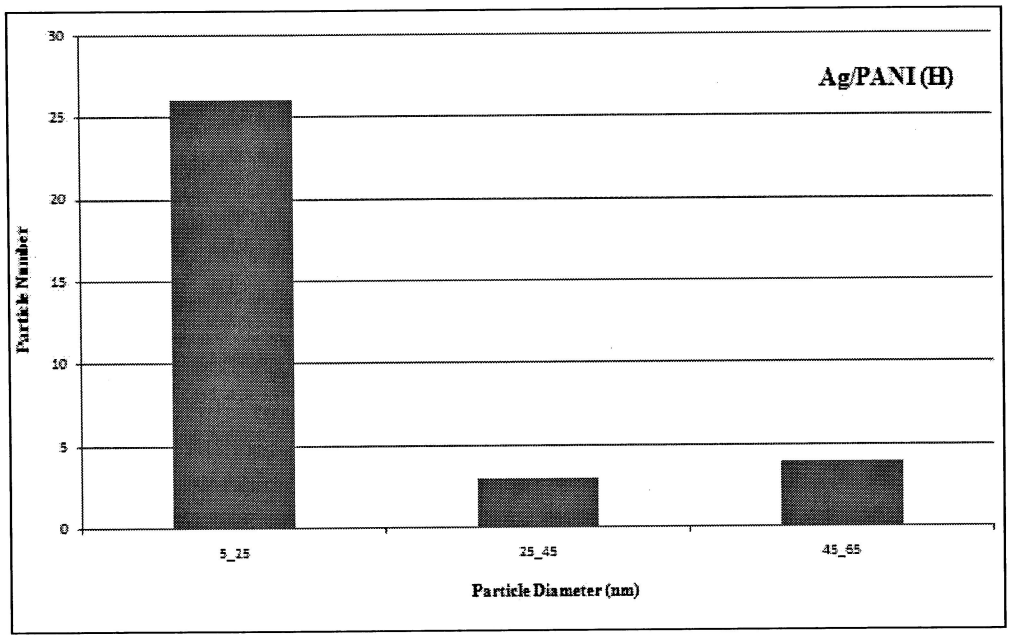

Figure 3. *The distribution of particle diameter for both Ag/PANI (L) and Ag/ PANI (H).*

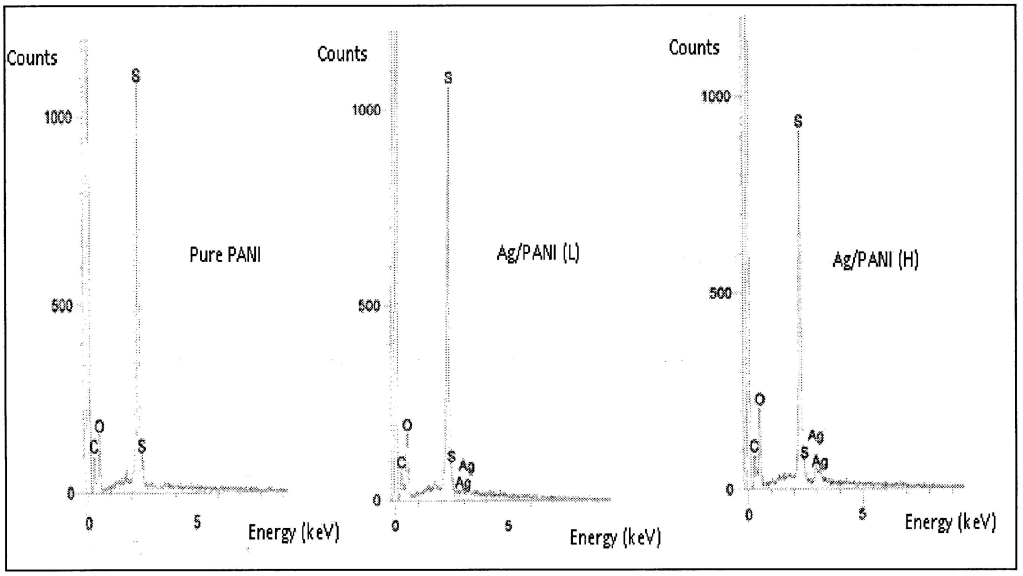

Figure 4. *EDX analysis data for pure PANI and Ag/PANI nanocomposite*

Figure 5 shows the XRD spectra of PANI nanoparticles (a) as a powder and (b) as coated on to a glass substrate to prove that PANI is applicable in other material. The presence of peak at $2\theta = 25^{o}$ and 9° are related to the formation of PANI. The XRD spectra (Figure 6) of PVP/PANI/Ag^{0} nanocomposites, showed six diffraction peaks located at 9°, 25°, 38°, 44°, 65° and 77°. The broad peak of $2\theta = 9^{o}$ is related to the overlapping of PVP and PANI. Another prominent peak at $2\theta = 25^{o}$ is related to PANI. However, a prominent diffraction peak at $2\theta = 38^{o}$ is associated to $AgNO_3$ and three strong peaks at $2\theta = 44^{o}$, 65° and 77° are related to Ag (111), Ag (200), Ag (220) Bragg's diffractions of cubic structure of silver nanoparticles, respectively. The observed values of 2θ and d-spacing for the PANI nanoparticles and for Ag/PANI core-shell nanocomposites prepared at similar conditions, with different wt % of Ag nanoparticles are given in Table 1. The higher d-spacing indicates a more conductive property of the composite due to easier pathway of the charge carrier to move inside the composite. This result is in complete agreement with the conductivity measurement.

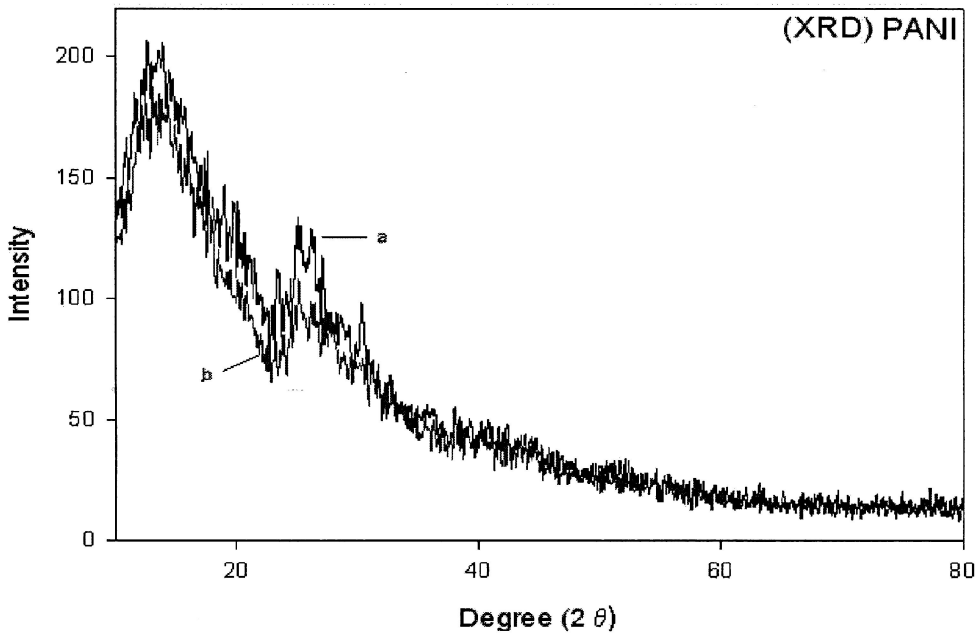

Figure 5. *The XRD spectrum for PANI nanoparticles (a) in powder form and (b) on a glass substrate*

Table 1. The 2θ with the d-spacing of the XRD spectra for Ag/PANI and pure PANI

Sample	Intensity (2θ = 25°)	d-spacing (2θ = 25°)
Ag/PANI (H)	140	2.7
Ag/PANI (L)	155	2.9
Pure PANI	160	3.3

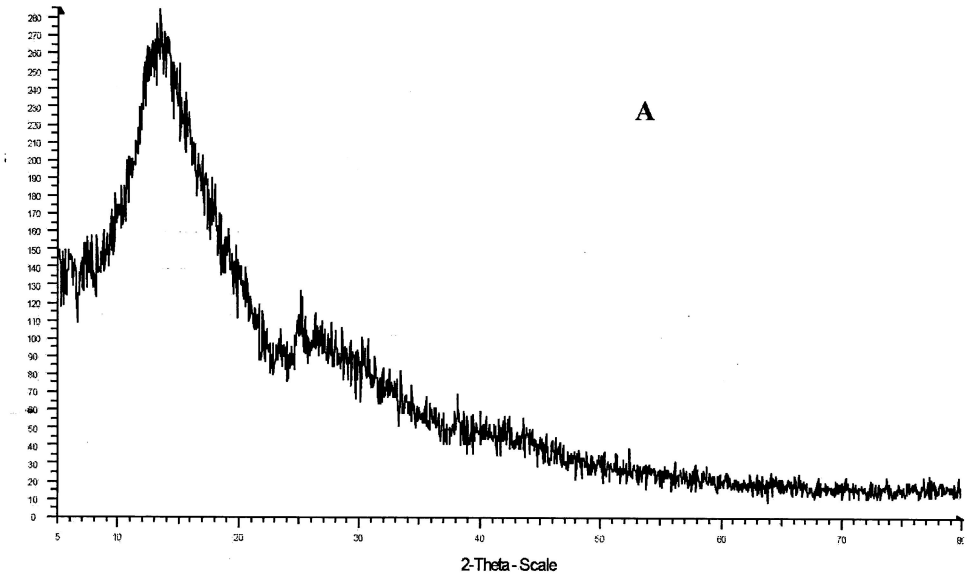

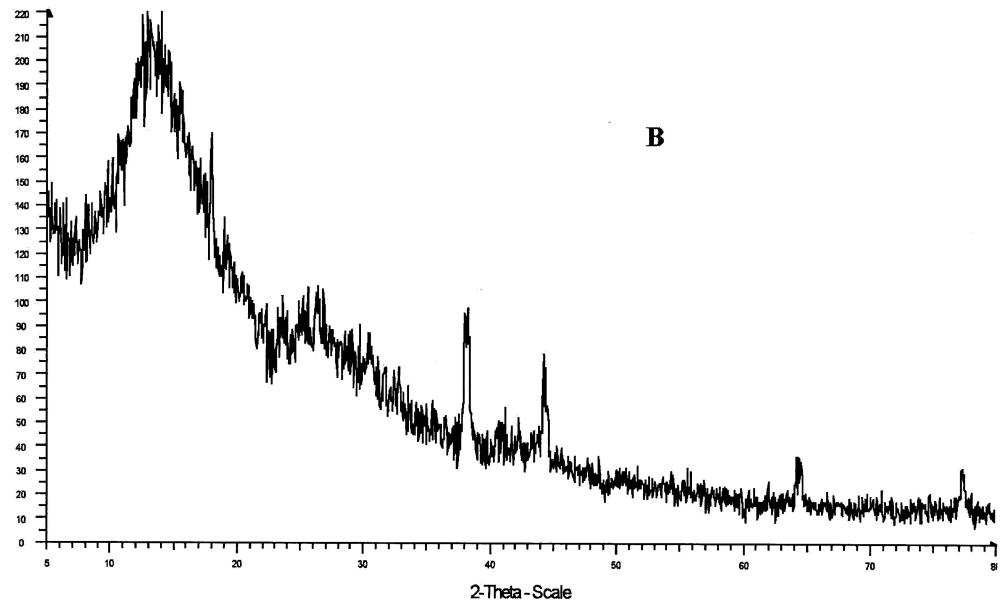

Figure 6. *The XRD spectrum for A.) Ag/PVP/PANI (L), B.) Ag/PVP/PANI (H)*

Figure 7 shows the FTIR spectra of pure PANI, AgPANI (L) and AgPANI (H). The band at 1580 cm^{-1} and 1480 cm^{-1} are attributed to the C=N and C=C stretching modes of vibration for the quinonoid and benzenoid units of the polymer respectively, while the bands at 1296 cm^{-1} and 1172 cm^{-1} are assigned to the C–N stretching mode of benzenoid units. The peak at 817 cm^{-1} is attributed to C–C and C–H of the benzenoid unit. The incorporation of Ag in the nanocomposites leads to a shift of some FTIR bands of the polymer in the composite when compared to pure PANI. However, the shift to a higher wavelength has a very weak intensity for most of the bands. This is due to the coating of Ag nanoparticles by the polymer, which avoids a suitable interaction of the silver particles with the incident radiation during IR measurements. Moreover, the band at 1480 cm^{-1} of PANI which is attributed to the aromatic ring C–C stretching mode is blue shifted to 1487 cm^{-1} at low Ag nanoparticles and to 1900 cm^{-1} at high Ag nanoparticles. The out-of-plane –NH bending vibration of PANI at 1296 cm^{-1} is present in the IR spectrum of PANI and Ag/PANI and this band is shifted to higher wavelength when Ag nanoparticles was added. The band at 1022 cm^{-1} corresponds to S=O stretching mode of the SO_4 group of sulfuric acid splits into two bands in the case of PANI and Ag/PANI, (Kang, *et al.*, 1998) , (Jing *et al.*, 2007) .

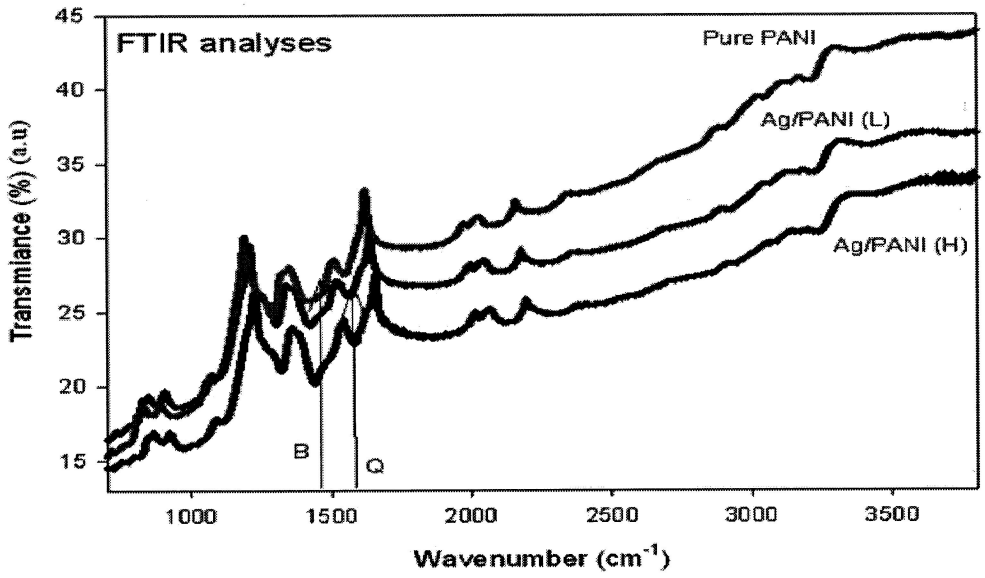

Figure 7. *FTIR spectra of PANI, and Ag/PANI having different Ag nanoparticles concentration*

Figure 8 shows the typical behaviour of the Cole-Cole plot. The result indicates an increase in the resistance with addition of Ag nanoparticles and this attributes to the decrease in the conductivity. However, the amount of polarons seems to decrease in the presence of Ag which is due to reduced amount of aniline converted to PANI during polymerization process and similar results were obtained by (Niu *et al.*, 2003, Devendrappa *et al.*, 2006; Zhu Jian 2005).

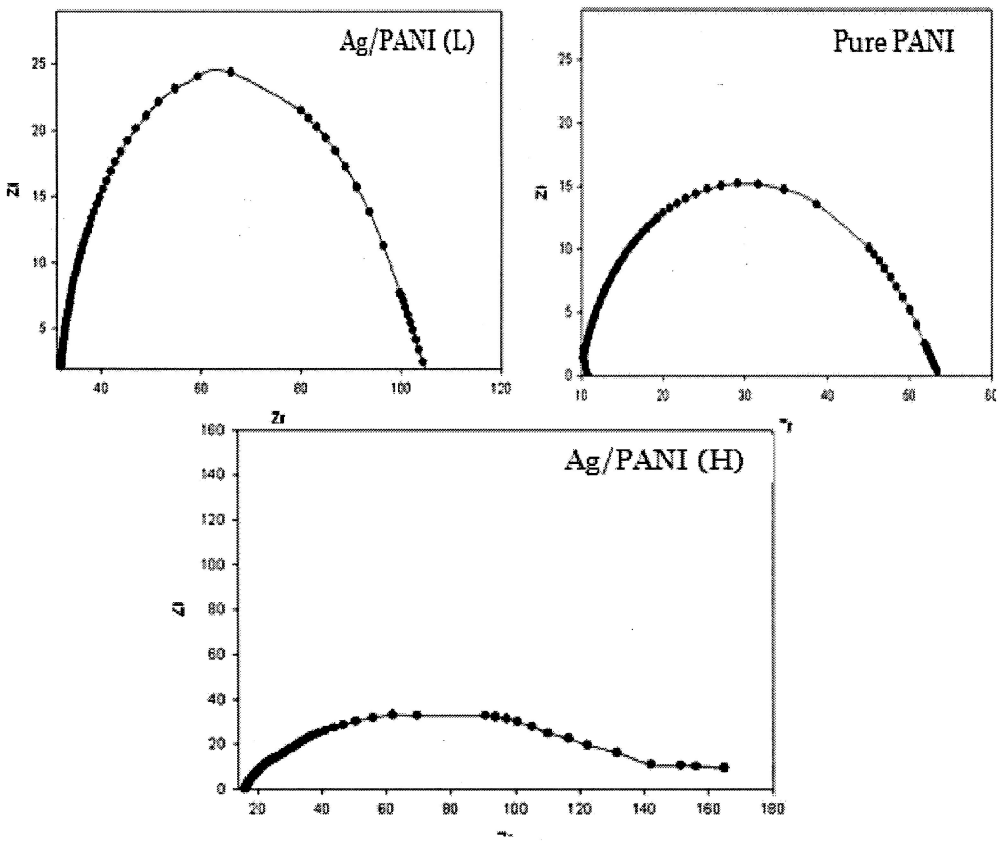

Figure 8. *The Cole-Cole plots for electrical conductivity of PANI and PANI/Ag⁰ nanoparticles at various Ag concentrations*

The ac conductivity shown in Figure 9, obeys the universal power law (UPL) introduced by Jonscher equation and has a wide application irrespective of their chemical and physical structures and the type of charge carriers they possessed. The ac conductivity of Ag/PANI decreases as Ag nanoparticles increased and this is similar to those of dc conductivity. The species of polarons or/and bipolarons are considered as the main criteria of conducting polymer emaldine salt that results in a remarkable shift of the dc conductivity to lower values with increasing Ag nanoparticles concentration. A study by Samrana *et al.*, (2007) where PANI was doped with different element concentration showed that the conductivity increased at certain concentration and decreased for other elements. However, their result was based on the increase in the conductivity and others were based on the decrease of the conductivity of PANI with addition of different dopants.

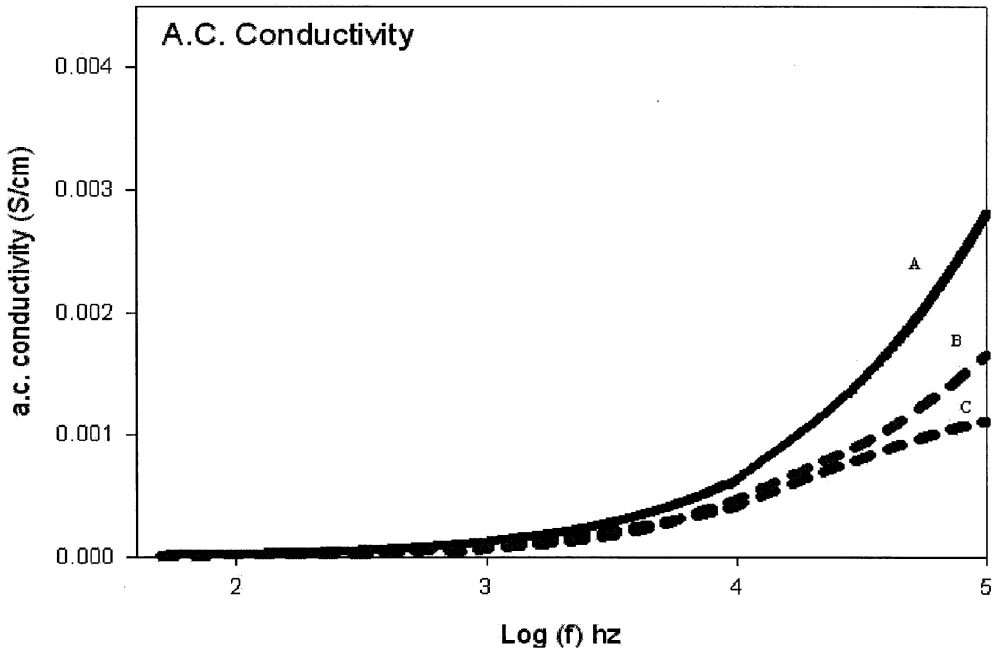

Figure 9. *The a.c. conductivity vs. frequency of A) Pure PANI, B) Ag/PANI at low concentration of Ag and C) Ag/PANI at high concentration of Ag*

In order to measure the solubility of PANI and Ag/PANI, the samples were dissolved in an organic solvent of (N-Methyl-2-pyrrolidone (NMP)) under stirring condition for 30 minutes followed by filtration. The partially soluble and conductive PANI and Ag/PANI core-shell of 15 mg/10 ml, 20 mg/10 ml possessed a conductivity of 2.6×10^{-3} S/cm, 1.1×10^{-3} S/cm, respectively.

CONCLUSION

This work has established that doping induced solphonation in aniline monomer can be used to prepare conducting polymer polyaniline (PANI) by chemical oxidation polymerization method due to the presence of sulfuric acid. The Ag/PVP nanoparticles were synthesized by the reduction of $AgNO_3$ with the presence of ascorbic acid 'in situ' thermal process. The prepared Ag nanoparticles were coated by the PANI to form Ag/PANI core-shell by 'in situ' encapsulation chemical method.

The formation of conductive PANI was confirmed by the FTIR measurement at IR shift of 1480 and 1580 cm^{-1} assigned for C=N double bond stretching of imines group, which implies the presence of polaron species, which is the charge carriers of PANI. The conductivity measurement reveals that the dc conductivity of conducting PANI composite decreased with increase concentration of Ag nanoparticles. The conductivity is mainly attributed to the creation of polarons in the PANI structure. The formation of Ag nanoparticles was shown as the change in colour from colourless before the reaction takes place to golden yellow and then to dark golden yellow. This was confirmed by XRD spectra in which the presence of three dominant diffraction peaks correspond to Ag (111) and Ag (200) of cubic structure of silver metal.

ACKNOWLEDGEMENT

We gratefully acknowledge University of Malaya for the financial support of this work.

REFERENCES

Akelah, A., El-Deen, N., Hiltner, A., Baer, E., and Moet, A. (1995). Organophilic Rubber-Montmorillonite Nanocomposites. *Mater. Lett.,* **22**: pp 97.

Chipara, M., Skomski, R., and Sellmyer, D. J. (2007). Electrodeposition and Magnetic Properties of Polypyrrole–Fe Nanocomposites. *Mater. Lett.,* **61**: pp 2412-2415.

Cho, M., Park, S., Hwang, J., and Choi, H. (2004). Synthesis and electrical properties of polymer composites with polyaniline nanoparticles, *Mater. Sci. Eng.,* **C 24**: pp 15–18.

Cui, G., Lee, J. S., Kim, S. J., Nam, H. Cha, G. S., and Kim, H.D. (1998). Potentiometric pCO_2 sensor using polyaniline-coated pH-sensitive electrodes. *Analyst,* **123**: pp 1855.

Devendrappa, H., Subba Rao, U. V., and Ambika Prasad M.V.N. (2006). Study of dc conductivity and battery application of polyethylene oxide/polyaniline and its composites. *Journal of Power Sources,* **155**: pp 368-374.

Feng, X., Liu, Y., Liu, C., Hou, W., and Zhu, J. J. (2006). One-step synthesis of AgCl/ polyaniline core–shell composites with enhanced electroactivity, *Nanotechnology,* **17**: pp 3578–3583.

Gangopadhyay, R., and De, A. (2000). Conducting polymer nanocomposites: a brief overview, *Chem. Mater.,* **12**: pp 608–622.

Grubbs, R. B. (2005). Hybrid Metal-Polymer Composites from Functional Block Copolymers. *J Polym Sci Part A: Polym. Chem,* **43**: pp 4323.

He, Y. J. (2005). Synthesis of polyaniline/nano-C_eO_2 composite microspheres via a solid-stabilized emulsion route. *Mater. Chem. Phys.,* **92**: pp 134.

Huang, W.S., Humphrey, B.D., and MacDiarmid, A.G. (1986). Polyaniline: doping structure and derivatives, *J. Chem. Soc., Faraday Trans.,* **82**: pp 2385–2400.

Jang, S. H., Han, M. G., and Im, S. S. (2000). Preparation and characterization of conductive polyaniline/silica hybrid composites prepared by sol-gel process. *Synth. Met.,* 110, pp 17.

Jing, S., Xing, S., Yu, L., Wu, Y., and Zhao, C. (2007). Synthesis and characterization of Ag/polyaniline core-shell nanocomposites based on silver nanoparticles colloid, *Mater. Lett.*, **61**: pp 2794–2797.

Kang, E.T., Neoh, K.G. and Tan, K.L, (1998). "Polyaniline: A polymer with many interesting intrinsic redox states". *Prog. Polym. Sci.*, **23**: pp 277-324.

Kang, Y., Choi, S., Gopalan, A., Lee, K., Kang, H., and Song, Y. (2006). Tuning of morphology of Ag nanoparticles in the Ag/polyaniline nanocomposites prepared by irradiation, *J. Non-Cryst. Solids,* **352**: pp 463–468.

Kumar, R. V., Diamant, Y., and Gedanken, A. (2000). Sonochemical Synthesis and Characterization of Nanometer-Size Transition Metal Oxides from Metal Acetates. *Chem. Mater.,* **12**: pp 2301.

Liu, Y. C., Lee, H. T., and Yang S. J. (2005). Strategy for the syntheses of isolated fine silver nanoparticles and polypyrrole/silver nanocomposites on gold substrates. *Electrochimica Acta,* **51**: pp 3441-3445.

Malta, M., Louarn, G., Errien, N., and Torresi, R. M. (2003). Nanofibers composite vanadium oxide/polyaniline: synthesis and characterization of an electroactive anisotropic structure. *Electrochem Commun,* **5**: pp 1011.

Morrin, A., Ngamna, O., Killard, A. J., Moulton, S. E., Smyth, M. R., and Wallace, G. G. (2005). An amperometric enzyme biosensor fabrication from polyaniline nanoparticles, *Electroanalysis,* **17**: pp 423–430.

Morrin, A., Wilbeer, F., Ngamna, O., Simon, E., Moulton, Killard, A. J., Wallace, G. G. and Smyth, M. R. (2005). Novel biosensor fabrication methodology based on processable conducting polyaniline nanoparticles. *Electrochemistry Communications,* **7**: pp 317–322.

Moulton, S.E., Innis, P.C., Kane-Maguire, L.A.P., Ngamna, O. and Wallace, G.G. (2004). Polymerisation and characterisation of conducting polyaniline nanoparticle dispersions, *Current Applied Physics,* **4**: pp 402–406.

Naderi, N., Sharifi-Sanjani, N., Khayyat-Naderi, B., and Faridi-Majidi, R. (2006). Preparation of organic-inorganic nanocomposites with core-shell structure by inorganic powders. *J. App. Poly. Sci.,* **99**: pp 2943- 2950.

Niu L., Li, Q. H., Wei, F. Wei, H. X., and Wang, H. (2003), "Electroactivity of Electrochemically Synthesized Poly(Aniline Boronic Acid) as a Function of pH: Role of Self-Doping". *J. Electroanal. Chemistry,* **544**: pp 121-125.

Pomogailo, A. D., Dzhardimalieva, G. I., Rozenberg, A. S. and Muraviev, D., (2003). Kinetics and Mechanism of in situ Simultaneous Formation of Metal Nanoparticles in Stabilizing Polymer Matrix. *J. Nanoparticle Res.,* **5**(5-6): pp 497-519.

Samrana Kazim, Vazid Ali, Zulfequar, M., Mazharul Haq, M., and Husain M. (2007) Electrical, thermal and spectroscopic studies of Te doped polyanilin. *Current Applied Physics,* **7** (1): pp 68-75.

Srivastava, A., Singh, V., Dhand, C., Kaur, M., Singh, T., Witte, K. and Scherer, U.W. . (2006). Study of Swift Heavy Ion Modified Conducting Polymer Composites for Application as Gas Sensor. *Sensors,* **6**: pp 262-269.

Xian, Y., Hu, Y., Liu, F., Xian, Y., Wang, H., and Jin, L. (2006). Glucose biosensor based on Au nanoparticles-conductive polyaniline nanocomposite, *Biosens. Bioelectron,* **21**: pp 1996–2000.

Xu, P., Wang, H., Lv, R., Du, Q., Zhong, W., and Yang, Y. (2006). Synthesis of TiO_2-SiO_2 /polymer core-shell microspheres with a microphase-inversion method. *J. Polym. Sci. Part A: Polym. Chem.,* **44**: pp 3911.

Xue, W., Qiu, H., Fang, K., Li, J., Zhao, J. and Li, M. (2006). Electrical properties of the composite pellets containing DBSA-doped polyaniline and Fe nanoparticles, *Synth. Met.,* **156:** 833–837.

Yakuphanoglu, F., Basaran, E., Senkal, B.F., and Sezer, E. (2006). Electrical and optical properties of an organic semiconductor based on polyaniline prepared by emulsion polymerization and fabrication of Ag/polyaniline/n-Si Schottky diode, *J. Phys. Chem. B.,* **110**: pp 16908–16913.

Zhu, J. (2005). "Theoretical study of the optical absorption properties of Au-Ag bimetallic nanoparticles". *Physics E,* **27**: pp 296-301.

Journal of Industrial Technology Vol. 19(1), 2010 - ICONT 2009, 97 - 110

EFFECT OF CLAY ORGANO-MODIFIER ON THE PROPERTIES OF NATURAL RUBBER BASED NANOCOMPOSITES

Nik Intan Nik Ismail, *Siti Salina Sarkawi and Che Su Mt Saad.

Malaysian Rubber Board, Technology Centre
RRIM Research Station Sg. Buloh,
47000 Selangor, Malaysia.

***(nikintan@lgm.gov.my)**

ABSTRACT : Natural Rubber / Clay nanocomposites were prepared with commercially available organophilic Montmorillonite (MMT) by melt compounding. In this study, two types of modified montmorillonite with different level of polarities, namely Cloisite 15A (C15A - modified MMT with quaternary ammonium) and Cloisite 30B (C30B - modified MMT with ternary ammonium) were used. The effect of organoclay type in rubber compound was analysed through cure characteristic and mechanical properties. In addition, the rubber-filler interaction was studied by the crosslink density and bound rubber content while, the dispersion state of the organoclay was investigated by X-ray diffraction and microscopy analysis. The results indicate that both organoclays accelerate the vulcanization process but more pronounced for the NR/C30B nanocomposites as confirmed by a decrease in the cure time and scorch delay. However, the mechanical tests showed that when loaded with 10 phr C15A, the modulus, tensile, tear strength and hardness of the nanocomposites were higher than those containing C30B at the same filler loading. It is suggested that, a significant improvement in the NR/C15A nanocomposites' properties relate to better dispersion of the filler in the rubber matrix at nanolevel as well as to the similarity of the polarity with rubber.

KEYWORDS : Montmorillonite (MMT), organoclay, polarity and natural rubber nanocomposite

INTRODUCTION

In recent years, hybrid organic-inorganic nanocomposites consisting of polymeric matrix and a layered silicate has inspired scientists to a range of potential applications. Due to their nanometer phase dimensions, nanocomposites exhibit significant improvements in physical and mechanical properties in relation to the polymer host. The addition of just a low percentage of nanolayered inorganic such as silicate layered can increase the stiffness and strength with minimal loss in ductility and impact resistance, decreases the permeability and swelling solvents, improves the abrasion and flame resistance. Although clay nanocomposites have been prepared for many thermoplastic and thermosetting polymers, rubber nanocomposites constitute only a minor proportion.

Rubber nanocomposites with an exfoliated morphology have been successfully prepared by several methods, which include in situ polymerization, solution blending, latex compounding and direct melt blending (Wu et *al.*, 2004, Varghese *et al.*, 2003, Manchodo *et al.*, 2004). Among the techniques used, melt blending is more often used to prepare NR nanocomposites with organoclays. This processing technique requires information on the rheological behaviour which depends on several factors, such as polymer-polymer or polymer-filler interactions that relates to the nature of host polymer and filler of the system. However, very little information about the compatibility between the organoclay and natural rubber can be found in the literature. Thus, the present work focuses on the effect of clay-organo modifier on the properties of natural rubber (NR) based nanocomposites prepared by melt blending.

Pristine layered silicate surfaces are hydrophilic, thus they are not compatible with most polymers. Cation exchange offers effective way of modifying the galleries of the clays, thereby rendering the silicate surfaces more organophilic and therefore more compatible with polymers. Nowadays, several modified clays or known as organoclays are commercially available at relatively low cost. However, selection of organoclays depends mainly on the type of polymer used.

In this study, NR nanocomposites were prepared by using two types of modified montmorillonites namely Cloisite 15A and Cloisite 30B. The properties of the nanocompoites were then evaluated and compared. To observe the effect of different organic modifier on the nanocomposites properties, the pristine clay was referred as a control. Closite 15A is apolar Na^{+}MMT clays modified with dimethyl, dehydrogenated tallow, and quaternary ammonium (2M2HT). HT stands for a tallow – based compound compound (-65 % C18, -30 % C16, and -5 % C14) in which, majority of the double bonds have been hydrogenated. The cation molecular structure of cloisite 15A is:

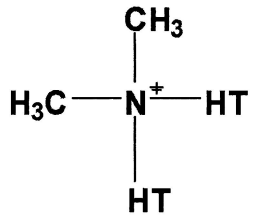

Cloisite 30B is a polar organoclay with the organic modifier methyl tallow bis-2-hydroxyethyl ammonium (MT2EtOH) having the formula of:

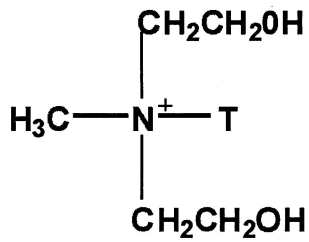

MATERIALS AND METHODS

Materials

Natural rubber was supplied by Malaysian Rubber Board under the trade name of SMR L [Mooney Viscosity, ML (1+4)100 °C = 75.9]. The pristine clay used in this work is the Na^+MMT acquired from Linfangzi Clay Factory, Jilin, China (cation exchange capacity = 92 mquiv/100 g of clay). While, commercial organoclays were supplied under the trade name of Cloisite 15A and Closite 30B, in particular a montmorillonite modified with quaternary ammonium salts.

Compounding

The NR/Clay nanocomposites of composition shown in Table 1 were prepared and their properties were evaluated and compared. The mixes were compounded in Banbury internal mixer (BR 1600) with rotor speed set at 120 r.p.m. The chamber temperature was set at 80 °C. Figure 1 shows the mixing cycle used for this study. The curatives were added separately on a two-roll mill with roll temperature of about 50 °C.

Time	Mixing Procedure
0 min	rubber
0.5 min	powder ingredients
2.5 min	sweep
4.5 min	dump

Figure 1. *Mixing procedure of NR/Clays Nanocomposites*

Table 1. Rubber Compound Formulation

Compounding ingredients	phr (parts per hundred of rubber)		
SMR L	100	100	100
Pristine clay	5-10	0	0
Cloisite 15A	0	5-10	0
Cloisite 30B	0	0	5-10
ZnO	4	4	4
Stearic Acid	2	2	2
Permanax TMQ[a]	1	1	1
Sulphur	1.8	1.8	1.8
TBBS[b]	1.8	1.8	1.8
Santogard PVI[c]	0.4	0.4	0.4

a 2,2,4 – trimethyl-1,2-dihydroquinoline
b N-t-butyl-2--benzothiazole Sulfanamide
c Prevulcanisation inhibitor

Characterisation

X-ray diffraction (XRD) was used to characterize the nature and extent of the dispersion of the clays in the filled samples. XRD patterns were collected using a Bruker D8 Advanced at λ Cu Kα = 1.54 Å and scan rate: 0.002. Bragg's law was used to compute the crystallographic spacing (d) of the clays.

Compound cure characteristics were analysed using a Monsanto ODR 2000 at 140 °C and frequency of 1.66 Hz. The characteristics of cure consist of time to optimum cure (T_{90}) and state of cure (M_H-M_L). The scorch time, t_2 of the mixes were also examined. The compounds were pressed using hot press and cut into standard shapes. Finally the mechanical properties of the samples were characterized.

Tensile properties were measured according to ISO 37 specifications on an INSTRON at a crosshead speed of 500 mm/min. Tear strength were determined according to ISO 34 by using INSTRON machine with the crosshead speed of 100 mm/min. Measurements of hardness were carried out according to ISO 48.

Freeze fracture surface morphology was observed using JEOL Field Emission Electron Microscopy (FESEM). The number of active network chain segments per unit of volume (crosslink density) was determined on the basis of solvent-swelling measurements (using toluene after 72 h, at room temperature) by application of the Flory-Rhener equation.

The bound rubber content (BRC) measurement was done on the samples after 7 days maturation. BRC measurements were performed in duplicate on single piece of each compound weighing between 0.25 g and 0.3 g and placed into a separate Erlenmeyer flask. About 50 cm^3 of toluene was added into each flask. The flasks were kept at room temperature in the dark for seven days. After seven days, the wet (swollen) weights were determined and placed in a drying cabinet (40 °C) for 24 hours. On the following day, the dry samples were weighed and bound rubber content values were calculated.

RESULTS AND DISCUSSION

Cure characteristics

The effect of clay organic modifier on the cure characteristics of NR/Clay nanocomposites is presented in Table 2. It can be seen that each compound exhibits different cure characteristics, which may be attributed to the fact that each type of filler possesses different properties, such as particle size, structure and aspect ratio.

Table 2. Cure characteristics of the compound

Parameters		5 phr			10 phr	
	NR/MMT	NR/C15A	NR/C30B	NR/MMT	NR/C15A	NR/C30B
Scorch time (Ts_2), min	9.39	2.23	2.94	9.11	1.63	2.43
Cure time (T_{90}), min	13.37	4.38	4.92	12.74	4.07	4.31
Minimum Torque (M_L), dNm	1.13	1.13	1.17	1.25	1.13	1.27
Maximum Torque (M_H), dNm	7.85	7.96	8.08	7.67	7.65	8.39
Max-Min Torque (M_H-M_L), dNm	6.72	6.83	6.91	6.42	6.52	7.12
Cure rate Index, CRI = 100/($t_{90} - ts_2$)	25.1	46.5	50.5	27.5	41.0	53.2
Crosslink density ($molml^{-1}$)	-	-	-	2.5×10^{-4}	2.7×10^{-4}	3.0×10^{-4}
Bound rubber (g/g)	-	-	-	- 1.549	1.133	9.968

Note that with the presence of both organoclays in natural rubber, the scorch time, (ts_2) and cure time (t_{90}) are dramatically reduced. As reported by other researcher, (Manchodo *et al.*, 2004) the organoclay behaves as an effective accelerator for natural rubber due to the formation of transition complex with amines and sulfur. These results are confirmed by the cure rate index values, *CRI*, which shows significant increase with addition of organoclay which is attributed to the amine functionalities in the nanosilicate structure. In this study, it shows that the acceleration effect is more pronounced with the presence of C30B as compared to C15A even at low filler loading.

On the other hand, the maximum torque and delta torque increased by the addition of the organoclays, showing the reinforcing effect of this filler at low strain, in particular with the presence of C30B. Furthermore, these results suggest that natural rubber became more crosslinked with the addition of the organoclay, as confirmed by crosslink density measurement presented in Table 2. These results are also in concordance with the bound rubber measurements, which give an indication of rubber/filler interactions that increased with the addition of the organoclays.

Mechanical properties

The summarized tensile properties of NR/Clay nanocomposites are shown in Figure 2 (a-d). The effect of the organoclay on the stiffness is more evident when measured at higher strains. In this case, both organoclays at 10 phr filler loading give rise to a noticeable increase in modulus at all strain namely 100 %, 300 % and 500 % which are 43 %, 25 %, 56 % and 23 %, 15 %, 23 % increment for C15A and C30B respectively compared to unmodified montmorilonite. This shows the strong reinforcing effect of these inorganic fillers.

However, when comparing both of the organoclays, it can be seen that the C15A-10 phr nanocomposites shows the best improvement in tensile modulus and stress at 500 % strain which is about 30.5 % higher than C30B at similar filler loading. The maximum strength of C15A-5phr and C15A-10phr has also increased up to 8 % and 33 % respectively compared to C30B without loss in elongation at breaks. It is interesting to note that, the degree of improvement increases at higher content of C15A, which may be another indirect evidence of interaction between C15A and natural rubber. By contrast, C30B tend to agglomerate at higher loading as indicated by decreasing tensile strength and modulus at 10 phr. These observations are in line with the fracture surface morphology analysis.

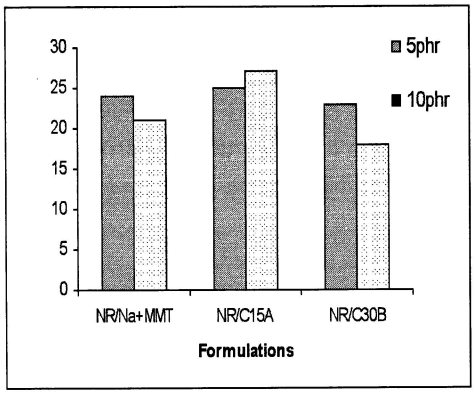

(a)

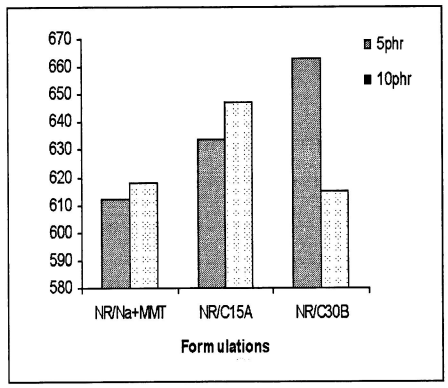

(b)

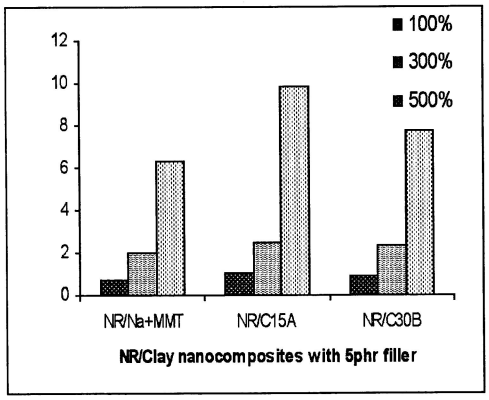

(c)

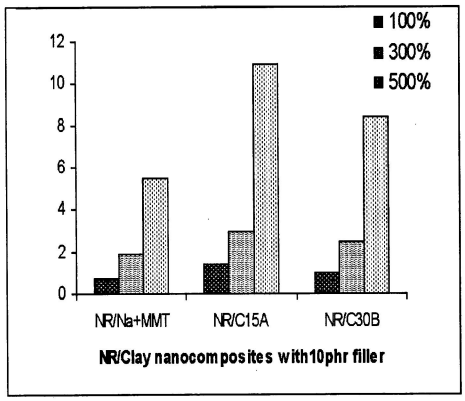

(d)

Figure 2. ***(a)*** *Tensile strength of NR/Clay nanocomposites with various formulations*
(b) *Elongation at break of NR/Clay nanocomposites with various formulations*
(c) *Tensile modulus of NR/Clay nanocomposites at 5 phr filler loading*
(d) *Tensile modulus of NR/Clay nanocomposites at 10 phr filler loading*

The tensile properties are in agreement with the results obtained from the analysis of the tear strength. The increase in tear strength is related to the reinforcing effect of the filler in the composites. The tear strength of the NR/C15A shows the highest value followed by NR/C30B at similar filler content as presented in Figure 3. Improved hardness is also in concordance with the tensile results. Figure 4 shows both organoclays which exhibit higher hardness compared to the unmodified clay where the highest value is obtained from NR/C15A – 10 phr.

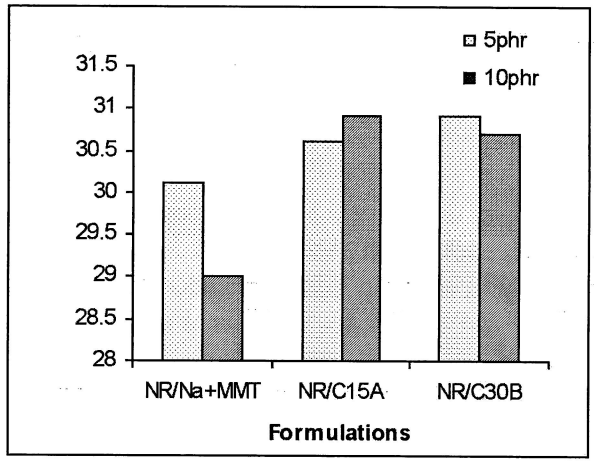

Figure 3. *Tear strength of NR/Clay nanocomposites with various formulations*

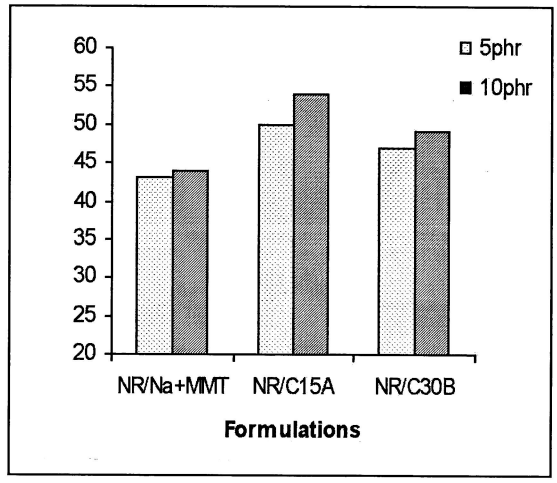

Figure 4. *Hardness of NR/Clay nanocomposites with various formulations*

A marginal improvement in the mechanical properties of nanocomposites with C15A can be attributed to the good dispersion of exfoliated silicate layers and compatibility between rubber and filler. As expected, the larger basal spacing of C15A (3.23 nm) make the layer separation much easier by shear during melt mixing since the modifier inside the layer weakens the electrostatic force between silicate layers compared to C30B (1.85 nm). In addition, C15A is more hydrophobic in nature than C30B which is close to the nature of natural rubber. The difference between C30B and C15A is that C15A has a longer alkyl chain at one branch of quaternary ammonium ion in the modifier which makes it less polar. While, C30B has the hyroxyethyl groups in the clay modifier that categorized it as polar clay and it is expected that this clay can dispersed well in polar rubber such as ENR through hydrogen bonding.

Structure characterization

The exchange of the interlayer cations of the pristine montmorillonite with alkylammonium ions enlarges the interlayer spacing from 15.2 Å to 31.5 Å and 18.5 Å for unmodified MMT, C15A and C30B respectively as shown in Figure 5. In addition, C15A shows a small second peak at higher angles (2θ = 7.1°) which suggests that a portion of the clay layers has not been intercalated after the chemical modification. Figure 6 shows X-ray diffraction patterns for C15A and NR/C15A nanocomposites containing 10 phr filler content.

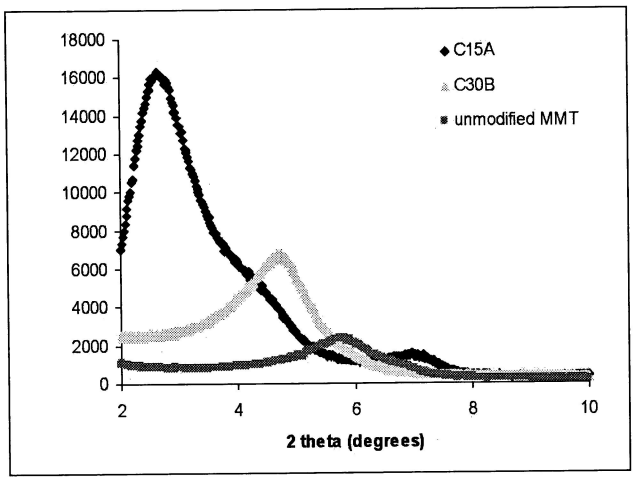

Figure 5. *XRD patterns of clays*

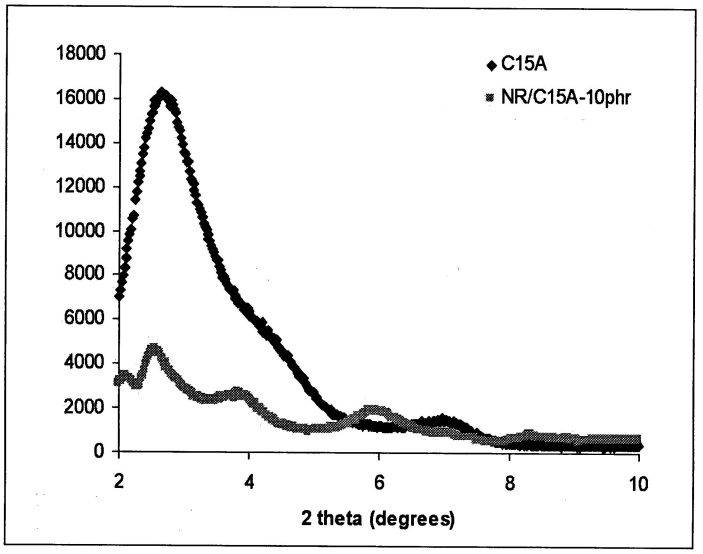

Figure 6. *XRD patterns of C15A and nanocomposites based on NR/C15A (10 phr)*

It can be seen that, C15A curve shows sharp peak at 2θ = 2.7° (d_{001} spacing of 3.15 nm). As for NR/C15A nanocomposites, a weak peak appears at the same 2θ. While, the second peak of the organoclay at 2θ = 7.1° shifted to lower angle to 2θ = 6.1°. The decrease in the peak intensity of 2θ of d_{001} peaks and the movement of the second peak to lower angle (Arroyo *et al.*, 2007) can be related to the change in the degree of clay dispersion. This observation may indicate that some changes occurred in the C15A platelets. The XRD result can be used as an indication of the intercalated or nearly exfoliated clay structures in the prepared nanocomposites.

Fractured surface analysis

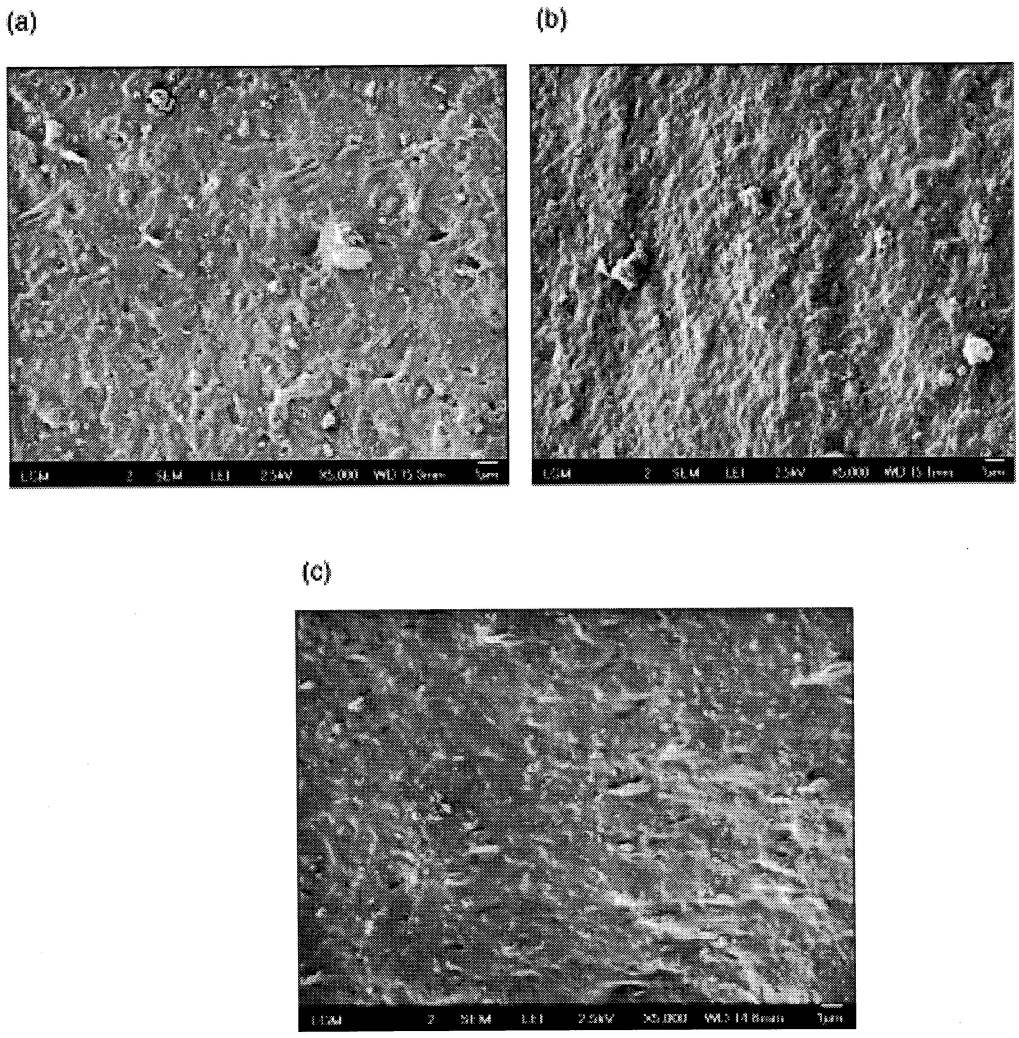

Figure 7. ***(a)*** *Fractured surface of NR/Na⁺MMT (10 phr) in 5000x magnification*
(b) *Fractured surface of NR/C30B (10 phr) in 5000x magnification*
(c) *Fractured surface of NR/C15A (10 phr) in 5000x magnification*

In this study, freeze fractured surface of the nanocomposites was characterized using Field Emission Scanning Electron Microscopy (FESEM). Figure 7(a-c) showed the fractured surface of (a) NR/Na^+MMT, followed by (b) NR/C30B and (c) NR/C15A in 5000x magnification. There is a significant difference in the morphological appearance between the NR/C15A compared to the NR/C30B and NR/Na^+MMT. The agglomerated clays can be seen clearly for fractured surface morphology of NR/Na^+MMT and NR/C30B in Figure 6a & Figure 6b respectively.

On the other hand, a more homogeneous morphology with a finer and more uniform dispersion of C15A is observed from the SEM micrograph in Figure 6c. From the results, it is believed that similar polarity of C15A with rubber gives rise to a more homogeneous structure. This perhaps explains why organoclay C15A shows better mechanical properties than the other organoclay C30B.

CONCLUSION

NR/Clay nanocomposites were successfully prepared by melt compounding using various types of clays. From the obtained results, it can be deduced that the low reinforcing effect of unmodified clay is evident. A poor compatibility between the unmodified clay and the matrix is proven by a decrease in the mechanical properties. Nevertheless, a marked increase of the mechanical properties is observed when the organoclay is used as filler in C15A. It is believed that a marginal improvement in the mechanical properties of NR nanocomposites with C15A can be attributed to the good dispersion of exfoliated silicate layers and compatibility between rubber and filler which is confirmed by XRD patterns and fractured surface analysis.

ACKNOWLEDGEMENT

The authors would like to thank Malaysian Rubber Board (MRB) and Ministry of Science Technology and Innovation (MOSTI) for the financial support. We are also grateful to Dr. Hafizuddin Hj Jumali (UKM) and Mr. Suhaimi (RRIM) for their technical assistance.

REFERENCES

Arroyo, M., Manchodo, M. L.,Valentin, J.L and Carretero, J. (2007). Morphology/behaviour relationship of nanocomposites based on natural rubber/expoxidised natural rubber blends. *Comp. Sci. and Tech.* **67:** pp 1330-1339.

Dan, H.C., Lee, M.H. Kim, Y. D., Min, B.Y., and Kim J.H. (2006). Effect of clay modifiers on the morphology and physical properties of thermoplastic polyurethane/clay nanocomposites. *Polymer.* **47:** pp 6718-6730.

Manchodo, M. L., Herrero, B., and Arroyo, M. (2004). Organoclay-natural rubber nanocomposites synthesized by mechanical and solution mixing methods. *Polym. Int.* **53:** pp 1766-1772.

Varghese, S., and Karger-Kocsis, J.(2003). Natural rubber-based nanocomposites by latex compounding with layered silicates. *Polymer.* **44:** pp 4921-4927.

Wu, Y.P., Ma, Y., and *et al.*, (2004). Effects of Characteristic of Rubber, Mixing and Vulcanisation on the Structure and Properties of Rubber/Clay Nanocomposites by Melt Blending. *J. Macromol. Mater. Eng.* **289:** pp 890-894.

Journal of Industrial Technology Vol. 19(1), 2010 - ICONT 2009, 111 - 123

SILVER ION RELEASE FROM CHITOSAN-AG COMPOSITE USING VOLTAMMETRIC METHOD FOR POSSIBLE WOUND TREATMENT APPLICATION

Nor Shahida Kader Bashah[1], Fatimah Suhaily Abdul Rahman[1], Ahmad Fuad Yahya[1], Ismail Zainol[2] and Kartini Noorsal[1]*

[1]Advanced Materials Research Centre (AMREC), SIRIM Berhad,
Lot 34, Jalan Hi-Tech 2/3, Kulim Hi-Tech Park
09000 Kulim, Kedah, Malaysia

[2]Jabatan Kimia Fakulti Sains dan Teknologi, Universiti Pendidikan Sultan Idris,
35100 Tanjung Malim, Perak

***(kartini@sirim.my)**

ABSTRACTS : The antimicrobial and antiviral actions of Ag demonstrated to be effective at killing a broader range of bacteria including antibiotic-resistance bacteria. Numerous studies have been performed on silver-based materials including silver-polymer composites. In this work, UV photo-reduction process was used to produce silver nanoparticles from $AgNO_3$ in chitosan solution in which the silver ions (Ag^+) is reduced to (Ag^o). The antimicrobial activity of silver is dependent of the silver cation Ag^+ which binds strongly to electron donor groups in biological molecules containing sulphur, oxygen or nitrogen. It is therefore very important to study the release of the active species of Ag^+ to a pathogenic environment in order to be effective. As the antimicrobial efficacy's limit and concentration of silver ions released from the chitosan composites lies in the parts per billion ranges, an accurate measurement of the low concentration silver is indispensable. The present study used voltammetric analysis to measure the very low concentration of silver released into the buffer medium. Transmission Electron Microscopy (TEM) analysis was used to demonstrate the existence of silver nanoparticles in the chitosan solution.

KEYWORDS : Antimicrobial, silver nanoparticles, chitosan, voltammetry

INTRODUCTION

Silver nanoparticles have been recognized as antimicrobial agent and used in various fields which include biomedical, food packaging, waste water treatment, etc. (Yoksan & Chirachanchai, 2009). The shapes and sizes of the silver nanoparticles were found to have a close relation to its antimicrobial activity. Attempts were made to prepare silver nanoparticles with controlled shape, size and size distribution and in most cases, fabrication starts from salt precursor, reducing agent and stabilizer. The reduction of silver ions (Ag^+) to silver metal (Ag^o) is achieved by using chemical reagents such as $NaBH_4$, (Van Hyning *et al.*, 2001) dimethylformamide (Pastoriza-Santos & Liz-Marzan, 2000) and hydrazine (Sakai *et al.*, 2006). Other techniques include γ-ray irradiation, UV irradiation, microwave and ultrasonics (Bogle *et al.*, 2006; Fang *et al.*, 2004) are used to overcome the purification step of removing the chemicals used in the process.

The present work focuses on using UV irradiation to reduce silver ions to silver metal in the in situ photo reduction process in chitosan solution. Transmission Electron Microscopy (TEM) images demonstrated the distribution of the silver nanoparticles in chitosan solution and this is confirmed with the Energy Dispersive X-ray (EDX) spectra. The entire process of silver ion release from silver filled polymer composites is crucial in understanding the relationship between the release profile and the antimicrobial properties. As the silver ion released from the polymer composites is relatively very low in concentration, Anode Stripping Voltammetry (ASV) is used in determining the trace amount of metal ions in the release medium (Radheshkumar & Munstedt, 2006). The voltammetric principle involves applying a pre-concentration potential that is more negative than that of the deposition potential of the species to be determined. In this stage, the electrolytic deposition of the reducible species (Ag^+) onto a working electrode (platinum) surface occurs at a constant potential. The second stage consists of the oxidation (stripping) of the reduced metal (Ag^o) by applying an anodic potential to extract the metal back into the solution at a potential characteristic of the species under concern. The principle of voltammetric lies in controlling the electrode potential and measuring the resulting current. The resulting current involved during the stripping of the metal from the electrode surface is proportional to the concentration of the redox species at the electrode surface according to the Ilkovik equation (equation 1).

$$Ip \approx n^{3/2}\ AD^{1/2}v^{1/2}tC \qquad (1)$$

where Ip is the peak current (μA); n is the number of electrons transferred per molecule; A is the electrode area (cm^2); D is the diffusion coefficient (cm^2/s); v is the scan rate (V/s); t is the enrichment time (s) time during which silver ions were deposited onto the electrode from the analyte); C is the concentration of the ions in the solution (g/l).

This work utilizes the ASV method to quantitatively monitor the silver ion release into the medium in which several chitosan samples in the form of paste, film and sponge were tested for their release profile.

MATERIALS AND METHODS

Local pharmaceutical grade non water soluble chitosan derived from prawn with deacetylation degree of 90 % and molecular weight of 100 kDalton was purchased from Hunza Nutriceuticals Sdn. Bhd. Perak, Malaysia. Whilst water soluble chitosan sourced from China was purchased from Sigma Aldrich. The analytical grade high purified silver nitrate salt was purchased from Sigma Aldrich, 100 % acetic acid, glycerol and sodium hydrogen carbonate in analytical grade were obtained from Fluka Chemical.

Preparation of silver-chitosan specimens

A range of 2 to 2.85 % w/v of non water soluble chitosan solution was prepared by dissolving chitosan powder in 1 % v/v acetic acid. The mixing process of the mixture was carried out for 24 hours and pH of the solution was maintained at 5.5 by using sodium hydrogen carbonate. In situ photo reduction of the solution was performed by ultraviolet irradiation (λ_{max} of 365 nm) with 250 W powers.

Transmission Electron Microscopy (TEM)

Specimens for TEM (Technai 12) were prepared by slowly evaporating one drop of non water soluble chitosan and water soluble chitosan at room temperature on a 400 mesh copper grid which was covered by a carbon supported film.

Sample preparation for silver ions release

Samples in film, paste and sponge form (triplicates for each type of samples) with different concentration of chitosan and Ag^+ were immersed in 100 ml of 0.01 M phosphate buffer saline (PBS) for 30 days. The samples were stored in shaking water bath at 37 °C with agitation of 20 rpm.

Anode Stripping Voltammetry (ASV)

Various solutions for standard calibration curve were prepared and the calibration curve was obtained by plotting the total peak current as a function of the silver ion concentration of the corresponding standard solution. The fit of the results represents the calibration curve which was used for the quantitative estimation of the silver ion release from various chitosan samples. 5 ml of sample solution was taken for the voltammetric experiment. The sample solution was placed in a mould equipped with three electrodes (working electrode, current electrode and reference electrode). All electrodes were attached with an alligator clip according to their functions respectively. The voltammetric set up used is the Wonnatech Battery Cycler (WBCS3000). The experimental parameters were shown in Table 1.

Table 1. Experimental parameters used for the voltammetric experiments

Discharge potential (V)	-0.55
Working electrode (diameter: mm)	3, platinum
Deposition time (s)	1000
Stripping potential range (V)	0-0.5
Scan rate (V/s)	0.05
Analyte	5 ml aqueous solution of Ag^+

RESULTS AND DISCUSSION

Formation of silver nanoparticles

Generally, silver ions could be reduced by irradiation to silver nanoparticles following the equations below (2 - 7). Upon irradiation, both reactions of chain scission of chitosan to lower molecular weight polymer (equation 4) and reduction of silver ions to silver nanoparticles (equation 5) could take place. In the case of chitosan, hydroxyl radicals and hydrogen atoms are intermediate products of water radiolysis (equations 2 and 3) react with chitosan molecules resulting in breakage of glycosidic bonds. Whilst, the hydrated electron (equation 5) will reduce Ag^+ to Ag^o and further reaction of Ag^o with other Ag^+ will form

stabilized Ag cluster (equations 6 and 7). The silver nanoparticle is formed from absorption of Ag^o by this cluster. Chitosan with the NH_2 group will attract the silver ions through ionic interaction and upon irradiation, the silver nanoparticles will be formed (Figure 1).

irradiation

$$H_2O \longrightarrow OH^o, e^-_{aq}, H^o, H_2O_2, H_2, H^+ \quad (2)$$

$$OH^o(H^o) + R\text{-}H \longrightarrow R^o (C_1\text{-}C_6) + H_2O (H_2) \quad (3)$$

$$R^o (C_1, C_4) \longrightarrow F_1{}^o + F_2{}^o \text{ (chain scission)} \quad (4)$$

reduction

$$Ag^+ + e^-_{aq} \longrightarrow Ag^o \quad (5)$$

$$Ag^o + Ag^+ \longrightarrow Ag^{2+} \quad (6)$$

$$Ag^{2+} + Ag^+ \longrightarrow Ag^{3+} \quad (7)$$

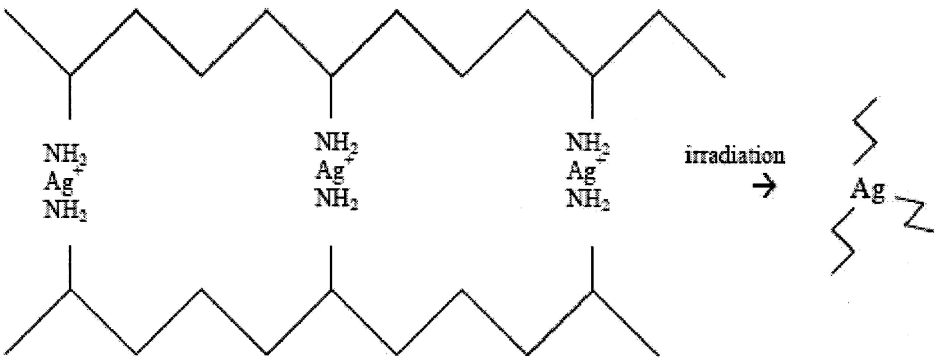

Figure 1. *Formation of silver metal from silver ions in chitosan solution*

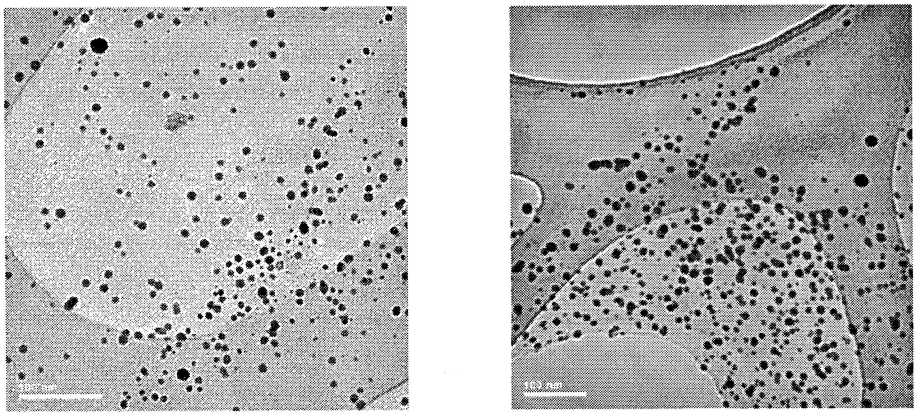

(a) (b)

Figure 2. *TEM images for (a) non water soluble chitsosan consisting of 2.85% w/v chitosan and 3 wt % w/w silver nitrate and (b) water soluble chitosan consisting of 3% w/v chitosan with 3% w/w silver nitrate*

Two types of chitosan samples were used in this work and this include the non water soluble and water soluble forms. With fixed amount of $AgNO_3$ at 3 wt %, the non water soluble chitosan exhibits a well distributed spherical shape silver nanoparticles with size range of 5 – 10 nm (Figure 2a). No agglomeration of the silver particles can be observed. The silver nanoparticles appear to be slightly bigger in size (Figure 2b) in water soluble chitosan samples. Even though no agglomeration can be observed in this TEM image, the nanoparticles tend to be at close proximity and not well distributed. As the chitosan samples are water soluble, it is assumed that the polymer chain is loosely packed during the fabrication process of the samples. This causes the silver particles to be at close proximity as opposed to the ones in the non water soluble chitosan. The existence of these silver nanoparticles is further supported by EDX (Electron Dispersive X-ray) results (Figure 3) which show peaks related to silver.

Quantification of silver ion release using Anode Stripping Voltammetry

Stripping voltammetric experiments with standard solutions of silver led to a calibration curve as shown in Figure 4. Using the fit from this figure, the concentration of the silver ion released into the medium was estimated from three different sample forms namely paste, film and sponge.

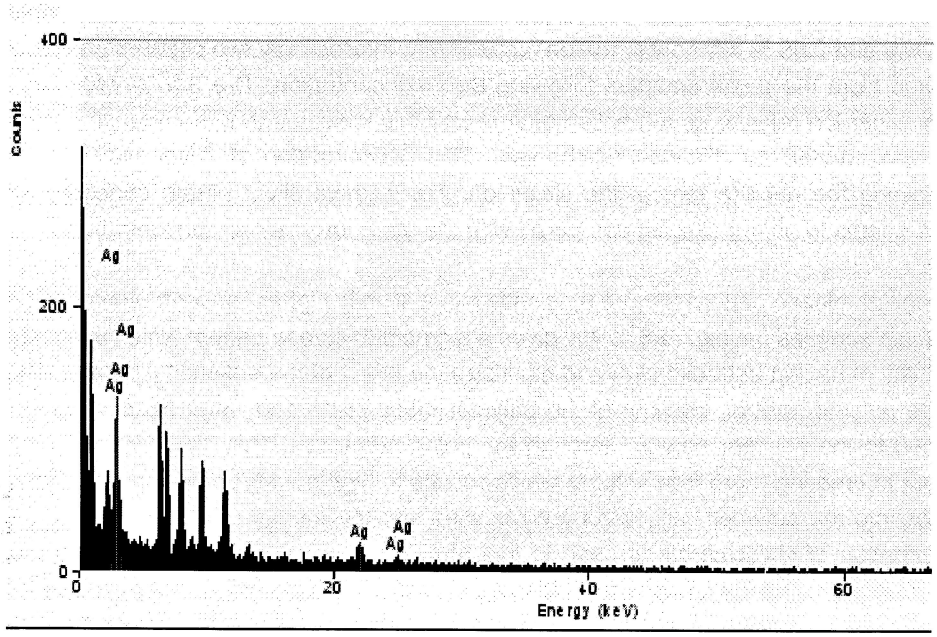

Figure 3. *EDX results showing the existence of silver metal in chitosan matrix*

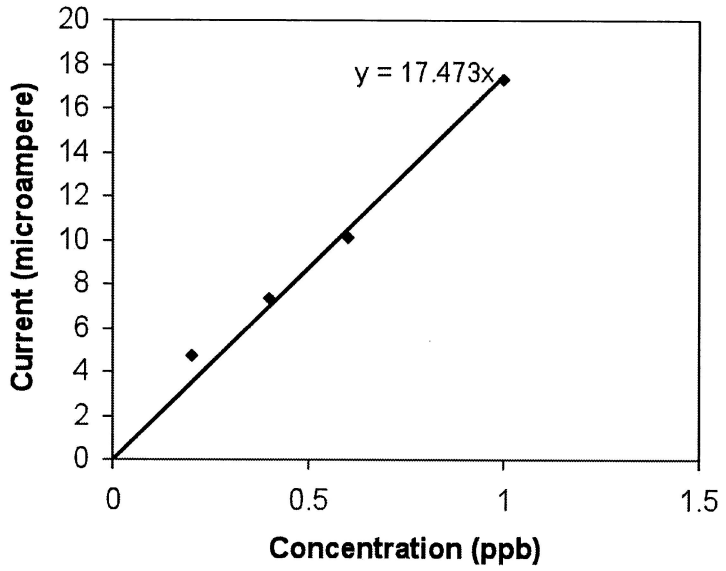

Figure 4. *Silver standard calibration curve obtained from voltammetric study*

Figures 5 and 6 demonstrated the release profile obtained from paste chitosan samples of 2.5 % w/v and 2.85 % w/v concentration respectively. Interestingly two different profiles were exhibited from the paste samples following their concentration. The 2.5 % w/v showed.a steady silver ion release as a function of time and this indicates that the release behavioris purely contributed by diffusion mechanism. The concentration of silver plays a role in determining the release rate of the silver ion. The highest silver nitrate concentration of 3 wt % seems to be the slowest compared with the other lower silver concentration.

A sigmoidal release pattern (Figure 6) is shown in a slightly higher concentration of chitosan. The paste samples having 2.85 % w/v gives a sigmoidal release pattern which indicates the possibility of having both diffusion and plasticization effect of the polymer. As water diffuses into the polymer matrix, swelling of the polymer takes place and water molecule might be attached to the polymer network through the polar interaction. This opens up the polymer network in creating more free volume which results in higher water diffusion rate. As water diffuses into the polymer bulk, silver ion releases into the medium. The effect of the initial concentration of silver nitrate is seen in this profile in which the highest concentration of 3 wt% demonstrates the slowest ion release.

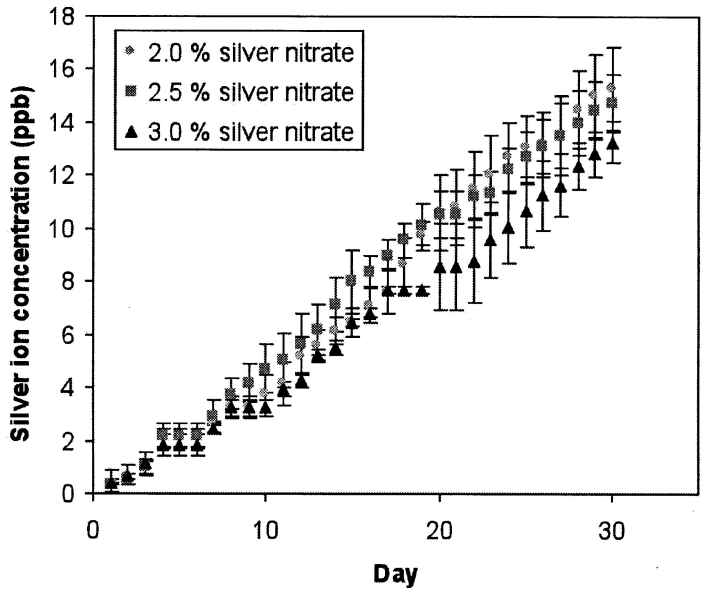

Figure 5. *Silver ion release from non water soluble chitosan (paste) for 2.5 w/v % chitosan with different silver nitrate concentration*

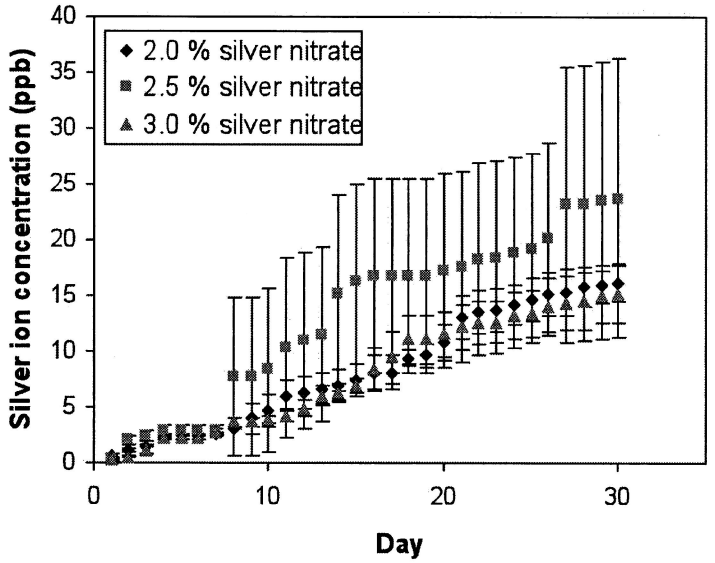

Figure 6. *Silver ion release from non water soluble chitosan (paste) for 2.85 w/v % chitosan with different silver nitrate concentration*

The sponge samples having a concentration of 2.85 w/v % (Figure 7) demonstrate a steady increase of silver release from two initial silver nitrate concentrations of 2 and 3 wt % with approximately 30 ppb of silver ion being released at 30 days period of time. A major increase is seen from the 2.5 wt% silver nitrate in which the silver release reached a concentration of almost 70 ppb in similar period of time. This is quite unexpected as we would have thought that the sponge samples containing 2.5 % silver nitrate lies in the same concentration region. What could have happened is that swelling of the chitosan sponge samples containing the 2.5 wt% silver is much greater than that of the other concentrations, which results in more silver ion being released at similar period of time.

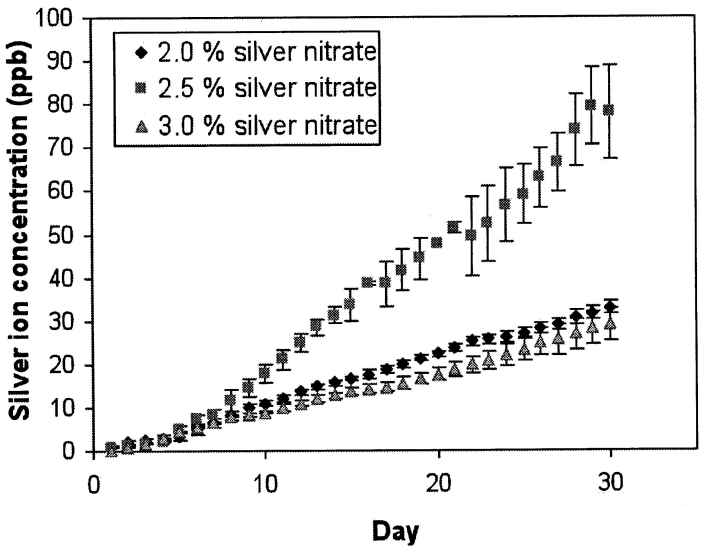

Figure 7. *Silver ion release from non water soluble chitosan (sponge) for 2.85 w/v % chitosan with different silver nitrate concentration*

The chitosan film samples (Figures 8, 9, 10) exhibited a totally different release profile from their counterparts. A pulse or staggered fashion release profile was demonstrated for the chitosan concentrations. There is a time lag in between 8 to 15 days depending on concentration for both chitosan and initial silver nitrate used. With the highest chitosan concentration at 2.85 w/v%, the time lag is the shortest at approximately 8 days, whilst the lowest chitosan concentration at 2 w/v% demonstrated the longest time lag which can reach 15 days depending on the initial silver nitrate concentration. Following the time lag, an increase in the silver ion release is observed before the release reaches its short term plateau. A major increase ensures right after this and prolongs for a certain time period reaching the last plateau at the end of the release period. The effect of concentration was again demonstrated in these profiles (Figures 8, 9, 10) in which the lowest silver nitrate concentration exhibits the highest release.

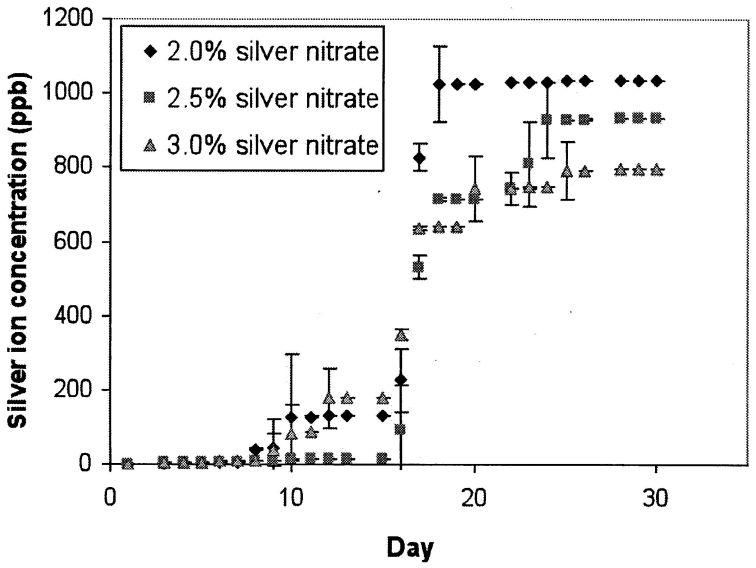

Figure 8. *Silver ion release from non water soluble chitosan (film) for 2.0 w/v % chitosan with different silver nitrate concentration*

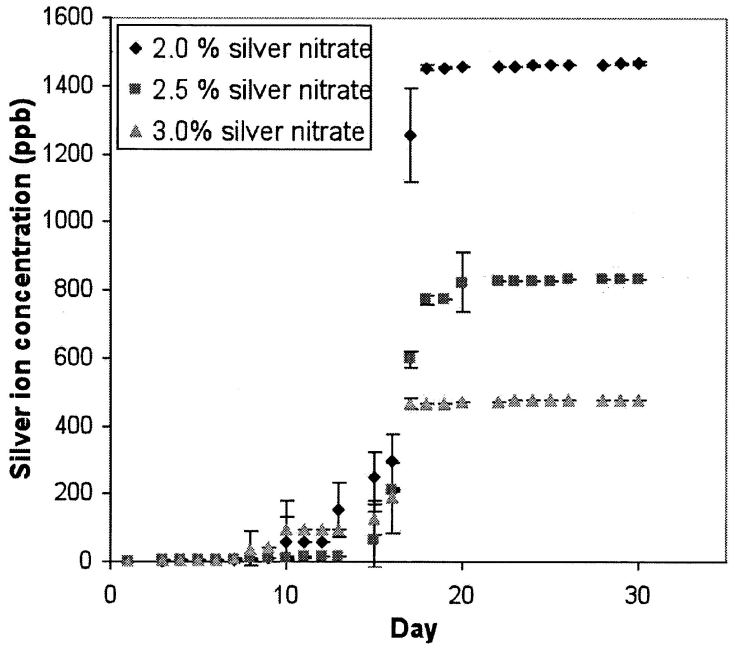

Figure 9. *Silver ion release from non water soluble chitosan (film) for 2.5 w/v % chitosan with different silver nitrate concentration*

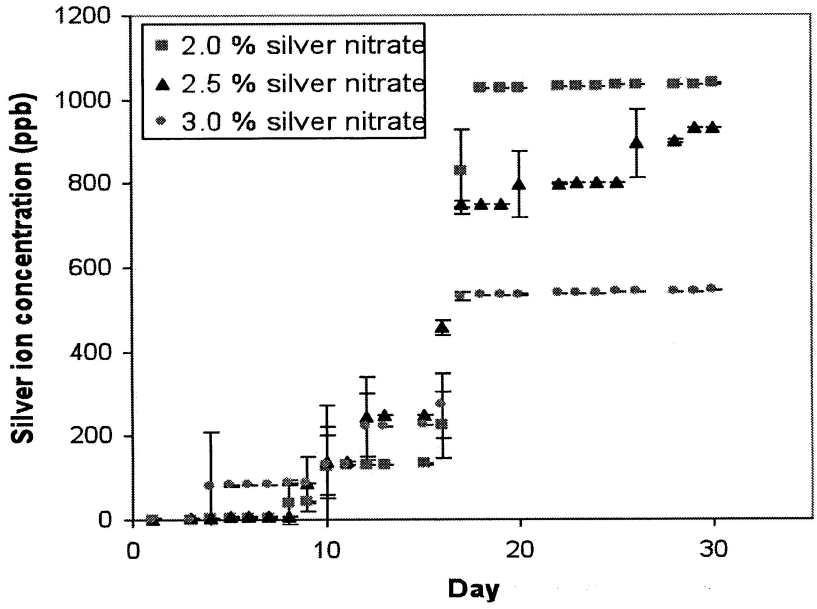

Figure 10. *Silver ion release from non water soluble chitosan (film) for 2.85 w/v % chitosan with different silver nitrate concentration*

It is possible that the penetration of water molecule into the chitosan film is firstly hindered due to the closely packed polymeric branches. An insoluble outer part of the film controls the degree of access of the buffer medium to the inner part of the film sample. At longer time points, films become quite porous and allow the increase of water diffusion into the sample. As more water diffuses in, the polymer begins to swell and the chitosan film expands, exerting force on the chitosan wall until it bursts, thus releasing the drug in large quantity. This is observed after the time lag, in which higher amount of drug is released before the release becomes stable. It is also worth nothing that the chitosan film samples manage to release the drug at quite a high concentration in the range of 1000 – 1500 ppb which is not seen in both paste and sponge samples. The pulsatile release could have caused the burst of the polymer film and results in higher release of the silver ion.

CONCLUSION

Anode Voltammetric Stripping method had been successfully employed in this work to measure the minute concentration of silver ion release into the medium. Chitosan silver composites prepared using various form of samples exhibit different release profile of silver ion. Steady release approaching zero order which resulted from the diffusion process is shown in 2.5 %w/v chitosan paste whilst a sigmoidal curve is observed for the 2.85 w/v% chitosan paste. The sponge demonstrated a steady release of silver ion with time. Interestingly, film samples showed a pulsatile release profile which gave a much higher concentration of silver ions at similar period of time.

ACKNOWLEDGEMENT

This research work was funded by Ministry of Science, Technology and Innovation of Malaysia under Science Fund with project number 03-03-02-SF0085.

REFERENCES

Bogle, K.A., Dohle, S.D., and Bhoraskar, V.N. (2006). Silver nanoparticles: synthesis and size control by electron irradiation. *Nanotechnology*, **17**: pp. 3204 – 3208.

Pastoriza-Santos, I., and Liz-Marzan L.M. (2002). Formation of PVP-protected metal nanoparticles in DMF. *Langmui*, **18**: pp. 2888 – 2894.

Radheshkumar, C., and Munstedt, H. (2006). Antimicrobial polymers from polypropylene/ silver composites – Ag^+ release measured by anode stripping voltammetry, *Reactive & Functional Polymers,* **66**: pp. 780 – 788.

Sakai, H., Kanda, T., Shibata, H., Ohkubo, T., and Abe, M. (2006). Preparation of highly dispersed core/shell-type titania nanocapsules containing a single Ag nanoparticle. *J. Am. Chem. Soc.,* **128**: pp. 4944 – 4945.

Van Hyning D.L., Klemperer, W.G., and Zukoski, C.F. (2001). Silver nanoparticle formation: Predictions and verification of the aggregative growth model. *Langmuir*, **17**: pp. 3128 – 3135.

Yoksan, R. and Chirachanchai, S. (2009). Silver nanoparticles dispersing in chitosan solution: Preparation by γ-ray irradiation and their antimicrobial activities, *Materials Chemistry and Physics,* **115**: pp. 296 – 302.

Journal of Industrial Technology Vol. 19(1), 2010 - ICONT 2009, 125 - 138

CONJUGATION OF POLYAMIDOAMINE-METHOTREXATE USING GLUTARIC ACID AS SPACER FOR POTENTIAL DRUG DELIVERY APPLICATION

Norhidayah Abu, Siti Noorzidah Mohd Sabri, Azreena Mastor, Kartini Noorsal

Advanced Materials Research Centre (AMREC)
SIRIM Berhad, Lot 34, Jalan Hi-Tech 2/3
Kulim Hi-Tech Park, 09000 Kulim, Kedah.

(kartini@sirim.my)

ABSTRACT : Dendrimers are perfect artificial macromolecules with well-defined shape and their suitability for drug delivery is affected by charge, end functionality, generation number and molecular weight. In this study conjugated polyamidoamine (PAMAM generation 4) with methotrexate (MTX) using glutaric acid (GA) as a spacer was studied. To initiate the conjugation, we have tailored the amine end functional group of PAMAM with carboxylate to lower the reactivity and the steric hindrance of the drug. The glutaric acid was first linked to methotrexate before conjugating them with PAMAM to get a relatively high payload. The conjugation of PAMAM-GA-MTX was confirmed through UV-Vis, FTIR, ^{1}H NMR and DSC.

KEYWORDS : Conjugation, steric hindrance, functional group.

INTRODUCTION

The advanced of biodegradable and biocompatible polymers has increased the versatility of polymers in the design of polymeric drug delivery device for many classes of bioactive agents (Khandare, 2005). Dendritic nanostructures can play a key role in drug delivery, due to their high density and variety of functional group that can facilitate and modulate the delivery process. Dendrimer (one of dendritic nanostructure) is usually spherical in shape and contain interior void spaces (Figure 1). They are often characterized by their terminal generation. Several polymer –based drug delivery methods are being investigated in which the drug is encapsulated, complexed or conjugated to the polymers. One of their most popular applications for these unique nanostructures is in cancer treatment. Dendritic nanostructures can play a key role in drug delivery, due to their high density and variety of surface functional group that can facilitate and modulate the delivery process. This includes the ability of the polymer to release drug in a controlled manner, prolong circulation times and to increase the drug solubility which makes able for drug carriers. Desirable to achieve increased efficacy of drugs, enhanced cellular entry, and reduced side effect were the three functions of this polymer in cancer therapy. Complexes and conjugates of dendrimers with different drugs can be prepared with high drug payloads. It can be prepared by decreasing the steric hindrance of the surface functional group which are very close to each other and also by increasing the reactivity of the drug molecule and the dendrimer surface functional groups (Jesse, 2008; Kolhe, 2006; Dhanikula, 2007).

High drug payload was still a major problem for methotrexate due to the steric hindrance of both dendrimer and the methotrexate itself. For in vivo application, covalently conjugated drug will be more stable at physiological pH compared with encapsulation or complexation because of their weak ionic interaction (Gurdag, 2006).

In this study, polyamidoamine (PAMAM) dendrimers (Figure 1) with amine end group of 4th generation were used to target cancer cells with conjugated methotrexate (MTX) using glutaric acid as a spacer. PAMAM dendrimers have received much attention due to their ability to solubilize water-insoluble drugs and the ability to promote the transport of drugs across biomembranes. Whilst, methotrexate act as inhibitors in cancer treatment in which it will interfere with the growth of cancer cells that should be destroyed (Svenson, 2009). In order to overcome the steric hindrance and at the same time to improve the stability and reactivity of methotrexate, glutaric acid was first attached to methotrexate before conjugating them with PAMAM. The conjugation was characterized by UV-Vis, FTIR, ^{1}H NMR, and DSC.

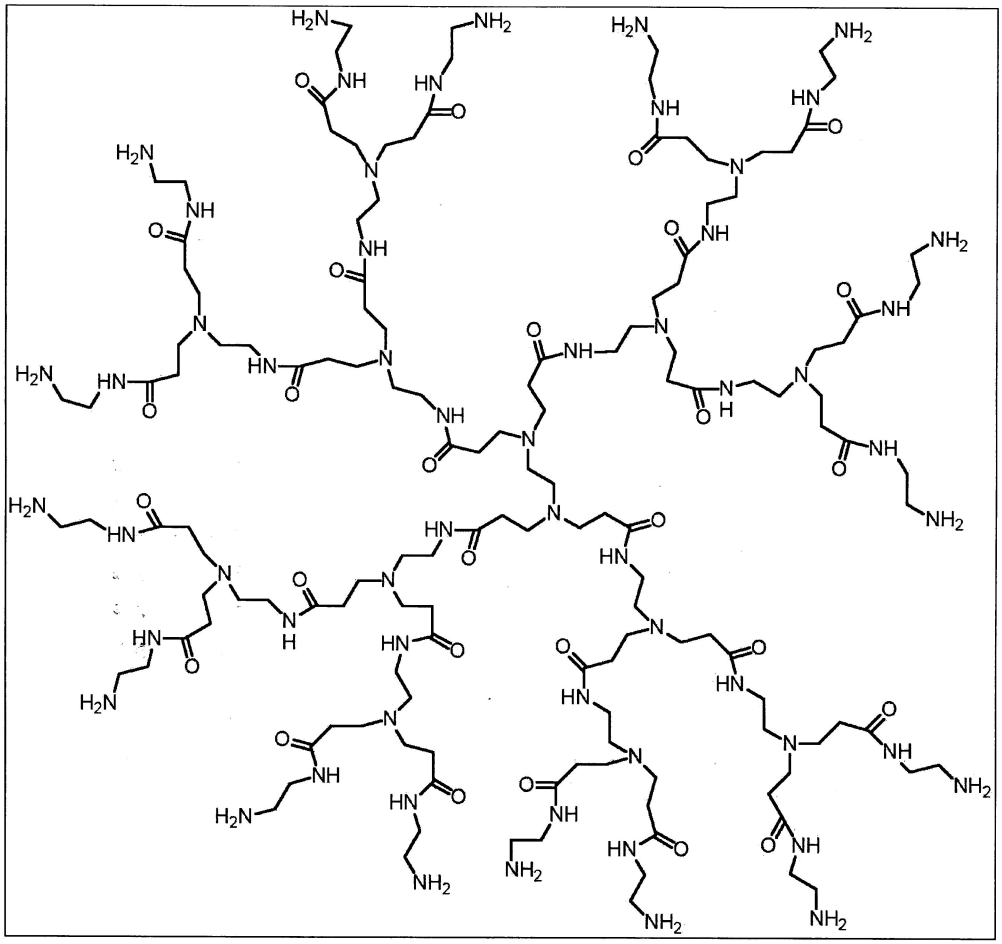

Figure 1. *PAMAM (polyamidoamine) 3rd generation (Gurday, 2006)*

MATERIALS

PAMAM dendrimer, generation 4 (Mw 14242.12 g/mol) and dicyclohexylcarbodiimide (DCC) were purchased from Aldrich, methotrexate (Fluka), glutaric acid (Acros), and dialysis membrane with molecular weight cutoff of 3500 Da was purchased from Spectra Pore. Dimethyl sulfoxide (DMSO) that was used as solvent was purchased from Fisher Scientific. All chemicals were analytical reagent grade and were used without further purification.

INSTRUMENTATION

UV absorbance for methotrexate was determined using Perkin Elmer and the data was obtained from Lambda 25 Software. A Perkin Elmer Spectrum 2000 Fourier Transform Infrared (FTIR) Spectrometer equipped with a diamond tip HATR (Horizontal Attenuated Total Reflectance) accessories was used to record the FTIR spectrum of methotrexate. The samples were pressed at a constant pressure using diamond tip and scanned from 4000 cm^{-1} - 400 cm^{-1}. Whilst ^{1}H Nuclear Magnetic Resonance (NMR) spectrometer obtained from Varian (VNMRS – 300 MHz) using deuterated DMSO as a solvent and tetramethylsilane (TMS) as an internal reference was used to confirm the molecular structure of the obtained conjugate. The DSC thermograms were analyzed using Mettler Toledo DSC 821e equipped with STARe software. Samples were placed in standard aluminium pans with weight of between 5 mg to 10 mg and were scanned in the temperature range of 0 °C -250 °C at a heating rate of 10 °C/min under nitrogen atmosphere.

METHOD

The conjugates were prepared following two steps. The first step describes the process of attaching glutaric acid (GA) to methotrexate (MTX). This is then followed by attaching the compound of GA-MTX to polyamidoamine (PAMAM) (Figure 2).

Synthesis of Glutaric Acid-Methotrexate conjugates (GA-MTX)

An equivalent mole number of glutaric acid and MTX was dissolved together in DMSO. Dicyclohexylcarbodiimide, (DCC) (0.026 mmol) was added as a coupling agent to facilitate the reaction (Figure 2). The reaction was then stirred at room temperature for 24 hours. The solution was filtered to remove dicyclohexylurethane (DCU) which was obtained as byproduct. Filtrate was further evaporated under vacuum to obtain the glutarate-MTX conjugate.

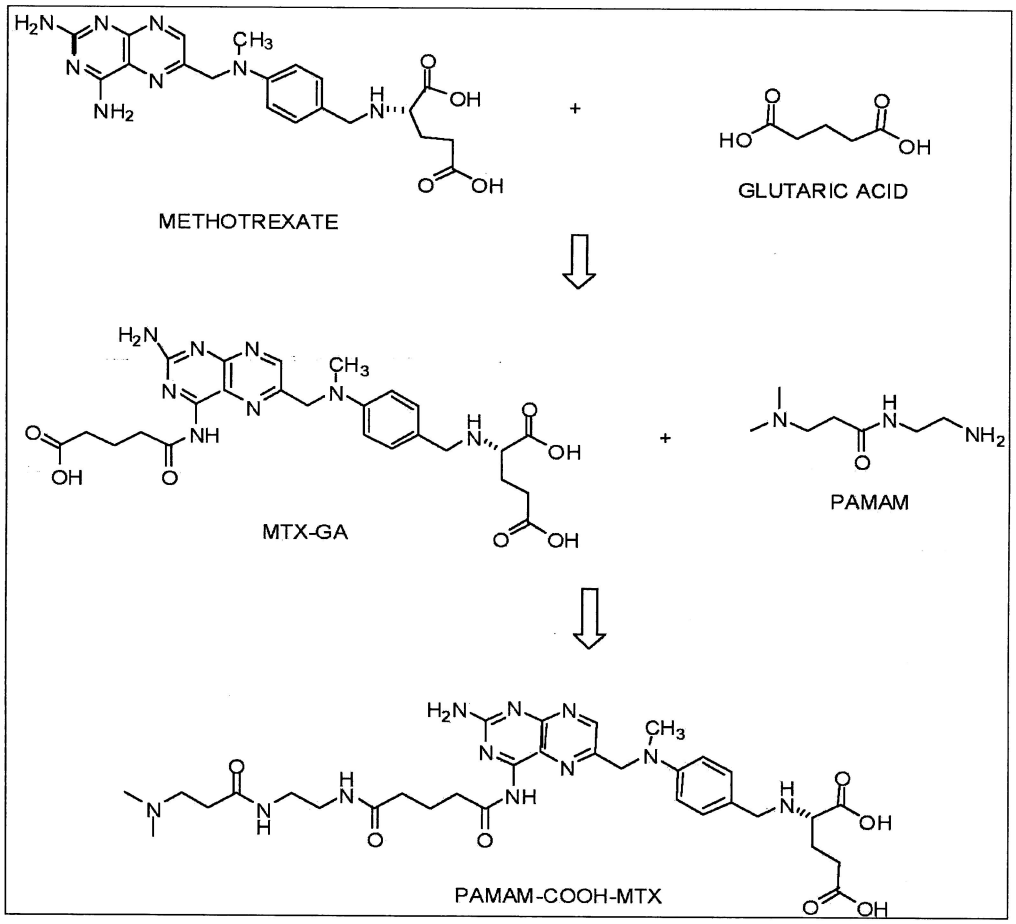

Figure 2. *Schematic reaction of dendrimer-glutaric acid-methotrexate conjugate synthesis*

Conjugation of PAMAM-G4-NH_2 dendrimer to glutarate-MTX (PAMAM-GA-MTX)

PAMAM-G4-NH_2 (0.0024 mmol) and glutarate-MTX (corresponds to a mole ratio of dendrimer to glutarate-MTX of 1:50) were dissolved in 10 ml of DMSO (Figure 2). DCC (0.26 mmol) was added as a coupling agent and the solution was stirred for 72 hours and filtered to remove the DCU. The filtrate was then dialyzed against DMSO for 24 hours using dialysis membrane of Mw cutoff of 3500 Da to remove the unreacted MTX, glutaric acid, DCC, and glutarate-MTX. The solvent was then removed from the dialysis bag, and the conjugate was evaporated under vacuum.

RESULTS AND DISCUSSION

Previous report (Khandare, 2005) indicates the importance to decrease the steric hindrance of the surface functional group and to increase the reactivity of the drug molecule and the dendrimer surface functional groups. Due to the conformationally unstable and bulkier drug of MTX, it might be difficult to directly conjugate the dendrimer with the drug. This problem can be solved by using glutaric acid as the spacer and DCC as the coupling agent. We have covalently conjugated the methotrexate with the dendrimer using "two-step synthesis reaction" by first conjugating the methotrexate to glutaric acid followed by conjugating the methotrexate-glutaric acid to the dendrimer. A high payload of drug is expected as the multiplet free surface functional groups that are available on the periphery of the dendrimer enables higher linking process.

UV-Vis spectroscopy was used to detect the existence of the drug in the synthesized compound (Figure 3). The presence of MTX is indicated by three shoulders at λ_{max} 268 nm, 296 nm and 384 nm respectively. Upon adding the glutaric acid, similar shoulders were observed but at higher absorbance. The addition of dendrimer to the MTX-GA conjugate also exhibits the existence of the drug through similar shoulders which appear at a lower absorbance.

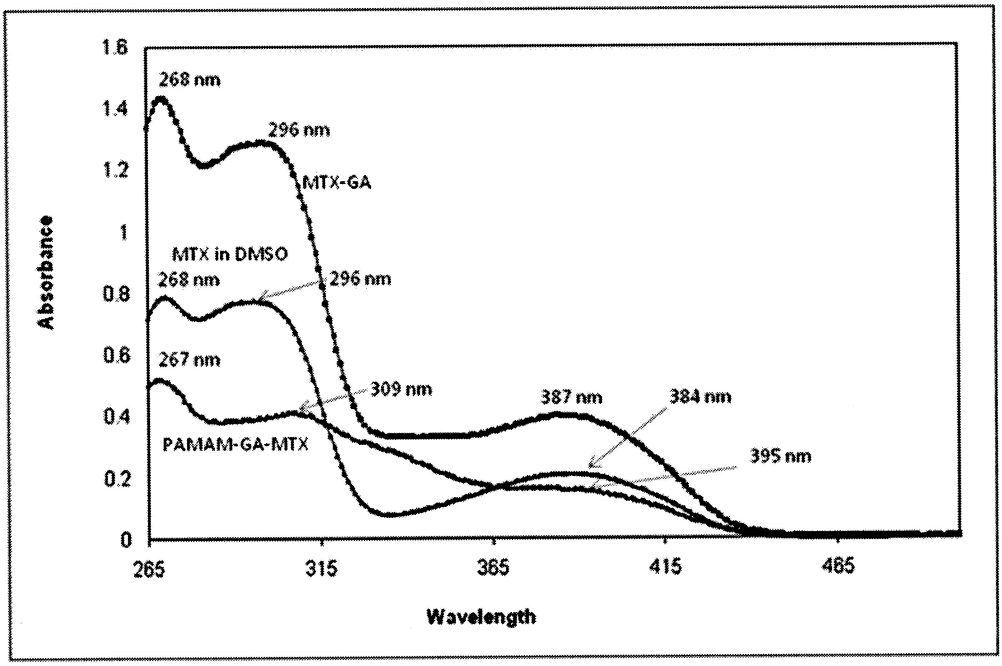

Figure 3. *UV-Vis spectra for methotrexate dissolved in DMSO*

It is interesting to know whether MTX-GA do conjugate with the dendrimer or it could actually be an encapsulation process in which MTX-GA could be incorporated into the cavity of the dendrimer. To verify the attachment of MTX-GA to PAMAM, FTIR was used. The characteristic peaks for MTX are depicted at 1639 cm^{-1} which are associated with the C=N stretch. Whilst, peaks at 1625 cm^{-1}, 2949 cm^{-1} and 1201 cm^{-1} correspond to the amine deformation, carboxylic stretch and C-H of phenyls group respectively. As PAMAM also possess similar functional groups, many peaks that appeared in the drug's spectrum can also be featured in the PAMAM's spectra (Figure 4). Once the drug is conjugated to the linker forming MTX-GA, new peak which corresponds to amide (C = O) appears at 1626 cm^{-1} (Figure 4). Other traces of MTX could also be featured in the MTX-GA spectrum at 1201 cm^{-1} and 1541 cm^{-1} which were associated with C-H bend (phenyl) and N-H stretch vibrations.

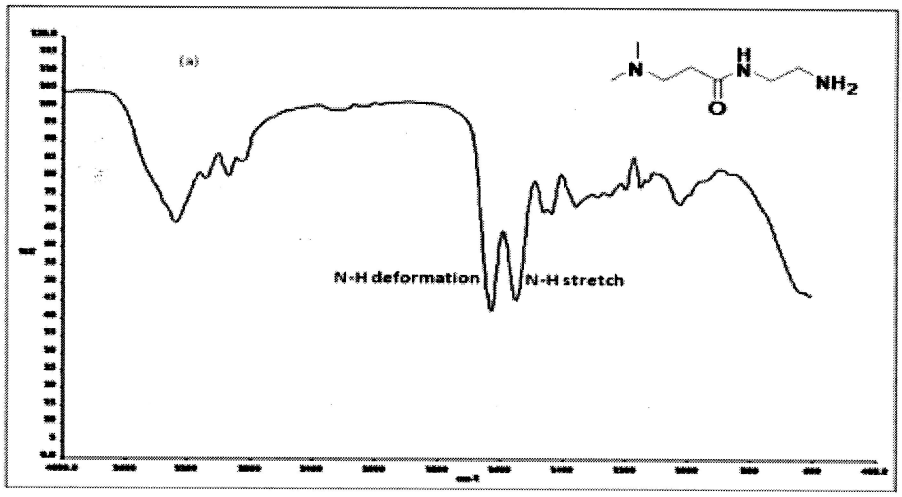

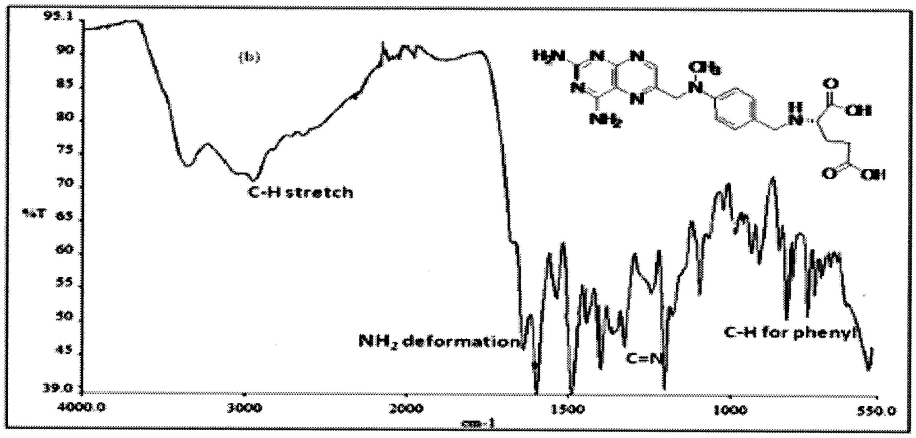

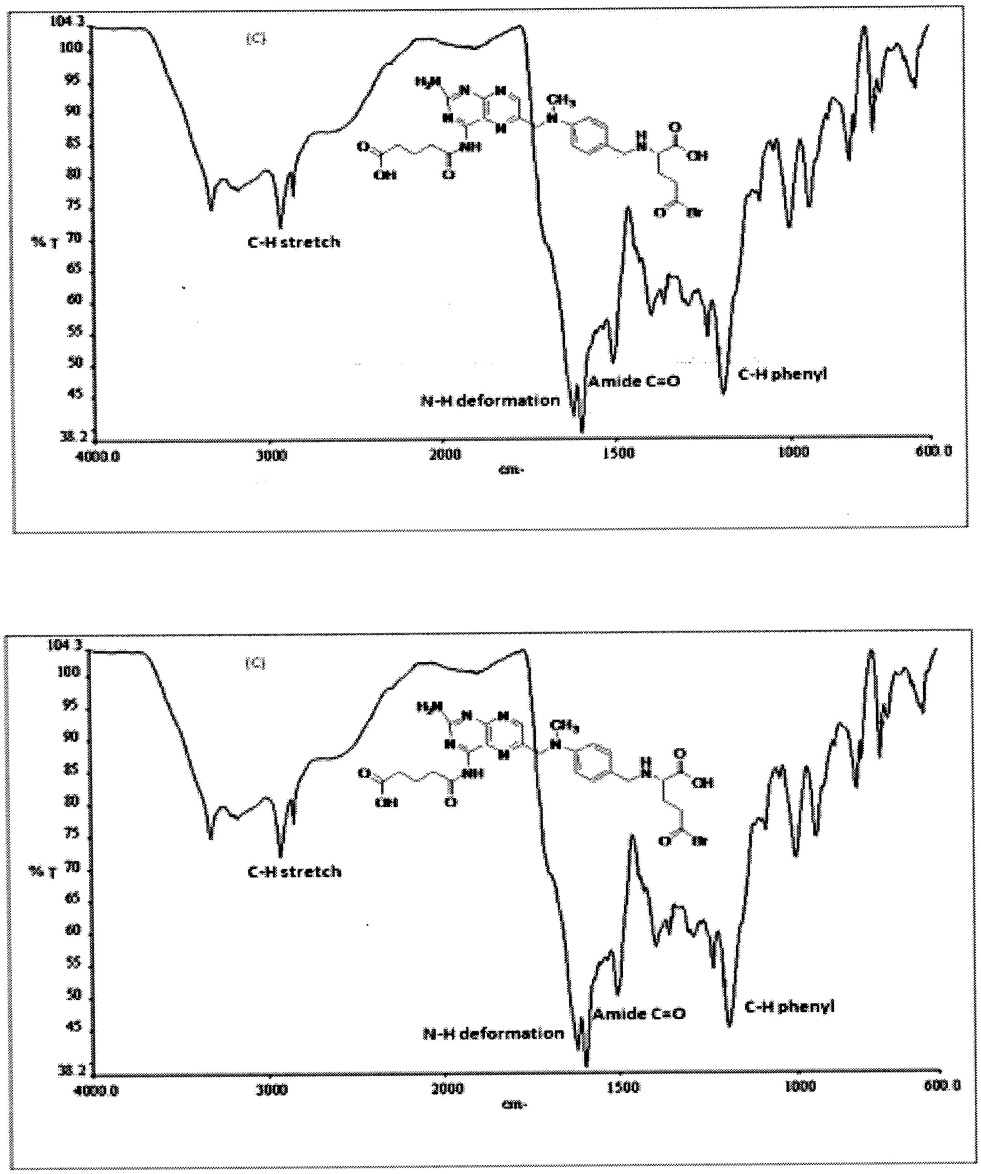

Figure 4. *FTIR spectra for (a) PAMAM (b) Methotrexate (c) MTX-GA and (d) PAMAM-GA-MTX*

The incorporation of PAMAM to MTX-GA is manifested by –HN-C=O group at 672 cm^{-1} which corresponds to the linkage between these molecules. As similar linkages were also found in the MTX-GA spectrum, it is expected that there would be an overlap of these functional vibrations, merging into a broader peak. The ^1H NMR (Figures 5-7) was further used to verify the linkage between PAMAM and MTX-GA. As we are aware of the –HN-C=O group which acts as the linking chain, the chemical shift of 1.20 ppm is thought to correspond to the amide C=O group. This also confirms the covalent bond that could possibly exists between PAMAM and MTX-GA through –HN-C=O group, a conjugation of the carbonyl group from glutaric acid with the amine end group from PAMAM. Other peaks related to MTX and MTX-GA are also present in Figures 5-7.

The aromatic protons of MTX occurred at the chemical shift of 6.8 ppm (2727Hz, 2H) (Figure 5), whilst the methylene group for glutaric acid could be seen at the chemical shift of 2.2 ppm- 2.6 ppm, (Figure 6). The aromatic protons of MTX are observed as singlet at chemical shift of 6.58 ppm (2646Hz, 2H), 6.82 ppm (2729Hz, 2H), 7.48 ppm (2995Hz, 2H), 7.82 ppm (3127Hz, 2H) and 8.56 ppm (3427Hz, 2H). The methylene protons of PAMAM can be seen at 2.30 ppm - 3.60 ppm whilst methylene signals for glutaric acid can be observed at 2.28 ppm -1.78 ppm (Figure 7).

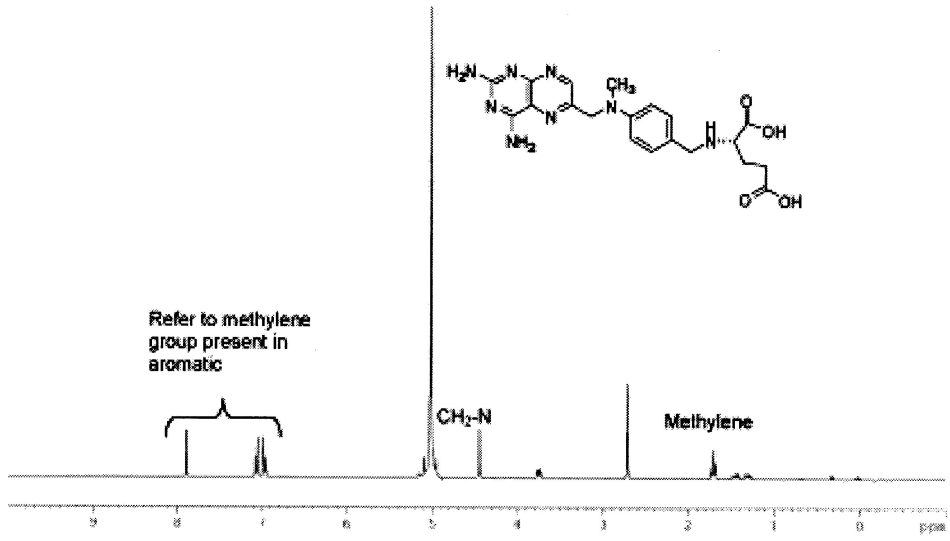

Figure 5. *^1H NMR spectrum of mix dissolved in Hcl*

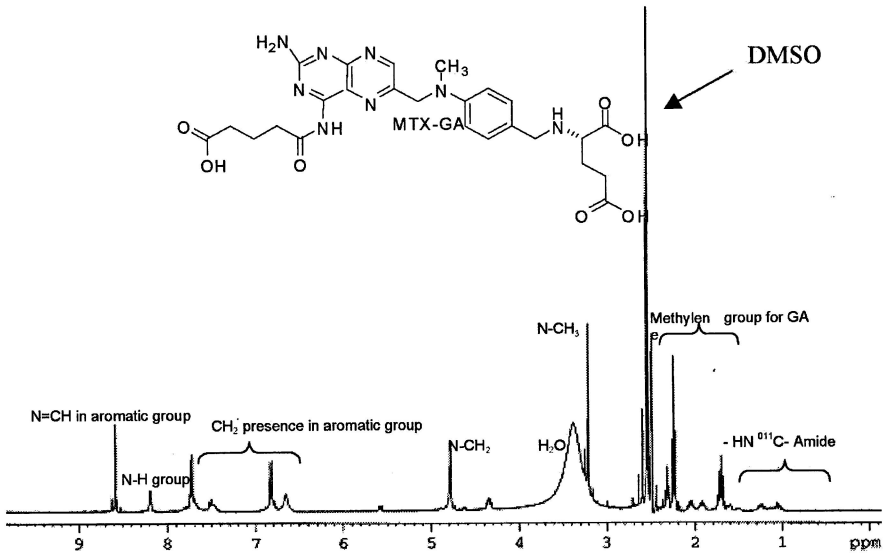

Figure 6. *^{1}H NMR spectrum of mix-GA-MTX dissolved in DMSO*

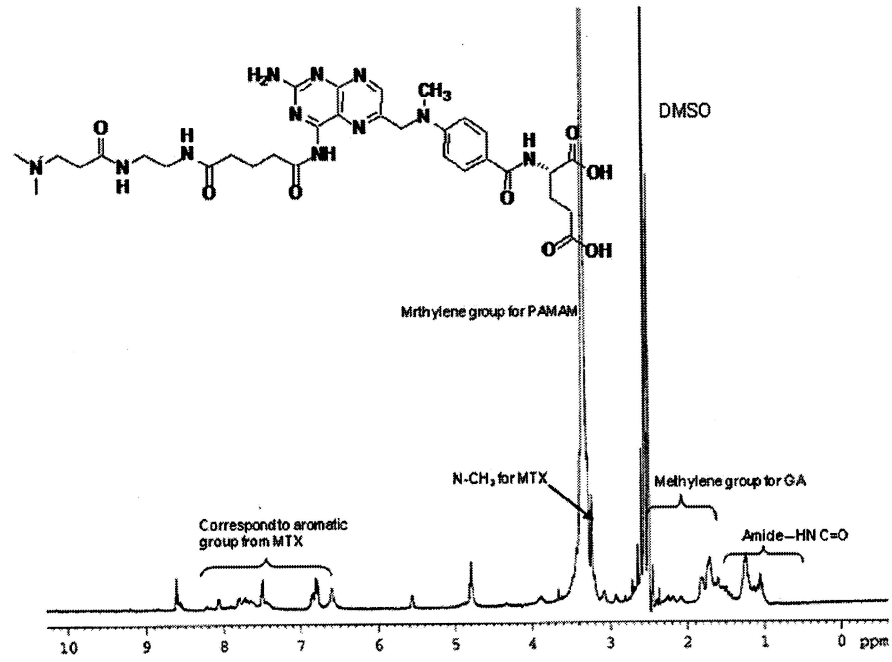

Figure 7. *^{1}H NMR of PAMAM-GA-MTX dissolved in DMSO*

Three endotherms referring to the thermogram of methotrexate (MTX) were demonstrated in the DSC studies (Figure 8a). The first two endotherms at 98 °C and 150 °C corresponds to the loss of free and bound water respectively, whilst the third endotherm at 215 °C corresponds to the melting of MTX. This also reveals that the commercial MTX was in a hydrate form. The endotherm for glutaric acid (Figure 6b) appears at about 100 °C.

Individual peaks from MTX-GA (Figure 8c) referring to both glutaric acid (100 °C) and MTX (215 °C) indicate the existence of both substance in the compounds without possible covalent bonding. This is true when no shifting of endotherms can be observed. Similar pattern was observed in the PAMAM-GA-MTX, the peaks for glutaric acid and MTX appear to be separated to their individual peaks without any major changes.

The data obtained from this study points to the fact that the drug might be well encapsulated in the dendrimer's cavity. First, there is no major peak's shift that can be observed in the UV-Vis spectra. This indicates that interaction of the dendrimer and the chromophore of the MTX through the π- π complexation is absent from the spectrum. Secondly, the drugs' peaks are very small in the ^{1}H NMR spectra, and third, the individual peaks referring to the drug and the linker were observed in the DSC thermograms. These indicate that there is a possible drug encapsulation process rather than chemical conjugation which could have taken place in the experiment.

CONCLUSION

The PAMAM-GA-MTX was successfully synthesized via encapsulation process. This is evident from the U.V. spectroscopy, FTIR, ^{1}H-NMR and DSC data which omits the possible drug conjugation to the dendrimer.

ACKNOWLEDGEMENT

This research was fully supported by the Ministry of Science Technology and Innovation (MOSTI) through Nano Initiative grant.

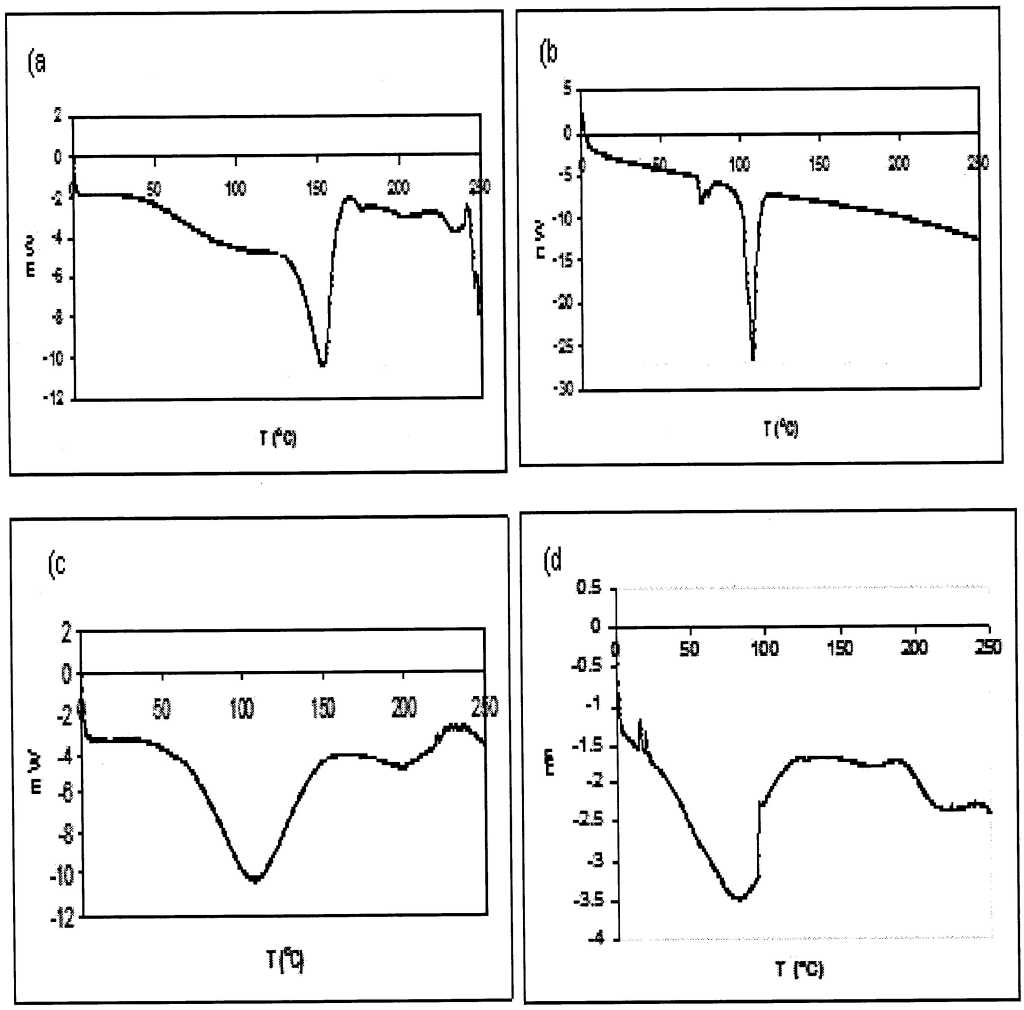

Figure 8. *DSC thermogram of (a) MTX (b) glutaric acid (c) MTX-GA and (d) PAMAM-GA-MTX*

REFERENCES

Dhanikula, R. S., and Hildgen, P. (2007). Influence of Molecular Architecture of Polyether-co-polyester Dendrimers on the Encapsulation and Release of Methotrexate, *Biomaterials*, **28**: pp 3140-3152.

Gurdag, S., Khandare, J., Staples, S., Matherly, L. H. and Kannan, R. M. (2006). Activity of Dendrimer-Methotrexate Conjugates on Methotrexate-Sensitive and Resistant Cell Lines, *Bioconjugate Chem.,* **17**: pp 275-283.

Jesse B., Wolonsky, and Grinstaff, M. W. (2008). Therapeutic and Diagnostic Application of Dendrimers for Cancer Treatment. *Advanced Drug Delivery Reviews*, **60**: pp 1037-1055.

Khandare, J., Kolhe P., Pillai, O., Kannan, S., Lieh-Lai, M., and Kannan, R. M. (2005). Synthesis, Cellular Transport, and Activity of Polyamidoamine Dendrimer-Methylprednisolne Conjugates, *Bioconjugate Chem.*, **16**: pp 330-337.

Kolhe, P., Khandare, J., Pillai, O., Kannan, S., Lieh-Lai, M., and Kannan, R. M. (2006). Preparation, Cellular Transport, and Activity of Polyamidoamine-Based Dendritic Nanodevices with a High Drug Payload, *Biomaterials,* **27**: pp 660-669.

Svenson, S. (2009). Dendrimers as Versatile Platform in Drug Delivery Applications, *European Journal of Pharmaceutics and Biopharmaceutics,* **71**: pp 445-462.

Journal of Industrial Technology Vol. 19(1), 2010 - ICONT 2009, 139 - 148

ELECTROPHORETIC DEPOSITION OF MULTI-WALLED CARBON NANOTUBES ON STAINLESS STEEL (SS) FOILS

Siti Hajar Kasim and Abdul Hakim Hashim*

Advanced Materials Research Centre (AMREC), SIRIM Berhad
Lot 34, Jalan Hi-Tech 2/3, Kulim Hi-Tech Park
09000 Kulim, Kedah, Malaysia

***(hakim@sirim.my)**

ABSTRACT : The effect of oxidation on the structural of MWCNTs through nitric acid has been studied. Raman spectroscopy analysis clearly revealed that the nitric acid treatment under reflux conditions suffered the highest degree of degradation and additional defect generation on the graphitic network and this would greatly aid the dispersion of CNTs in ethanol to form a stable and homogenous CNTs suspension. The amount of charger salt that was added into the suspension also influenced the microstructure of the CNTs films, as shown by the SEM analysis. SEM and EDX analyses also revealed that deposition from lower concentration of charger salt in the CNTs suspension produced a more uniform CNTs film with lower magnesium and oxygen content compared to CNTs films deposited from higher content of charger salt suspension.

KEYWORDS : Carbon nanotubes, coating, charger salt, electrophoretic deposition, deposition voltage

INTRODUCTION

The discovery of buckyballs led to the discovery of other forms of carbon that are structurally related, for example, carbon nanotubes (CNTs), which are the third allotropic carbon form in addition to diamond and graphite. Carbon nanotubes are cylinder-shaped macromolecules with a radius as small as few nanometers, which can be grown up to 20 cm in length. The walls of these tubes are made of a hexagonal lattice of carbon atoms analogous to the atomic planes of graphite. They are capped at their ends by one half of a fullerene-like molecule (Burghard *et al.*, 2005). There are two types of carbon nanotubes' morphology. One is single wall nanotubes (SWNTs) which consist of a honeycomb network of carbon atoms and can be visualized as a cylinder rolled from a graphitic sheet. On the other hand, multi-walled nanotubes (MWNTs) that are a coaxial assembly of graphitic cylinders generally separated by the plane space of graphite (Sayago *et al.*, 2005). They have attracted scientific interest with a great number of potential applications in numerous areas because of their special properties and features. Carbon nanotubes (CNTs) have been demonstrated to be exciting new materials for electrode of electrochemical energy storage and conversion devices, owing to their unique internal structures, high surface area, remarkable chemical stability and electronic conductivity as well as light weight (Du *et al.*, 2006). The aim of this research is to produce CNTs films on conducting electrode; especially for batteries and capacitor applications.

The oxidation of carbon nanotubes (CNTs) has gained a lot of attention in an attempt to purify and also enhance the chemical reactivity of the graphitic network. Typically, through the oxidation treatment, the chemical modification promotes the opening of the tube caps and the formation of the functional groups at defects sites along the sidewalls. The pristine carbon nanotubes (CNTs) can be effectively purified and functionalized with oxygen-containing groups, mainly carboxyl and hydroxyl. The grafting of chemical functionalities on the carbon nanotubes surface, such as carboxylate, imparts negative charges and, therefore, creates the electrostatic stability required for a colloidal suspension. Nanotubes functionalized in this manner basically retain their pristine electronic and mechanical properties (Burghard *et al.*, 2005).

Electrophoretic deposition (EPD) is one of the processing method which is gaining interest as a simple and versatile technique for the production of coatings and films from carbon nanotubes. The technique allows the fabrication of coatings, thin and thick film of CNT on conductive substrates. EPD is achieved via the motion of charged CNTs, dispersed in suitable solvent, towards an electrode under an applied electric field (Aldo *et al.*, 2006). EPD is a rapid, cost-effective method which requires simple equipment enabling material layers (thin and thick films) to be made in only seconds or minutes. EPD is essentially a two-step process. In the first step, particles suspended in a liquid are forced to move towards an electrode by applying an electric field (electrophoresis). In the second step, the particles are

collected at the electrode and form a coherent deposit (deposition). Deposition occurs only on conducting surfaces, however non-conductive substrates can be infiltrated by using EPD (Aldo *et al.*, 2006).

MATERIALS AND METHODS

The nanotubes used in this study, purchased from Shenzen Nanoport (NTP), China, were made via Chemical Vapor Deposition (CVD). The nanotubes need to be purified, and this was done by refluxing the nanotubes with concentrated nitric acid (10.6 N) for 8 hours using refluxing apparatus. The nanotubes were then repeatedly washed with distilled water and filtered, followed by rinsing with absolute ethanol and drying at 50 °C for 5 hours. By doing this, the metallic impurities were removed. This process would functionalize the nanotubes with COOH. Furthermore, this treatment also introduces defects or imperfections onto the carbon nanotubes, thus providing sites for functionalization with various chemical components such as COOH, and OH. The functionalized multi-walled carbon nanotubes (MWCNTs) were analyzed by Raman Spectroscopy (RENISHAW) to ascertain the effect of acidic reflux treatment on the structure and the integrity of the nanotubes.

5 mg of purified and functionalized nanotubes were then dispersed ultrasonically in 100 ml ethanol, by ultrasonic equipment (VCX 500, Sonics USA) with 50 % amplitude for 2 hours. In order to charge the carbon nanotubes, two different concentration of $Mg(NO_3)_2.6H_2O$ were added into the suspension as electrolyte for EPD which were 1.1×10^{-5} mol and 3.4×10^{-4} mol, respectively.

Two 3 cm X 5 cm stainless steel foils were used as electrophoretic deposition (EPD) electrodes (Figure 1), and were put in parallel at 2 cm distance facing each other into the suspension. An electric field with various DC voltages (10 V, 50 V and 100 V) were applied across the two electrodes using high voltage DC power supply (KENWOOD Regulated DC power supply, model PD110-5AD). The positively charged nanotubes were attracted toward the opposite polarity electrode resulting in CNT film on the respective electrode.

The microstructure of the CNTs coated electrodes were investigated by high resolution Scanning Electron Microscopy (LEO 1525). The effect of different concentration of charger salt on the chemical composition of CNT films were analyzed by EDX.

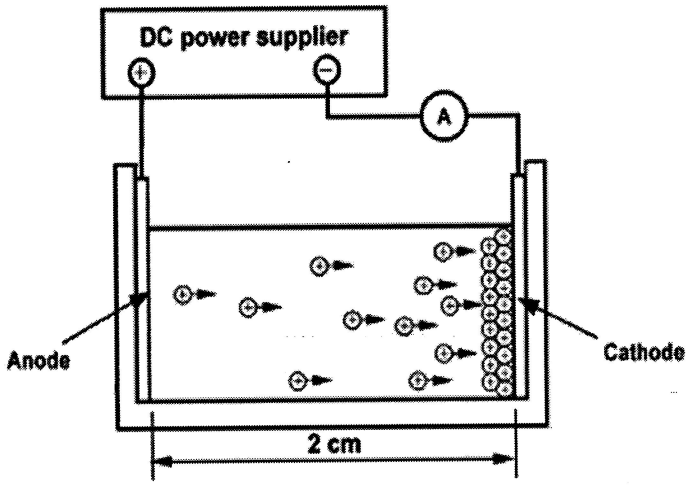

Figure 1. *Schematic diagram of the electrophoretic deposition of CNTs on the cathode of an EPD cell with planar electrodes*

RESULTS AND DISCUSSION

Acidic Oxidative Treatment

As reported earlier (Datsyuk *et al.*, 2008) oxidation treatment with nitric acid to the CNT materials may cause major alteration in its structural properties. This treatment causes large population of defect sites and also introduces the carboxyl group into the sidewalls of the nanotubes. The above observation is in full agreement with the Raman spectroscopic result presented in this paper. Raman spectroscopy is a very valuable tool for the characterization of carbon-based nanostructures. The Raman spectra of pristine and treated MWCNTs excited with the 514 nm laser line are shown in Figure 2. Each of them consist of three characteristic bands, which are the D-band at ~1350 cm^{-1}, the G-band at ~1580 cm^{-1} and the G'-band at ~2700 cm^{-1}. The D-band is a disorder induced feature arising from double resonance Raman scattering process from a non-zero-center phonon mode and it is usually attributed to the presence of amorphous or disordered carbon in the CNT samples. The carbon structural disorder is due to the finite or nanosized graphitic planes and other forms of carbon, such as rings along with defects on the nanotube walls, vacancies, heptagon-pentagon pairs, kinks and heteroatoms. The G-band originates from in-plane tangential stretching of the carbon-carbon bonds in graphene sheets. In Figure 2(b), the Raman spectra of the CNTs shows an increase of D-band after treatment with nitric acid. By integrating the areas of the D and G peaks, a significant enhancement of the corresponding ratio I_G/I_D was estimated.

The I_G/I_D ratio for pristine MWCNTs is 1.03 as opposed to the treated MWCNTs of only 0.92. This reduction in ratio occurred due to increasing intensity of the D-band which is caused by the defect of the CNTs.

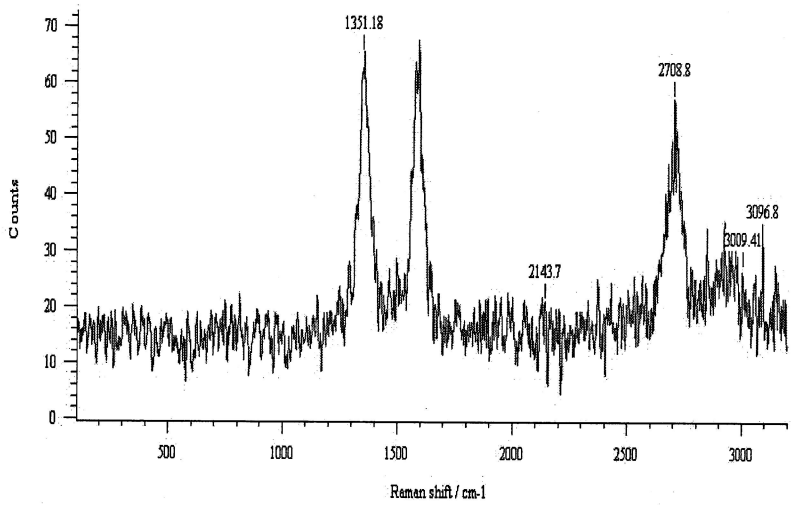

Figure 2 . *(a) The Raman spectra of pristine MWCNTs*

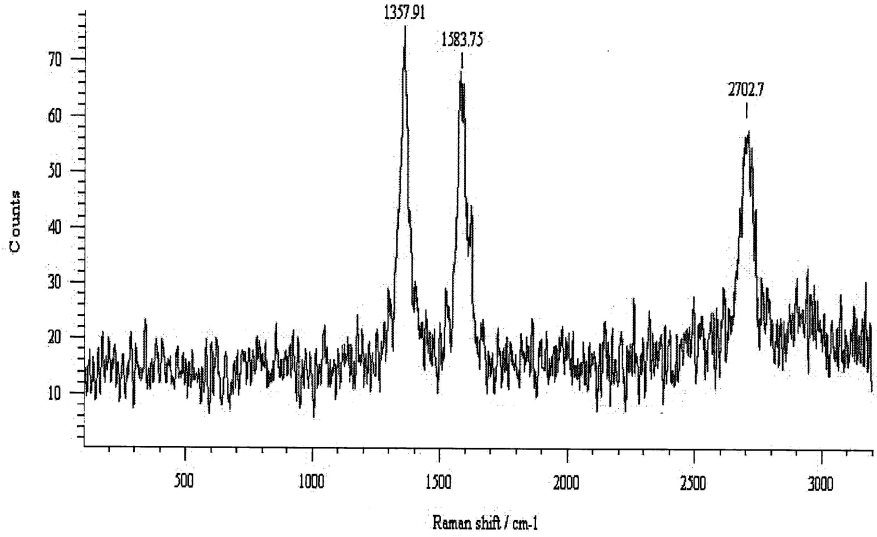

Figure 2. *(b) The Raman spectra of functionalized WMCNTs*

Colloidal stability of CNT suspension

CNTs have a strong tendency to agglomerate due to their nano size and their respective high surface energy (V. Datsyuk *et al.*, 2008). However, the introduction of chemical functionalities on the CNT surface, such as carboxyl groups, give negative charges to the CNTs and this will create the electrostatic stability that is required for the stability of the colloidal dispersion. This is confirmed by comparing the dispersion of pristine CNTs in both functionalized and pristine conditions, as shown in Figure 3.

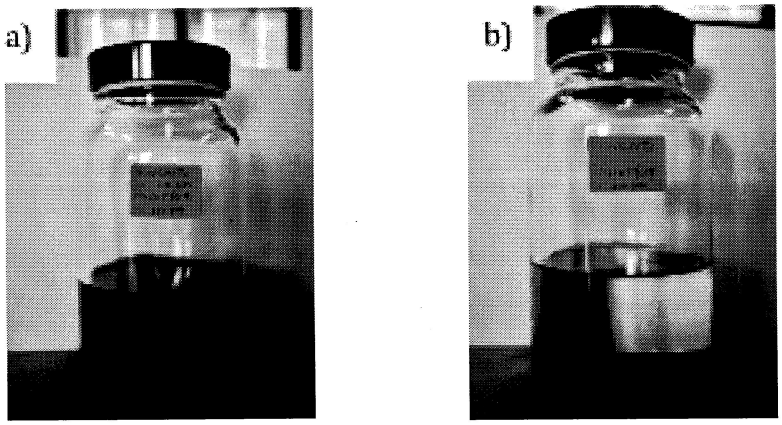

Figure 3. *The suspension of (a) functionalized MWCNTs (b) pristine MWCNTs dispersed in ethanol*

Microstructure

The charger salts, namely $Mg(NO_3)_2.6H_2O$ was then added into stable colloidal suspension. This will give positive charge to the nanotubes as a result of the adsorption of Mg^{2+}, onto the nanotubes surface. Hence under an electric field, it moves towards the negative electrode of a stainless steel foil and was deposited to form a thin film. Two different concentrations of $Mg(NO_3)_2$ was used in this suspension.

The EDX analysis of all samples revealed the existence of C, Mg and O in the coating. According to Pan *et al.*, 2006, during electrophoretic deposition of CNTs, hydrogen gas evolved on the negative electrode surface. Since the Mg^{2+} was attached to the CNT surfaces, reaction occurred between Mg^{2+}, water and hydrogen at the surface near to the deposition electrode, hence forming MgOH compound which was incorporated together into the coating.

The effect of deposition voltages on the morphology and structure of the coating can also be observed in Figure 4. At lower voltage (10 V), CNT film deposited showed some void and recesses on the substrate's surface. By increasing the deposition voltages to 50 V and 100 V, it can be seen that CNTs film deposited has a uniform pore structure formed by the open spaces between entangled annotates, without clear voids and recesses. However, this observation can only been seen for the suspension with lower concentration of the charger salt. The microstructure of the thin film with higher concentration (3.4 x 10^{-4} mol) of charger salt shows a non continuous coating, with cracks and recesses all over the surface. Elemental analysis by EDX exhibited a high count of Mg and O, indicating the deposition of predominantly MgOH.

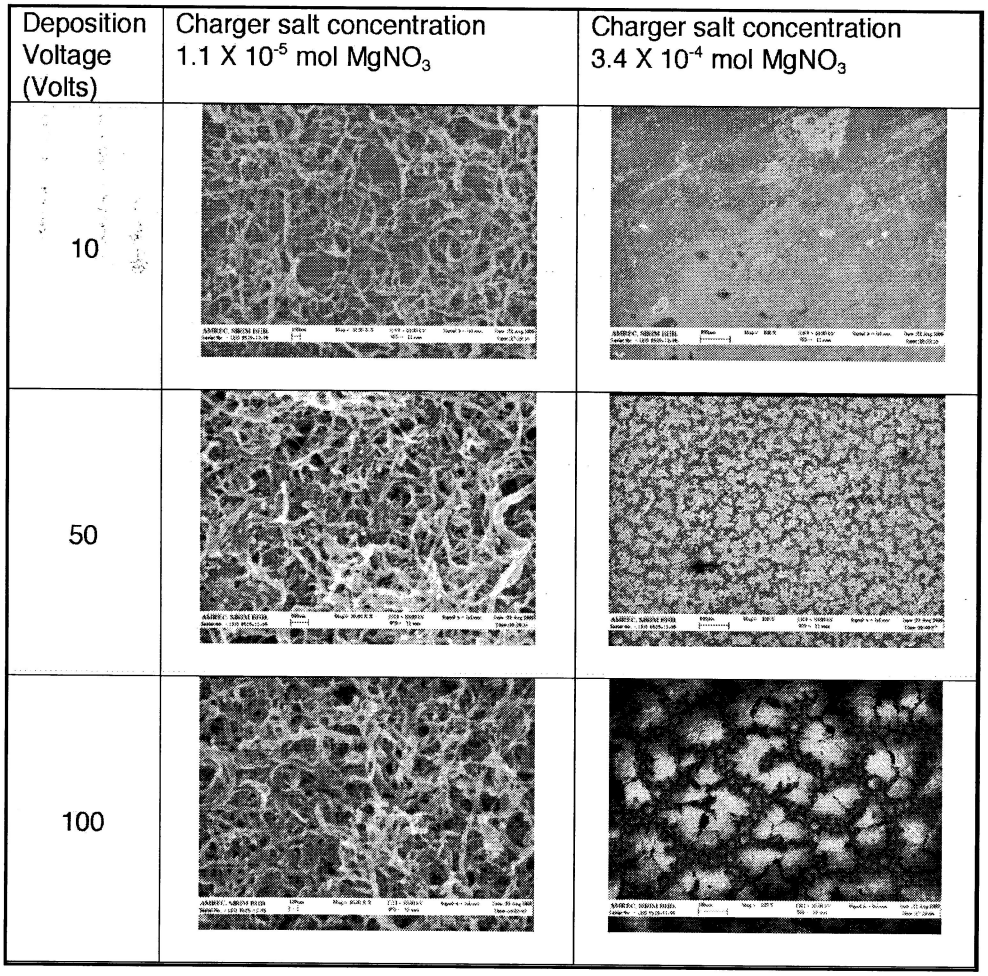

Figure 4. *SEM images at magnification of 30 000 x of functionalized MWCNTs films obtained by EPD on stainless steel foil with different concentration of* $Mg(NO_3)_2.6H_2O$

The composition of elements analyzed by EDX is shown in Table 1 and Table 2 for film deposited from suspension containing higher and lower charger salts respectively. It can be seen clearly that films deposited from higher concentration charger salts suspension contained higher Mg and O content as compared to films deposited from lower concentration suspension.

The films deposited from lower charger salt concentration suspension have a more consistent elemental composition, even though the deposition voltages were varied. However, significant effect of deposition voltages was observed on films deposited from higher concentration suspension. It can be seen that deposition at higher voltage favoured the film formation of increased oxygen content and decreased Mg. At this point we can only speculate the reason for that occurrences which was related to higher charger salt concentration as there was more OH ions (from dehydrated $MgNO_3.OH$) available in that particular suspension. Because of this, at higher deposition voltage, a lot more of hydrogen molecules evolve at the surface of the depositing electrode. Some reaction involving Mg ions and OH occurred to form MgOH. In addition, the high potential difference between the electrodes caused more electrons to flow out from the deposited CNTs. Through electrochemical reactions at the electrodes, the CNTs were further functionalized with OH functional groups, hence the higher composition of O in EDX analysis.

Table 1. EDX analysis on CNTs Thin Film deposited from suspension with higher concentration of charger salt (3.4×10^{-4} mol)

DEPOSITION VOLTAGE	AVERAGE CONTENT		WEIGHT PERCENT	AVERAGE CONTENT		ATOMIC PERCENT
	C	Mg	O	C	Mg	O
10	12.91	35.63	51.47	18.66	25.46	55.88
50	11.82	25.33	62.85	16.53	17.5	65.98
100	16.76	22.66	60.59	22.82	15.24	61.94

Table 2. *EDX analysis on CNTs thin film deposited from suspension with lower concentration of charger salt (1.1 X 10^{-5} mol)*

DEPOSITION VOLTAGE	AVERAGE CONTENT		WEIGHT PERCENT	AVERAGE CONTENT		ATOMIC PERCENT
	C	Mg	O	C	Mg	O
10	46.79	8.64	44.57	55.36	5.05	39.59
50	45.92	8.11	48.35	54.38	4.74	40.88
100	42.93	8.72	45.97	51.39	5.16	43.45

CONCLUSIONS

Chemical oxidation of MWCNTs with nitric acid causes more defect on the sidewalls of the tube and also introduce oxygen-containing group, for example, carboxyl group on the CNTs. This defect and carboxyl group increase the stability of CNTs in polar media, thus produced a very stable suspension of CNTs. Charger salt consisting of Mg ions was introduced into the suspension to charge the CNTs. By employing EPD method, a film of CNTs was obtained on the stainless steel foil. It was found that lower concentration of charger salt in CNTs suspension was more suitable and produced a more uniform pore structure coating compared to the deposition of CNTs with higher charger salt concentration. Lower concentration of charger salt in CNTs suspension produced CNTs films with lower Mg and O content.

ACKNOWLEDGEMENT

This work was funded under science-fund project (03-03-02-SF0095). The authors would like to express their gratitude to the Ministry of Science, Technology and Innovation (MOSTI) and AMREC SIRIM Berhad for their support.

REFERENCES

Aldo R. Boccaccini, Johann Cho, Judith A. Roether, Boris J. C. Thomas, E. Jane Minay, Milo S. P. Shaffer. (2006). Electrophoretic Deposition of Carbon Nanotubes. *Carbon* **44**: pp 3149 3160.

Burghard M., Balasubramaniam, K. (2005). Chemically Functionalized Carbon Nanotubes. *Small.* pp 180-192.

Chetna Dhand, Sunil K. Arya, Surinder Pal Singh, Bhanu Pratap Singh, Monika Datta, B. D. Malhotra. (2008). Preparation of polyaniline/multiwalled carbon nanotubes composite by novel electrophoretic deposition. *Carbon.* **46**: pp 1727-1735.

Datsyuk V., Kalyva M., Papagelis K., Parthenios J., Tasis D., Siokou A., Kallitsis I., Galiotis C. (2008). Chemical oxidation of Multi-Walled Carbon Nanotubes. *Carbon.* **46**: pp 833-840.

Du C., Pan N. (2006). Supercapacitor using Carbon Nanotubes films by Electrophoretic Deposition. *Journal of Power Sources.* **160**: pp 1487-1494.

Sayago I, Terrado E, Lafuente E, Horrillo M.C, Maser W. K, Benito A. M., Navarro R., Urriolabeitia E. P. , Martinez M. T. , Gutierrez J. (2005). Hydrogen sensors based on carbon nanotubes thin films. *Synthetic Metals.* **148**: pp 15-19.

Journal of Industrial Technology Vol. 19(1), 2010 - ICONT 2009, 149 - 166

OPTIMIZATION OF ELECTROPHORETIC DEPOSITED MANGANESE OXIDE THIN FILMS AS ELECTRODE MATERIALS FOR ELECTROCHEMICAL CAPACITORS

Suh Cem Pang*, Suk Fun Chin and Yen Yuan Tay

Department of Chemistry,
Faculty of Resource Science and Technology
University Malaysia Sarawak,
94300, Kota Samarahan, Sarawak,
Malaysia.

***(scpang@frst.unimas.my)**

ABSTRACT : Nanostructured thin films of tetrapropylammonium manganese oxide (TPA-MO) were prepared by depositing TPA-MO nanoparticles in the form of stable colloidal suspension directly onto supporting stainless steel plates using the electrophoretic deposition technique. Electrochemical characterization by cyclic voltammetry indicated that TPA-MO thin films exhibited high charge capacity, good cycling reversibility and stability in 1.0 M Na_2SO_4 aqueous electrolyte. TPA-MO thin films with optimized film thickness, mass loading, and microstructure exhibited enhanced electrochemical properties with a specific capacitance of about 700 F/g. These films are therefore potential electrode materials for the fabrication of electrochemical capacitors.

KEYWORDS : Nanostructures, thin films, oxides, electrochemical properties, microstructure

INTRODUCTION

Electrochemical capacitors are charge-storage devices which consist of an electrolyte being sandwiched between two electrodes of appropriate electroactive materials, and possess high power density, excellent reversibility and long cycle life (Kötz & Carlen, 2000; Park *et al.*, 2004; Hu & Tsou, 2003; Fabio *et al.*, 2001). The unique pulse-power characteristic of electrochemical capacitors offers various potential applications including load-leveling, start-up, acceleration and regenerative braking in hybrid electric vehicles, and as back-up memory for electronic devices such as laptop, cellular phones, camcorders and personal digital assistant (PDA) (Reddy & Reddy, 2003; Jiang & Kucernak, 2002). Electrodes of electrochemical double layer capacitors (EDLC) are usually composed of very high surface area materials, for instance, carbon with surface area of 2,500 m^2/g, whereas electrodes of redox electrochemical capacitors (or pseudocapacitors) consist mainly of electroactive materials with multiple oxidation states or structures such as hydrous metal oxides and conducting polymers (Jang *et al.*, 2002; Broughton & Brett, 2004).

During past decades, much research attention have been focused on developing electrode materials which are environmentally benign and cheap, as well as possessing high specific surface areas such as carbon, transition-metal oxides and conducting polymers for the fabrication of electrochemical capacitors of high power and energy density. Specific capacitance values as high as 720 F/g had been obtained using amorphous ruthenium oxide as electrodes in a pseudocapacitor with H_2SO_4 as the electrolyte and operating at 2 mV/s scan rate (Zheng, 1999). Ruthenium oxide has been known to be an ideal electrode material for pseudocapacitors, but it is very expensive and therefore not economically feasible for commercialization. On the other hand, manganese dioxide (MnO_2) appears to be a promising electrode material for electrochemical capacitors due to its superior electrochemical performance, environmentally benign in nature, and low cost. Manganese dioxide has received considerable attentions since a capacitance value of about 700 F/g had been demonstrated for ultra-thin MnO_2 films prepared by the sol-gel techniques (Pang *et al.*, 2000; Chin *et al.*, 2002). Such nanoparticulate MnO_2 thin-film electrodes were formed by either "dip-coating" or "drop-coating" of stable colloidal MnO_2 suspension directly onto clean nickel foils. However, these thin-film deposition techniques tend to produce MnO_2 thin films of low uniformity and weak adherence to the supporting substrate, which could have contributed towards the observed capacity fading upon long-term cycling as consequences of 'peeling off' and partial dissolution of electroactive films in the electrolyte.

In this study, thin films of tetrapropylammonium manganese oxide (TPA-MO) were prepared by depositing preformed manganese oxide nanoparticles in the form of stable TPA-MO colloidal suspension directly onto the supporting stainless steel plates electrophoretically. The electrophoretic deposition technique has been recognized as a versatile and

cost-effective deposition technique for conformal coatings on supporting substrate of complex shapes with controllable thickness and tailored microstructure (Zhitomirsky, 2002; Ghaemi & Binder, 2002). The main focus of this study was to enhance the electrochemical properties of tetrapropylammonium manganese oxide thin films through the optimization of film thickness and associated electroactive mass loading, as well as microstructural parameters such as specific surface area and porosity.

MATERIALS AND METHODS

Synthesis of Stable Colloidal Manganese Oxide Suspension (Sol)

A stable colloidal suspension of tetrapropylammonium manganese oxide (TPA-MO) was prepared by the reduction of tetrapropylammonium permanganate with 2-butanol in aqueous solution at room temperature based on the method reported in literature (Brock *et al.*, 2002). Typically, an aqueous solution of tetrapropylammonium bromide (TPABr) (15.5 mol) was added drop-wise with stirring to an aqueous solution of potassium permanganate ($KMnO_4$) (13.9 mol). The resulting purple precipitate of $TPAMnO_4$ was filtered and dried at room temperature. A measured amount of $TPAMnO_4$ salt was then added to a mixture of distilled water and 2-butanol (1:1 v/v), and stirred continuously for 2 hours. A dark-red-brown colloidal suspension of tetrapropylammonium manganese oxide (TPA-MO) was formed as the lower aqueous layer. The concentration of the TPA-MO colloidal suspensions was determined quantitatively by an Atomic Absorption Spectrophotometer (AAS).

Preparation of TPA-MO Xerogels and Thin-Films

TPA-MO xerogels were prepared by evaporating a measured volume of colloidal suspension at room temperature followed by heating in an oven at 105 °C until a constant weight had been achieved. TPA-MO thin films were deposited directly onto thoroughly cleaned stainless steel plates by depositing TPA-MO nanoparticles in the form of stable colloidal suspension using the ElectroPhoretic Deposition (EPD) technique. The deposition of TPA-MO thin films was conducted at room temperature by applying a constant positive direct current (DC) potential of +3 V, and an initial current density of 10 mA/cm^2. In order to enhance film adherence to the supporting substrate, film uniformity and to minimize film cracking on the stainless steel surface, an ethanolic solution containing about 0.5 g/L each of polyvinyl butyral (PVB) and phosphate ester (PE) which served as a binder and dispersant, respectively, was mixed with a measured volume of the TPA-MO colloidal suspension. The rate of deposition and relative film thickness were controlled by the initial current density and the deposition duration which was varied between 1 to 5 minutes. All deposited films were air-dried at room temperature and then calcined at various temperatures up to 400 °C in air for 1 hour.

Characterization of Xerogels and Thin Films

The specific surface area and cumulative pore volume of TPA-MO xerogels were determined based on the nitrogen gas adsorption-desorption method at 77 K using the Brunauer-Emmett-Teller (BET) analyzer (Sorptomatic 1990). The surface morphologies of both TPA-MO xerogels and thin films that had been heat treated at various temperatures were characterized using a Scanning Electron Microscope (SEM) (LEO Model 1525). The mass loading of TPA-MO thin films was determined quantitatively using an Atomic Absorption Spectrophotometer (AAS) by dissolving these films in a H_2O_2/HNO_3 mixture. Using the measured concentration of Mn, the mass loading of TPA-MO per unit area of electrode was calculated based on the stoichiometric MnO_2 formula weight of 86.94 g/mol.

Electrochemical Characterization of Thin Films

The electrochemical properties of TPA-MO thin films were characterized by Cyclic Voltammetry (CV) based on a standard three-electrode cell configuration. A saturated calomel electrode (SCE) fitted with a Vycor bridge, and a platinum foil (~2 cm^2) were used as the reference electrode and the counter electrode, respectively. In all cyclic voltammetric experiments, a geometric area of 0.1257 cm^2 of each thin-film sample was being exposed to 1.0 M Na_2SO_4 aqueous electrolyte. Cyclic voltammograms were generated by scanning within the potential range of 0.0 V – 1.0 V (vs. SCE) at a scan rate of 50 mV/s.

RESULTS AND DISCUSSION

Nitrogen Adsorption-Desorption (BET) Analysis

Table 1 shows the specific surface area and cumulative pore volume of TPA-MO xerogels calcined at various calcination temperatures between 100 °C and 400 °C. Both the specific surface area and cumulative pore volume were observed to increase substantially as the calcination temperature was increased from 100 to 300 °C, but decreased thereafter as the calcination temperature was increased to 400 °C. The specific surface area and cumulative pore volume of xerogel samples reached a maximum of 36 m^2/g and 0.29 cm^3/g, respectively at 300 °C, but decreased to 20 m^2/g and 0.22 cm^3/g, respectively at 400 °C. The substantial increase in the specific surface area and total pore volume of xerogels calcined at temperatures between 100 °C and 300 °C could be

attributed to the removal of both physisorbed and chemisorbed water molecules, the residual solvent molecules (2-butanol), and the combustion of organic templates, all of which would lead to the formation of micro- or mesopores within the xerogels. The removal of structural water content and organic templates from TPA-MO xerogels upon calcination had been confirmed by thermal analysis in our previous studies (Chin *et al.*, 2002). At temperature beyond 300 °C, increased densification of xerogel samples was observed, due to the collapse of micro- and mesopores which therefore resulted in the observed decrease in the specific surface area and pore volume.

Table 1. Specific surface area and cumulative pore volume of TPA-MO xerogel samples calcined at different calcination temperatures

Calcination Temperature (°C)	Specific Surface Area (m^2/g)	Cumulative Pore Volume (cm^3/g)
25	3.59	0.0203
100	1.33	0.0367
200	21.37	0.1177
300	35.59	0.2904
400	20.00	0.2238

However, the specific surface area of the TPA-MO xerogels calcined at 300 °C was somewhat lower than those reported in earlier studies. Chin *et al.* reported that TPA-MO xerogels calcined at 300 °C showed a specific surface area of 53 m^2/g (Chin *et al.*, 2002). Xerogels and ambigels forms of MnO_2 were reported to have specific surface areas of 63 m^2/g and 72 m^2/g, respectively (Reddy & Reddy, 2003). The comparatively lower specific surface areas of TPA-MO xerogel samples obtained in this study could be attributed to differences in the synthesis conditions such as the gelation and sintering conditions used. In this study, the gelation of TPA-MO colloidal suspensions was hastened by mild heating, and the calcination of xerogels was performed using a conventional furnace without any preprogrammed heating regime.

Scanning Electron Microscopy (SEM)

Figure 1 shows SEM micrographs of TPA-MO thin films on supporting stainless steel plates that had been heat treated at various temperatures in air for 1 hour. These films were observed to be nanoparticulate and porous in nature, with average particle sizes ranging from 10 to 30 nm in diameter. The porous nature of these films could be attributed to the aggregation of primary particles and the subsequent formation of larger agglomerates upon evaporation of the solvent. TPA-MO films calcined at 200 °C were observed to consist of densely packed nanoparticulate clusters probably due to the presence of residual water and organic template molecules which occupied the interlayer spaces and pores. This was further supported by the observed negligibly low cumulative pore volume.

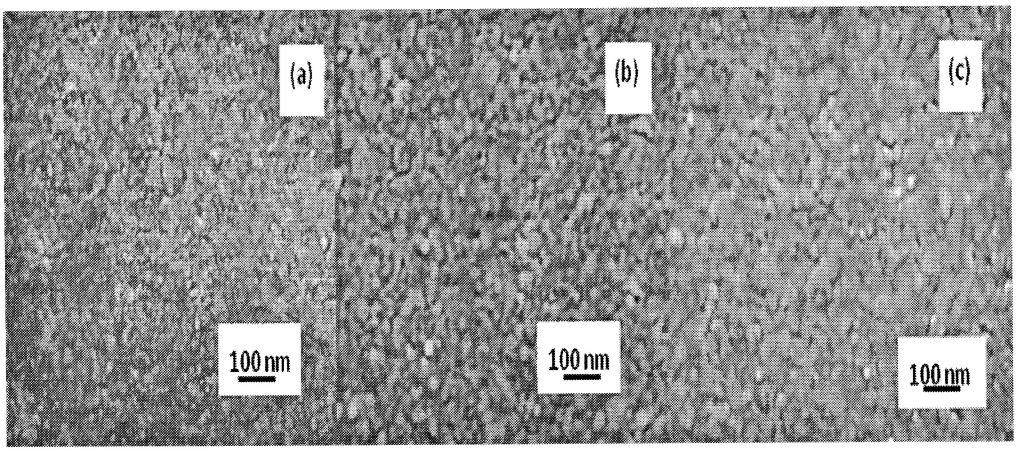

Figure 1. *SEM micrographs of TPA-MO thin films deposited on stainless steel plates and calcined at different temperatures in air for 1 hour (a) 200 °C, (b) 300 °C and (c) 400 °C*

However, films calcined at 300 °C showed the presence of void spaces among loosely packed nanoparticulate clusters as a consequence of the complete removal of structural water andorganic template molecules. This observation is consistent with our previous thermal analysis on the TPA-MO samples (Chin *et al.*, 2002). TPA-MO films calcined at 400 °C had achieved higher degree of densification as evidenced by the coarser grain sizes, and smoother and denser surface morphologies. Incidences of cracking were also observed due to shrinkage of films upon heat treatment. According to Hu *et al.* microstructural changes upon heat treatment were attributed to the reconstruction of MnO_x which occurred significantly at ≥ 350 °C (Hu *et al.*, 1999).

The microstructural morphologies of TPA-MO films with different relative films thicknesses deposited at various EPD deposition durations were shown in Figure 2. For thinner films prepared with shorter deposition durations of 1 to 3 minutes (Figure 2(a) and (b)), void spaces or pores were clearly visible among loosely packed nanoparticulate clusters. However, thicker film deposited at longer deposition duration of 5 minutes was observed to be comparatively denser and more compact without any observable cracks.

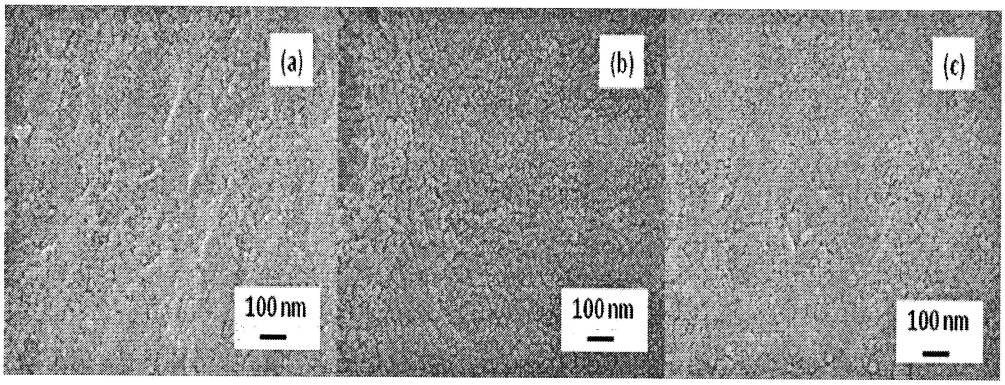

Figure 2. *SEM micrographs of TPA-MO thin films deposited on stainless steel plates at deposition duration of: (a) 1 minute, (b) 3 minutes, and (c) 5 minutes*

Effect of Calcination Temperature

Figure 3 shows the cyclic voltammograms (CV) of TPA-MO thin films that have been heat treated at different temperatures of between 100 °C and 400 °C in air for 1 hour. All CVs were observed to be mostly featureless and rectangular in shape within the potential window of 0.0 V – 1.0 V (vs. SCE) at a scan rate of 50 mV/s. The CV curve of TPA-MO film calcined at 300 °C showed almost perfect rectangular shape over the potential range of 0.0 V to 1.0 V, indicating that it exhibited excellent capacitive behaviour and cycling reversibility. Both the anodic and cathodic currents were observed to increase with higher calcination temperature between 100 °C and 300 °C, but decreased substantially at the calcination temperature of 400 °C.

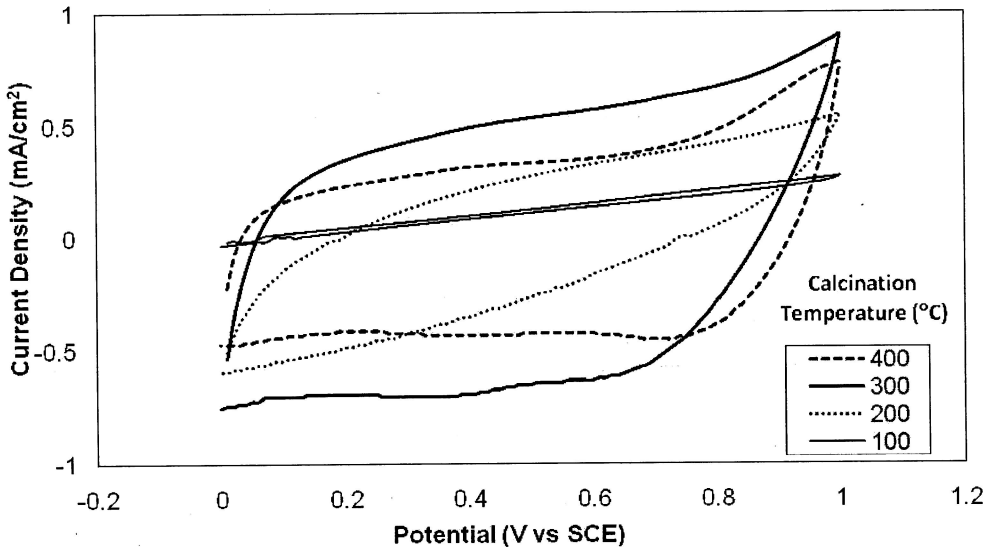

Figure 3. *Cyclic Voltammograms (CV) of TPA-MO films at different calcination temperatures (°C)*

The charge capacity of TPA-MO films was calculated by integrating the anodic charges within the scan range based on equation (1):

$$Q\ (mC/cm^2) = \int I\,dt = \int I.dV/(dV/dt) = \int {}^{1}{}_{0}\ (I/SR)\,dV \qquad (1)$$

where I is the instantaneous anodic current in ampere and dV/dt is the scan rate. If one expresses current as current density based on the geometric electrode area, then charge capacity, Q, would be expressed in units of farads per unit area (F/cm^2). For nanoparticulate electrode materials, the specific capacitance which has units of farads per unit mass of electroactive material (F/g) is more commonly being reported (Pang *et al.*, 2000). The specific capacitance (C) for TPA-MO films with different MnO_2 mass loadings can be calculated based on equation (2):

$$C = I / m \cdot R \qquad (2)$$

where I is the average current in amperes, m is the mass loading of MnO_2, and R is the scanning rate. A maximum charge capacity of 142 mF/cm^2 was obtained for TPA-MO thin films that have been calcined at 300 °C whereas those of films calcined at 200 °C and at

400 °C were substantially lower at 47.6 mF/cm^2 and 60.6 mF/cm^2 respectively (Figure 4(a)). Similar trend was observed for the specific capacitance of the TPA-MO films with the maximum value achieved at the calcination temperature of 300 °C, but considerably lower at the calcination temperature of 400 °C.

The quantity of chemically bound water within the TPA-MO films could have played a major role in the observed variations of the charge capacity. The water content in manganese oxides was known to affect the electrochemical reactivity and thermodynamic stability of various MnO_2 phases due to the variation of crystal lattice, and consequently of electrical conductivity and electrode potential (Desai *et al.*, 1985; Era *et al.*, 1967). The effect of structural water content on the specific capacitance of oxide materials have been reported (Gamby, 2001). The presence of structural water content was considered to be essential for the transportation of active ionic species by promoting proton diffusivity in manganese oxide. However, its resistivity increased with increasing water content. Thermal treatment of TPA-MO films at 300 °C in air for 1 hour could have the effect of lowering their structural water content retained within the oxide lattice as has been shown by thermal analysis in our previous studies (Chin *et al.*, 2002).

The associated lower activation energy of electrical conductance would therefore lead to higher electronic conductivity of calcined TPA-MO films. Besides, the thermal treatment of TPA-MO xerogels at 300 °C in air for 1 hour could have the effect of increased densification, grain size and electronic conductivity of these films. The specific conductivity of different types of γ-MnO_2 formed under different conditions and thermal treatments had been reported to increase exponentially with decreased in their water contents and the associated lower activation energy of electrical conductance (Ruetschi & Giovanoli, 1998). As shown in Table 1, the specific surface area and pore volume were the highest for TPA-MO xerogel samples calcined at 300 °C. Higher surface area and pore volume would allow more electrolyte ions to penetrate deeply into the oxide matrix. A combination of these factors could have contributed collectively to the substantial higher charge capacity of films calcined at 300 °C.

The cycling reversibility of the TPA-MO thin films was evaluated by determining the respective anodic and cathodic charge ratios (Q_a/Q_c). TPA-MO thin films that have been heat treated at 300 °C, exhibited high reversibility as evidenced by the anodic and cathodic charge ratio (Q_a/Q_c) approximately equaled to 1(Figure 4(b)).

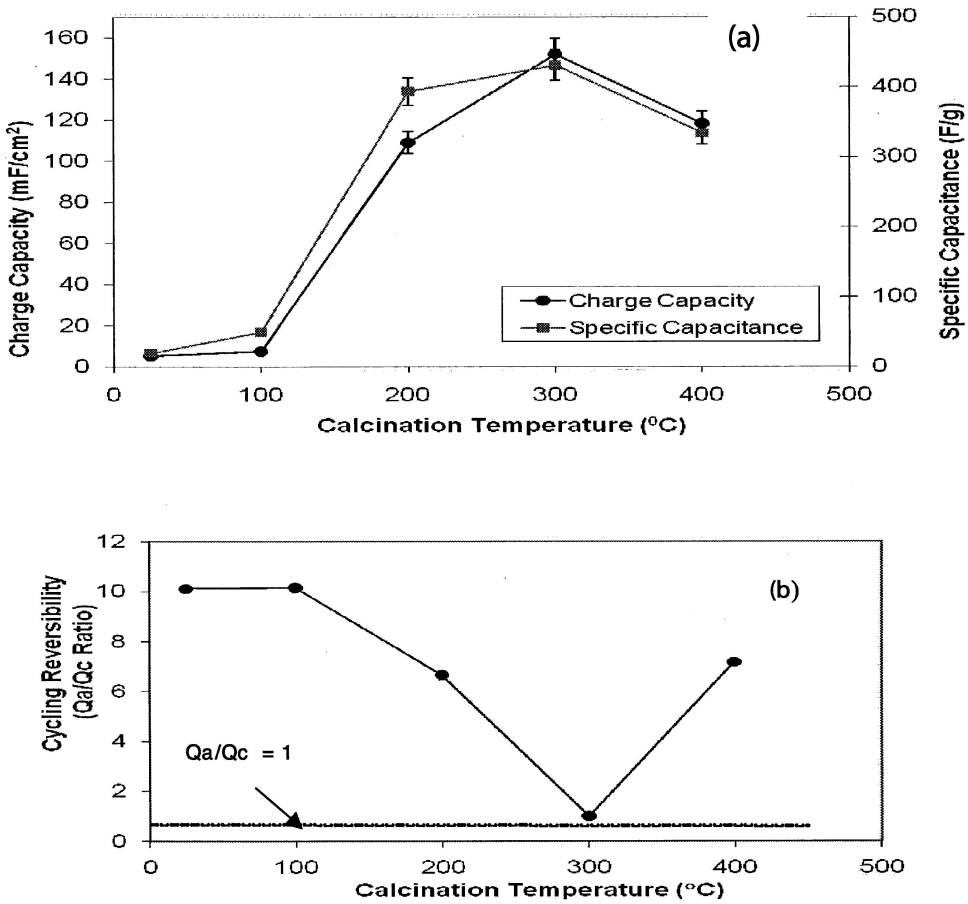

Figure 4. *Effect of calcination temperature on (a) the charge capacity and specific capacitance, and (b) the cycling reversibility (Qa/Qc Ratio) of TPA-MO films*

Effect of Relative Film Thickness and MnO_2 Mass Loading

The electrophoretic deposition of TPA-MO films on stainless steel substrates were observed to depend on both the deposition duration and applied current density. In this study, the deposition duration at constant applied current density provided a good measure of the relative thickness of TPA-MO films deposited on stainless steel foils. The deposition duration was being varied between 1 and 5 minutes, whereas the applied current density was being fixed at 10 mA/cm². Figure 5 shows the cyclic voltammograms (CV) of TPA-MO films being

deposited at different deposition durations. The CV curve of TPA-MO film deposited for 3 minutes was almost rectangular in shape. However, CV curves for films deposited at deposition duration lower or higher than 3 minutes (i.e. 1, 2, 4 and 5 minutes) showed somewhat distorted rectangular shapes. Such distorted CV curves of larger anodic areas could be attributed to inherent irreversible cycling behaviors of ultra-thin and exceedingly thick films.

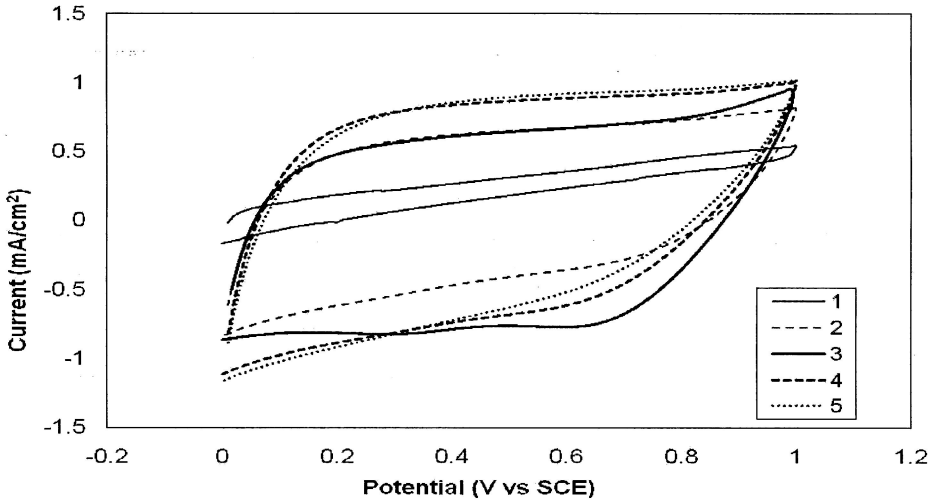

***Figure 5**. Cyclic Voltammograms of TPA-MO films of different relative film thickness deposited with various deposition durations*

Figure 6 shows the effect of deposition duration on both the MnO_2 mass loading and charge capacity of TPA-MO films calcined at 300 °C in air. The charge capacity of deposited films was observed to increase more rapidly initially, but the rate of increase abruptly declined at longer deposition durations of more than 2 minutes. This could be partly attributed to the higher resistance of thicker films being deposited at longer deposition durations. Any increase in the film thickness being deposited on the stainless steel substrate during the EPD process should, in turn, be accompanied by a corresponding increase in the MnO_2 mass loading of TPA-MO films. As shown in Figure 6, the MnO_2 mass loadings at various deposition durations between 1 and 5 minutes were observed to increase continuously albeit non-linearly with increased deposition duration. The highest MnO_2 mass loading of 0.18 mg/cm^2 was achieved for TPA-MO films deposited at deposition duration of 5 minutes, which could represent the maximum film thickness achievable under the specific deposition conditions. As such, insignificant increase in the MnO_2 mass loading of film would be anticipated at deposition duration of exceeding 5 minutes.

The relative film thickness and associated MnO_2 mass loading of TPA-MO films was observed to have significant effect on both their charge capacities and cycling reversibility (Q_a/Q_c ratio). While the charge capacity was observed to increase with increased MnO_2 mass loading and associated film thickness, the cycling reversibility was observed to be lower for both thinner and thicker films. TPA-MO films deposited at deposition duration of 3 minutes exhibited excellent cycling reversibility as evidenced by the anodic and cathodic ratios (Q_a/Q_c) of ~1.00 (Inset, Figure 6).

All these results therefore demonstrated that optimized TPA-MO films should show high capacitive behavior and excellent cycling reversibility at a scan rate of 50 mV/s. The observed decrease in the reversibility of thinner films could be attributed to low uniformity in their thicknesses. On the other hand, thicker films possess higher resistivity and substantially reduced accessibility of active sites within the oxide matrix towards electrolyte ions during charge discharge cycling. Henceforth, films that exhibited CV curves of almost rectangular in shape and high cycling reversibility was deemed to possess optimum film thickness and MnO_2 mass loading. TPA-MO films with enhanced electrochemical properties such as charge capacity, cycling reversibility and stability could therefore be prepared by optimizing the electrophoretic deposition conditions.

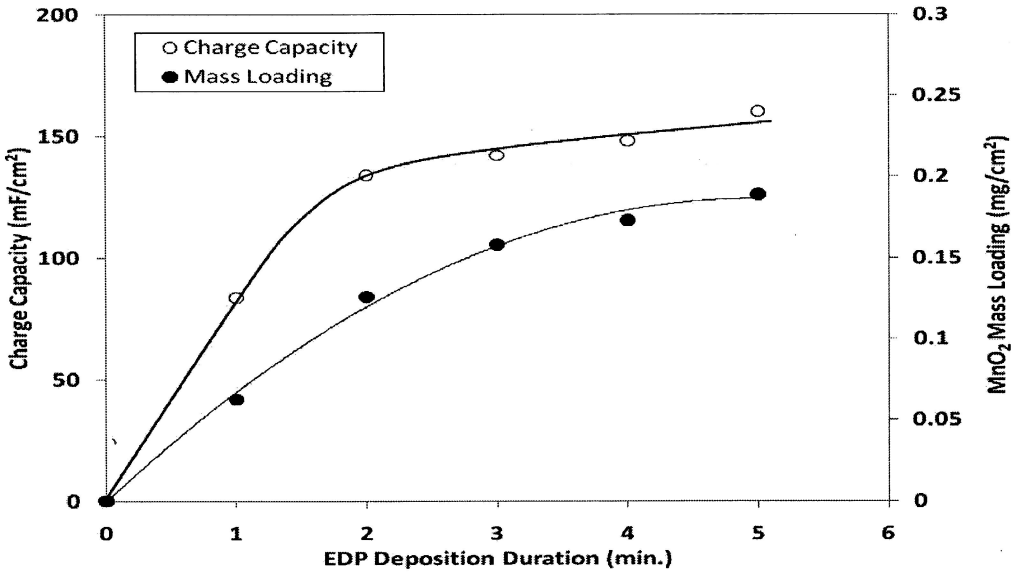

Figure 6. *Effect of deposition duration on the MnO_2 mass loading and the charge capacity of TPA-MO films calcined at 300 °C. Inset: The cycling reversibility (Q_a/Q_c ratio) of TPA-MO film as a function of deposition duration*

Figure 7 shows the contrasting effects of MnO_2 mass loadings on the charge capacity (mF/cm^2) and specific capacitance (F/g) of TPA-MO films. Generally, the charge capacity increased linearly with MnO_2 mass loading, whereas the specific capacitance decreased almost exponentially with increasing MnO_2 mass loading. As shown in Figure 7, the charge capacity was observed to increase linearly from 83.6 to160 mF/cm^2 as the MnO_2 mass loading was increased from 5.00×10^{-3} to 0.42 mg/cm^2. On the contrary, the specific capacitance of TPA-MO films was observed to decrease almost exponentially with increasing MnO_2 mass loadings to about 400 F/g at high MnO_2 mass loadings. The highest specific capacitance value of 967 F/g was obtained for ultra-thin film with MnO_2 mass loading of about 0.115 mg/cm^2. The specific capacitance was observed to decrease from 967 F/g to 412 F/g (-57 %) as the MnO_2 mass loading was increased from 0.115 to 0.416 mg/cm^2 (+262 %). Such rapid decrease in the specific capacitance with higher MnO_2 loadings and film thickness could be attributed to reduced porosity and specific surface area of thicker films. As a consequence, the accessibility of active sites within the bulk electrode material towards electrolyte ions would be substantially reduced (Lee *et al.*, 2001). The combined effect of higher resistivity and reduced porosity of thicker films could have led to the substantial reduction of their specific capacitances.

On the contrary, exceptionally high specific capacitance values (>1,000 F/g) were observed for ultra-thin films which could be in part due to the high uncertainty in the determination of its mass loadings. A very low mass value would, in turn, erroneously magnified the value of specific capacitance substantially. Ultra-thin films of porous microstructure should possess high specific surface area and provide easy access of active sites for electrolyte ions during the charging and discharging cycles. As such, the observed high specific capacitance of ultra-thin films could be attributed to the high utilization efficiency of electroactive materials. Besides, thinner films should provide shorter diffusion path-length with enhanced kinetics of proton diffusion into and out of bulk electrode materials (Lee *et al.*, 2001). As shown in Figure 7, the cross-over point between plots of the charge capacity and specific capacitance should represent the optimal level of MnO_2 mass loading and associated film thickness of TPA-MO films which would in turn exhibit both moderately high charge capacity and specific capacitance. For instance, a film of about 0.18 mg/cm^2 MnO_2 mass loading would exhibit a charge capacity of 110 mF/cm^2, which corresponded to a specific capacitance of about 700 F/g. Under the specified deposition conditions, films with 0.18 mg/cm^2 of MnO_2 loading required a deposition duration of about 3 minutes. Obviously, the high divergence between plots of the charge capacity and specific capacitance for thicker films with high MnO_2 mass loadings indicating that there is ample scope for further enhancing the electrochemical properties through microstructural optimization of these TPA-MO films.

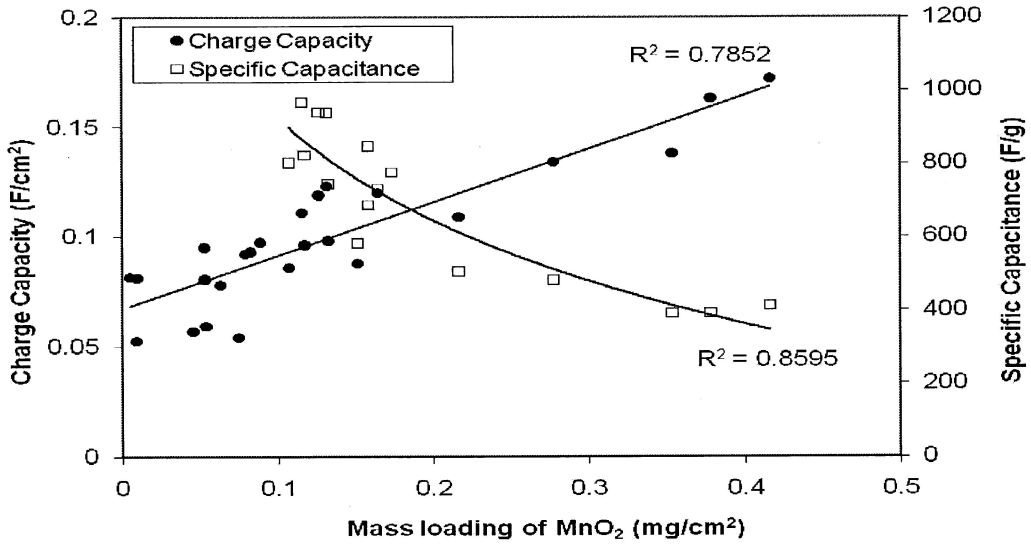

Figure 7. *Effect of MnO_2 mass loading on the charge capacity and specific capatance of TPA-MO films*

Effect of Long-Term Cycling

The effect of long-term cycling on the charge capacity of TPA-MO thin films of various relative film thicknesses in 1.0 M Na_2SO_4 aqueous solution are shown in Figure 8. The charge capacities of thicker films, in particular, were observed to decline more rapidly for the initial 200 cycles, but very gradual decline was observed thereafter within the span of 1,500 cycles. All films of various thicknesses showed varying degree of changes in their CV shapes and decrease in their CV areas after 1,600 cycles. Films that had been cycled for more than 500 cycles showed CVs of slightly distorted rectangular shape which could be attributed to a combination of factors such as chemical degradation, microstructural changes, or partial film dissolution into the electrolyte.

Generally, thinner films appeared to be comparatively more reversible and stable towards long-term cycling than thicker films. The overall decrease in charge capacities after 1,600 cycles for thinner films and thicker films were about 26 % and 46 %, respectively. Thicker films showed rather high capacity loss during the initial 200 cycles which accounted for more than 15 % of the total charge capacity loss upon cycling for 1,600 cycles. As reported by Pang *et al.*, the observed charge capacity fading upon cycling could be attributed mainly to loss of electroactive material through partial dissolution of films into the electrolyte, rather than structural or chemical degradation of the films (Pang & Anderson, 2000). Dissolution of MnO_2

during discharge in neutral electrolyte could occur by both the disproportionation reaction and solid phase diffusion. The slow dissolution of TPA-MO films into the aqueous electrolyte due to the disproportionation reaction of Mn^{3+} into Mn^{4+} and soluble Mn^{2+} could have resulted in the capacity fading observed. However, it is speculated that other factors may also be involved, especially changes in the electronic conductivity of the films during cycling which was associated with changes in the oxidation states and structural water content.

This capacity fading problem needs to be addressed critically by investigating factors such as the type and nature of electrolytes, film thickness, composition and microstructure of TPA-MO films. It is noteworthy that even though thicker film possesses higher capacity, excessively thick film could be detrimental to its cycle life as evidenced by the higher net loss in the charge capacity (%Q loss) due to its higher rate of dissolution during charge and discharge cycling.

Optimization of film thickness, mass loading, and microstructure of electroactive materials is therefore necessary in order to enhance the electrochemical performances and cycle life of electrochemical capacitor devices. Although the electrophoretic deposition technique have been successfully employed for the deposition of TPA-MO films on stainless steel plates, a better understanding of the deposition mechanisms and kinetics is essential for optimizing the deposition parameters such as the applied current density, voltage and deposition duration, as well as the composition, concentration and rheology of the colloidal suspensions in order to obtain thin films of high uniformity and tailored microstructure.

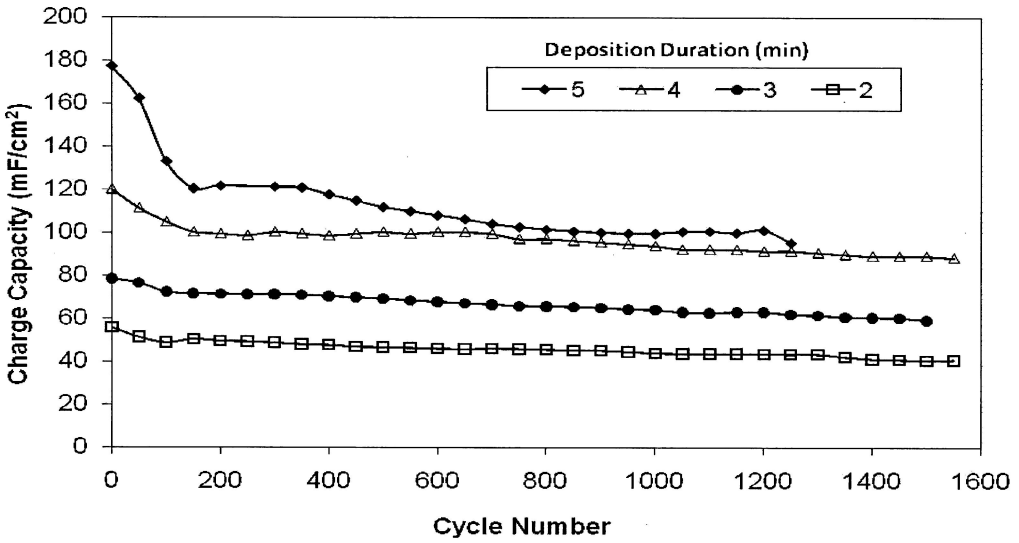

Figure 8. *Effect of long-term cycling on the charge capacity of TPA-MO films of various relative thicknesses*

Figure 9 shows the effect of long term cycling on the charge capacity of optimized TPA-MO thin films in 1.0 M Na_2SO_4 solution at 50 mV/s scan rate for 1,600 cycles. The charge capacity was observed to fade more rapidly for the initial 200 cycles, but such decline was very gradual thereafter. The overall net loss in the charge capacity was determined to be less than 30 % for optimized TPA-MO films upon cycling for 1,600 cycles. All optimized TPA-MO films were observed to exhibit good cycling reversibility throughout the duration of cycling as indicated by the Q_a/Q_c ratios being very close to 1.00.

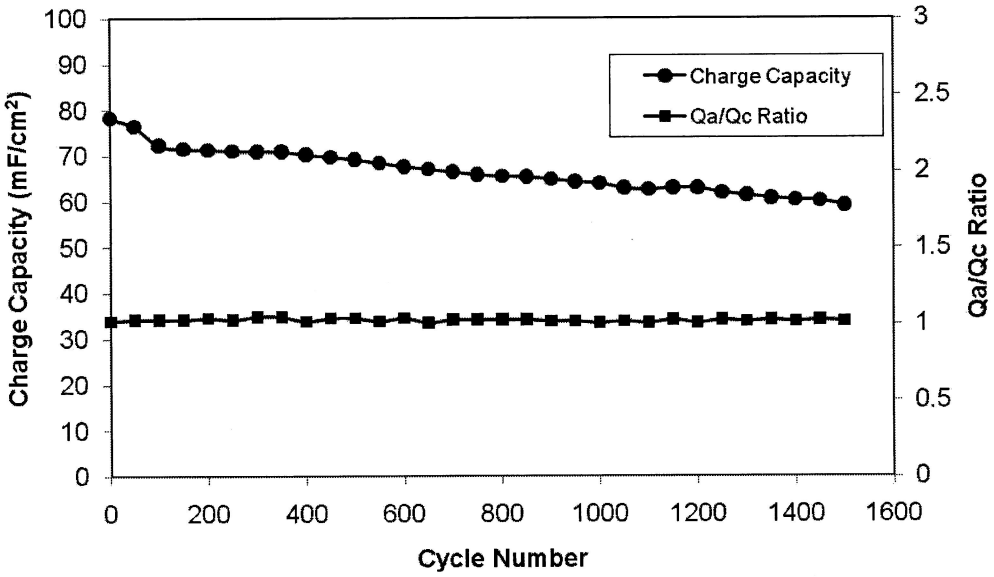

Figure 9. *Effect of long-term cycling on the charge capacity and cycling reversibility of optimized TPA-MO thin films*

CONCLUSION

We have demonstrated that optimized TPA-MO thin films on stainless steel plates prepared by the electrophoretic deposition technique exhibit high charge capacity, excellent cycling reversibility and stability in a mild aqueous electrolyte. Coupled with their low cost and environmental friendliness, these thin films offer greater advantages over other transition metal oxides as novel electrode materials for the fabrication of electrochemical capacitors. However, the wide divergence between the charge capacity and specific capacitance values at various film thicknesses indicates that there is ample scope for further optimization of TPA-MO films and enhancing their electrochemical performances.

ACKNOWLEDGEMENT

The authors acknowledge the financial support rendered by the Malaysian Ministry of Science Technology and Innovation (MOSTI) through the IRPA Grant No. 03-02-09-1019 EA001.

REFERENCE

Brock, S.L., Sanabria, M., and Suib, S. L. (1999). Particle size control and self-assembly processes in novel colloids of nanocrystalline manganese oxide. *J. Phys. Chem.* **103**: pp 7416.

Broughton, J. N. and Brett, M. J. (2004). Electrochemical capacitance in manganese thin films with chevron microstructure. *Electrochim.* Acta. **49(25)**: pp 4439.

Chin, SF., Pang, S.C. and Anderson, M.A. (2002). Material and electrochemical characterization of tetrapropylammonium manganese oxide thin film as novel electrode materials for electrochemical capacitors. *J. Electrochem. Soc.* **149(4)**: pp A379.

Desai, B. D., Fernandes, J. B. and Kamat Dalal, V. N. (1985). Manganese dioxide — a review of a battery chemical Part II. Solid state and electrochemical properties of manganese dioxides. *J. Power Sources.* **16**: pp 1.

Era, A., Takehara Z. and Yoshizawa,S. (1967). Discharge mechanism of the manganese dioxide electrode. *Electrochim. Acta.* **12**: pp 1199.

Fabio, D., Giorgi, A., Mastragostino, M and Soavi, F. (2001). Carbon poly(3-methylthiophene) hybrid supercapacitos. *J. Electrochem. Soc.* **148(8)**: pp A845.

Gamby, J., Taberna, P.L, Simon, P., Fauvarque, J.F., Chesneau, M. (2001). Studies and characteri isations of various activated carbons used for carbon/carbon supercapacitors. *J. Power Sources.* **101**: pp109.

Ghaemi, M. and Binder, L. (2002). Effects of direct and pulse current on electrodeposition of manganese dioxide, *J. Power Sources.* **111**: pp248.

Hu, C. C and Tsou, T. W. (2003). The optimization of specific capacitance of amorphous manganese oxide for electrochemical supercapacitors using experimental strategies. *J. Power Sources.* **115**: pp 179.

Hu, C. C. and Huang, Y. H. (1999). Cyclic voltammetric deposition of hydrous ruthenium oxide for electrochemical capacitors. *J. Electrochem. Soc.* **146**: pp 2465.

Jang, J. H., Han, S. Hyeoun, T. and Oh, S. M. (2003). Electrochemically capacitor performance of hydrous ruthenium oxide / mesoporous carbon composite electrodes. *J. Power Sources.* **123**: pp 79.

Jiang, J. H. and Kucernak, A. (2002). Electrochemical supercapacitor material based on manganese oxide: preparation and characterization. *Electrochim. Acta.* **47**: pp 2381.

Kótz, R and Carlen, M. (2000). Principles and applications on electrochemical capacitors. *Electrochim. Acta.* **45**: pp 2483.

Lee, H. Y., Kim, S. W. and Lee, H. Y. (2001). Expansion of active site area and improvement of kinetic reversibility in electrochemical pseudocapacitor electrode. *Electrochem. Solid-State Lett.* **4**: pp A19.

Pang, S. C., Anderson M. A. and Chapman, T. W. (2000). Novel electrode materials for thin-film ultracapacitors: Comparison of electrochemical properties of sol-gel derived and electrodeposited manganese dioxide. *J. Electrochem. Soc.***147(2)**: pp 444.

Pang, S. C. and Anderson, M.A. (2000). Novel electrode materials for electrochemical capacitors: Part II. Material characterization of sol-gel derived and electrodeposited manganese dioxide thin films. *J. Mater. Res.* **15**: pp 2096.

Park, B. O., Lokhonde, C.O., Park, H.S., Jung, K.D. and Joo, O.S. (2004). Performance of supercapacitor with electrodeposited ruthenium oxide film electrodes—effect of film thickness. *J. Power Sources.* **134 :** pp 148.

Reddy, R. N. and Reddy, R. G. (2003). Sol-gel MnO_2 as an electrode material for electrochemical capacitors. *J. Power Sources.* **124**: pp 330.

Ruetschi, P and Giovanoli, R. (1998). Cation vacancies in MnO_2 and their influence on electrochemical reactivity. *J. Electrochem. Soc.* **135**: pp 2663.

Zheng, J. P. (1999). Ruthenium oxide-carbon composite electrodes for electrochemical capacitors. *Electrochem. Solid-State Lett.* **2**: pp 359.

Zhitomirsky, I. (2002). Cathodic electrodeposition of ceramic and organoceramic materials. Fundamental aspects. *Adv. in Colloids and Interface Sc.* **97**: pp 279.

Journal of Industrial Technology Vol. 19(1), 2010 - ICONT 2009, 167 - 178

GENE TRANSFER INTO MOUSE AIRWAYS USING POLYCATION BASED NANOPARTICLE GENE DELIVERY SYSTEM

Wai Yeng Wendy-Yeo [1,2], Sabariah Abdul Rahman [1], Rozita Rosli [1,2] and Syahril Abdullah [1,2*]

[1] UPM-MAKNA Cancer Research Laboratory
Institute of Bioscience, Universiti Putra Malaysia
43400 UPM Serdang, Selangor, Malaysia.

[2] Medical Genetics Laboratory
Faculty of Medicine and Health Sciences, Universiti Putra Malaysia
43400 UPM Serdang, Selangor, Malaysia.

***(syahril@medic.upm.edu.my)**

ABSTRACT : The emergence of gene therapy has attracted attention in the recent years as this technology enables a myriad of diseases to be treated at the root of the cause. The generation of a non-viral gene delivery vector with high transfection efficiency is highly required for this treatment strategy to be successful. Dextran-spermine (D-SPM) is a biodegradable polycation capable of complexing with plasmid DNA (pDNA). Yet, no study has been performed on its transfection efficiency in the lung via intranasal delivery technique. In this study, first, we showed that the *in vitro* transfection efficiency for D-SPM is higher than its PEGylated form. Next, we determined the optimal conditions for reporter gene expression in the lungs of mice via instillation delivery of the D-SPM/pDNA complex. Three conditions tested were: (i) different weight-mixing ratios of the complex, (ii) amount of pDNA in the complex and (iii) its expression time-point profile. The size of the D-SPM/pDNA complex was also evaluated. Results showed that the maximum reporter gene expression level in the mouse lungs was observed at weight-mixing ratio of 16, with 13.5 μg of pDNA and at day 1 post-treatment. The size measurement of the complexes was evaluated at different DNA concentrations with weight-mixing ratio kept at the ratio that gave the highest reporter gene activity. The results show that the sizes of the complexes were in a nanometer range and were directly proportional to the amount of pDNA. In conclusion, this study has shown that the D-SPM/pDNA is a polymeric nanoparticle able to transfect mouse lungs, albeit at moderate efficiency.

KEYWORDS : Gene delivery, lung instillation, non-viral vector, nanoparticle, gene therapy

INTRODUCTION

The promise of gene therapy to cure human genetic diseases at the root of their cause, that is, at the level of defective genes, has drawn much attention. Earlier studies have shown that the primary challenges for successful gene therapy application in the lung are the gene transfer efficiency and the safety of the gene delivery vector used. Therefore, major efforts have been directed to develop a safe and effective vector, which is capable of delivering therapeutic gene into target cells effectively and safely, for functional repairing, genetic modification and therapeutic level of gene expression.

A number of DNA delivery vector systems have been developed to improve the efficiency of gene transfection into target cells. The two main gene vector systems are classified into viral and non-viral vectors. The viral vectors have received a remarkable attention for its high transfection efficiency, persistent gene expression and its ability to transduce many cell types (El-Aneed, 2004; Lundstrom & Boulikas, 2003; Robbins & Ghivizzani, 1998). To date, about two thirds of the clinical trials for gene therapy are employing viral vectors (Edelstein *et al.*, 2007). However, viral vectors face serious drawback from the safety aspect, as they pose immunogenicity and toxicity risks or even the likeliness of mutagenesis in the transduced cells (Kushibiki & Tabata, 2004).

On the contrary, the non-viral vectors are much safer and can be easily modified (Jo & Tabata, 2008; Li & Huang, 2007). One of the prospective non-viral vectors for efficient and safe gene delivery is the polycationic dextran-spermine (D-SPM). Based on the study by Hosseinkhani *et al.*, 2004), dextran-spermine is a polycationic polysaccharide capable of transfecting cell lines and tissues *in vivo* via intramuscular and intravenous routes in mice. Eliyahu *et al.*, (2006), corroborated the findings by showing that the same polycation was efficient at delivering reporter gene to mice, via a combination of intramuscular and intranasal administrations.

However, to date, no study has been performed to determine the efficacy of this polycation to deliver gene exclusively to the lung, via intranasal delivery. Therefore, this study seeks to address whether dextran-spermine is capable to efficiently transfer gene to the lung of mouse, in the prospect of developing a potential nanoparticle vector for lung disease gene therapy in the near future.

MATERIALS AND METHODS

Preparation of plasmid DNAs

Plasmid pCIKLux expressing luciferase reporter gene was generously provided by the Gene Medicine Research Group, Oxford University, UK. The pCIKLux was replicated in the high-copy AG 1 competent cells (Stratagene, USA). The plasmids were cloned and purified into larger quantity by using S.N.A.P.™ Midiprep Kit (Invitrogen, USA). Following the plasmid DNA (pDNA) extraction, the purified plasmids were verified based on their size by restriction enzyme analysis in 1% agarose gel electrophoresis.

Endotoxin-free Mega-Preparation of pDNA

QIAGEN EndoFree® Plasmid Mega kit (Qiagen, Germany) was used for preparing a large-scale plasmid for the purpose of animal studies. As stated by the manufacturer, EndoFree Mega Kit would produce less than 0.1 Endotoxin Unit (EU)/μg pDNA. The elimination of the endotoxin from the lipopolysaccharides of *E.coli* post pDNA extraction will ensure that the pDNA for *in vivo* use will not elicit toxic response in animal.

D-SPM/pDNA and PEGylated D-SPM/pDNA Complex Preparation

For the cell culture study, dextran-spermine (D-SPM) and pDNA complexes were prepared at various D-SPM/pDNA weight-mixing ratios of 4 to 14 (μg dextran-spermine/ μg pDNA) (w/w). The PEGylated dextran-spermine (PEGylated D-SPM) and pDNA complexes were also prepared at similar weight-mixing ratios as for the D-SPM/pDNA complexes. Increasing amount of D-SPM or PEGylated D-SPM solutions was added to 0.5 μg pDNA solution, each accounting for the increasing N/P weight ratio, in a microcentrifuge tube to obtain a final volume of 200 μl by topping up with Opti-MEM (Invitrogen, Carlsbad, CA, USA). The complexes were vortexed briefly and incubated at room temperature for 30 min prior to being used.

For the *in vivo* study, complexes of D-SPM and pDNA were prepared at various D-SPM/ pDNA weight-mixing ratios of 13 to 18 (μg D-SPM/ μg pDNA) (w/w). D-SPM solutions were added to 10 μg of pDNA solution to a final volume of 100 μl for dosing. The resulting solution was vortexed briefly and allowed to stand at room temperature for 30 min prior to use to allow spontaneous complex formation.

To determine the most optimal amount of pDNA in complex that would give the highest level of expression *in vivo*, varying amounts of pDNA (7.5 to 17.5 μg) were added to D-SPM with the w/w kept at a constant ratio. The resulting solution was vortexed briefly and allowed to stand at room temperature for 30 min prior to use.

Following the determination of the D-SPM/pDNA weight-mixing ratio and amount of pDNA in the complex that would give the highest level of expression *in vivo*, the mice were dosed with the complex at its optimal conditions and the reporter gene activities were measured over a period of 7 days post-treatment.

Cell Culture

For the *in vitro* assays, African green monkey kidney fibroblast (COS-7) cell line was used. The COS-7 cell lines were cultured in Dulbecco's Modified Eagle's Medium (DMEM) (Sigma-Aldrich, USA) supplemented with 10 % fetal bovine serum (Gibco BRL, UK), 4.5 g/L D-glucose, 1.0 mM sodium pyruvate and 1.5 g/L sodium bicarbonate (Sigma-Aldrich). The cells were kept at 37 °C in humidified 5 % CO_2 atmosphere.

Transfection of cells grown *in vitro*

Prior to the transfection experiment, COS-7 cells were seeded at a density of 5 x 10^4 cells/ well in a 24-well plate. The adherence cells were grown in 1 ml of DMEM/FBS at 37 °C for about 24 hr in order to reach 90 % confluency at the day of transfection. Each transfection experiment was done in triplicate. On the day of transfection, the cell growth medium was aspirated and replaced with a final volume of 200 μl D-SPM/pDNA complexes or PEGylated D-SPM/pDNA complexes in Opti-MEM medium at various weight-mixing ratios (4 to 14 w/w). After the incubation period, the cells were washed with PBS and lysed by using 1X reporter lysis buffer (RLB) (Promega, USA).

Experimental Mouse and Anaesthesia

Female BALB/c mice, age from 6 to 8 weeks were used in the experiment, with n=6 for each experimental group unless stated otherwise. Mice were maintained under conventional housing conditions. They were fed with standard chow and water *ad libitum* and were allowed to acclimatize for at least 7 days prior to procedures being performed. All animal experiments were carried out in accordance with the Guidelines for Animal Experiments of Universiti Putra Malaysia.

The mice were anaesthetized in a fume hood until a balanced state of anesthesia was achieved. After dosing, mice were allowed to recover in a warmed environment and monitored for any signs of illness. Mice were euthanized by neck-dislocation. The lung and trachea of the mice were harvested for reporter gene expression analysis.

Luciferase Assay

The Luciferase Assay System (Promega, USA) was used for luciferase reporter quantification in mammalian cell lines. A total volume 20 µl from each sample was used to measure luciferase activity using a luciferase assay kit (Promega, USA) on a GloMax™ 20/20 luminometer (Promega, USA).

The obtained relative light units (RLUs) from luciferase assay were normalized against protein concentration in the cells extracts, which was quantified using a Bio-Rad DC Protein Assay (Bio-Rad Laboratories, CA, USA) based on colorimetric assay.

Size Determination of D-SPM/pDNA Complex

The size of D-SPM/pDNA complexes formed at various mass ratios was determined by using a particle size analyzer (Nanophox, Sympatec, Germany). D-SPM/pDNA complexes were prepared by using the same amount of D-SPM with varying amount of pDNA. All samples were dispersed in nuclease-free water and three measurements were taken for each sample to be certain that there was no clump that could affect the reading.

Statistical Analysis

Distribution free, non-parametric Mann-Whitney U test was used to compare two unpaired groups of variable, whereas ANOVA parametric test was applied to multiple group comparison. Data were presented as value ± SEM and considered to be statistically significant if p values were < 0.05. Analyses were performed using SPSS for Windows, Version 15.0.

RESULTS AND DISCUSSION

In Vitro Transfection Efficiencies of D-SPM/pDNA and PEGylated D-SPM/pDNA with Different Weight-Mixing Ratios

Several studies have shown that better stability and higher transfection efficiencies were achieved when the positive charge of the polycation is concealed by hydrophilic polymers, such as polyethylene glycol (PEG) (Guosen *et al.*, 2008; Lee & Kim, 2005; Sung *et al.*, 2003). In this study, we evaluated the transfection efficiency of dextran-spermine-based polycation conjugates and its PEGylated form in COS-7 cell line. The cells were transfected with 0.5 µg of pDNA complexed with different amount of D-SPM or PEGylated D-SPM.

For the D-SPM/pDNA complexes, reporter gene activity was negligible at weight ratio of 4 to 10 (Figure 1). Maximum level of expression of D-SPM/pDNA was detected at the weight-mixing ratio of 12 with reading reaching 2.9 x 10^6 RLU/mg protein. On the other hand, PEGylated D-SPM showed negligible reporter gene expression at the weight-mixing ratio of 4 but then gradually increased until it reached a maximum level of 1.3 x 10^5 RLU/mg protein at w/w ratio of 10. Unfortunately, further increase in the weight-mixing ratio resulted in a decrease of the reporter gene expression.

Surprisingly, the D-SPM/pDNA exhibited higher gene expression when compared to PEGylaed D-SPM/pDNA for all various weight-mixing ratios, with significant differences at w/w ratio of 12 and 14. This discrepancy could be explained by the different strength of electrostatic interaction between the DNA helices of each plasmid and the D-SPM and the grafted D-SPM with PEG, which may play a significant role in the efficiency of cell transfection. As the D-SPM exhibited the higher luciferase activity in the cell culture, D-SPM was chosen for subsequent *in vivo* studies.

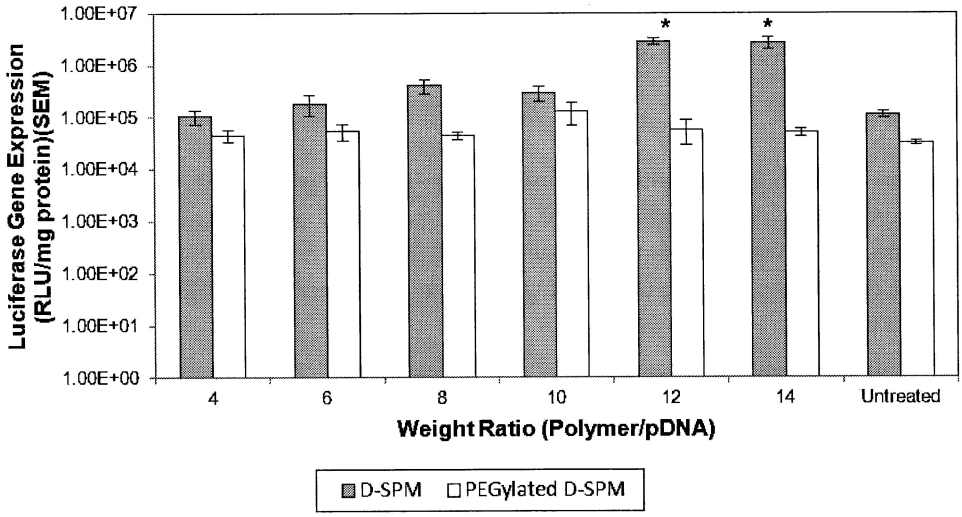

Figure 1. *Transfection efficiency of D-SPM/pDNA and PEGylated D-SPM/pDNA complexes at various weight-mixing ratios with 0.5 μg pCIKLux in COS-7 cells. Luciferase expression was measured as RLU/mg protein at 48 h post-transfection. Data are presented as mean ± S.E.M of experiments conducted in triplicate. Asterisks signify significant statistical differences*

Optimal w/w Ratio of Complex Preparation in Vivo

In order to determine the most optimal D-SPM/pDNA weight-mixing (w/w) ratio, BALB/c mice were instilled intranasally with 10 μg of pDNA complexed with different amount of D-SPM to give w/w ratio ranging from 13 to 18. Reporter gene levels were plotted as a function of complex weight-mixing ratio at 2 days post-treatment (Figure 2). The D-SPM/pDNA complex ranging from ratio 13 to 15 showed almost similar levels of gene expression to the untreated group. The maximal reporter gene expression was observed at weight-mixing ratio of 16, where 91.23 ± 30.18 RLU/mg protein was obtained, although not statistically significant compared to the rest of the group. Unfortunately, the subsequent increase ratio of the polycation failed to improve the reporter gene activity. It is speculated that increasing the w/w ratio may lead to the increase of the cationic dextran moiety and resulted in the increase of the size of the complex. This may eventually impedes its uptake once it reaches certain size due to the steric effect of the random charge distribution surface of the cationic carrier (Eliyahu *et al.*, 2007).

Subsequent studies to determine the optimal amount of pDNA for complexation and gene expressions time point profile employed D-SPM/pDNA w/w ratio of 16, as this ratio has been shown to exhibit the highest luciferase activity.

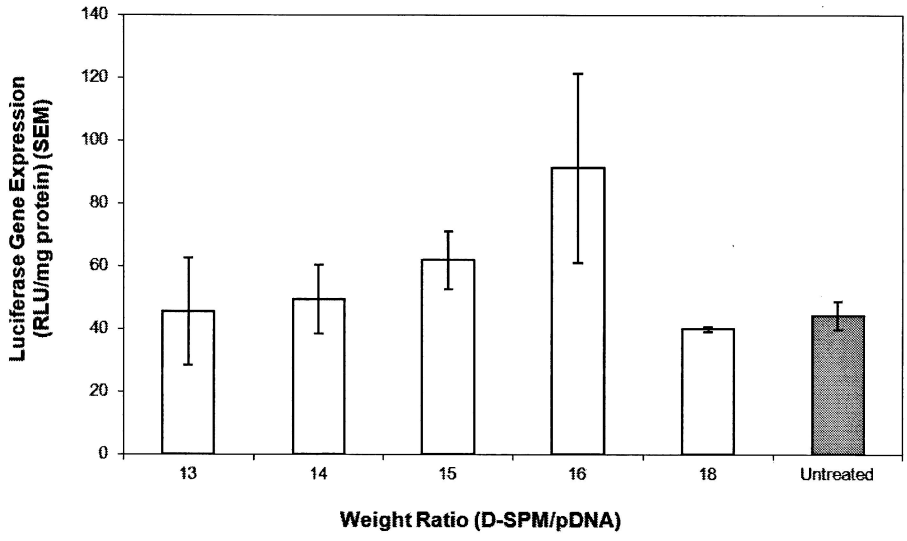

Figure 2. *Luciferase expression (RLU/ mg protein) in the trachea and lung of BALB/c mice following the administration of various weight-mixing ratios of D-SPM/pDNA complexes. Untreated mice were served as the control. Data are presented as mean ± S.E.M from 6 animals*

Optimal Amount of pDNA for Complex Preparation

To evaluate whether pDNA concentration can influence the transfection efficiency of the D-SPM at a fixed weight-mixing ratio, mice were intranasally instilled with D-SPM/pDNA complexes containing varying amount of pDNA. The weight-mixing ratio of the complexes was set to 16 while the amount of pDNA in the complex was varied from 7.5 μg to 17.5 μg per mouse.

A bell-shaped curve is presented in the graph as the amount of pDNA gradually increased (Figure 3). The highest gene expression level was detected from the D-SPM/pDNA complex containing 13.5 μg of pDNA, accounting for 158.1 ± 79.6 RLU/mg protein, which was approximately 3-fold higher compared to the untreated group. Unfortunately, this result was not significantly different to the rest of the group. Increasing the amount of the pDNA beyond 13.5 μg did not improve the level of reporter gene expression. Instead, a gradual decrease of luciferase activities was observed. As D-SPM/pDNA complex with 13.5 μg pDNA showed the highest reporter gene expression, subsequent experiments employed this amount of pDNA, while the w/w ratio was kept to 16.

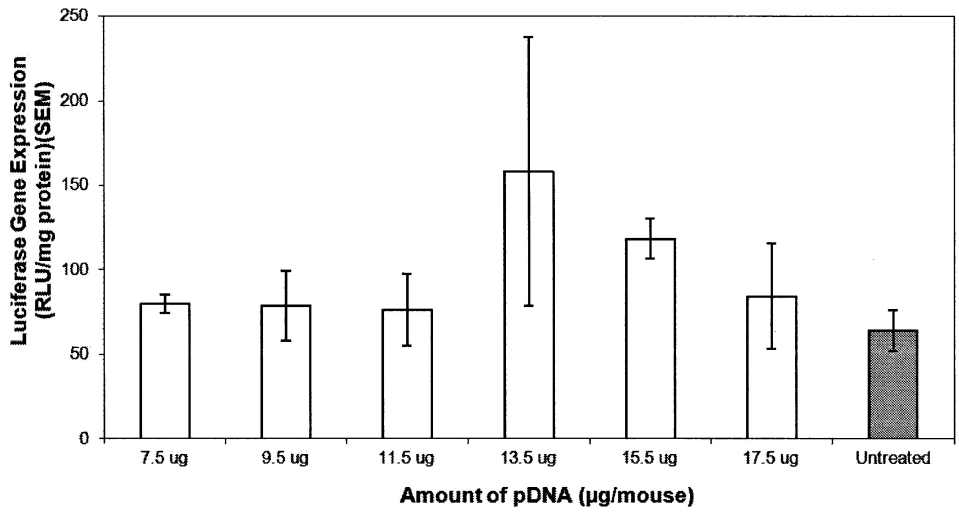

Figure 3. *Luciferase expression (RLU/ mg protein) in the trachea and lung of BALB/c mice following the administration of D-SPM complexed with different amount of pDNA, at 2 days post-treatment. Untreated mice were served as the control. Data are presented as mean ± S.E.M from 6 animals*

Time Point Profile

In the previous experiments, all the luciferase assays were performed at 2 days post-treatment, as suggested in the luciferase assay protocol (Promega, USA) and based on the study done by Hosseinkhani *et al.*, (2004), where it has been shown that the optimum gene expression was detected at 2 days post-treatment in mice. As this current study targeted different organ and cell types, a new time point that would show the maximal level of gene expression needed to be ascertained. To determine the time point, mice were instilled with D-SPM/pDNA complex at w/w ratio of 16, with the amount of pDNA kept to 13.5 μg. Maximum time point of seven days was chosen as the level of reporter gene expression mediated by a non-viral vector would normally reach negligible value by day 4 post-instillation (Gill *et al.*, 2001). The mice were sacrificed and the lungs were harvested for luciferase analysis at 6 hr, 1, 2, 4 and 7 days post-treatment.

The result shows that the luciferase gene expression peaked at day 1 post-treatment, with modestly significant luciferase activity of 234.6 ± 109.8 RLU/mg protein (Figure 4), almost 4-fold higher than the background level. However, after day 1 post-treatment, the luciferase activity declined gradually, such that at day 4 post-treatment, the value was statistically insignificant when compared to the background level (57.9 ± 11.3 RLU/mg protein).

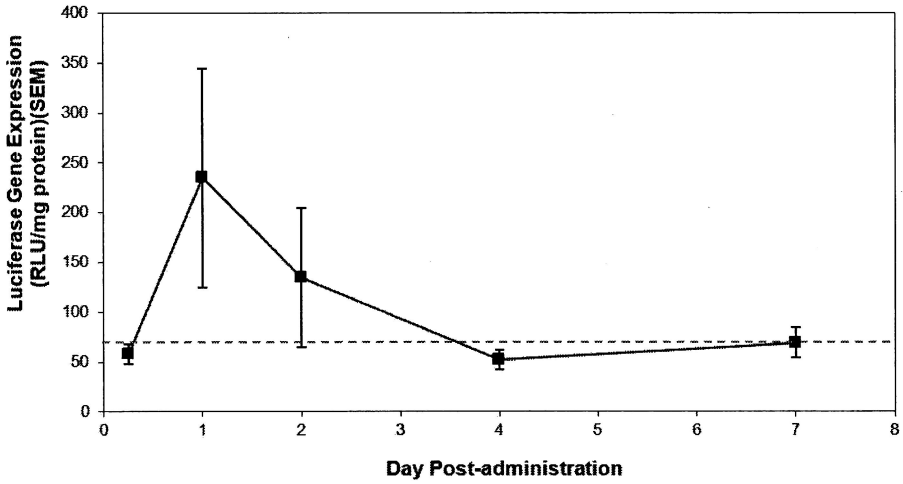

Figure 4. *Time-profile luciferase expression (RLU/ mg protein) in the trachea and lung of BALB/c mice following the administration of D-SPM/pDNA at ratio 16, containing 13.5 μg DNA. The horizontal dash line represents the approximate sensitivity of the assay. Data are presented as mean ± S.E.M from 6 animals*

Taken together, we have shown that the highest reporter gene activity was detected with D-SPM/pDNA at w/w ratio of 16, with complex containing 13.5 μg pDNA and at day 1 post-treatment. Unfortunately, the maximum value detected was only modestly higher compared to the untreated animals. This phenomenon could be due to several factors. The D-SPM/pDNA complexes could be efficiently removed by the reticuloendothelial system from the capillaries in the lung, which consequently resulted in the inefficiency of specific targeting capability of the polycation to the lung epithelial cells (Hosseinkhani *et al.*, 2004). Another possibility is the tendency of the pDNA to be released from the complex due to the interaction of the complexes with the serum proteins such as albumin, which consequently reduced the interaction between the intact pDNA with target cells (Eliyahu *et al.*, 2007).

Particle Size of D-SPM/pDNA Complex

The physical characteristic analysis of D-SPM/pDNA by the size measurement was carried out at w/w ratio of 16 and DNA concentrations of 15, 20, 25 and 30 μg. In concordance to the observation by Hosseinkhani *et al.*, (2005), all the D-SPM/pDNA complexes formed in this study were in nanometer range (Figure 5). At the concentration of 15, 20 and 25 μg of pDNA, the approximate mean diameters were 52.44, 68.85 and 93.41 nm, respectively. The complex loaded with 30 μg pDNA resulted in the largest complex size with a mean diameter of 115.49 nm. The overall results indicate that the size of the particle is directly proportional to the amount of pDNA used to prepare the complex. This phenomenon may be due to the interaction of the positively charged D-SPM and the increasing amount of negatively charged pDNA, which eventually contribute to the formation of less compact complexes.

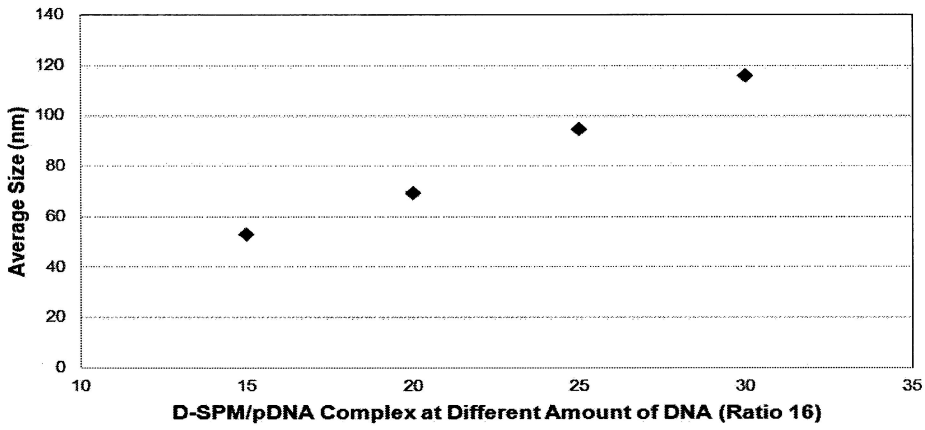

Figure 5. *Average particle size of D-SPM/pDNA as a function of the pDNA amount loaded to D-SPM at w/w ratio of 16, determined by Nanophox particle size analyzer*

CONCLUSION

The main objective of this project was to find the most optimal conditions for D-SPM gene delivery in the lungs of mice. Prior to the *in vivo* experimentation, we have shown that the D-SPM was more efficient at gene delivery when compared to its PEGylated form. Due to this reason, only the non-PEGylated form of the D-SPM was used in the subsequent *in vivo* study. Three variables examined in the lungs of mice were; (1) the weight-mixing (w/w) ratio of D-SPM to pDNA, (2) the amount of pDNA complexed with the D-SPM, and (3) the reporter gene expressions time point profile. We have observed that the highest gene expression in the lung was detected at w/w D-SPM/pDNA of 16, carrying 13.5 (g pDNA, and at 24 hr post-treatment. Although the maximum gene expression value observed was statistically significant, it was only a modest increase from the background value of the untreated mice. Concurrently, the physical characteristic of the D-SPM/pDNA, in term of its size was also analyzed. The size of all D-SPM/pDNA complexes produced was in a nanometer range. A directly proportional relationship was seen between the amount of the pDNA added to the D-SPM and the size of the complex. In a nutshell, these results demonstrate that D-SPM was able to deliver gene to the lung of mouse, with moderate efficiency. Improvement on the physiochemical properties of D-SPM may deem necessary to increase the transfection efficiency of this polycation in the mouse lung for future use in gene therapy for lung diseases.

ACKNOWLEDGEMENT

The researchers would like to thank the members of Medical Genetics Laboratory and UPM-MAKNA Cancer Research Laboratory. This work is supported by Research University Grant Scheme (RUGS), UPM.

REFERENCES

Edelstein, M. L., Abedi, M. R. and Wixon, J. (2007). Gene therapy clinical trials worldwide to 2007-an update. *J. Gene Med.* **9(10)**: pp 833-842.

El-Aneed, A. (2004). An overview of current delivery systems in cancer gene therapy. *J.Control Release.* **94(1)**: pp 1-14.

Eliyahu, H., Joseph, A., Schillemans, J.P., Azzam, T., Domb, A.J. and Barenholz, Y. (2007). Characterization and *in vivo* performance of dextran–spermine polyplexes and DOTAP/ cholesterol lipoplexes administered locally and systemically. *Biomaterials.* **28(14)**: pp 2339-2349.

Eliyahu, H., Joseph, A., Azzam, T., Barenholz, Y. and Domb, A. J. (2006). Dextran-spermine-based polyplexes-evaluation of transgene expression and of local and systemic toxicity in mice. *Biomaterials.* **27(8)**: pp 1636-1645.

Gill, D.R. , Smyth, S.E, Goddard, C.A., Pringle, I.A., Higgins, C.F., Colledge, W.H. and Hyde, S.C. (2001). Increased persistence of lung gene expression using plasmids containing the ubiquitin C or elongation factor 1alpha promoter. *Gene Ther.* **8(20)**: pp 1539-1546.

Guosen, H., Min, F., Xin, L. and Venkatraman, S. (2008). Design, synthesis and in vitro evaluation of a novel "stealth" polymeric gene vector. *Int. J. Pharm.* **350(1-2)**: pp 344-350.

Hosseinkhani, H. and Tabata, Y. (2005). Ultrasound enhances in vivo tumor expression of plasmid DNA by PEG-introduced cationized dextran. *J. Control Release.* **108(2-3)**: pp 540-556.

Hosseinkhani, H., Azzam, T., Tabata, Y. and Domb, A.J. (2004). Dextran-spermine polycation: an efficient nonviral vector for *in vitro* and *in vivo* gene transfection. *Gene Ther.* **11(2)**: pp 194-203.

Jo, J. and Tabata, Y. (2008). Non-viral gene transfection technologies for genetic engineering of stem cells. *Eur. J. Pharm. Biopharm.* **68(1)**: pp 90-104.

Kushibiki, T. and Tabata, Y. (2004). A new gene delivery system based on controlled release technology. *Curr. Drug Deliv.* **1(2)**: pp153-63.

Lee, M. and Kim, S.W. (2005). Polyethylene glycol-conjugated copolymers for plasmid DNA delivery. *Pharm Res.* **22(1)**: pp 1-10.

Li, S.D. and Huang, L.J. (2007). Non-viral is superior to viral gene delivery. *J.Control Release.* **123(3)**: pp181-183.

Lundstrom, K. and Boulikas, T. (2003). Viral and non-viral vectors in gene therapy: technology development and clinical trials. *Technol. Cancer Res.Treat.* **2(5)**: pp 471-486.

Robbins, P.D. and Ghivizzani, S.C. (1998). Viral Vectors for Gene Therapy. *Pharmacol.Ther.* **80(1)**: pp 35–47.

Sung, S.J., Min, S.H., Cho, K.Y., Lee, S., Min, Y.J., Yeom, Y.I. and Park, J.K. (2003). Effect of polyethylene glycol on gene delivery of polyethylenimine. *Biol Pharm Bull.* **26(4)**: pp 492-500.

Journal of Industrial Technology Vol. 19(1), 2010 - ICONT 2009, 179 - 196

A NOVEL FORMULATION AND OPTIMIZATION OF ASPIRIN NANO-EMULSION PREPARED BY CAVITATION INDUCED BY ULTRASONIC WAVES

Siah Ying Tang, Manickam Sivakumar*

School of Chemical and Environmental Engineering,
The University of Nottingham Malaysia Campus,
Jalan Broga, 43500 Semenyih, Malaysia

***(Sivakumar.Manickam@nottingham.edu.my)**

ABSTRACT : The preparation of poorly water soluble drugs in the form of nano-emulsion is of increasing interest in the current drug delivery system, as it appears as an excellent drug vehicle to facilitate the delivery of hydrophobic pharmaceutical ingredients into gastrointestinal tract, thereby improve the drug oral bioavailability. In the present study, an energy efficient ultrasonic cavitation method was utilized to prepare a well- optimized formulation of aspirin nano-emulsion by using a 20 kHz ultrasonic horn processor. It was found that the optimum level in terms of emulsion composition, acoustic amplitude, and ultrasonic processing time is crucial to achieve minimum droplet size. The present paper demonstrated that O/W nano-emulsions system of 20 wt% Lauroglycol® FCC and balance water with average droplet diameter as low as 232 nm could be achieved with the presence of 5 wt% Cremophore-EL as surfactant. Results are comparable to those emulsions prepared with a magnetic stirrer and an ultra-turrax homogenizer. The microscopic results showed that the emulsion droplet after 1 min ultrasound irradiation were almost spherical in shape and excellently stable with no apparent flocculation and coalescence over the two-week storage at room temperature. It is strongly suggested that the use of ultrasound for preparation of O/W aspirin nano-emulsions was superior in terms of droplet size and energy efficiency, as compared to conventional magnetic mechanical devices.

KEYWORDS : Nanoemulsion, aspirin, bioavailability, ultrasound, cavitation, efficiency

INTRODUCTION

The poorly water soluble aspirin (acetylsalicylic acid) is well-known as a non-steroidal anti-inflammatory drug (NSAID) which has been widely used in treatment of variety of pains and diseases due to its multi-therapeutic properties; for instance, anti-inflammatory, antipyretic, anti-rheumatic, analgesic and anti-platelet effect. Because of its established efficacy and proven safety record, aspirin appear to be one of the highly recommended medications in the pharmaceutical market and furthermore, it is always available over-the-counter (Amann & Peskar 2008, Vane & Botting 1998). However, the long-term administration of high dosage of aspirin can often result in several systemic adverse side effects like gastrointestinal (GI) intolerance, stomach bleeding, hypersensitivity and angio-edema (Laine & Mcquaid 2005). An attractive alternative drug delivery system had recently been proposed for administration of aspirin, and it revealed that the anti-inflammatory property of aspirin was significantly enhanced if delivered in the form of nano-emulsions prepared by Microfluidizer® processor (Li & Fogler 1978).

The production of nano- (submicron) emulsion with a narrow size distribution is of intensive research interest and has been attracting considerable attention in food (Kentish *et al.*, 2008, Jafari *et al.*, 2007, 2006, 2008, Floury *et al.*, 2003), pharmaceuticals (Subramanian *et al.*, 2008, Singh & Vingkar 2008, Mou *et al.*, 2008), personal care and cosmetics (Tal-Figiel 2007) industries in recent years. In pharmaceutical, nano-emulsion drug delivery system has become one of the promising and popular approaches, as it had been reported as an excellent candidate for efficient delivery of poorly soluble active pharmaceutical ingredients (API) by enhancing the drug dissolution as well as permeation due to its extremely low surface tension of the whole system and interfacial tension of O/W droplets.

According to (Stig *et al.*, 1996), emulsions are a class of disperse systems consisting of two immiscible liquids: the liquid droplets (dispersed/internal phase) are dispersed in another liquid medium (continuous/external phase). Nano-(submicron) emulsions are kinetically stable systems that they appear to be either transparent (droplet diameter < 200 nm) or milky (droplet diameter ≈ 500 nm) (Izquierdo *et al.*, 2002). They were also referred to as mini-emulsions. Their long term physical stability associated with leading small nanosized droplet enables the system to remain dispersed with no apparent flocculation or coalescence (Tadros 2005). Theoretically speaking, emulsion formation is non-spontaneous and a large amount of surfactant or energy is required to break a drop into smaller ones (submicron, as is the case with nano-emulsions).

The use of low frequency ultrasound for production of nano-(submicron) emulsions has been the focus of much recent work and they can be applied in variety of processes; biological, physical and chemical processes as it had been reported to intensify and enhance the

process of extraction, chemical reactions and micro-encapsulation (Suslick 1989). Recent studies has shown that, for production of nano-(submicron) emulsions, ultrasound had emerged as an excellent yet superior tool as compared to rotor stator in terms of droplet size and energy efficiency (Tadros 2005, Abismail *et al.*, 1999, Kentish *et al.*, 2008). Additionally, the results indicated that, in the case of producing an emulsion with desired diameter, the required amount of surfactant was significantly reduced; the energy consumption was considerably lower than other classical mechanical devices. More interestingly, the resulting ultrasonic–treated emulsions were all found to be excellently stable and more homogeneous with low polydispersity.

Admittedly, the final droplet size distribution of an emulsion is controlled by the rate between two opposing processes; droplet break-up and droplet re-coalescence (Floury *et al.*, 2004). Therefore, acquiring the knowledge of the effect of operating parameters and the emulsion formulation on droplet break-up and coalescence is essential as to obtain smaller droplet size with narrower distribution. The balance between these two dominant processes strongly depends on the energy input during emulsification and the geometry design of the device (Jafari *et al.*, 2008). Hence, in the present paper, the aims of the present study were to investigate the practicability and efficiency of an ultrasonic probe (or horn) system with acoustic power amplitude control in producing and developing an optimal novel aspirin O/W nano-emulsion, preferably with minimum surfactant concentration, prepared using ultrasound cavitation technique with an ultimate purpose to improve its oral bioavailability when delivered as liquid nano-emulsion.

MATERIAL AND METHODS

Chemicals and reagents

Aspirin (acetylsalicylic acid) were obtained from Fischer Scientific Co. Ltd, (Malaysia). Free samples of propylene glycol monolaurate (Lauroglycol™FCC), medium chain triglycerides (Labrafac lipophile®WL 1349), propylene glycol dicaprylocaprate, (Labrafac PG), diethylene glycol monoethyl ether (Transcutol®HP) were generously provided by Gattefosse Co, (Cedex, France). Isopropyl palmitate (IPM), and polyoxy 35 castor oil (Cremophore EL) were purchased from Sigma Aldrich Chemicals Company, (Malaysia). Water used in the preparation of formulations was obtained from a Milli-Q® Integral 5 water purification system (Millipore, Billerica, USA). All other chemicals used were of analytical grade.

Solubility study

The solubility of aspirin in various oils was determined. An excess of aspirin (approximately 1 g) was added into 2 ml of each vehicle in 15 ml screw-capped centrifuge tubes, followed by vortex mixing (Vortex Mixer; VM-10, Malaysia) for 5 min to ensure final solubilisation. Mixtures were shaken for 48 h at 37 ± 1.0 °C in a thermostatically controlled shaking water bath (Certomat® IS Incubator-shaker, France), followed by equilibrium at 25 °C for 24 h. Mixtures were then centrifuged at 5000 rpm for 5 min and the supernatant was filtered through a 0.22 μm PTFE (Teflon) membrane filter. Samples were suitably diluted with methanol and drug concentration in each oil was obtained via UV validated method at 275 nm using methanol as a blank. Results were reported in unit of mg/ml.

Ultrasonic experimental set-up for preparation of nano-emulsions

The apparatus used in this present study was a 20 kHz Ultrasonic Processor VCX 750 with 1/4" (6 mm) stepped microtip (Sonics & Materials, Inc, Newtown, USA). This ultrasonic immersion horn system primarily consisted of a power generator, a sealed converter and a horn microtip. The interior part of converter was made up from piezoelectric lead zirconate titanate crystals (PZT). The horn microtip (probe) was used to amplify and radiate the ultrasonic energy into the smaller volume sample (10 ml - 50 ml). The maximum peak-to-peak amplitude ζ of the probe is 123 μm. The maximum power output of 750 W can be delivered with the flexible control of amplitudes. The magnitude of amplitude ζ was displayed on the screen as a percentage of the maximum amplitude ζ_{max}. Due to the constraint of operating amplitude of microtip (ζ_{max} = 40 %), 3 levels of the maximum amplitude ζ_{max} : 25 %, 30 % and 35 % were tested in the current study.

Prior to the ultrasonic horn processing, the horn tip was submersed in the emulsion before the sonication was turned on to any desired amplitude. The control of ultrasonic processing time (2 - 6 min) was done using integrated process timer. During ultrasonic emulsification, all experiments were performed in a 20 ml scintillation vial containing about 10 ml of the pre-emulsion initially prepared by Bandelin SONOREX® Ultrasonic Bath. All emulsions formed were of the oil-in-water type. All experimental studies were carried out in batch type operation. As to allay the sonication thermal effect, cooling is provided to the samples of pre-emulsion immersed in an icebath while the ultrasonic treatment is applied. Despite applying the cooling effect, it is unlikely to keep the temperature of sample at constant level, especially when the longer sonication time with higher operating amplitude is performed through out the experimental study. For that matter, further investigations could possibly be carried out to study the thermal effect of ultrasonic processing on particle size distributions of final emulsions. Therefore, each

emulsion was carefully sampled and subjected to particle size analysis after 24 hr preparation.

Experimental parameters

The present study investigated the influence of composition of emulsion and processing variables of ultrasonic horn tip system on production of a novel oil-in-water type aspirin nano-emulsion with acoustic cavitation. The characteristics of emulsions after the preparation formed were observed in terms of particle size distributions and stability.

The studied parameters and experimental conditions are summarized in Table 1.

Table 1. Experimental parameters

No.	Parameters studied		
1	Oil dispersed phase (wt%)	:	7.5,15, 20, 25, 30, 35
2	Surfactant concentration (wt%)	:	1, 3, 5, 5.5, 6
3	Co-surfactant concentration (wt%)	:	0, 1, 2, 3, 4
4	Ultrasonic amplitude (μm)	:	30.75, 36.90, 43.05

Emulsification induced by acoustic cavitation

First of all, as noted above, in an ultrasonic processor system, the electrical energy is converted into mechanical energy in the form of oscillating vibration due to the repetitive expansion and contraction action induced by piezoelectric lead zirconate titanate crystals. Secondly, this mechanical vibration is transmitted to the horn tip and then transformed into acoustical energy in the form of ultrasonic waves which propagate through the surrounding liquid medium. At high intensity ultrasound, the liquid molecules oscillate in phase with the expansion and compression cycles caused by the pressure fluctuations of the acoustic waves. Millions of microbubbles or cavities are formed when the local vapor pressure is reduced to that of the liquid medium resulting from the large negative pressure associated with the expansion cycle of the sound waves. These bubbles will continue to grow and contract under the two alternating cycles. The growing bubbles will eventually reach their critical size where they no longer sustain themselves, and then leads to the subsequent collapse of the microbubbles. This local phenomenon is referred to as cavitation (Suslick 1989). This event causes extreme levels of highly localized turbulence driven by the millions of intense shock waves generated at the implosion sites.

The generated enormous concentrated energy as a result of the micro-implosions acts as a powerful yet efficient tool of breaking up the larger primary oil droplets into a liquid medium. However, the exact process of oil droplet formation and disruption due to acoustic cavitation is not yet fully understood because of scant supporting evidence, rendering these crucial explanations unsubstantiating as it stands. There are two possible mechanisms which are believed to be responsible for acoustic emulsification (Li & Fogler 1978). (1) Droplet formation as a consequence of the instability of interfacial waves produced within the acoustic field. (2) Droplet break-up by the acoustic cavitation: the formation, growth, and subsequent collapse of cavities.

Emulsion droplet size analysis

The particle size of the finer emulsions were analyzed by Zetasizer Nano ZS (Malvern Instruments, UK) at a wavelength of 635 nm and at a scattering angle of 90° at 25 °C. The size measurement of the emulsions formed was performed by Dynamic Light Scattering particle size analyzer, which was used to measure the Brownian motion of the particles, which indirectly proportional to particle size.

Microscopic Observation

An inverted microscope (Olympus, model IX51) equipped with a mounted CCD video camera module was used to perform a morphological image study of the geometric shape of droplets formed in the emulsions prepared by MST Basic magnetic stirrer, Ultra-Turrax T18® Basic, and Ultrasonic Processor VCX 750. During the image characterization, a 25 μl emulsion of each sample was placed on the glass slide without any dilution. Phenomenon of flocculation and coalescence that bear on the instability of emulsions after two-week storage was carefully studied.

RESULTS AND DISCUSSION

Solubility study

The solubility of poorly soluble drug in oil is an essential pre-requisite for the screening of oily phase component for nano-emulsion. The main reason is that the increased solubility of drug in oil phase will commensurately enhance the ability of nano-emulsion to maintain drug in solubilized form. The solubility of aspirin in various oil vehicles is presented in Figure 1. Amongst the various oily vehicles tested in this study, Lauroglycol™FCC was identified to have the highest drug solubility compared to other oils. This is attributable to its

virtue of good solvent properties which promote the solubility of aspirin and water penetration. In this work, Cremophore EL, a non-ionic surfactant was selected for study due to its superior emulsifying performance with higher HLB number (Mou *et al.*, 2008, Suclick 1989, Li & Fogler 1978) and its nature of low toxicity and tastelessness. Additionally, Cremophore EL was reported to possess inhibitory effects on p-gp ad CYP enzymes, thus it was usually accepted for oral use (Chen 2008). Besides, the good miscibility of Lauroglycol™FCC with Cremophore EL was visually confirmed by the clarity study of different oil/surfactant solution mixture (result not shown) where the resulting emulsion is relatively stable without no apparent flocculation or creaming being observed. The proper selection of oil and surfactant having maximal solubilizing potential is of paramount importance in improving the drug loading capacity and promoting the formation of emulsion prior to the preparation of optimal formulation.

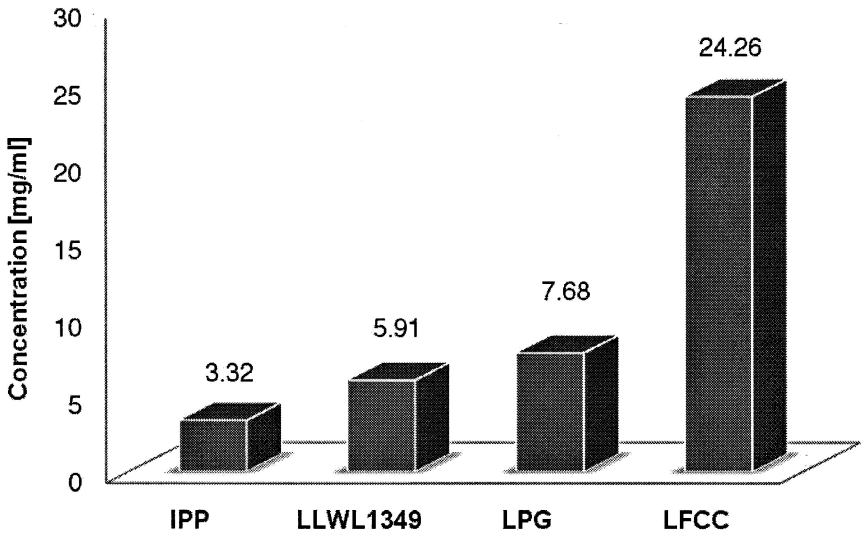

IPP - Isopropyl Palmitate	LPG - Labrafac PG
LL WL 1349 - Lipophile ®WL 1349	LFCC - Lauroglycol™ FCC

Figure 1. *Solubility of aspirin in various oily vehicles*

Optimization of dispersed phase weight fraction

At constant energy density in terms of operating amplitude, the average emulsion droplet size increased strongly with increasing weight fraction of dispersed phase, namely the oil content (Figure 2). This typical trend is in consistent with the result of some earlier experimental works and comparative investigations by ultrasonic emulsification (Kentish *et al.*, 2008, Jafari *et al.*, 2007, 2006, 2008, Pangu & Feke 2004, Gaikwad & Pandit 2008, Behrend & 2000, Majumdar *et al.*, 1998, Leong *et al.*, 2009). To elucidate this result, several possible reasons had been proposed which were believed to be responsible for the observed increased droplet size. Firstly, with rising of oil content, droplet disruption process would be more difficult as due to increased viscosity of the dispersed phase which leads to the rising of the critical Weber Number, ($N_{we_{Crit}}$), and hence the droplet break-up rate would be severely restricted. Secondly, for an emulsion with fixed surfactant concentration, it is entirely possible that there is an insufficient amount of surfactant present to cover the freshly formed interface completely and thus this limitation increases the average droplet size. Thirdly, part of the effect could be attributed to the increased rate of collision frequency, particularly at low surfactant concentration, between the emulsion droplets followed by an ultimate increase of coalescence frequency. In this study, all the resulting emulsions appeared to be milky except the emulsion with oil content of 7.5 wt% where clear aqueous solution with slightly bluish was formed. Both emulsions of 7.5 wt% and 15 % exhibited the minimum average droplet size vis-à-vis other emulsions, with Z-average diameter at 84 nm and 165 nm,

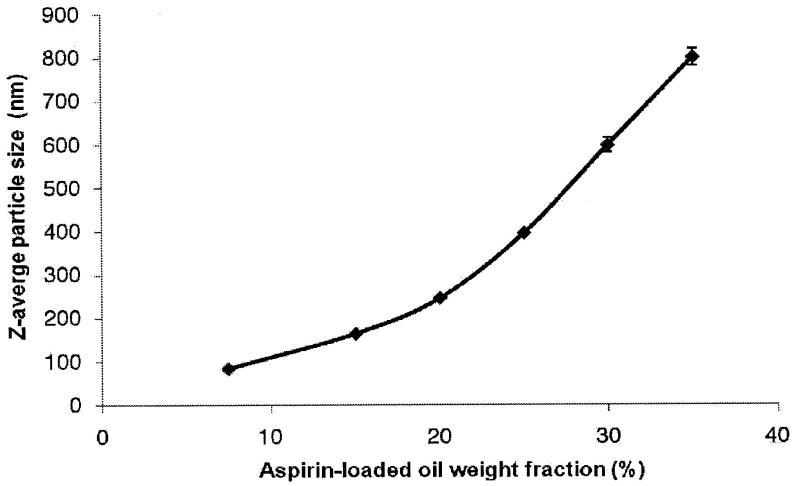

Figure 2. *The effect of oil concentration on the average droplet diameter of O/W emulsions initially stabilized by 5 wt% Cremophore EL. About 10 g samples were sonicated for 3 min at operating amplitude of 24.60 μm*

respectively. In spite of this, the incorporation of larger amounts of oil (≈ 20 wt %) is always preferred in pharmaceutical dosage form as it correspondingly increases the drug content presented in the emulsions, and thus increases the efficacy of the drug when orally administered.

Optimization of surfactant concentration

As mentioned earlier, the final particle size of an emulsion is the result of equilibrium of droplet break-up and droplet coalescence. The rate of droplet break-up is primarily controlled by the type and amount of shear applied to droplets as well as the droplet resistance to deformation whereas the rate of droplet coalescence is determined by the ability of the surfactant to rapidly form an absorbed monolayer onto the newly formed interface (Tadros, 2004). The latter is mainly governed by the surfactant surface activity and concentration. As shown in Figure 3, there is a clear correlation of the surfactant concentration with the average emulsion droplet size. Initially, a dramatic decline in average droplet diameter was achieved with the incorporation of increasing amount of Cremophore EL. However, above 5.5 wt% of Cremophore EL content, the opposing trend was being observed where there was an increase of average emulsion size. It infers that, at low Cremophore EL concentration, there is an insufficient amount of surfactant molecules for complete coverage of fresh interface; thereby the newly formed droplets tend to coalesce and hence the resulting average emulsion size is increased.

At the beginning, the initial increasing amount of surfactant results in a steady reduction in term of average emulsion droplet size as there are more and more surfactant molecules available for surface coverage of newly formed droplets. But, the trend reverses, that is, the emulsion droplet size increases once the surfactant amount present is in excess. This indicates that the surfactant concentration in the emulsion system is apparently sufficient for rapid interfacial absorption onto newly formed droplets. Therefore, any further increase of surfactant content will, when a surfactant concentration plateau is reached, not lead to further reduction in average emulsion size droplet.

Similar result had been reported in previous work, (Abismail *et al.*, 1999) and it was found that the resulting particle size of both O/W emulsions prepared by ultrasonic horn and rotor-stator system was significantly decreased with increasing of surfactant concentration (Tween 60), but remained unchanged when it approached the saturation absorption of surfactant. Nonetheless, an increase of emulsion droplet size after surfactant concentration plateau may due to the increased continuous phase viscosity in the O/W emulsion system (Behrend *et al.*, 2000). In other words, the addition of hydrophilic surfactant leads to the increase of the viscosity of the continuous phase, thereby partly suppresses the further emulsion droplet disruption mechanism from cavitation.

Figure 3 demonstrates that the surfactant concentration region where minimum average droplet size can be obtained is lying in the range of 5 to 6 wt% of Cremophore EL. Therefore, the least amount of 5 wt% Cremophore EL was selected for the subsequent studies. Again, most importantly, it indicates that, for a desired emulsion droplet size, less surfactant is needed when ultrasonic emulsification is applied.

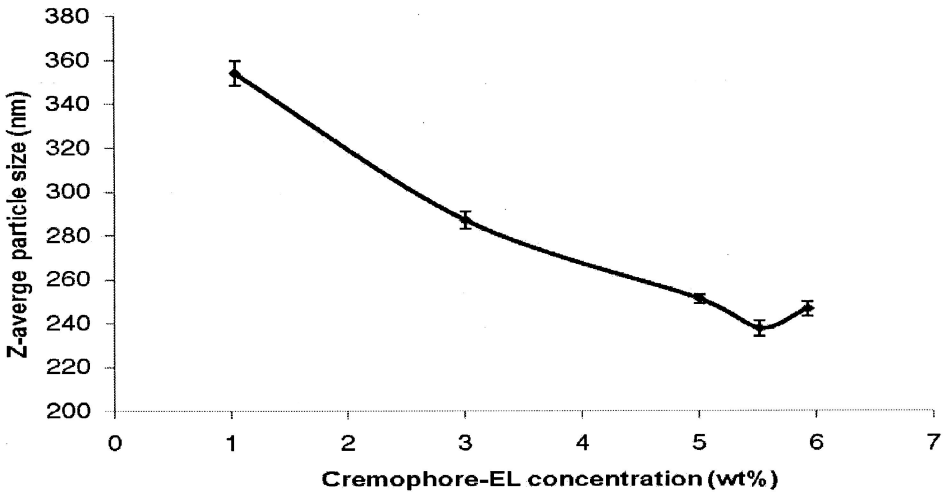

Figure 3. *The effect of Cremophore EL content on the average droplet diameter of 20 wt% O/W emulsions. About 10 g samples were sonicated for 3 min at operating amplitude of 24.60 μm*

Influence of co-surfactant concentration on droplet size

Regarding the effect of co-surfactant concentration, the result shown in Figure 4 is opposite of what is expected, which the average emulsion particle size increased slowly with the incorporation of increasing amount of Transcutol®HP. The gradual increase of emulsion droplet size is possibly caused by the poor solubilizing potential of Transcutol®HP as well as its poor surfactant/co-surfactant synergy with Cremophore EL despite its larger content of diethylene glycol. The inefficiency of Transcutol®HP as a lipophilic co-surfactant may partially be attributed to its longer linear molecular chain length which restricts its solubility behaviour. Consequently, the obtained average emulsion size tends to be bigger rather than expected smaller droplet size. Hence, in the present work, O/W emulsion with single surfactant system was used for the subsequent study on the ultrasonic processing parameter in preparation of optimal emulsion.

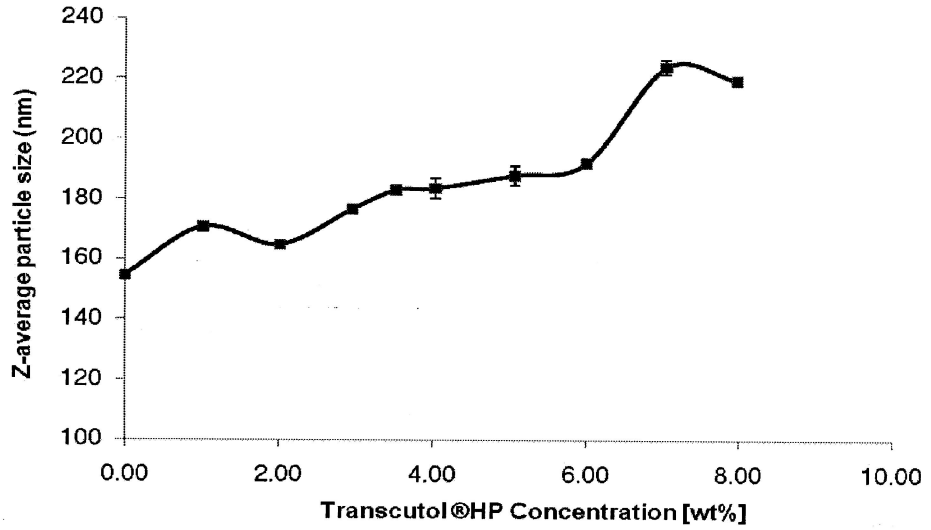

Figure 4. *The effect of Transcutol®HP content on the average droplet diameter of 20 wt% O/W emulsions initially stabilized by 5 wt% Cremophore EL. About 10 g samples were sonicated for 3 min at operating amplitude of 24.60 μm*

Optimization of applied ultrasonic amplitude

Figure 5 shows the emulsion droplet size distribution for a set of 20 wt% Lauroglycol™FCC O/W emulsions stabilized by 5 wt% Cremophore EL. At operating ultrasonic amplitude of 36.90 and 43.05 μm, it was found that smaller average emulsion droplet size was, surprisingly, achieved with a total sonication time of only 30 seconds whereas an optimum sonication time of 1 min was required, as for the case of low ultrasonic amplitude of 30.75 μm, in order to produce desired result with smaller droplet size. As shown in Figure 5, it has been observed that emulsion droplet sizes reach a minimum point at initial operating time of ultrasound and then increase at specific higher energy densities. This typical trend has been found to be similar with the earlier investigations of high-energy emulsification, but at an intermediate processing point (Jafari *et al.*, 2007 and Desrumaux & Marcand, 2002). In these studies, this phenomenon has been described as "over-processing" (Jafari *et al.*, 2007, 2006, Floury *et al.*, 2003). This effect can be explained by the so called secondary acoustic forces.

As mentioned earlier, in the present study, the use of stepped microtip with smaller diameter (6 mm) is known to amplify and radiate the ultrasonic energy in a narrower and more concentrated field. Because of this, the intensity of cavitation (number of collapsed event) will increase with an increase of sonication time, eventually gives rise to a higher value of secondary acoustic force. According to Pangu and Feke (Pangu & Feke, 2004), owing to the negative value of acoustic contrast factor of the dispersed oil droplets, they will be driven towards the pressure antinodes of the standing ultrasonic wave field by the primary acoustic forces and then followed by subsequent coalescence caused by the secondary acoustic forces. Therefore, the surrounding droplets adjacent to the region of acoustic radiation forces would tend to coalesce and form larger emulsion droplets thereby result in increased particle size.

On the other hand, the effect of ultrasonic amplitude on the average emulsion droplet size can also be seen in Figure 5. It shows that as the operating acoustic amplitude increases, the particle size distribution level of resulting emulsion reduces, but at a small degree of extent. Evidently, the energy conversion of the ultrasonic power input is less efficient when higher operating acoustic amplitude is applied. It indicates that the efficiency of the horn transducer decreases with an increasing amplitude. Three main reasons had been proposed to explain this observed phenomenon: (1) Increase of dielectric and mechanical losses in the immersion horn system at increased operating amplitude (Lin & Zhang, 2000). (2) Microbubble cloud cushioning effect as a result of increased cavitation intensity at higher acoustic amplitude. This effect hinders the remaining emulsion from further exposure to ultrasonic radiation forces and thus results in lower efficiency of horn transducer. (3) Strong decrease of acoustic load of irradiated liquid caused by the decreased acoustic impedance $(Z_0 = \rho_f c_f)_0$. As a consequence of decreasing acoustic load, the amount of energy required for constant amplitude of the vibrating horn tip is therefore reduced which, in turn, leads to a reduction of measured power quantity delivered to the emulsion system (Loning *et al.*, 2002). Despite of these effects, the resulted emulsions with Cremophore EL as surfactant, when ultrasonic immersion horn system is used, presented excellent result of monomodal particle size distributions with Z-average droplet diameter of around 200 nm and low polydispersity index (PdI) after 1 min sonication (Figure 6).

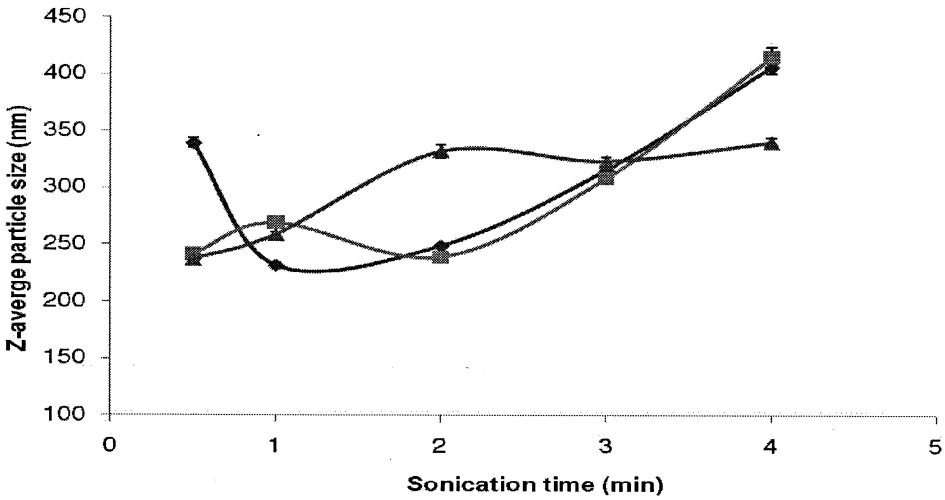

Figure 5. *Average emulsion droplet size (Z-average diameter) as a function of sonication time at three different ultrasonic amplitude for 20 wt% oil emulsions stabilized by 5 wt% Cremophore EL. Emulsions were prepared in the 20 ml batch vial using Ultrasonic Processor VCX 750*

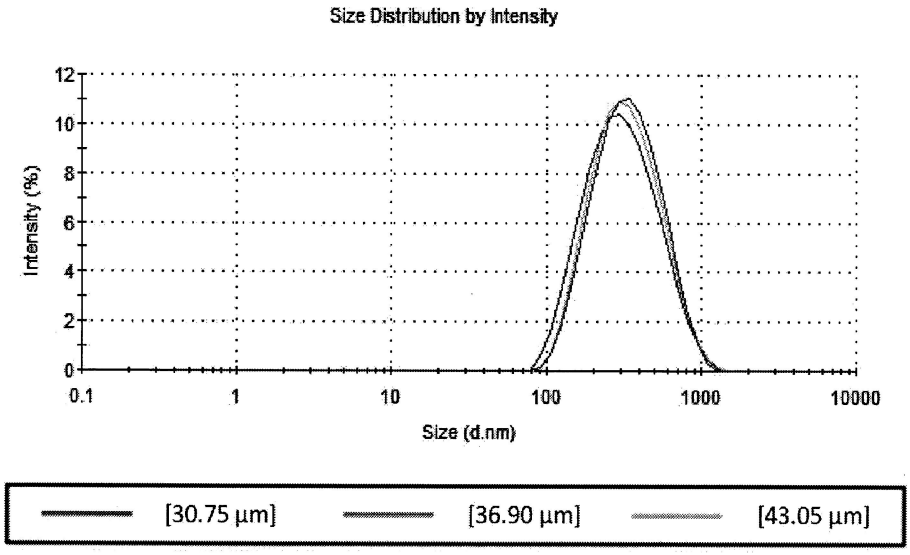

Figure 6. *Intensity-weighted particle size distributions of 20 wt% oil /5 wt% Cremophore EL O/W emulsions. Emulsions were sonicated for 1 min at three different ultrasonic amplitudes on the specific power densities*

Emulsion stability

As shown in Figure 7, microscopic observations reveal that the oil droplets of aspirin nano-emulsions prepared by three different processes were almost spherical in shape after they were being stored at room temperature for two weeks. Most interestingly, it shows that the emulsion prepared by ultrasonic horn processor exhibited superior homogeneity with its nanosized oil droplets, as compared to other emulsions. Additionally, the oil droplets of ultrasonic-treated emulsion were all finely dispersed in the water medium in more uniform manner relative to emulsion prepared by Ultra-Turrax homogenizer. The result is in line with Dynamic Light Scattering particle size analysis, showing that the aspirin emulsion droplets are present in nanometer scale, ranging around 200 nm (Table 2). Further study to increase the stability of the aspirin nano-emulsions against Ostwald Ripening effect will be the future subject of investigations of this project.

Table 2. Comparison of particle size distributions of emulsions produced by different mechanical methods.

Emulsion Preparation Method	Magnetic Stirring	Ultra-Turrax Homogenization	Ultrasonic Emulsification
Z-average size (d.nm)	1160	359	232
Polydispersity Index (PdI)	0.971	0.379	0.309

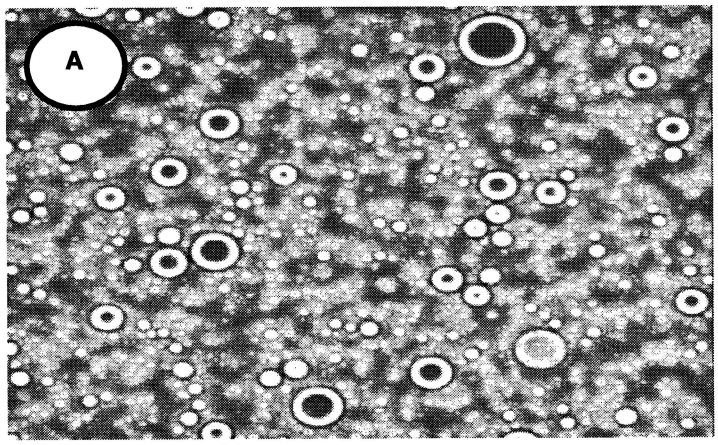

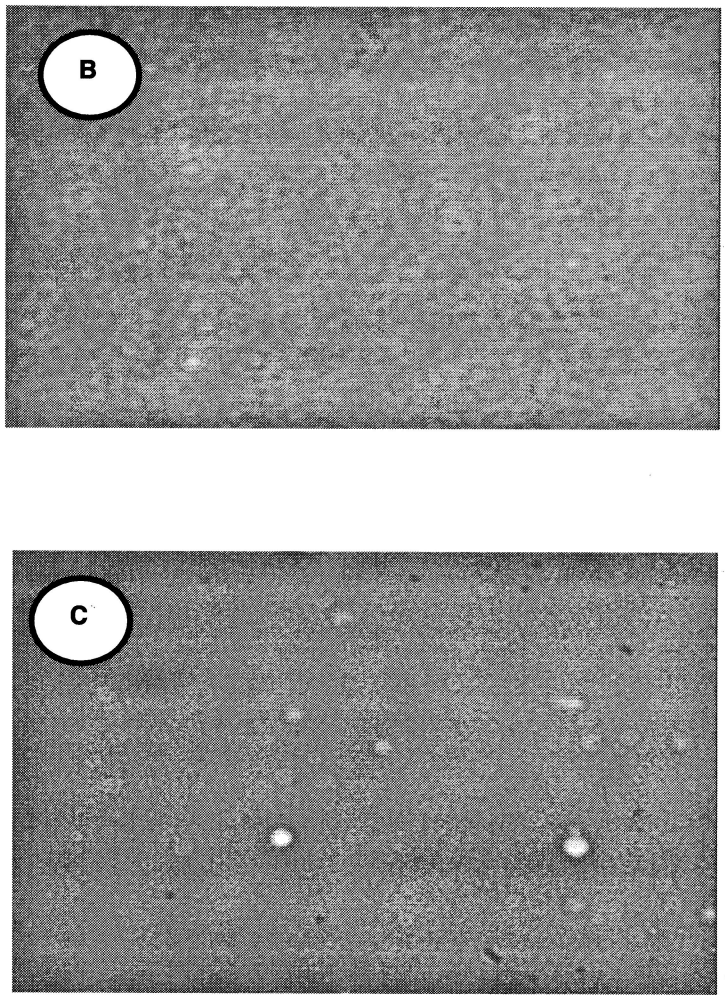

Figure 7. *Microscopic views (× 200) of 20 wt% oil /5 wt% Cremophore EL with balance water after 2-week storage, prepared at T = 25 °C through three different methods: (A) Magnetic stirring (7 hrs) ; (B) Ultra-Turrax homogenization (5 min at 13,500 rpm); (C) Ultrasonic emulsification (1 min at 30.75 μm amplitude)*

CONCLUSIONS

In the present paper, it has been evidently shown that ultrasound cavitation is a powerful yet promising approach in efficient production of aspirin nano-emulsions with smaller average particle size around 230 nm. Similar to prior works, the results has confirmed that there is an optimum level of emulsion composition, acoustic amplitude, and ultrasonic processing time where minimum droplet size could be achieved. On the one hand, an improvement of the efficiency of ultrasonic horn processor, particularly when operating at higher acoustic amplitude, is essential in order to effectively further reduce the mean particle size of emulsion below 200 nm. Nevertheless, prior to this, a study on the influence of dug loading on the droplet size and stability is underway of current investigations in this optimization study for preparation of optimal aspirin nano-emulsion.

ACKNOWLEDGMENT

This project was financially supported by the research grant from Malaysia Ministry of Science, Technology and Innovation *(MOSTI).* This financial assistance is gratefully acknowledged.

REFERENCES

Abismail, B., Canselier, J.P., Wilhelm, A.M., Delmas, H., and Gourdon, C. (1999). Emulsification by ultrasound: drop size distribution and stability. *Ultrasonics Sonochemistry.* **6(1–2)**: pp 75–83.

Amann. R., and Peskar. BA. (2002). Anti-inflammatory effects of aspirin and sodium salicylate. *European Journal of Pharmacology.* **447**: pp 1-9.

Behrend, O., Ax, K., and Schubert, H. (2000). Influence of continuous phase viscosity on emulsification by ultrasound. *Ultrasonics Sonochemistry.* **7**: pp 77–85.

Chen, M. L. (2008). Lipid excipients and delivery systems for pharmaceutical development: a regulatory perspective. *Advance Drug Delivery Reviews.* **60**: pp 768–777.

Floury, J., Desrumaux, A., Axelos, M.A.V., and Legrand, J. (2003). Effect of high pressure homogenization on methylcellulose as food emulsifier. *Journal of Food Engineering.* **58**: pp 227–238.

Gaikwad, S.G., and Pandit, A.B. (2008). Ultrasound emulsification: effect of Ultrasonic and physicochemical properties on dispersed phase volume and droplet size. *Ultrasonics Sonochemistry.* **15**: pp 554–563.

Izquierdo, P., Esquena, J., Tadros, T.F., Dederen, C., Garcia, M.J., Azemar, N., *et al.* (2002). Formation and stability of nano-emulsions prepared using the phase inversion temperature method. *Langmuir.* **18**: pp 26–30.

Jafari, S.M., Assadpoor, E., He,Y., and Bhandari, B. (2008). Re-coalescence of emulsion droplets during high-energy emulsification. *Food Hydrocolloids.* **22**: pp 1191-1202.

Jafari, S.M., He, Y., and Bhandari, B. (2006). Nano-emulsion production by sonication and microfluidization – A comparison. *International Journal of Food Properties.* **9**: pp 475–485.

Jafari, S.M., He, Y., and Bhandari, B. (2007). Production of sub-micron emulsions by ultrasound and microfluidization techniques. *Journal of Food Engineering.* **82 (4)**: pp 478–488.

Kentish, S., Wooster, T.J., Ashokkumar, M., Balachandran S., Mawson, R., and Simons, L. (2008). The use of ultrasonics for nano-emulsion preparation. *Innovative Food Science and EmergingTechnologies.* **9**: pp 170–175.

Laine, L., and McQuaid, k. (2005). Bleeding complications related to aspirin dose. *American Journal of Cardiology.* **96**: pp 1035-1036.

Leong, T.S.H., Wooster, T.J., Kentish, S.E., and Ashokumar, M. (2009). Minimising Oil droplet size using ultrasonic emulsification. *Ultrasononic Sonochemistry.* **16**: pp 721-727.

Li, M.K., and Fogler, H.S. (1978a). Acoustic emulsification. Part 1. The instability of the oil- water interface to form the initial droplets. *Journal of Fluid Mechanics.* **88(3)**: pp 499–511.

Li, M.K., and Fogler, H.S. (1978b). Acoustic emulsification. Part 2. Break-up of the larger primary oil droplets in a water medium. *Journal of Fluid Mechanics.* **88(3)**: pp 513–528.

Lin, S., and Zhang, F.(2000). Measurement of ultrasonic power and electro-acoustic efficiency of high power transducers. *Ultrasonics.* **37**; pp 549-554.

Loning, J., Horst, C., and Hoffman, U. (2002). Investigations on the energy in sonochemical processes. *Ultrasononic Sonochemistry.* **9**: pp 169-179.

Majumdar, S., Kumar, P.S., and Pandit, A.B. (1998). Effect of liquid-phase properties on ultrasound intensity and cavitational activity. *Ultrasononic Sonochemistry.* **5**: pp 113-118.

Mou. D., Chen. H., Du D., Mao. C., and *et.al.*, (2008). Hydrogel-thickened nanoemulsion system for topical delivery of lipophilic drugs. *International Journal of Pharmaceutics.* **353**: pp 270–276.

Pangu, G.D., and Feke, D.L. (2004). Acoustically aided separation of oil droplets from aqueous emulsions. *Chemical Engineering Science.* **59(15)**: pp 3183-3192.

Singh, K.K., and Vingkar, S. (2008). Formulation, antimalarial activity and biodistribution of oral lipid nanoemulsion of primaquine. *International Journal of Pharmaceutics.* **347**: pp 136–143.

Stig, E.F., Lisa, G.Q., and Martha, L.H. (1996). Theory of emulsions. In: Pharmaceutical dosage forms disperse system volume 1, ed. Herbert, A.L., Martin, M.R., and Gilbert, S.B., Marcel Dekker, Inc., New York, pp 53-89.

Subramanian, B., Kuo, F., Ada, E., Kotyla, T., Wilson, T., Yoganathan, S., and Nicolosi, R. (2008). Enhancement of anti-inflammatory property of aspirin in mice by a nano-emulsion preparation. *International Immunopharmacology.* **8**: pp 1533-1539.

Suslick, K.S . (1989) The chemical effects of ultrasound. *Scientific American.* February : pp 80-86.

Tadros, T.F. (2005). Surfactant in nano-emulsions. In: *Applied surfactants: Principles and applications.* Wiley-VCH Verlag GmbH & Co. KGaA, Weinheim, Germany, pp 285-298.

Tadros, T.F., and Vincent, B. (1983). Encyclopedia of Emulsion Technology, ed. Becher, P. Marcel Dekker, New York. pp 129-209.

Tadros, Th.F., Izquierdo, P., Esquena, J., and Solans, C. (2004). Formation and stability of nano-emulsions. *Advance Colloid Interface Science.* **108–109**: pp 303–31.

Tal-Figiel, B. (2007). The formation of stable W/O, O/W, W/O/W cosmetic emulsions in an ultrasonic field. *Chemical Engineering Research and Design.* **85 (A5)**: pp 730–734.

Vane. J.R., and Botting. R.M. (1998). Mechanism of action of nonsteroidal anti-inflammatory drugs. *American Journal of Medicine.* **104(3A)**: pp 2S – 8S discussion 21S- 22S.